NASA Technical Memorandum 82433

Space Processing Applications Rocket Project SPAR VI Final Report

OCTOBER 1981

NASA

NASA Technical Memorandum 82433

Space Processing Applications Rocket Project SPAR VI Final Report

R. Chassay, Compiler
George C. Marshall Space Flight Center
Marshall Space Flight Center, Alabama

NASA
National Aeronautics
and Space Administration

Scientific and Technical
Information Branch

1981

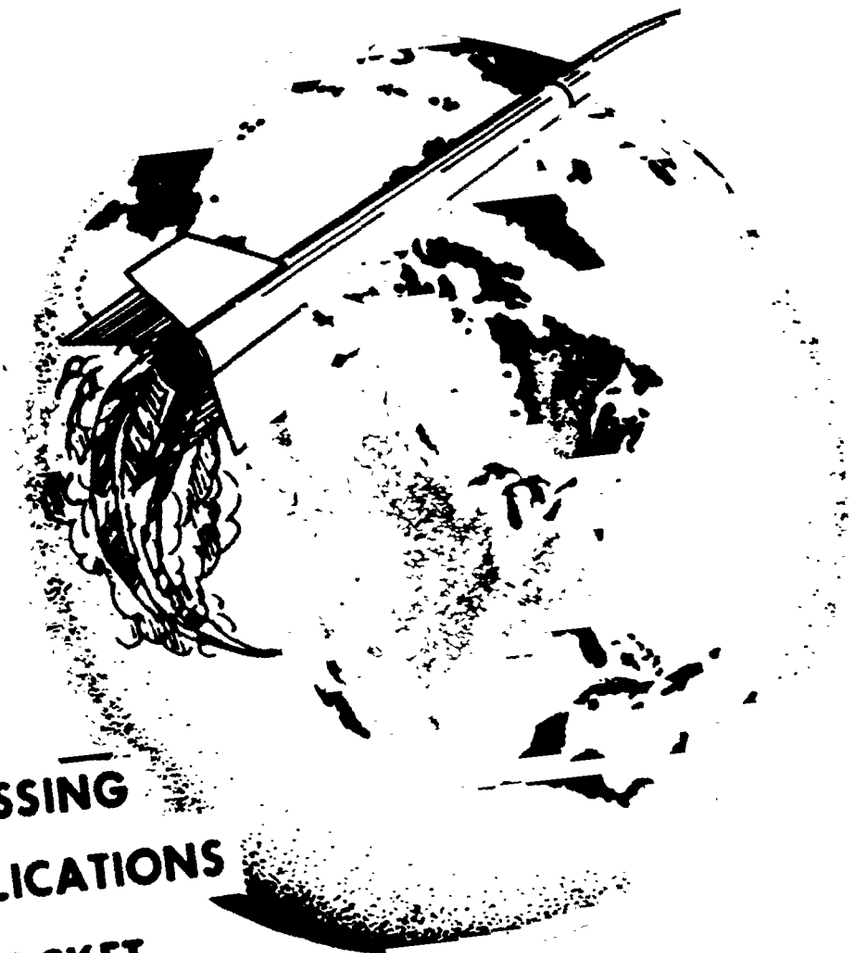

SPACE
PROCESSING
APPLICATIONS
ROCKET

TABLE OF CONTENTS

CHAPTER I

SPACE PROCESSING APPLICATIONS ROCKET (SPAR) PROJECT

SPAR VI - FINAL REPORT

INTRODUCTION

The unique low-g environment of space affords an opportunity for exploring and developing techniques for processing a variety of materials without the constraining gravitational influences as evidenced with the processing of liquid phase materials or melts on Earth. The Materials Processing in Space (MPS) program is directed toward the stimulation and development of the associated science and technology required to pursue these investigations. This NASA activity is undertaken in cooperation with the scientific community and includes follow-on studies of specific areas of scientific research emphasizing those selected nvestigations of materials and processes which best demonstrate potential benefit from the enhanced sensitivity of the controlled processing in a low-g environment. Examples of interest in the program are the reduction and/or elimination of adverse thermal effects such as convection, sedimentation of heavy particles, buoyancy rise and positioning aspects of bubbles in liquids or melts, and the stratification effects of particulates of variable densities in solution. These and similar studies are considered to be the means to expand the limiting frontier in the development of new materials and processes which are envisioned ultimately to be of immeasurable benefit to mankind. As complementary to the research and technological nature of the investigations, the evolving emphasis is being directed, with the advent of the Shuttle and increased payload potential, toward commercialization and the development of self-sustaining programs yielding direct product benefit.

The initial precursory zero-g demonstrations and investigations associated with this family of scientific experiments were proposed and developed for the Apollo flights beginning in the late 1960's and conti. ued with Skylab and Apollo-Soyuz flights through the mid-1970's. During the period between the close of that era and the orbital space flights on the Space Shuttle in the 1980's, the Space Processing Applications Rocket (SPAR) project has provided the only viable flight opportunity for low-g scientific investigations for experimenters and is serving in a precursory role for planned and approved Shuttle investigations. It is also anticipated that sounding rocket flights could satisfy a continuing need and a complementary role for the establishment and definition of future precursory Shuttle experiments.

The SPAR project is part of the Materials Processing in Space (MPS) program of the Office of Space and Terrestrial Applications which is responsible for directing research into the scientific effects of materials processing in the unique environment of space. This effort involves participation and interaction from various disciplines of the scientific community, government-supported laboratories, universities, and industrial organizations, in addition to foreign participation.

The Black Brant VC (BBVC) sounding rocket series, which is currently the carrier vehicle for the scientific payloads, with a Nike-boosted configuration available for heavier payloads, provides the opportunity to process materials in a low-g environment for periods up to five minutes in duration during a sub-orbital flight.

The rocket flights, which are conducted at the White Sands Missile Range, afford experimenters and apparatus developers a flight opportunity for a proof-of-concept verification and/or refinement of equipment operation and procedures prior to the longer duration, more sophisticated Shuttle flights.

This SPAR flight, which is sixth in a planned series of rocket flights, occurred on October 17, 1979, and carried four experiments. The investigations for the experiments comprising the payload manifest were managed and coordinated by the MPS Projects Office of the Marshall Space Flight Center. Three such experiments were proposed and devised by industrial firms and one by a government-supported laboratory.

Previous experiments flown on the first five SPAR flights include the measurement of liquid mixing due to spacecraft motion and the dispersion of normally immiscible materials in the area of fluid dynamics. Solidification experiments involving the gravitational effects on dendritic growth, epitaxial growth, and solidification of eutectic materials with widely differing densities have flown previously, in addition to solidification studies of interactions between second-phase particles and an advancing crystal-liquid interface and gravity-induced convection on cast microstructures. In the area of multiphase particle interaction, various experiments were conducted on the migration and coalescence of bubbles and particles, closed-cell metal foam, and dispersion strengthening of composites.

The SPAR project has been increasingly active in supporting research in the promising area of containerless processing with previous flights, including experiments on cast beryllium and the processing of amorphous ferro-magnetic materials in an electromagnetic field, and control of liquid droplets by an acoustic field in the furtherance of state-of-the-art of acoustic containerless processing technology.

The SPAR flights have, through an evolutionary program, addressed experiments of increasing complexity and refinement and have afforded additional flight opportunities consistent with the maturity of each investigation. The payloads selected for this flight manifest were based on the advanced state-of-preparedness of their ground-based research activity.

The following experiments are included in this SPAR VI report: a) "Containerless Processing of Glass" (Experiment No. 74-42), describing the ground-based research, including experiments leading to selection of the flight sample composition; b) "Epitaxial Growth of Single Crystal Films" (Experiment No. 74-45), dealing with the successful design, fabrication and performance of the experiment apparatus; c) "Containerless Processing Technology" (Experiment No. 76-20), illustrating stability, oscillation and rotation as the three major aspects of containerless processing technology in space; and d) "Directional Solidification of Magnetic Composites" (Experiment No. 76-22), investigating the plane-front solidification of eutectic Bi/MnBi during both low-g and 1-g experiments.

The post-flight results and analyses of each experiment flown on SPAR VI as prepared by the respective flight investigators, in addition to an engineering report on the performance of the SPAR VI Science Payload, are contained in separate sections of this technical memorandum. With the successful completion of this flight and subsequent data analysis, much useful data and information were accumulated for directing and developing experimental techniques and investigations toward an expanding, commercially beneficial program of materials processing in the coming Shuttle era. One of the most significant aspects of SPAR VI is that it carried the first experiment of melted glass in low-g, Experiment No. 74-42. It was also the first of a series of materials processing low-g flights using a Nike-booster, which provides increased payload-carrying capability.

CHAPTER II

SPACE PROCESSING APPLICATIONS ROCKET PROJECT

SPAR VI

POST-FLIGHT ENGINEERING REPORT

Edited

by

Robert C. Edwards

October 1980

MATERIALS PROCESSING IN SPACE
ASSOCIATE DIRECTOR FOR ENGINEERING
SCIENCE AND ENGINEERING
GEORGE C. MARSHALL SPACE FLIGHT CENTER
MARSHALL SPACE FLIGHT CENTER, ALABAMA

TABLE OF CONTENTS

LIST OF FIGURES

LIST OF TABLES

SPAR VI POST-FLIGHT ENGINEERING REPORT

1.0 SUMMARY

The SPAR VI Nike-Black Brant VC rocket lifted off the launch pad at WSMR on Wednesday, October 17, 1979, at 1240:00:00 G.m.t. (6:40 a.m., MDT). The launch was successful and the payload was recovered intact.

Payload power was applied to all experiments as planned, and all experiments operated within the predicted near zero gravity. All MSFC flight support requirements to each experiment were met as indicated by the reduced flight data. Power to the payload experiments was programmed to be removed at T+728 seconds, but this could not be verified due to LOS at T+703 seconds.

2.0 SPAR VI (R-16) PAYLOAD CONFIGURATION

The SPAR VI (R-16) science payload consisted of four materials experiments, the Experiment Support Module (ESM), and the Abbreviated Measurement Module (AMM). The SPAR VI experiments are:

74-42	Containerless Processing of Glass
74-45	Epitaxial Growth of Single Crystal Films
76-20	Containerless Processing Technology
76-22	Directional Solidification of Magnetic Composites

The orientation of the experiments within the SPAR VI rocket vehicle is shown in Figure 1.

3.0 ROCKET PERFORMANCE

3.1 Flight Sequence

The SPAR VI flight profile is shown in Figure 2. The predicted and actual sequence of events are shown as a function of flight time.

3.2 Low Gravity

The predicted low-g (10^{-4} or less) time was based upon an all-up payload weight of 1139 pounds. The science payload furnished by MSFC weighed 818 pounds.

The measurement module low-g accelerometer measurements indicated that the low-g period on all three axes began at T+84, T+83, and T+89 seconds on the X, Y, and Z axes, respectively, and ended at T+369, T+352, and T+364 seconds, giving a low-g period of 263 seconds. The minimum low-g period required by experiments was 240 seconds.

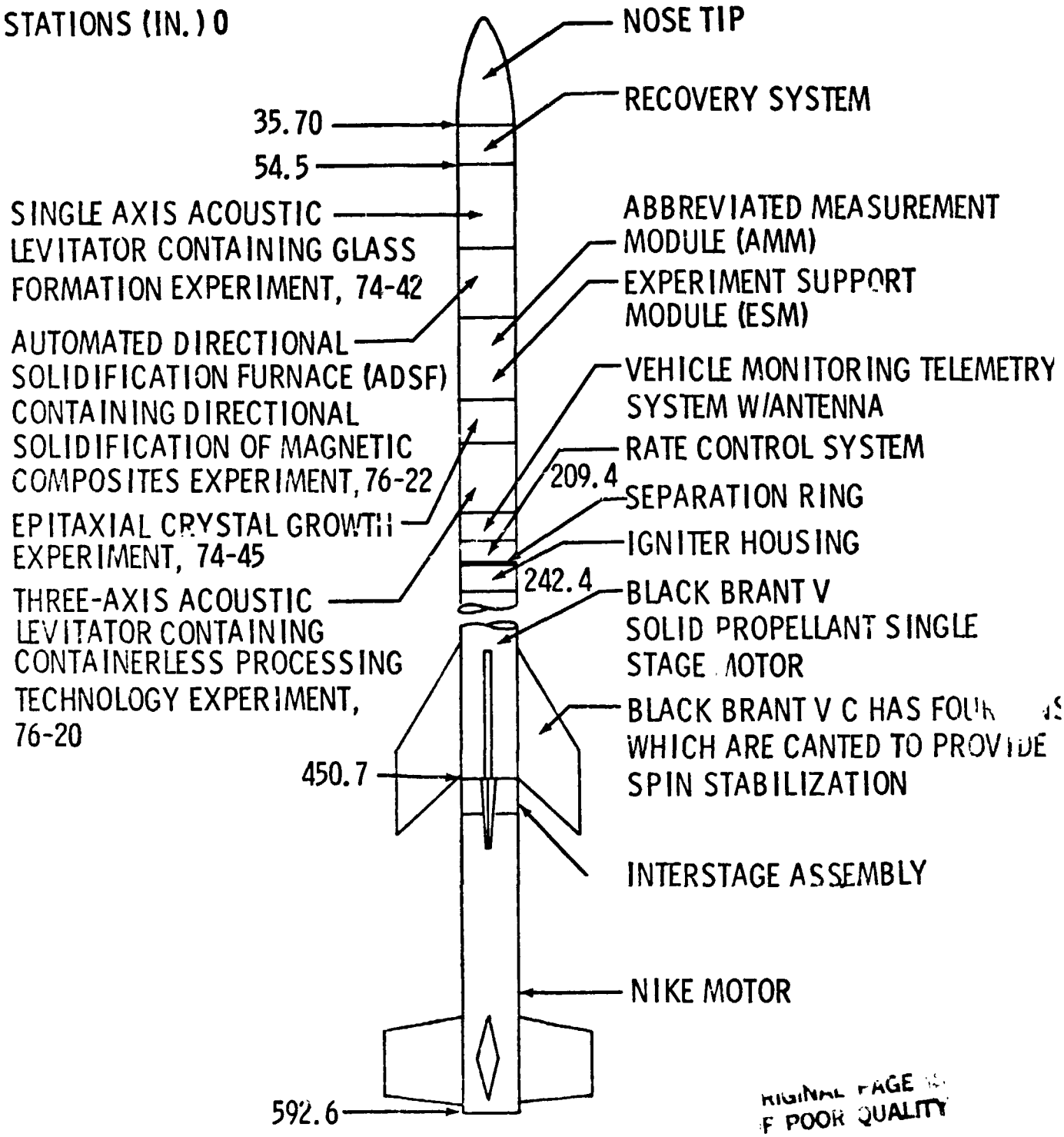

SPAR VI LAUNCH VEHICLE AND R-16 PAYLOAD CONFIGURATION

FIGURE I

SPAR PROJECT
NIKE BLACK BRANT VC ROCKET 27.016
FLIGHT PROFILE AND EVENTS/CONDITIONS

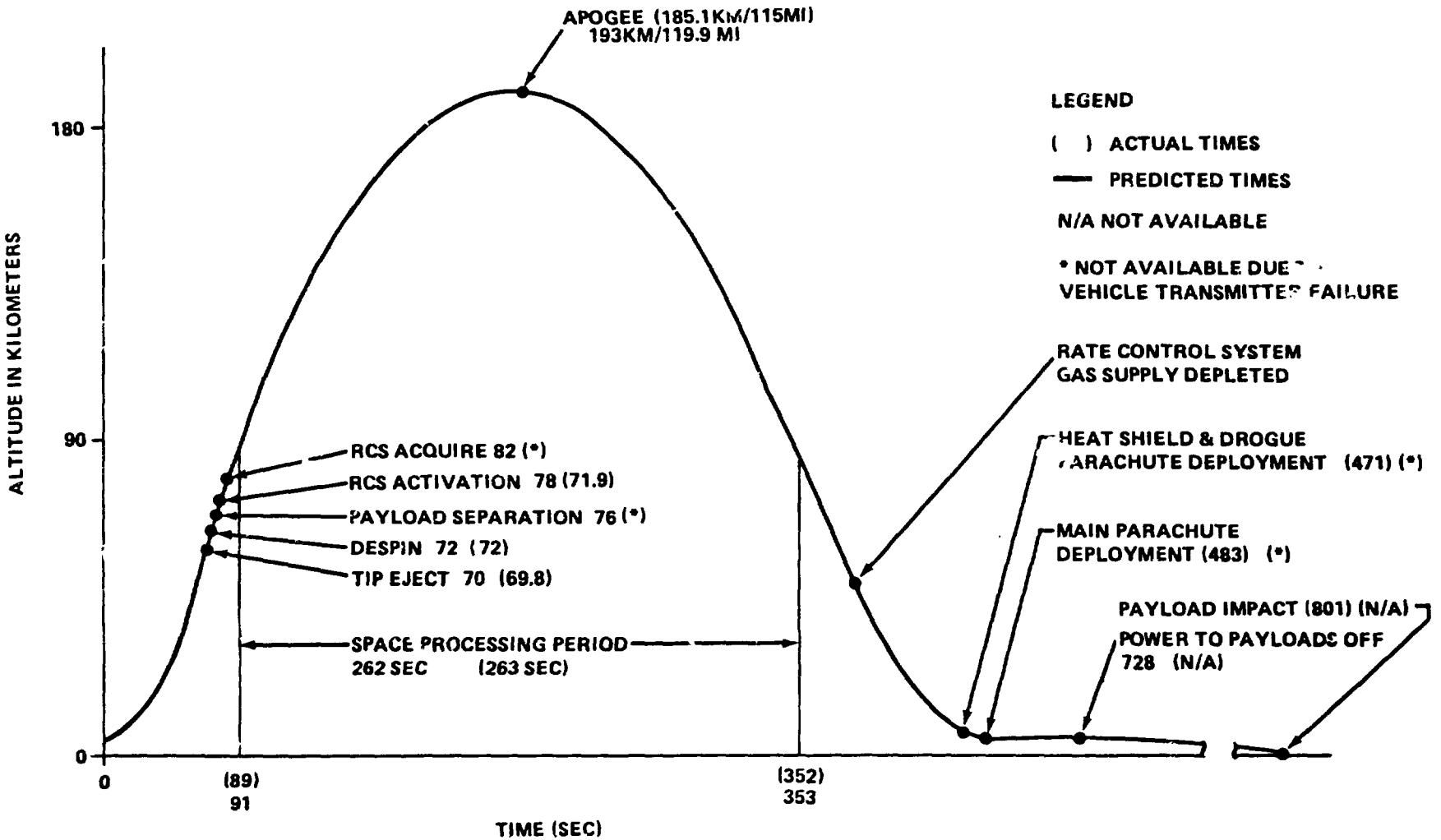

FIGURE 2. FLIGHT PROFILE AND EVENTS

4.0 PAYLOAD SUPPORT

4.1 Payload Sequence of Events

Experiments 74-42, 74-45, and 76-22 required preheat power prior to launch that was supplied by ground power. At T-0, a lift-off signal was given which activated a timer within each experiment for control of events during the flight. These events are shown in Figure 3.

The actual timelines were well within the acceptable limits of each experiment. The planned power removal to experiments at T+728 seconds could not be verified due to the Loss of Telemetry Signal (LOS) coverage at T+703 seconds.

4.2 Payload Power

Transfer of electrical power from ground support equipment to the flight battery was accomplished at T-3 minutes. The science payload battery, located in the Experiment Service Module, supplied power to all experiments. Battery voltage measurement (M01-SM) indicates that the battery voltage was 31.0 volts at lift-off and jumped to 34.0 Vdc at T+270 seconds, corresponding to Experiment 74-42 power cut-off. Here it remained essentially constant until T+703 seconds. The battery current measurement (M39-SM) indicates that the current was about 113 amperes at lift-off, which is 16 amperes higher than had been calculated from battery load profiles, and six amps above the battery rating. However, the shunt circuit which monitors the battery current was found to be in error by approximately 16 amps on the high side. Since the error cannot be precisely determined, the following amperage values, taken from the flight telemetry, are indicated values only, and are probably excessive by some 16 amps. The data are very noisy in the early part of the flight, but the current appears to have dropped to about 100 amps at T+11 seconds. At T+107 seconds, it increased to 113 amps as the 76-22 motors were activated. This was predicted to be 109 amps, thereby agreeing favorably. At T+271 seconds, the current dropped to 45 amps, whereas 31 amps had been predicted due to the 74-42 furnace power cut-off at this point. At T+337 seconds, it dropped to 39 amps, whereas 23 had been predicted due to completion of the 76-20 spin function. Finally, it dropped to 36 amps at T+355 seconds, where it remained essentially constant until LOS at T+703 seconds. The flight voltage and current profile (Figure 4) agree favorably with what had been predicted except for the 16 amp offset noted above.

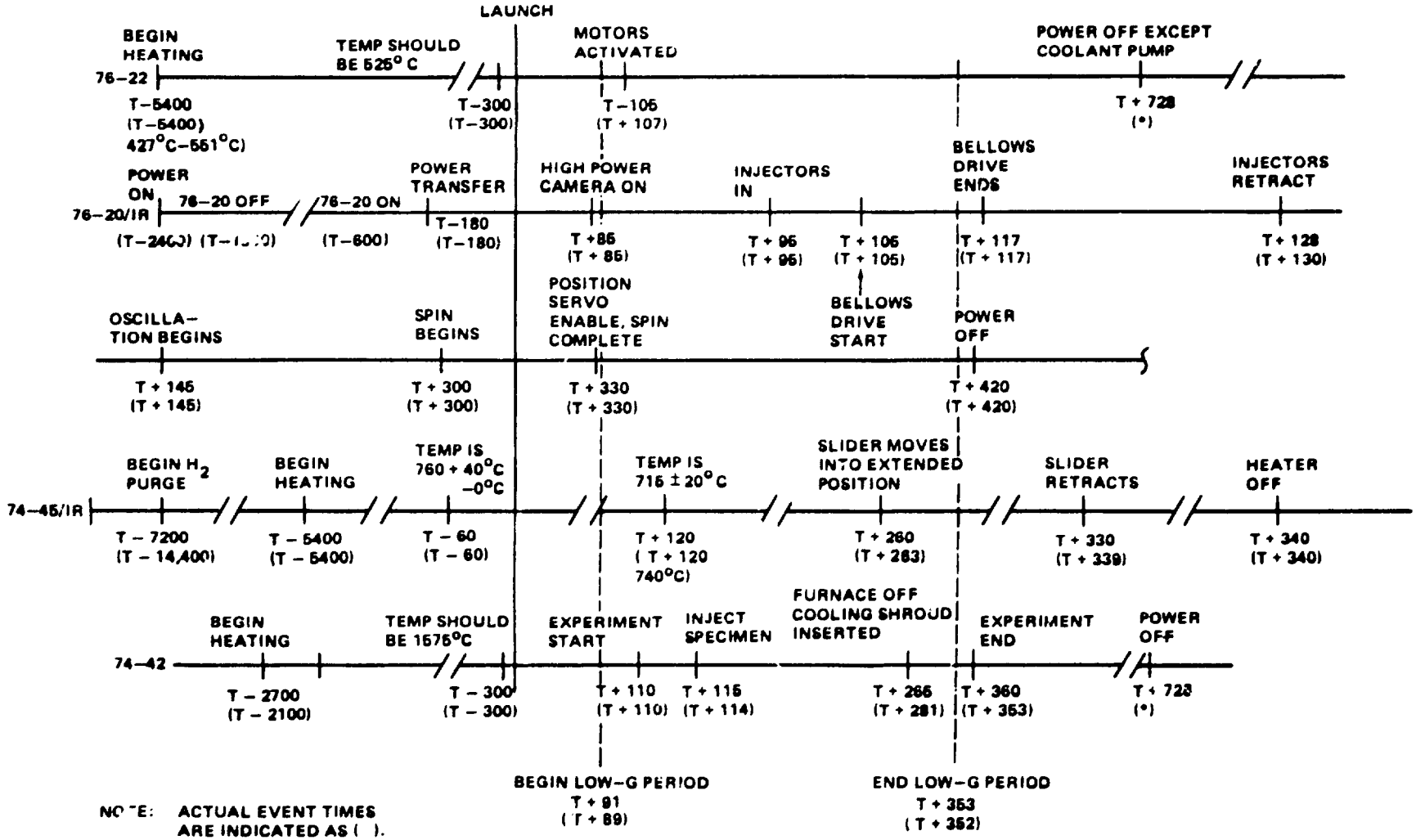

FIGURE 3 EXPERIMENT TIMELINE
(IN SECONDS)

SPAR VI

VOLTAGE AND CURRENT PROFILES

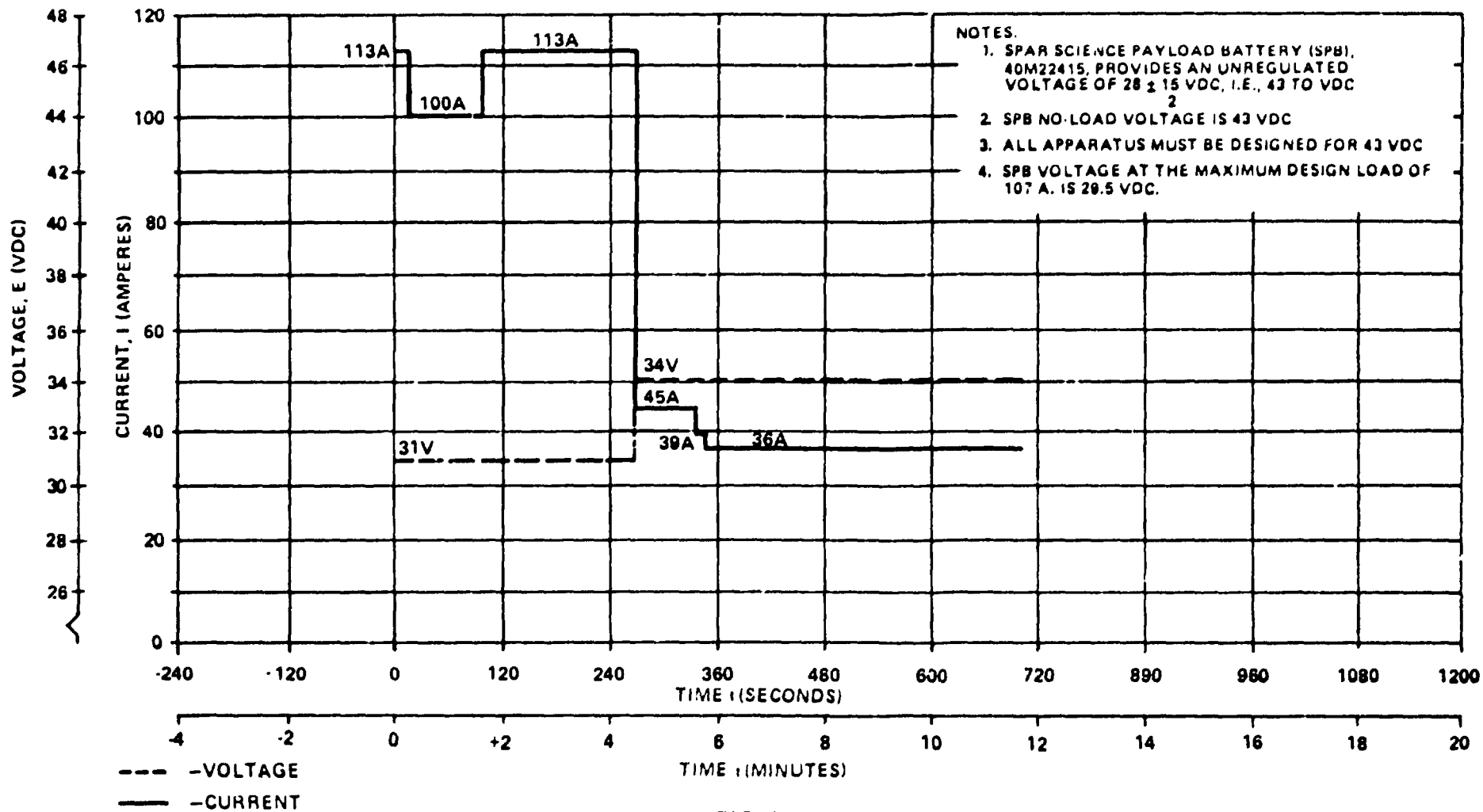

FIG. 4

5.0 EXPERIMENTS

5.1 Experiment 74-42 - Containerless Processing of Glass

This experiment consisted of processing a glass specimen in a containerless manner in a single axis acoustic levitation furnace at 1575°C in a low-g environment. Figure 3 shows the flight sequence timelines.

The preheat temperature measurement (C160-42) shows that the specimen preheat temperature at lift-off was about 120°C and increased steadily to 160°C at T+114 seconds when sample injection occurred.

The Hot Zone Temperature Measurement (C159-42) indicates that the temperature was approximately 1580°C at lift-off, increased to 1590°C at T+113 seconds, and decreased steadily to 1555°C at T+170 seconds, then increased slowly to 1565°C at T+269 seconds, at which point the furnace power was cut off and the cooling shroud inserted. From this point, the temperature decreased at an average rate of 14.3°C/sec to reach 114°C at T+348 seconds. At T+359 seconds, an unusual signal appears on both the hot zone and preheat zone channels indicating an instantaneous temperature drop of greater than 100°C. This could have been caused by an electrical transient of unknown origin, since a rapid temperature change of this magnitude is not physically possible in this apparatus. Temperature data after this time was not reliable, but the experiment had already been completed.

The gate position monitor indicated that the camera gate, the sound source gate, and the sample gate all opened correctly at T+110 seconds. The sound source turned on at T+111 seconds and showed the proper drive amplitude until experiment shutdown.

Injection of the sample occurred at T+114 seconds. At T+270 seconds, the cooling shroud gate opened, power to the furnace heaters was removed, and by T+281 seconds, the cooling shroud was fully inserted.

At T+353 seconds, the experiment was shut down and the camera and sound gates closed. The injector gate closed partially. This could have been caused by a partial retraction of the sample injector; however, this cannot be verified, since there was no instrumentation to indicate partial retraction of the sample injector. At T+413 seconds, 60 seconds after the experiment turned off, all gates show some motion, possibly caused by the shock of the parachute deployments.

The Cylinder Pressure Monitor (D014-42) indicates that the pressure was about 14.4 psia at lift-off and increased steadily to 17 psia at T+703 seconds when LOS occurred. The Air Temperature Measurement (C177-42) indicates that the air temperature was 25°C at lift-off and increased steadily to reach 50°C at LOS at T+703 seconds.

The acoustic driver amplitude measurement (M075-42) indicated nominal operation throughout flight. However, the acoustic amplitude apparently significantly decreased as evidenced by the inflight photographs. The molten experiment sample was to have avoided any contact with the restraining cage during melting, hot soak, and resolidification. During this flight the molten experiment sample contacted the cage and solidified while in contact with the platinum cage wires. A thorough failure analysis was performed after SPAR VI and, as a result, the configuration was revised to provide considerable additional instrumentation for the SPAR VIII mission. A similar flight anomaly was experienced on SPAR VIII and, as a result of the data from the additional instrumentation, it was determined that the loss of sample position control was due to water vapor in the acoustic chamber. Appropriate revisions are being incorporated into the acoustic levitation furnace to be flown in the Materials Experiments Assembly (MEA) on the Space Shuttle

5.2 Experiment 74-45 - Epitaxial Growth of Single Crystal Films

This experiment consisted of bringing a substrate crystal into brief contact with a molten solution near its melting point by means of a slider mechanism in a low-g environment and then removing it before leaving the low-g environment.

The Location 1 Solution Temperature Measurement (C35-45) indicates that the solution temperature at this location was 900°C prior to lift-off, but the measurement shifted downward slightly to 880°C at lift-off, due to experiment 76-20 turn-on at this time. From this point, the temperature decreased steadily to each 640°C at LOS, which occurred at T+703 seconds. Two slight shifts occurred in the data at T+263 seconds when the slider inserted and at T+339 seconds when the slider retracted.

The Location 2 Solution Temperature Measurement (C36-42) displays exactly the same characteristics as were noted in the Location 1 data described above. The Slider Position Monitor (K004-45) shows that the slider was inserted at T+263 seconds and retracted at T+339 seconds. The Hydrogen Bottle Pressure (D003-45) was 640 psia prior to lift-off. There was a slight decrease in this value until LOS at T+703 seconds. No Experiment 74-45 anomalies could be determined by examination of the SPAR VI flight engineering data by MSFC.

5.3 Experiment 76-20 - Containerless Processing Technology

This experiment consisted of levitating a drop in low-g environment and photographing its stability and controllability in the 3-axis acoustic levitator.

The Experiment Voltage Monitors, M076-20 (+5 Vdc), M077-20 (-5 Vdc), M078-20 (-12 Vdc), M079-20 (-15 Vdc), M080-20 (-18 Vdc), M081-20 (+12 Vdc), M082-20 (+15 Vdc) and M083-20 (+18 Vdc), all displayed midscale readings throughout the flight, indicating that the various power supplies were operative and producing the correct voltages.

The Commutator Reference Monitors, M040-20 (high) and M049-20 (low), indicate that the commutator references remained constant throughout the flight at +5 Vdc and 0 Vdc, respectively, as expected. Regulator Surface Temperature Measurement (C174-20) shows a temperature rise during flight of 18°C which is normal. The Chamber Wall Temperature (C173-20) was 22°C at lift-off; it increased 5 to 10 degrees during flight.

The Syringe Position Monitor (M050-20) indicates that the bellows drive was initiated at T+105 seconds and ended at T+117 seconds, exactly as predicted by Figure 3.

The reader is referenced to the experiment 76-20 section of this report for details concerning the acoustic amplitude and frequency monitors. No experiment 76-20 anomalies could be determined by examination of the SPAR VI flight engineering data by MSFC.

5.4 Experiment 76-22 - Directional Solidification of Magnetic Composites

This experiment consisted of processing MnBi/Bi eutectic materials samples in a four-furnace assembly; these samples were heated during prelaunch countdown and directionally cooled in the low-g environment.

The Coolant Pump 1 Current Measurement (M053-22) indicates that the pump current was 349 mA at lift-off and dropped suddenly to 40 mA at T+184 seconds, indicating a failure of the pump, the cause of which is unknown. Since there are two pumps in this coolant loop, no harmful quench block temperature changes occurred due to the loss of one pump.

The Coolant Pump 2 Current Measurement (M073-22) indicates that the pump current was 300 mA at lift-off, fell to 100 mA while recovering from the Pump 1 failure, returned to 300 mA, and remained constant throughout the flight until LOS at T+703 seconds. The Input Voltage Monitor (M070-22) shows that the input voltage was 34.7 Vdc at lift-off and increased to 36.4 Vdc when the experiment 74-42 heaters were cut off at T+267 seconds, and remained at this value until LOS. The Coolant Pressure Measurement (D10-22) indicates the coolant pressure to have been 30 psia at lift-off, falling to 25.5 psia at T+40 seconds. Here it remained until T+184 seconds when it fell to 11.3 psia as Pump 1 failed. From this point, it gradually increased, reaching 28.5 psia at LOS. A 4-second transient may be seen on the traces of both pump currents and on the coolant pressure trace at T+86 seconds, corresponding to the experiment 76-20 high power activation. During this time, the Pump 1 current fell 120 mA, the Pump 2 current fell 80 mA, and the coolant pressure fell 8.3 psia.

The Furnace No. 1 Coolant Temperature Monitor (C149-22) indicates that the coolant temperature was 46°C at lift-off and increased steadily to 54°C at LOS. The Ambient Pressure Measurement (D009-22) did not change after lift-off; therefore, the pressure gage was apparently inoperative during flight, since normal operation would have indicated minor pressure fluctuations in the

data. Loss of this measurement was of no significance to the experiment performed on this flight. The High Level Multiplexer Reference Voltages, M056-22 (high) and M055-22 (low), remained at 5 Vdc and 0 Vdc, respectively, throughout the flight, as was expected.

The Upper Limit Switch Monitors, Furnace No. 1 (K069-22), Furnace No. 2 (K070-22), Furnace No. 3 (K071-22), and Furnace No. 4 (K072-22), all indicate no change of state throughout the flight, and were activated the whole time. The Lower Limit Switch Monitors, Furnace 1 (K073-22), Furnace 2 (K074-22), Furnace 3 (K075-22), and Furnace 4 (K076-22), all indicate activation at lift-off for a duration of 101 seconds, and a return to no activation at T+101 seconds.

The Furnace 1 Cold Junction Temperature Measurement (C144-22) shows that the temperature at lift-off was 47°C and steadily increased to 52°C at LOS. The Furnace 2 Cold Junction Temperature (C145-22) also was 47°C at lift-off and increased to 51°C at LOS. The Furnace 3 Cold Junction Temperature (C146-22) was 48°C at lift-off and increased to 52°C at LOS. The Furnaces 1 and 3 Sample Cold Junction Temperature (C141-22) was 46°C at lift-off and increased to 49°C at LOS. The Furnaces 2 and 4 Sample Cold Junction Temperature (C142-22) was 46°C at lift-off and increased to 51°C at LOS.

The Motor Linear Speed Monitors, T001-22 (Furnace 1), T002-22 (Furnace 2), T003-22 (Furnace 3), and T004-22 (Furnace 4), all indicate motor activation at T+107 seconds. For details concerning the furnace translational rates, the reader is referred to the Experiment 76-22 report.

The Low Level Multiplexer Reference Voltages, M059-22 (low) and M060-22 (high), were 0 Vdc and 5 Vdc, respectively, throughout the flight, as was expected, and the Sync 2 Voltage (M062-22) was constantly 0 Vdc, as expected.

The 2 cm location temperature (C123-22) in Furnace No. 1 was 254° at lift-off and increased gradually to 277°C at LOS. The 1 cm location temperature (C125-22) was 214°C at lift-off and increased gradually to 249°C at LOS. The Sample 1 Temperature (C124-22) was 273°C at lift-off and decreased gradually to reach 61°C at LOS. Sample 2 Temperature (C126-22) was 223°C at lift-off, increased to a maximum of 228°C at T+75 seconds, and decreased steadily to reach 61°C at LOS. The Sample 3 Temperature (C122-22) was 193°C at lift-off and decreased gradually to reach 59°C at LOS. The Sample 4 Temperature (C121-22) was 100°C at lift-off, increasing to 107°C maximum at T+112 seconds and decreasing gradually to reach 57°C at LOS. The sharp transients seen on the Sample 1 and 3 traces between T+40 seconds and T+75 seconds are unexplainable, although the starting time (T+40 seconds) is coincident with the burnout of the BBVC rocket motor. These transients are seen in the Furnace 3 sample temperature also.

The 2 cm location temperature in Furnace No. 2 (C128-22) was 254°C at lift-off and remained constant until LOS. The 1 cm location temperature (C129-22) was 204°C at lift-off and increased gradually to reach 218°C at LOS. The Sample Temperature (C130-22) was 286°C at lift-off and decreased steadily to reach 63°C at LOS.

The 2 cm location temperature in Furnace No. 3 (C132-22) was 291°C at lift-off and increased gradually to reach 311°C at LOS. The 1 cm location temperature (C135-22) was 258°C at lift-off and increased gradually to reach 277°C at LOS. The Sample 1 Temperature (C131-22) was 277°C at lift-off and decreased steadily to reach 68°C at LOS. The Sample 2 Temperature (C136-22) was 254°C at lift-off and decreased steadily to reach 69°C at LOS. The Sample 3 Temperature (C133-22) was 261°C at lift-off and decreased steadily to reach 64°C at LOS. The Sample 4 Temperature (C134-22) was 233°C at lift-off and decreased steadily to reach 59°C at LOS. Transients occurring at T+402 seconds are visible in the Furnace 3 sample temperature traces, but are unexplainable.

The 2 cm location temperature in Furnace No. 4 (C137-22) was 289°C at lift-off and increased gradually to reach 313°C at LOS. The 1 cm location temperature (C139-22) was 260°C at lift-off and increased gradually to reach 290°C at LOS. The Sample Temperature (C140-22) was 270°C at lift-off and decreased steadily to reach 56°C at LOS. No experiment 76-22 hardware anomalies, other than the failure of coolant pump 1, could be determined by examination of the SPAR VI flight engineering data.

6.0 SCIENCE PAYLOAD INSTRUMENTATION

6.1 Low-G Accelerations

The low-g data indicate that a low-g environment considerably less than 1×10^{-4}g was achieved in all 3 axes. The X-Axis Linear Acceleration Measurement (A02-MM) indicates that low-g entry in that axis was at about 84 seconds and exit at about 369 seconds with the g levels during this period ranging from -0.12 to $.01 \times 10^{-4}$g. The Y-Axis Linear Acceleration Measurement (A03-MM) indicates the same low-g entry time as the X-Axis and exit at 352 seconds with the g levels ranging from -0.16 to $.01 \times 10^{-4}$g. The Z-Axis Linear Acceleration Measurement (A04-MM) indicates the low-g entry in that axis was at 89 seconds and exit at 364 seconds with the g levels ranging from $+0.04$ o 0.28×10^{-4}g.

A spike of 0.21×10^{-4}g occurred on the X-axis plot in the +X (downrange, north) direction at approximately T+112 seconds. A corresponding spike of 0.37×10^{-4}g occurred on the Y-axis plot in the +Y (cross range, east) direction. These spikes were probably caused by the movement of the 76-22 furnaces, which were initiated at T+107 seconds.

A spike of -0.04×10^{-4}g in the -Z (flight) direction occurred at approximately T+122 seconds and is unexplainable since no experiment functions were programmed to occur at this time. The closest programmed functions were 74-42 specimen injection at T+115, 76-20 bellows drive end at T+117, and 76-20 injector retraction and low power on at T+120 seconds.

A period of acceleration activity on the X-axis is seen between T+254 seconds and T+320 seconds with spikes ranging between $\pm 0.21 \times 10^{-4}$g occurring. During this period, the experiment 74-45 slider mechanism and the experiment 74-42 cooling shroud were inserted, and the experiment 76-20 spin cycle began.

6.2 Engineering Temperatures

Engineering thermistors were located on the SPAR VI Science Payload (SPL) in the following locations (see Figure 5).

C28-SM	Transmitter Plate Temperature
C33-MM	Linear Accelerometer Block Temperature
C39-MM	AMM External Temperature
C117-20	76-20 External Temperature
C148-22	76-22 External Temperature
C161-42	74-42 Cylinder End Plate Surface Temperature
C162-42	74-42 Electronics Plate Surface Temperature

The Engineering Temperature Thermal Analysis (Figure 6) was performed by Joseph Sims, EP41, MSFC. The data shows the SPAR VI temperatures to have been well within the nominal range of the previous SPAR engineering temperatures of 20°C to 60°C.

6.3 Pressures

Ambient pressure in the AMM (D01-MM) was 13.4 psia at lift-off, and 0.6 psia ($\approx$ 30 torr) at T+43 seconds. The SPL ambient pressure measuring device (D06-MM) was also located in the AMM, and was capable of monitoring from 30 to 10^{-4} torr in six ranges. It indicated that the ambient pressure continued to decrease until a minimum of 6.8 torr was reached at approximately T+372 seconds. From this point, the pressure rose rapidly to 30 torr at T+405 seconds and increased rapidly to reach 5.5 psia at T+478 seconds when the heat shield and drogue chute were deployed. From this point, the pressure increased steadily until it reached 17.9 psia when telemetry contact was lost at T+703 seconds.

FIGURE 5 SPAR VI ENGINEERING MEASUREMENT LOCATIONS

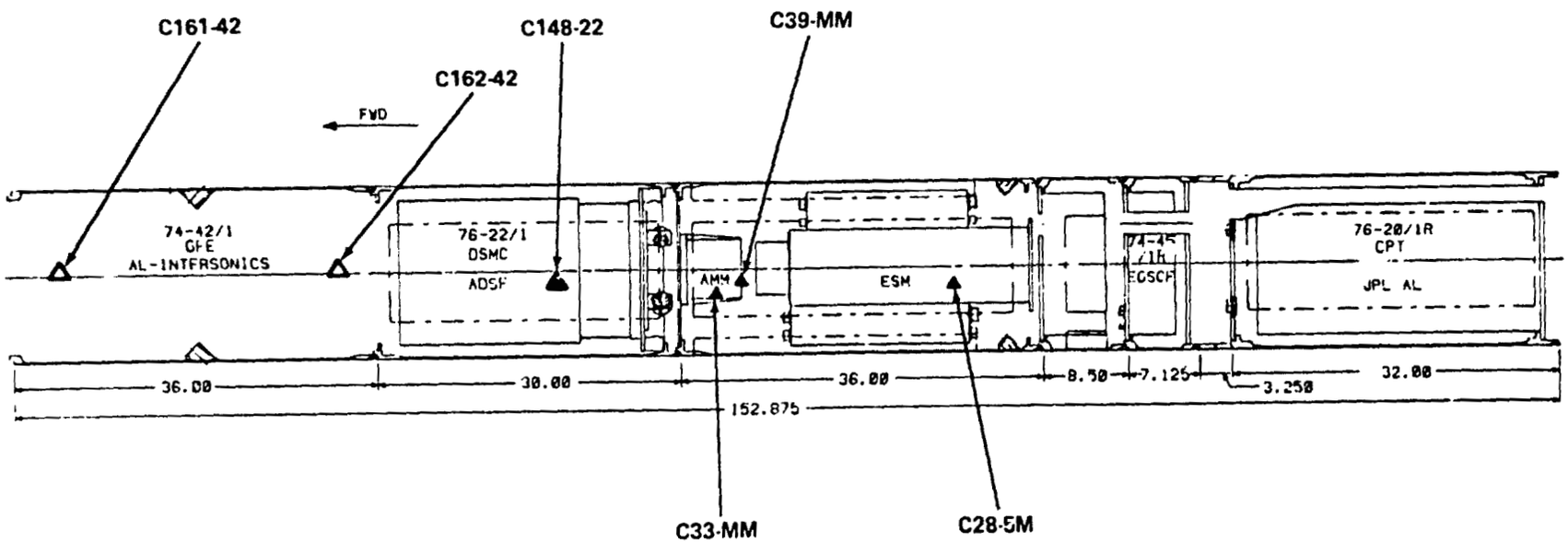

FIGURE 6 ENGINEERING MEASUREMENTS

SPAR VI

2998--80

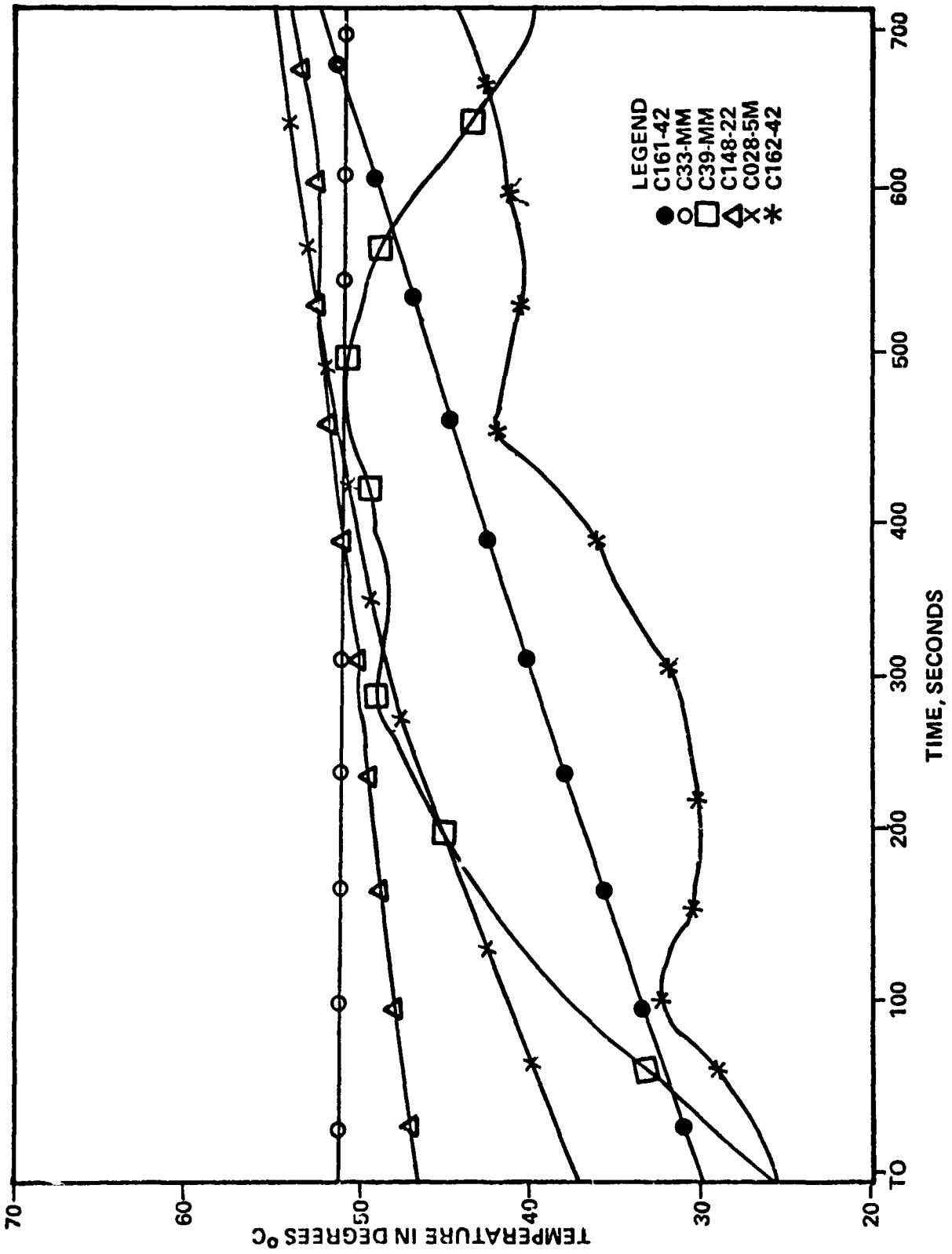

6.4 Vibration and Shock

The engineering evaluation of the SPAR VI vibration data was made by Mr. William Clever of the Systems Dynamics Laboratory. His comments are that vibration data from the X, Y, and Z vibration measurements (E02-MM, E03-MM, and E04-MM) are of very low level and are barely detectable above the noise floor. The maximum measured response was approximately 1 grms and represents only about 3 1/2 percent of the calibrated $\pm$ 40g range. The data indicates a predominant frequency near 1100 Hz, but at extremely low levels. On the whole, the data is extremely noisy and nothing of significance is apparent. The oscillogram trace and results of the statistical analysis were sent to GSFC.

Seven impact-o-graphs, capable of measuring shock levels from 120 G's to 650 G's, were mounted on the forward side of the GSFC Telemetry Module Extension (Figure 7). The impact-o-graph results are tabulated in Table I. Note that none of the springs or balls was unset at impact and the shock level experienced was less than 120 G's. This is considerably less than the 600 G's experienced by the SPAR V payload which impacted a rock upon landing.

7.0 PAYLOAD RECOVERY

The payload landing/recovery site was a steep sloping western rock-covered foothill of the San Andres Mountains which borders the west side of the range. The payload landed on its aft end sinking approximately eight (8) inches into semi-soft sandy soil. Apparently, the payload was then dragged by the parachute down the steep slope for approximately fifty (50) feet before falling downhill, forward end first, striking and breaking a large rock; this caused the payload cylinder enclosing the automated directional solidification furnace (Experiment 76-22) to be damaged beyond repair.

Upon arrival of the recovery team at the payload landing area, the electrical safing box was used to ensure the payload was de-energized. The parachute was detached from the four (4) webb risers. These risers were grouped into two pairs and attached to a webb sling furnished by the helicopter crew. The payload was then lifted by a cargo helicopter and transported, while slung beneath the helicopter, to a level area approximately one (1) mile northwest of the landing site.

Before loading into the helicopter for transportation back to the vehicle assembly building (VAB), the payload was separated into two sections to minimize the hazard of lifting the heavy payload by hand. The separation plane was between the automated directional solidification furnace (Experiment 76-22) and the Experiment Service Module; the electrical cables bridging this interface were cut as planned, using cable cutters. The two payload sections were then loaded aboard the cargo helicopter, secured, and transported to the VAB without incident.

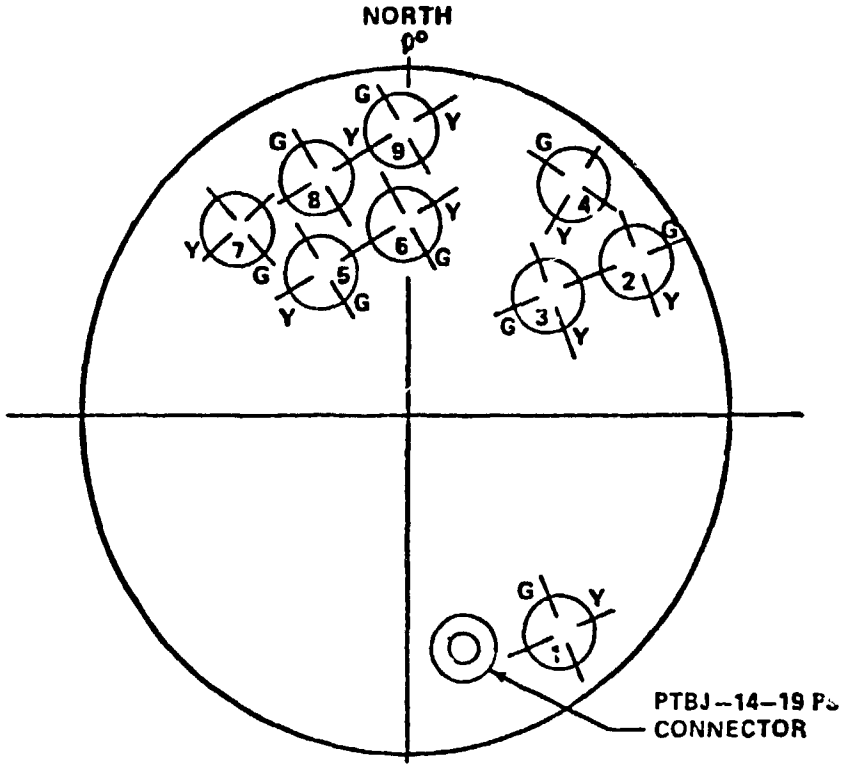

FIGURE 7 LOCATION OF THE IMPACT–O–GRAPHS ON THE FORWARD SIDE OF GSFC'S SPAR RATE CONTROL SYSTEM EXTENSION

IMPACT–O–GRAPH		SPRINGS AND BALLS FOUND UNSET AFTER LANDING		REMARKS
NO	Gs ±5G	G (GREEN) AXIS	Y (YELLOW) AXIS	
1				NO IMPACT–O–GRAPH WAS FLOWN IN THIS POSITION DUE TO CLEANIRING PROBLEM
2	120	NO	NO	
3	150	NO	NO	
4				NO IMPACT–O– GRAPH WAS FLOW IN THIS POSITION DUE TO CLEARANCE PROBLEM
5	250	NO	NO	
6	200	NO	NO	
7	650	NO	NO	
8	400	NO	NO	
9	600	NO	NO	

TABLE I LOCATION, NOMINAL G - LEVELS AND THE RESULTS ON SPAR VI

8.0 CONCLUSION

In conclusion, the flight data and post-flight analysis show the launch, flight, and recovery of SPAR VI to have been highly successful. However, anomalies did occur, primarily in Experiment 74-42, as discussed in paragraph 5.1.

CHAPTER III

SSD 80-0045

SPAR VI EXPERIMENT REPORT CONTAINERLESS PROCESSING OF GLASS EXPERIMENT 74-42

March 1, 1980

Contract NAS8-32023

By

Ralph A. Happe

TABLE OF CONTENTS

ILLUSTRATIONS

SUMMARY

The first containerless glass melting experiment, NASA experiment 74-42, was flown on the SPAR VI sounding rocket on October 17, 1979.

This report describes pertinent portions of the ground-based research, including experiments leading to selection of the flight sample composition, a silica-modified gallia-calcia glass of the composition, in mol percent, 39.3 Ga_2O_3 : 35.7 CaO : 25.0 SiO_2. Included are details of the preparation of an approximately one-fourth-inch-diameter flight sample.

During the flight experiment, a single sample of the silica-modified gallia-calcia glass was containerless-melted and cooled in a single-axis acoustic positioning apparatus built under contract to NASA by Intersonics, Inc. Since this was the first containerless glass flight, the principal objective of the experiment was to determine the functioning of the flight experimental hardware under actual flight conditions. The flight hardware included a silicon carbide element furnace equipped with a single-axis positioning device designed to prevent contact of the molten sample with other than the gaseous (approximately one-ground-level air) atmosphere during the 4 minutes of low-gravity flight. At the completion of the melting and soaking portion of the processing cycle, which was performed at a nominal temperature of 1575 C, a massive copper cooling shroud was introduced into the hot zone of the furnace to radiation-cool the sample. An injection cage fashioned from platinum and 30-percent rhodium alloy was used to inject the sample into the sonic well, and a single motion-picture camera was provided to observe the flight sample during the entire processing cycle. The hardware package included necessary electronics, timers, temperature control equipment, and mechanical devices, the last for operation of the injection mechanism, furnace wall gates, and cooling shroud.

The sample was completely melted during the flight and was cooled to a clear glass. Injection into the furnace hot zone was accomplished. After it touched the cage four times in the first 9 seconds, the sample remained in suspension 27 seconds, at which time it drifted to the injection cage and attached itself to one of the platinum alloy wires making up the cage. It remained attached and centered on the cage wire during the remainder of the processing cycle.

During the post-flight evaluation, the sample was found to be free of unmelted, crystalline, material. It contained three small bubbles near the platinum wire. The shape of the sample was spherical except for projections caused by wetting the wire by the glass at either pole where the platinum wire emerged from the sample. Unexpectedly, the surface of the sample was found to contain numerous small crystal rosettes not large enough to be seen by the

unaided eye. Analysis of the crystal rosettes with a scanning electron microscope showed them to be of approximately the same composition as the glass. Platinum (with some rhodium present) was found to be the probable cause of crystal nucleation. The principal constituent of the rosettes was found by indirect methods to be $Ca_2Ga_2SiO_7$. The most probable causes of the platinum contamination of the surface are thought to be either (1) mechanical transfer from the loose-fitting injection cage during lift-off of the rocket or (2) surface diffusion from the platinum-rhodium wire which was in contact with the glass sample during most of the flight experiment cycle.

It is felt that, if during the next flight experiment the platinum cage grips the sample firmly to eliminate or substantially reduce rattling and the acoustic positioning device prevents physical contact with the injection cage during the entire processing cycle (eliminating the possibility of surface diffusion), the chances for platinum contamination of the surface and consequent crystal nucleation will have been substantially reduced.

INTRODUCTION

If the promise of containerless melting and cooling, made possible by space processing, is realized fully in the years that lie ahead, an important new area of optical glasses will become a reality. In part, this new area may be visualized by referring to the schematic of Figure 1. The ordinate is the index of refraction, and the abscissa, the Abbe number (ν), an inverse measure of dispersion. The higher Abbe numbers, to the left, of the diagram indicate a low dispersion (i.e., a flatter slope of the index versus wavelength curve). The lower Abbe numbers, to the right, have high dispersion (steep index versus wavelength curve). A century ago flint glasses were developed. This permitted construction of the first achromatic, or color-corrected, multi-element lenses. Responding to the demands for better quality lenses, the optical glass industry developed more glasses with properties between those of the crown and flint glasses. More recently glasses have been developed to fill out the vertically hatched commercial glass area. The trend has been to push the area up and to the left with glasses of complex compositions.

If glasses beyond the reach of current terrestrial technology could be prepared from the more reluctant glass forming oxides, the area of useful

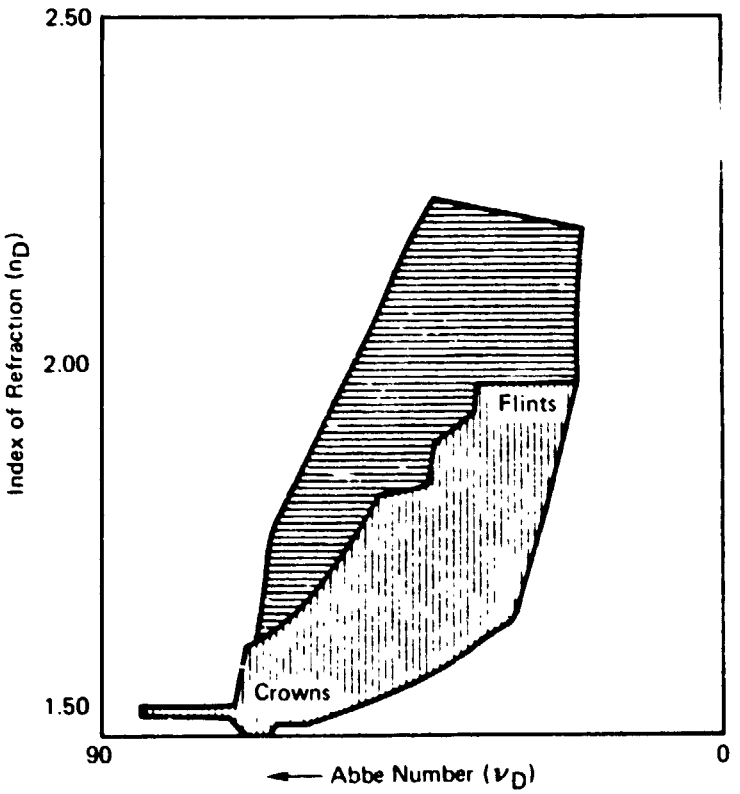

Figure 1. n-ν Diagram for Optical Glasses

properties could be expanded significantly. The expansion would occur by the addition of space-prepared glasses (horizontally hatched area of Figure 1) to the terrestrial base.

THE RATIONALE FOR SPACE PROCESSING

For most of the past decade, the Principal Investigator has been investigating possibilities for producing new optical glasses by containerless melting and cooling utilizing the near-zero-gravity environment available in earth orbit. The paragraphs that follow cover the technical thinking behind the concept of containerless processing in space, a summary of experience to date, and reasons for the interest in space processing of optical glasses.

When a molten oxide is cooled slowly enough to approach equilibrium conditions, it crystallizes near its crystalline melting point. In the case of the conventional glasses, usually based on oxides such as SiO_2, P_2O_5, B_2O_3, or GeO_2, the viscosity of the molten glass is very high. With this high viscosity, the molecular mobility is very low. Thus, when such substances are cooled from the molten state, it is difficult for the molecules to rearrange themselves into the orderly state of the crystalline lattice. Because of this sluggishness, the movement of the molecules into the crystalline lattice positions is incomplete on cooling with normal cooling rates. In these cases, the semi-random molecular arrangement of the liquid state is essentially preserved on cooling, and the substance remains amorphous, the resulting product being called a glass.

The crystallization phenomenon may be considered to occur in two stages: (1) nucleation and (2) crystal growth. In conventional glasses the sluggishness effectively inhibits both of these processes, especially the latter. Therefore, even if the substance manages to nucleate on cooling from the melt, the crystal growth rate is so slow that the nuclei remain, for practical purposes, undetectable in the glass. There are, however, only a few oxides that have sufficiently high viscosities to permit glass formation under normal circumstances.

For the past two decades, glasses have been made terrestrially in the laboratory from some of the less viscous oxides. Invariably, the technique used for preparing them involves extremely high cooling rates from the liquid state. The familiar splat-cooling technique (Reference 1) is a case in point. While such techniques yield valuable research information about the nature of the glasses so prepared, their application for commercial purposes is extremely limited. By the nature of the technique, only very thin films can be prepared. With this technique the liquid, as a very thin layer, is cooled in contact with a chill plate, usually of copper. While the copper provides numerous nucleation sites, the very rapid cooling effectively suppresses crystal growth.

Containerless melting in space offers the first practical opportunity to prepare glasses in massive form from the large number of oxides whose liquid viscosity* is not high. If nucleation can be prevented on cooling, then crystal growth obviously cannot occur, and a glass should result.

It is generally recognized that there are two kinds of nucleation: (1) heterogeneous and (2) homogeneous. Heterogeneous nucleation results from contact of the cooling liquid with crystalline material. Such a material may be entirely different in chemical composition from the melt. Common container wall materials are cases in point. Of course, it can also be of the same or similar composition, for example, unmelted portions of the bath or cool seed crystals of similar composition deliberately introduced into the cooling melt. In practice it is very difficult, or virtually impossible, to eliminate heterogeneous nucleation sites with conventional, terrestrial practice. Normally, a crystalline container must be used both for melting and for cooling. Further, the impingement of cool dust particles on the cooling melt may be enough to cause heterogeneous nucleation, and if the viscosity remains low enough in the supercooled liquid, crystal growth rates will be high and the glassy state will not be obtained.**

Homogeneous nucleation is another matter. Theoretical studies (Reference 2) have shown that homogeneous nucleation rates for oxide glasses are much slower than for heterogeneous nucleation. Experimentally, it is difficult to determine whether nucleation is truly homogeneous. There are those who believe that it may never truly have been observed in an oxide glass. Since only a few molecules of a heterogeneous nucleator need be present, the detection of such a small amount is a formidable technical problem. Thus, the assumption, *a priori*, that nucleation which occurs, for example, throughout the mass of a cooling substance is homogeneous may be erroneous. One can always argue that an undetectably small amount of a crystalline substance was present at the nucleation sites. At any rate, if heterogeneous nucleation can be effectively prevented, it is probable that homogeneous nucleation, if it can occur, will not occur unless the cooling rate is quite slow.

Over the past several years, the writer has successfully prepared numerous approximately 6-mm-diameter (about 3/4 gram) glass boules of roughly spherical shape from several oxide compositions that have low viscosity in the molten state. That work is covered in detail in References 3 and 4. Among the compositions prepared are the gallia-calcia eutectic at approximately 19 weight percent calcia, an alumina-calcia composition with 30 weight percent calcia, and a ternary, 40 weight percent lanthana--40 weight percent alumina--20 weight percent calcia composition. The alumina-calcia composition is well outside the reported glass-forming region based on 20 mg melts (Reference 5). The gallia-calcia composition had been reported to be a glass former in the laboratory, but in sizes less than 40 mg (Reference 6). Furthermore, water

*It is recognized that the slope of the viscosity versus temperature curve below the crystalline melting point (i.e., in the supercooled region) is very important to the glass formation process. However no such data exist for the oxides proposed here. It is probable that the general tendencies of viscosity change in the supercooled region can be inferred from future terrestrial and space studies.

**The presence of insoluble crystalline material in the melt could also cause heterogeneous nucleation. Fortunately oxides are very good solvents. It therefore follows that with enough melting time this problem should be held to a minimum.

quenching was required to achieve the glassy condition. Thus the preparation of crack-free boules with 50 times the mass of those of the earlier work represents a significant technical achievement. A glass of the ternary composition, to the writer's knowledge, has never been reported in the literature.

The method for preparing the 6-mm boules is described in detail in Reference 3. Briefly, the samples in contact with a silica (glass) sting are suspended in a vertical air column. The energy for melting comes from a CO_2 laser beam aimed at one side of the boule. The silica sting was found necessary to stabilize the motion of the melt and is a definite convenience for getting the process started. The oxide is transferred to the sting from a laser melted area of well-mixed powders of the desired composition. While the technique developed by the writer is excellent for demonstrating that new glasses can indeed be prepared with containerless melting and cooling techniques, it does suffer from several limitations, as follows:

1. Because of the relationship among viscosity, surface tension, and mass, 6 mm is very near the maximum sized boule that can be prepared in this fashion.

2. A small amount of silica sting material is continuously dissolving into the sample while the latter is being melted and held at superheat temperature. While the residual silica content of the boules averages well under one percent, an amount which may be considered too small to significantly affect conclusions regarding glass formation behavior, it apparently is not distributed uniformly, a possible explanation for the presence of marked striae in the glass boule.

3. It is very difficult to eliminate dust in the air from the wind tunnel. Thus the molten sample can be considered to be continually bombarded by dust particles while it is cooling. For this reason the technique may be unnecessarily restrictive compared with the more favorable conditions expected to accrue from space melting.

Space melting promises to eliminate or significantly reduce all three of the shortcomings inherent in the air suspension/laser melting equipment. Very large boules should ultimately be possible if enough power for melting can be made available. The silica sting will not be required with the acoustic positioning technique being developed by NASA. Space melting can be accomplished in a static atmosphere, significantly reducing the possibilities for dust-caused nucleation. It is entirely possible that some of the compositions that failed to form glass in our terrestrial experiments may prove to be glass formers under space melting and cooling conditions.

THE SOUNDING ROCKET PROGRAM

The Space Processing Applications Rocket (SPAR) program is considered a precursor to the Shuttle and later manned orbital programs. While conditions are not ideal for glass melting aboard a sounding rocket, largely because of

the rather short melting time (less than five minutes) available, the program does afford a good opportunity to gain early experience with glass melting within the limitations and, more importantly, with space glass melting equipment development.

The gallia-calcia composition mentioned in the previous section of this report was originally chosen as a suitable composition for two sounding rocket experiments and for early Shuttle experiments using the NASA-provided Materials Experiment Assembly (MEA). The composition is a eutectic between the compounds $CaO:Ga_2O_3$ and $CaO:2Ga_2O_3$ and its composition, under equilibrium conditions, is approximately 19 wt. % CaO, balance Ga_2O_3 (approximately 56 mol % CaO). The phrase diagram for the binary gallia-calcia system is shown in Figure 2.

This particular composition was chosen for the following reasons:

1. It has the lowest melting temperature of any of the new optical glass compositions studied by the principal investigator prior to the initiation of the SPAR program.

2. It is a relatively good glass former in the 1/4-inch (approximately 0.6-cm) (about 0.8 gm.) size under terrestrial containerless melting conditions.

3. It potentially has optical properties of interest to the optics industry.

4. Prior to our terrestrial melting work, it had not been prepared in a size exceeding 50 mg (0.050 gm).

OBJECTIVES AND RATIONALE OF THE SPAR VI EXPERIMENT

The 74-42 SPAR VI flight experiment was the first SPAR experiment to deal with sonic positioning coupled with very high temperature (approximately 1575 C). The prime objective of the experiment, then, was to learn as much as possible about the functioning of the flight equipment, built under contract to NASA by Intersonics, Inc. of Northbrook, Illinois, during actual flight conditions.

A silica-modified gallia-calcia composition was flown on SPAR VI to gain as much information as possible about the functioning of the flight hardware. One such composition had been developed by the writer earlier in the program for other reasons. The reason for modifying the composition is to increase the glass formation tendency so that a glass would result when it is melted and cooled in contact with a container. The binary gallia-calcia composition has such low viscosity that it cannot be prepared in sizes of interest to this program as a glass when it is in contact with virtually any crystalline material. Thus, for example, if such a material is incompletely melted and allowed to cool, the residual crystalline material would initiate crystallization on cooling so that the entire mass would be returned from flight in the 100 percent crystalline condition. By contrast, the silica-modified composition can be incompletely melted, and the molten portion is

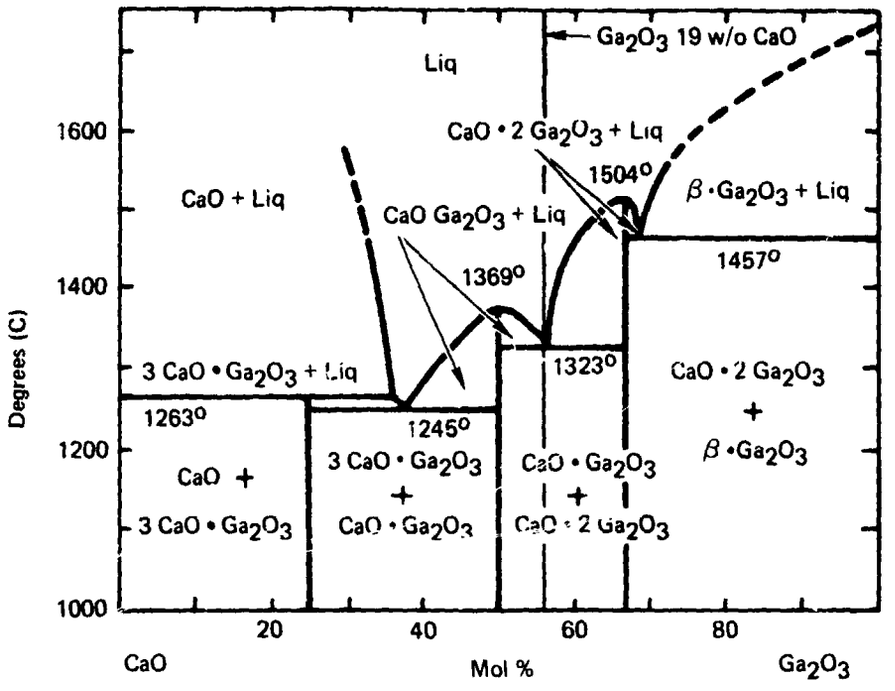

Figure 2. The CaO - Ca_2O_3 Phase Diagram (From Reference 2)

retained as a glass on cooling. Thus it is possible to detect from examination of the returned specimen whether complete melting had indeed occurred, the unmelted portion being clearly visible as nontransparent crystalline material within the body of the transparent glass. Had the binary gallia-calcia composition been flown in the first experiment and the sample returned in the crystalline condition, it would have been difficult, if not impossible, to determine if melting had been complete or, alternatively, if the crystallization had occurred during cooling because the melt had been contacted by a foreign crystalline material. Occurrence of such an event would have left us in the position of not knowing which of two entirely different mechanisms had caused failure and, consequently, not knowing how to correct the situation in future flights.

It was also decided to reduce the size of the first specimen from the earlier planned 1/2-inch diameter to 1/4 inch. This improved the chances for success by (1) increasing the probability of obtaining complete melting during the short time available during a sounding rocket flight and (2) reducing the mass that must be positioned by the single-axis sonic system.

Subsequent sections of this report describe in more detail the experiments to determine the flight composition and the preparation of the flight samples.

PREPARATION OF SAMPLES FOR FLIGHT EXPERIMENT

SELECTION OF FLIGHT SAMPLE COMPOSITION

During earlier work a ternary composition, 69 wt. % Ga_2O_3-19 wt. % CaO - 12 wt. % SiO_2 (41Ga_2O_3: 36 CaO : 23 SiO_2, in mol %) was used to study the effects of time at various furnace temperatures above the melting point on the progress of melting 6 gram melts. The silica addition stabilized the melt so that only the unmelted portion would be crystalline upon removal from the furnace and rapidly cooling to room temperature. The melted portion is retained as a clear glass.

It was decided to develop a silica-modified composition with similar characteristics for use on the SPAR VI flight, as discussed in the previous section. To obtain optical properties as close as possible to those of the binary gallia-calcia composition, it was desirable to utilize a silica content as low as possible.

Lacking a published ternary phase diagram for the Ga_2O_3 - CaO - SiO_2 system, it was assumed, as an expedient, that an eutectic valley existed in the ternary system which extended from the 56 wt. % gallia eutectic composition in the binary gallia-calcia system (Figure 2) to the 62 mol % silica eutectic in Figure 3.

A series of compositions made from high purity oxides was prepared with varying silica contents near the postulated eutectic valley. Nominal compositions are given in the following:

SiO_2, mol % (wt. %)	Ga_2O_3, mol % (wt. %)	CaO, mol % (wt. %)
5 (2.3)	57 (81.4)	38 (16.3)
10 (4.8)	53 (78.8)	37 (16.4)
15 (7.4)	49 (75.9)	36 (16.7)
20 (10.4)	45 (72.7)	35 (16.9)
22 (12)	40.6 (69)	37.4 (19)
25 (13.8)	39.3 (67.8)	35.7 (18.4)
33.3 (19.8)	33.3 (61.7)	33.3 (18.5)

After the pure oxide powders were weighed and blended by tumbling, 100-gram (approximately 40 cc) melts were prepared in platinum crucibles and held molten at least one hour. The crucible was then removed from the furnace, placed on a relatively massive aluminum slab, and allowed to cool. The appearance of the higher silica-content cooled melts can be seen in Figure 4. It was observed that in those compositions that crystallized completely, i.e. 5, 10, 15, and 20 mol % silica, the crystal growth rate slowed perceptibly with increasing silica content, an indication of the expected increase in viscosity.

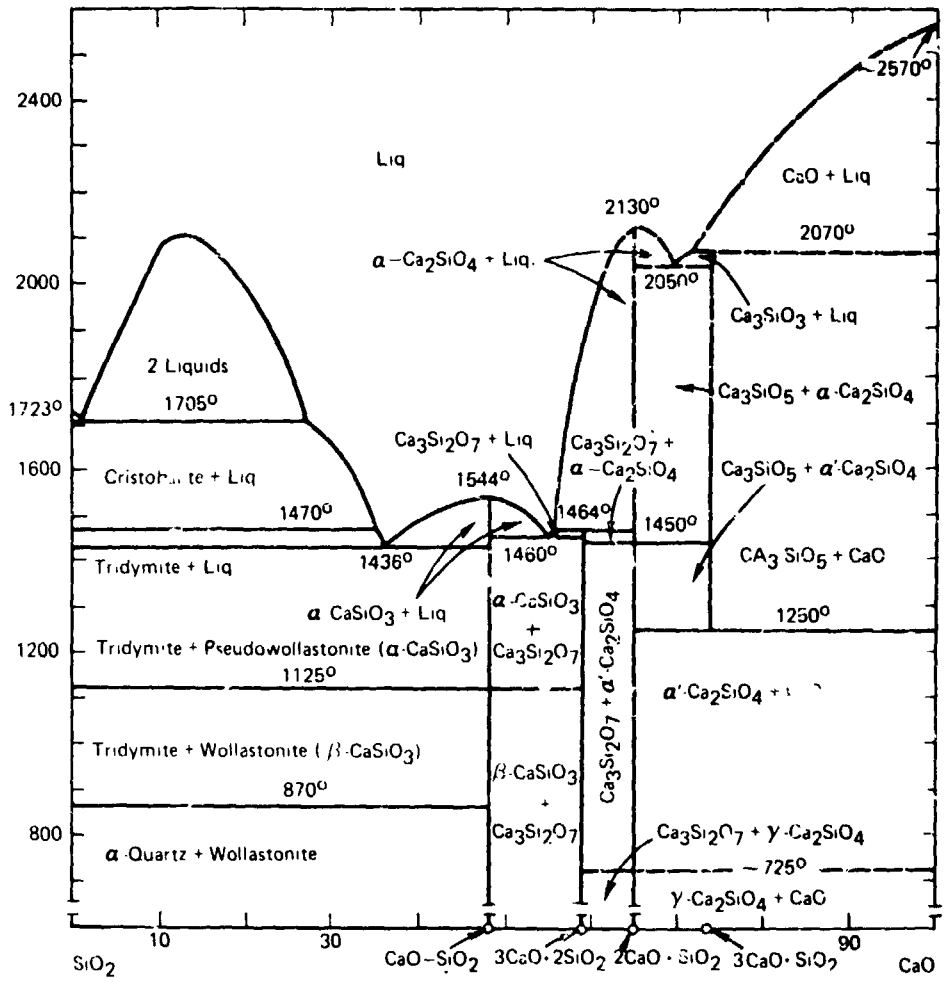

Figure 3. The CaO-SiO_2 Phase Diagram (From Reference 9)

20 Mol % SiO_2

22 Mol % SiO_2

25 Mol % SiO_2

33.3 Mol % SiO_2

Figure 4. Cooled Melts, 20 to 33 Mol % SiO_2

After photographing as shown in Figure 4, the melts were remelted and heated to 1550 C and held molten approximately one hour. Each crucible was again removed from the furnace and a "loaf"* casting was poured. The loaf castings are shown in Figure 5,** and the furnace and chill mold for preparing the castings are shown in Figure 6.

The behavior with the more rapid cooling conditions of the loaf castings was similar to that of the cooled melts, with the exception that the 20 mol % silica composition was glass plus crystal in the case of the loaf casting, while it appeared to be 100-percent crystal in the case of the cooled melt.

Based on these results, it was decided to select the 25 mol % silica content composition for preparing the flight samples. The 20 mol % silica content was the lowest in silica that showed any glass retention on cooling, and glass retention appeared to increase rapidly between 20 and 25 mol % silica.

PREPARATION OF FLIGHT SAMPLES

A loaf casting was prepared from the 39.3 Ga_2O_3: 35.7 CaO : 25.0 SiO_2 (mol %) composition with the procedure shown in the flow chart of Figure 7. Both the gallia and calcia powders used were of 99.999-percent purity and were manufactured by Johnson Matthey Chemicals Limited of England under their trade name "Puratronic." The silica was of 99.9-percent purity and was obtained from the Spectrum Chemical Manufacturing Corp. of Los Angeles.

The platinum crucible was embedded*** in a castable, high alumina refractory to (1) increase the thermal mass and slow cooling after removal from the furnace and (2) stiffen the crucible so that it could be handled repeatedly with tongs without crushing. Two such crucibles are shown in Figure 8. Figure 9A shows a print made of the "flight" loaf casting. The print was made by placing the casting, after polishing of opposite faces, on photographic print paper and exposing by means of a light placed above the sample. Note the improvement in striae as compared with Figure 9B, one of the earlier experimental castings made with less stirring with a silica rod. The flight casting was poured near one end, as can be seen by the crystalline material (white in the print). The left one centimeter of the casting is being held in reserve for possible future optical properties measurements. Five of the flight samples were taken from the area to the left of the crystal zone, and one (number 1) was taken from the area to the right bottom.

For convenience for suspending in the flight acoustic positioner, the flight samples were hand-diamond-ground to a roughly spherical shape at a lapidary shop. Figure 10 shows the six samples so prepared. Figure 11 shows them after devitrifying by heating 10 minutes at 1250 C.

*So named because their shape resembles that of a common loaf of bread

**Regrettably, the loaf casting for the 20 percent silica content was lost in a spill during a remelting experiment before it was photographed. It appeared to be about 20 percent glass and 80 percent crystal

***At the suggestion of Dr. D. Day of Missouri School of Mines, Rolla

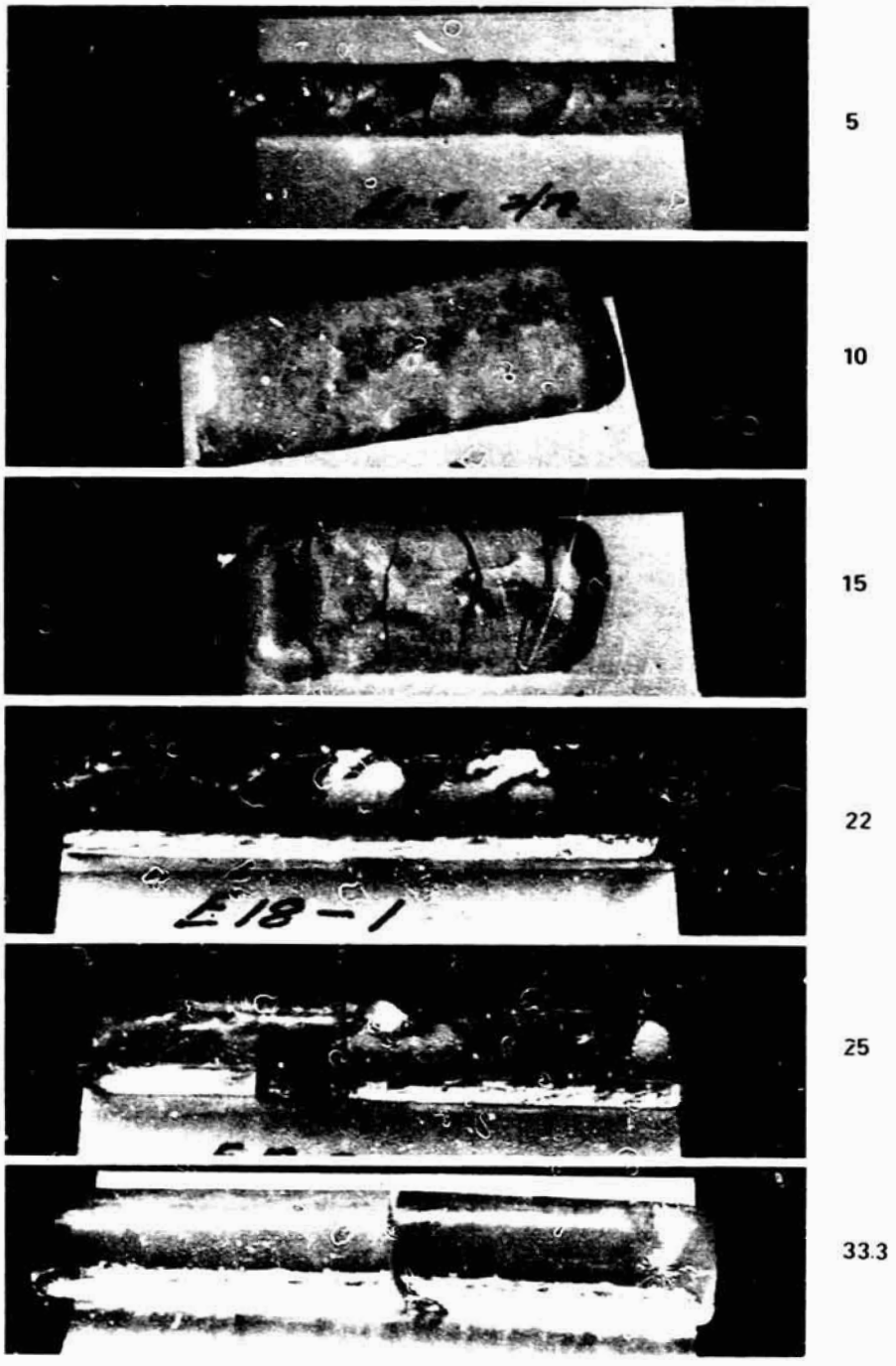

Figure 5. Loaf Castings of 5, 10, 15, 22, 25, and 33.3 Mol % SiO_2 Experimental Compositions

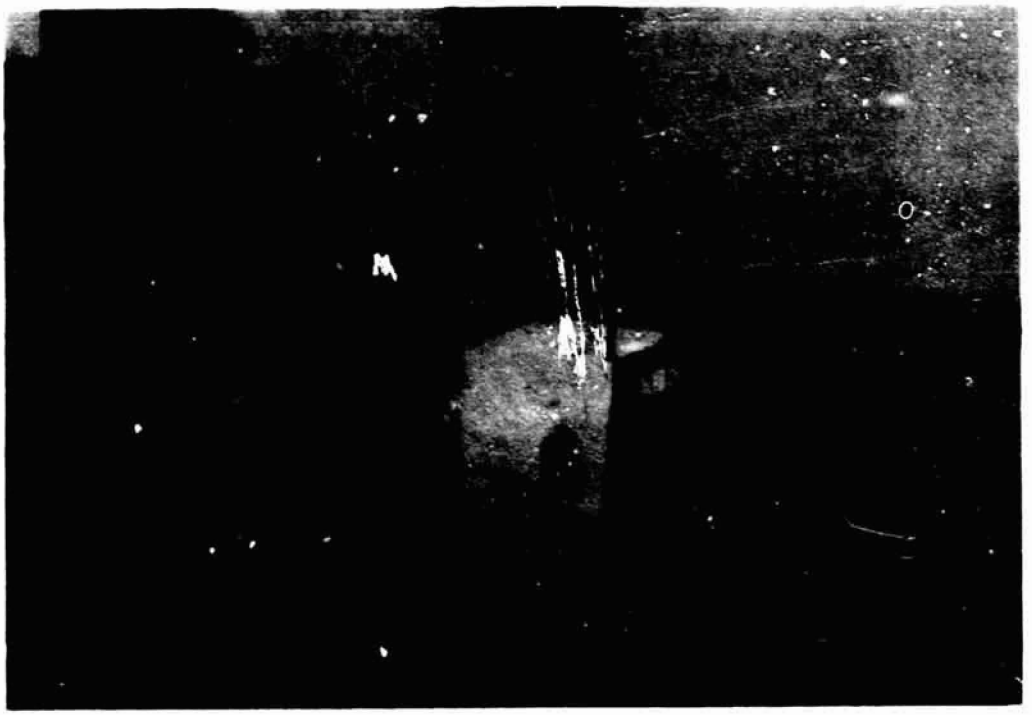

Figure 5. SiC-Element Furnace (Mold for Preparing "Loaf" Castings Shown in Front of Furnace)

Data on the six flight samples are given in the following:

Sample No.	Wt (gm)	Diameter (in.)		
		Average	Max	Min
1	1.2578	0.3364	0.3390	0.3305
2	-	0.3180	0.3242	0.3117
3	0.8972	0.2866	0.3014	0.2790
4	0.8975	0.2972	0.3163	0.2825
5	0.8965	0.2875	0.3079	0.2746
6	0.5778	0.2544	0.2670	0.2473

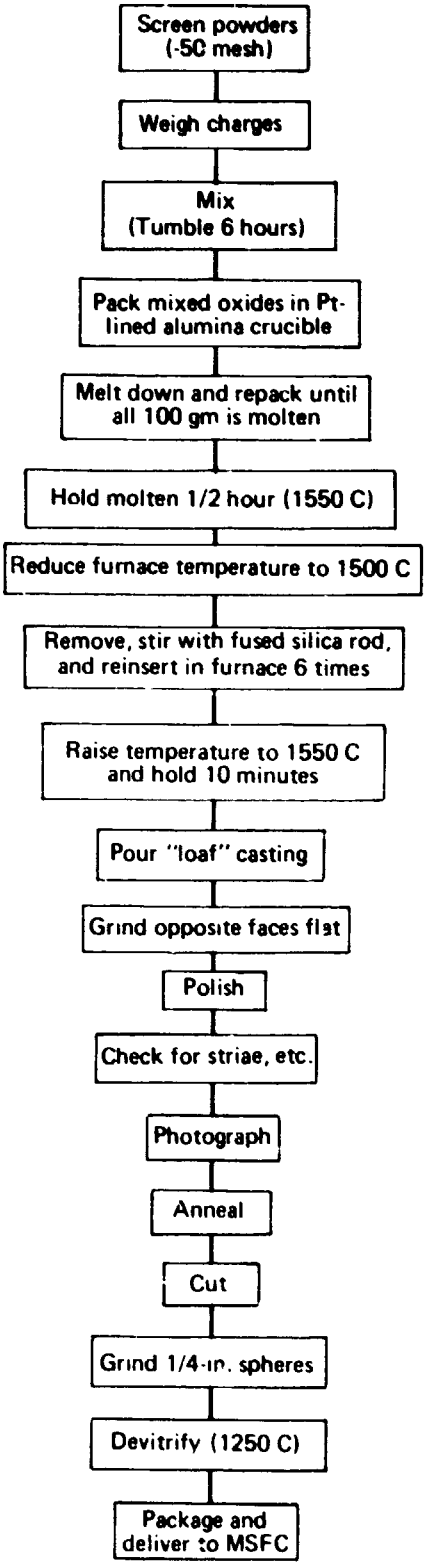

Figure 7. Preparation of Flight Samples

Figure 8. Pt Crucible With Alumina Castable

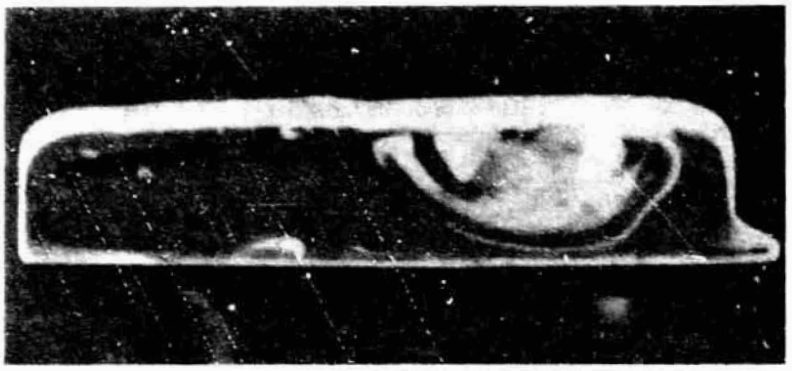

A. Flight Casting

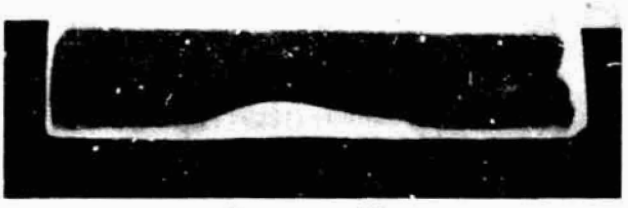

B. Experimental Casting

Figure 9. Contact Prints of "Loaf" Castings

Figure 10. Flight Samples Before Devitrifying

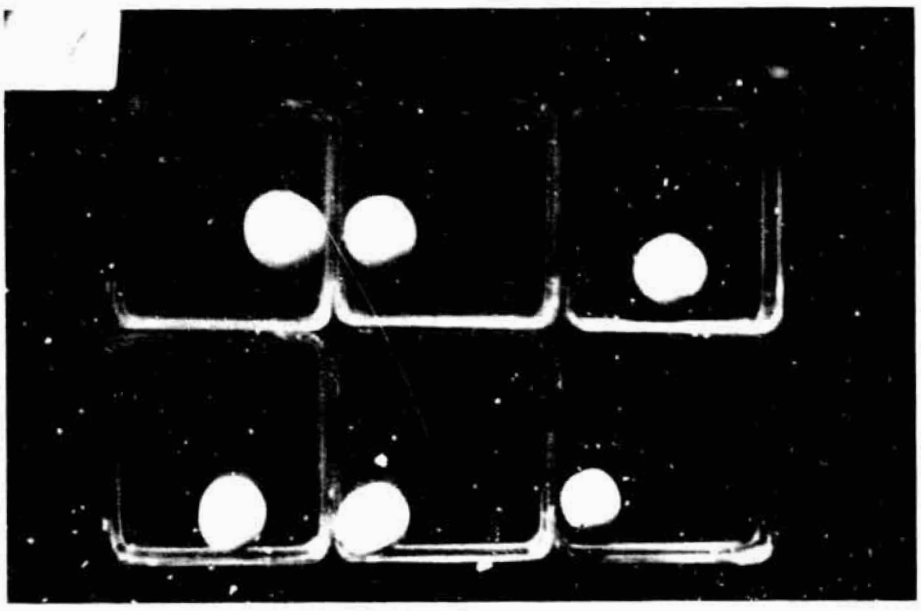

Figure 11. Devitrified Flight Samples

FLIGHT EVENTS

In this section the writer will attempt to give only details pertinent to an understanding of the flight sample examination, which follows later. A detailed reporting on the flight hardware will be issued by Intersonics after the second SPAR flight containing the glass melting experiment, 74-42.

SPAR VI, with flight sample Number 6 loaded in the injection mechanism, was launched at 6:40 a.m., MST at the White Sands Missile Range, New Mexico, on October 17, 1979. The payload suffered a rough landing as discussed in more detail in Appendix A.

Shortly after the payload was returned to the Vertical Assembly Building at White Sands, the access doors on experiment 74-42 were removed, and the injection mechanism containing the flight sample was removed from the furnace. Figure 12 shows the injection unit with the platinum wire cage and glass sample immediately after removal from the flight furnace. During the landing, the copper cooling shroud inside the furnace was torn from its moorings and crashed into the injection cage. The damage to the cage is apparent in Figure 12B.

The glass sample was found "impaled" on one of the finer platinum wires of the cage. Figure 13 shows two closeups of the cage with the glass sample. The latter photographs were taken four days after the rocket flight. Note that the glass sample appears to be quite well centered on the platinum wire. Distortion of the platinum wires near the sample is further evident in Figures 13A and B.

FLIGHT MOTION PICTURES

Appendix A discussed in detail the processing of the flight motion picture film developed under the supervision of the writer's organization. The timeline for the flight experiment beginning with the "camera on" after low g is achieved is given in the following tabulation:

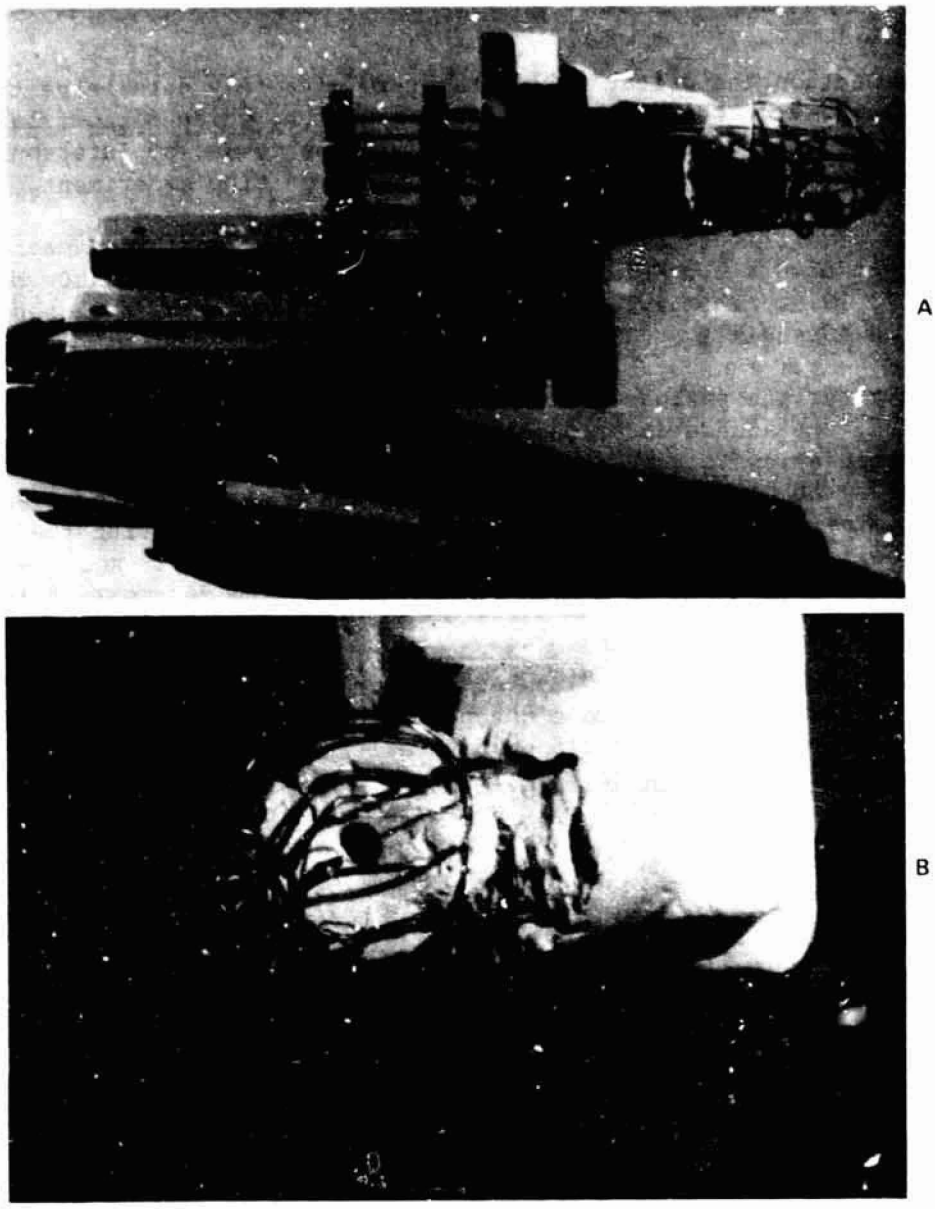

Figure 12. Two Views of Injection Mechanism With Flight Glass Sample (Photographed October 17, 1979, Immediately After Removal From Payload)

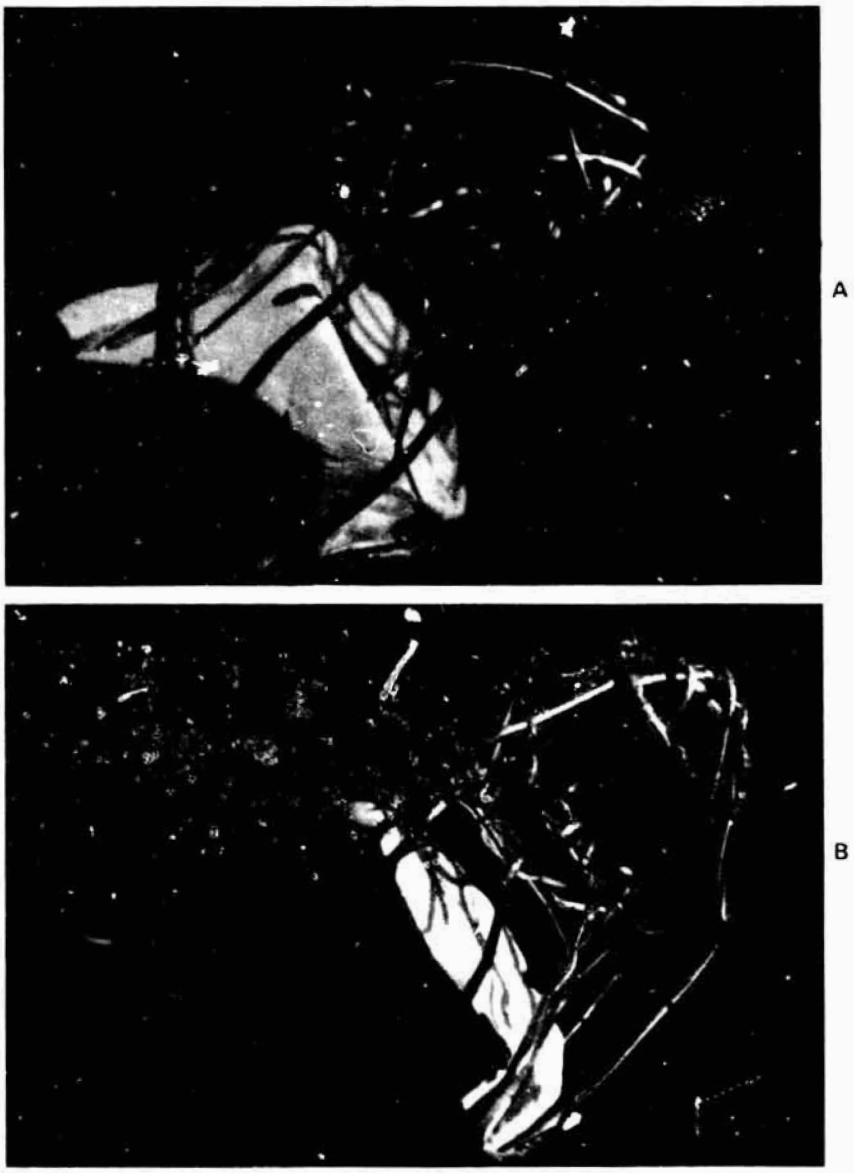

Figure 13. Two Views of Injection Cage With Flight Glass Example
(Photographed October 21, 1979)

Event	Cumulative Time (sec)
Camera on	0
Injection into furnace hot zone and start of heating sample	5
Cooling shroud gate open and start of insertion of cooling shroud	160
Cooling shroud fully inserted	170
End of sample cooling and sample retraction	243
Camera off	248

Examination of the flight film showed that immediately after the injection mechanism released the sample, it moved around inside the cage and touched the cage wires four times during the first 9 seconds after injection. During this time sample melting had not begun. It remained in suspension in the sonic well without touching for another 27 seconds, at which time it contacted the cage at 36 seconds after injection. Since the sample was, by this time largely molten (to be discussed in more detail later), it stuck to one of the cage wires. As best as can be judged by appearance of the sample in the film, it seemed to be largely molten about 30 seconds after injection, or about 6 seconds before it contacted the cage wire for the last time.

Table 1 shows significant events on the flight film, and Figure 14 shows prints of selected frames from the flight film. The contrast is low in the early frames because the exposure settings of the flight camera were chosen so the furnace wall, at a nominal 1575 C, would be on the verge of overexposure. This permitted maximum tracking during the cooling cycle. Of course, as the sample and cage approach the furnace wall temperature, the contrast would be very low regardless of exposure setting. In frame 1 the injector has just appeared, and the sample is trapped between the outer and inner (to the right) portions of the cage. In frame 4 the inner portion of the cage is retracting (moving to the right), the outer portion is moving to the left, and the sample has been released. In frame 11 the cage has fully opened, and the sample can be seen near the bottom of the cage just before it contacts the cage in the next frame. In frame 721, 30 seconds after injection, the sample is suspended near the center of the cage. In frame 860, 36 seconds after injection, the sample has moved upward and is just making contact with a cage wire. Five frames (0.2 seconds) later the sample has centered itself on the platinum wire. By frame 1303, 54 seconds after injection, the sample and cage have both closely approached the furnace wall temperature and are almost invisible. In frame C5, which is the fifth frame after the cooling shroud gate opened, a portion of the glass sample can be seen clearly still on the cage wire. In this frame the hot sample and injection cage can be seen in sharp contrast to the cold background of the cooling shroud. In the 316th frame (13 seconds) after the cooling shroud gate opened, the sample and cage can be seen to have cooled considerably. By frame C914 (not shown), 38 seconds after the gate opened, the sample and cage have merged with the cool-

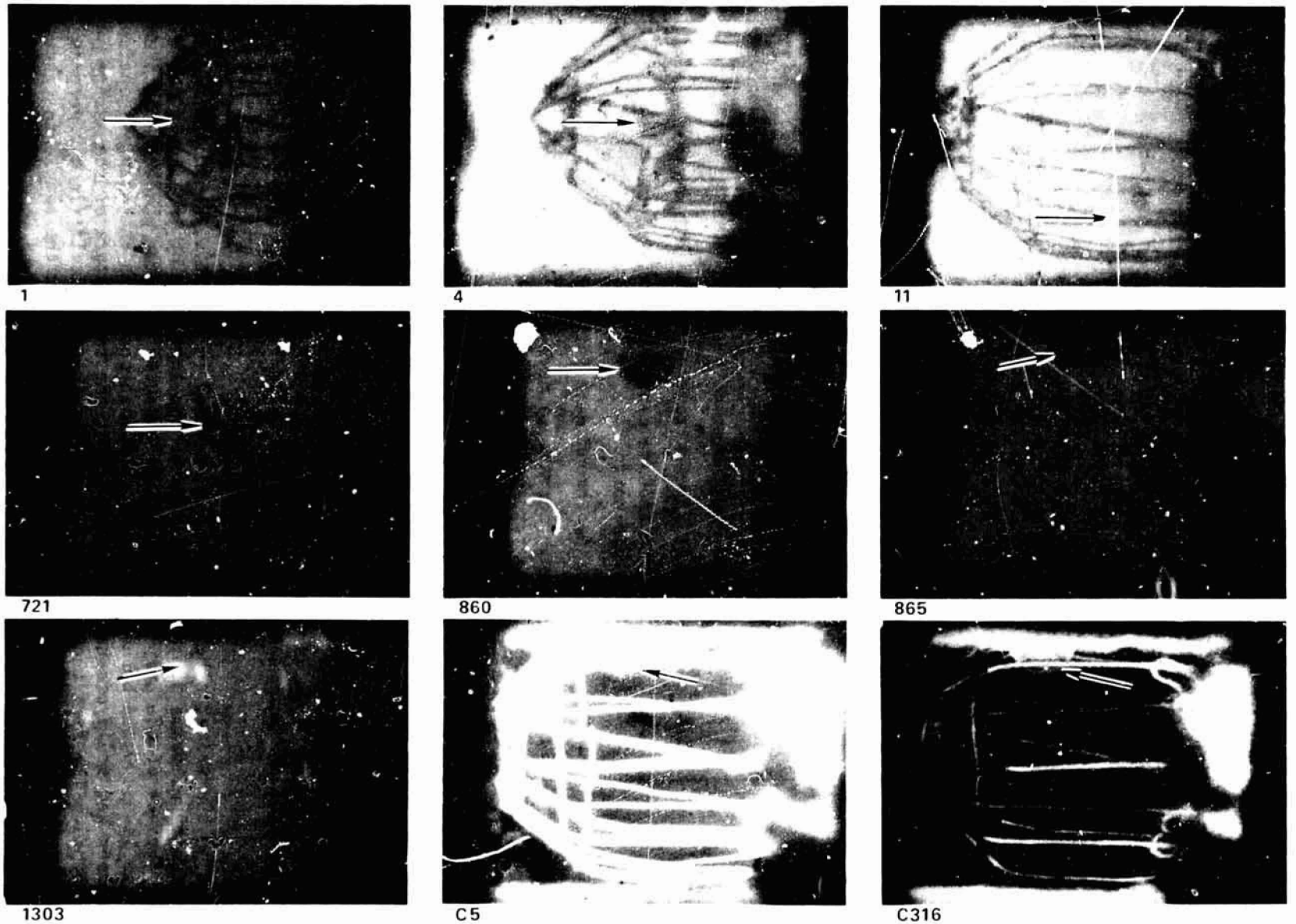

Figure 14. Selected Frames From Flight Motion Pictures

Table 1. Significant Events on Flight Film

Frame Number	Seconds*	Event
0	0	Clear
1	0.042	Injection cage first visible
4	0.17	Cage begins to open
11	0.46	Cage fully open
12	0.50	Sample touches bottom of cage (1st touch)
41	1.7	Sample touches top of cage (2nd touch)
124	5.2	Sample touches right side (inner cage)(3rd touch)
207	8.6	Sample again touches right side (4th touch)
530 $\pm$ 10	22.1 $\pm$ 0.4	Contrast has increased, sample appears darker than before
577	24.0	"Jiggling" (or rotation of sample) first noticed
780	32.5	Contrast best (sample appears darkest) since frame 530
859	35.8	Sample begins to move upward
860	35.8	Sample appears to touch wire (5th touch)
865	36.0	Sample appears centered on wire, no further motion
C2	0.08	Cooling shroud gate fully open
C914	38	Sample appears to have reached cooling shroud temperature (everything is dark)

*All of the times given here necessarily assume that the flight camera was running at exactly 24 frames a second during the entire flight.

ing shroud background and can no longer be seen in the film. After about 21 seconds (in the vicinity of frame 500) the sample has blended with the background and cannot be seen. This is not shown in Figure 14. At about frame 530 (22 sec) the sample appears to begin to become darker than the background again. This darkening of the sample with respect to the background continues, and maximum contrast is achieved again by frame 780, 8 seconds later.

It is the writer's belief that the reversal in contrast, beginning in the vicinity of frame 530, is indicative of the formation of the liquid phase on the surface of the sample. It is to be expected that the phase change from solid to liquid would be accompanied by a sudden change in the sample's optical properties and would create the illusion that the temperature of the sample had dropped. The fact that the sample quickly centers itself (in 0.2 seconds) after contacting and wetting the cage wire indicates that the sample must have been largely molten at that time.

ANALYSIS AND EVALUATION OF RETURNED FLIGHT SAMPLE

Magnified views of the flight sample are shown in Figures 15 and 16. Note that the sample is entirely free of internal* crystalline material. This indicates that melting was complete during the flight. Any unmelted material would have remained as opaque or translucent material within the body of the glass sample.

It is also apparent from Figures 15 and 16 that the sample is well centered on the 0.014-inch-diameter Pt-Rh wire. The diameter of the sample, as measured by micrometer, is 0.2501 $\pm$ 0.0001 inches. As measured from 8-in. by 10-in. photographs, the centering appears to be within 0.002 inches. Good centering is to be expected since the sample, which wets the platinum alloy, would like to spread along the platinum as much as possible. The maximum length it can achieve along the platinum is at the centered position in the absence of significant sonic forces at that location. The wetting angle between the glass and the platinum was measured at about 50 degrees.

In Figure 15, three bubbles can be seen in proximity to the wire. It is suspected that the bubbles result from entrapment of air caused by localized zones of slower wetting of the platinum alloy by the glass as the glass spreads along the wire. A similar effect has been frequently noted by the writer in brazed and soldered metallic joints where spreading of the brazing alloy or solder through the joint is not uniform, resulting in formation of voids within the joint.

Figure 17 shows two end views taken at two different angles to the wire. In both of these views, the sample is circular to within less than 0.0001 inch.

Figure 18 shows the sample under polarized light. It appears to be quite free of residual stress except near the glass/platinum interface. This is not unexpected because the glass and the platinum alloy undoubtably have different thermal expansion coefficients. Since the glass wets the wire, a stress field must therefore be set up as the sample and the wire cool.

An attempt was made, without success, to measure the index of refraction of the flight sample by immersing it in a series of fluids with indices that varied in 0.005 steps. Subsequently, a small chip was removed from the loaf casting from which the flight sample had been removed and was, therefore, of the same composition, i.e., 35.7 CaO : 39.3 Ga_2O_3 : 25 SiO_2, in mol % as the flight sample. The index, measured with sodium D illumination, was determined as falling between 1.710 and 1.715.**

*In Figure 16 particularly, surface crystallites may be seen out of focus. This subject is discussed in more detail later.

**This compared with a reported value in Reference 7 of 1.712 for the $Ca_2Ga_2SiO_7$ glass. The composition of the latter, in mol %, is 50 CaO : 25 Ga_2O_3 . 25 SiO_2.

~26 X

Figure 15. Flight Sample

~26 X

Figure 16. Flight Sample, Opposite Side From Figure 15

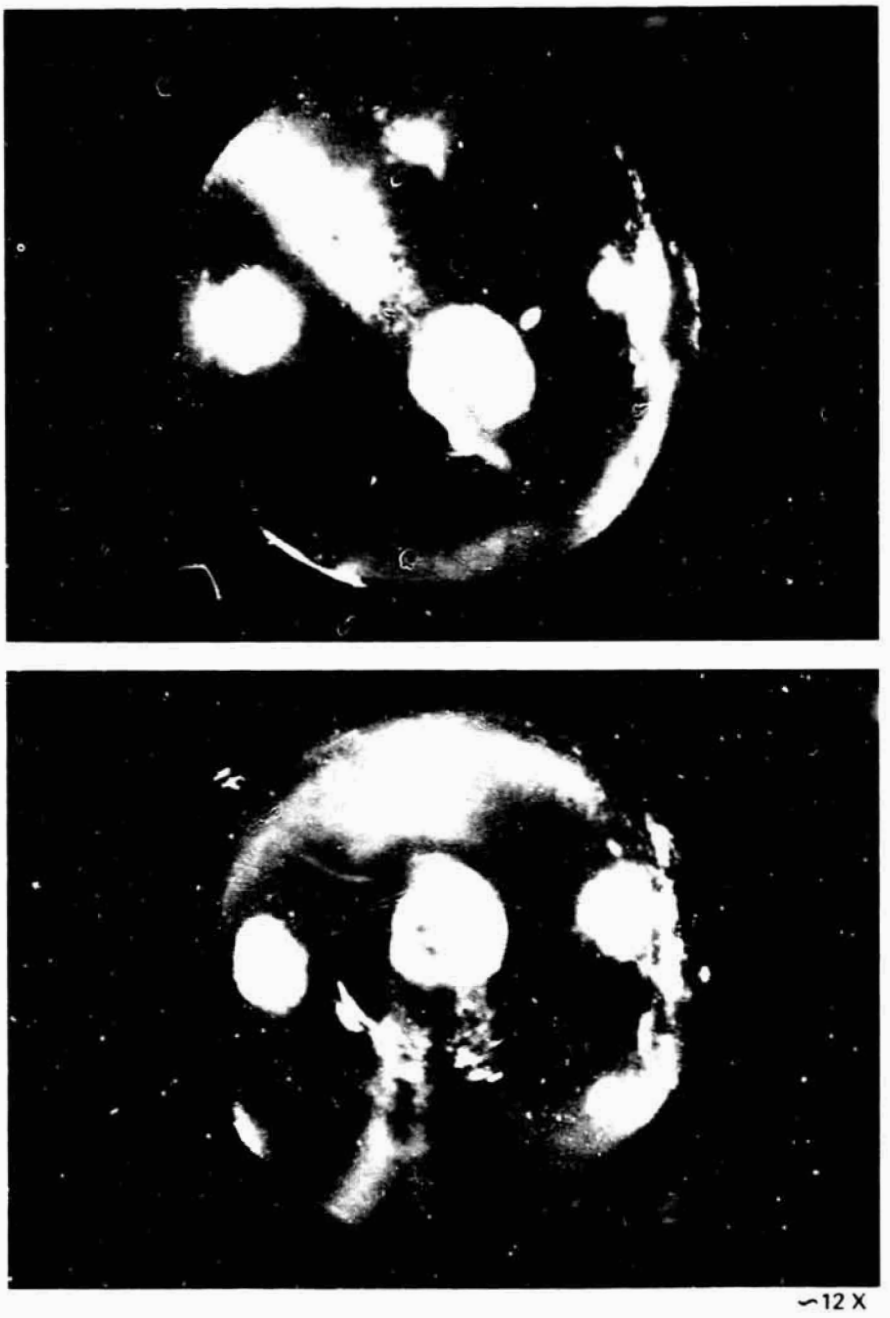

Figure 17. Two End Views of Flight Sample

(Sample immersed in α-bromonaphthalene and photographed by transmitted light with the two polarizers at 90° to each other.)

Figure 18. Stress in Flight Sample - Polarized Light Photograph

SURFACE CRYSTALS

After the flight sample had been in the possession of the writer about four weeks, it was noted that the surface of the sample contained numerous surface crystal rosettes not visible to the unaided eye. They are shown in Figure 19. There appears to be a greater concentration of crystals in one hemisphere than in the other (Figure 19 B). Similar appearing, but much larger, crystals had been noted on the free surface of the cooled melt (Figure 4) and on the free surface (only) of the loaf casting (Figure 5). Figure 20 shows a portion of the free (upper) surface of the loaf casting from which the flight material was removed. There are two forms of crystals present on the casting's free surface. The larger white rosettes are similar to those predominating on the surface of the flight sample. The smaller, darker appearing crystals are invaribly roughly rectangular in shape when examined at high magnification. This subject will be addressed again later.

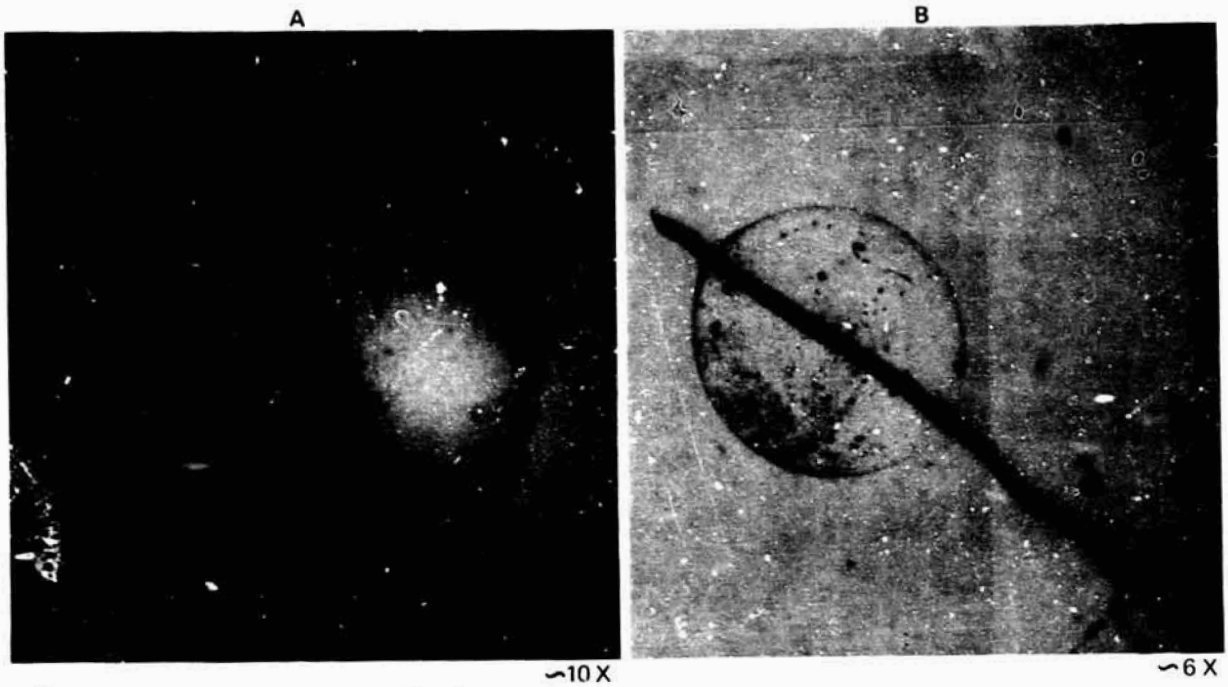

Figure 19. Two Views of Flight Sample Showing Surface Crystals

Figure 20. Crystals on Top Surface of "Loaf" Casting

The finding of crystalline material on the flight sample's surface was of concern to the writer because of the possible ramifications in connection with the next SPAR flight experiment. Because of the relatively high silica content of the SPAR VI material, crystal growth is quite slow so that any crystal growth is arrested during cooling from the melt. However, in the binary gallia-calcia material being considered for the next SPAR flight experiment, the crystal growth rate is estimated to be several orders of magnitude greater than with the silica-modified material. Therefore, it is probable that such crystallization, if it occurs on the surface of the gallia-calcia flight sample, would result in conversion of the entire mass to the crystalline condition upon cooling. It then becomes imperative to learn as much as possible, within time and funding limitations, about the small crystallites on the surface of the present flight sample.

A portion of the flight loaf casting was remelted with the laser/air suspension unit (Reference 3). The surface of the sample so prepared was found to be free of crystallites. A sample of the binary gallia-calcia glass prepared also by laser/air suspension melting was also found to be entirely free of crystallites.

The remelted (laser) sample was immersed for four weeks in the same fluid, (α bromonaphthalene) that the flight sample had been exposed to prior to noting of the crystallites. After exposure the sample was still free of crystallites. This convinced the writer that the crystals must have formed on cooling during the SPAR VI flight.

Next, the flight sample was gold-coated and examined with a scanning electron microscope. Results are shown in Figures 21 through 28. Figure 21 shows the appearance of a typical crystallite at about 700X magnification. EDAX (energy dispersive analysis by X ray) analysis (Figure 22) of the rosette material showed it to be of about the same composition as the surrounding glass. Examination of the center of several rosettes failed to reveal a compositional difference that could give a clue to the nucleating material if indeed it is different from the crystallite composition.

The sample was then etched by immersing several hours in dilute KCN. The sample was again gold-coated, and about a dozen rosettes were examined with the SEM (scanning electron micrograph). In about one-third of them, the etching had left a different material in relief at the center. Two such rosettes are shown in Figures 23 and 25. The EDAX analysis of Figure 26 (a and b) shows that the material in the center is largely platinum. Since about one-third of the rosettes examined after etching were found to contain platinum in the center, it would appear that platinum is the nucleating agent. Failure to find platinum in the center of the remaining two-thirds of the rosettes examined probably indicates that etching had not been carried far enough to expose the underlying platinum.

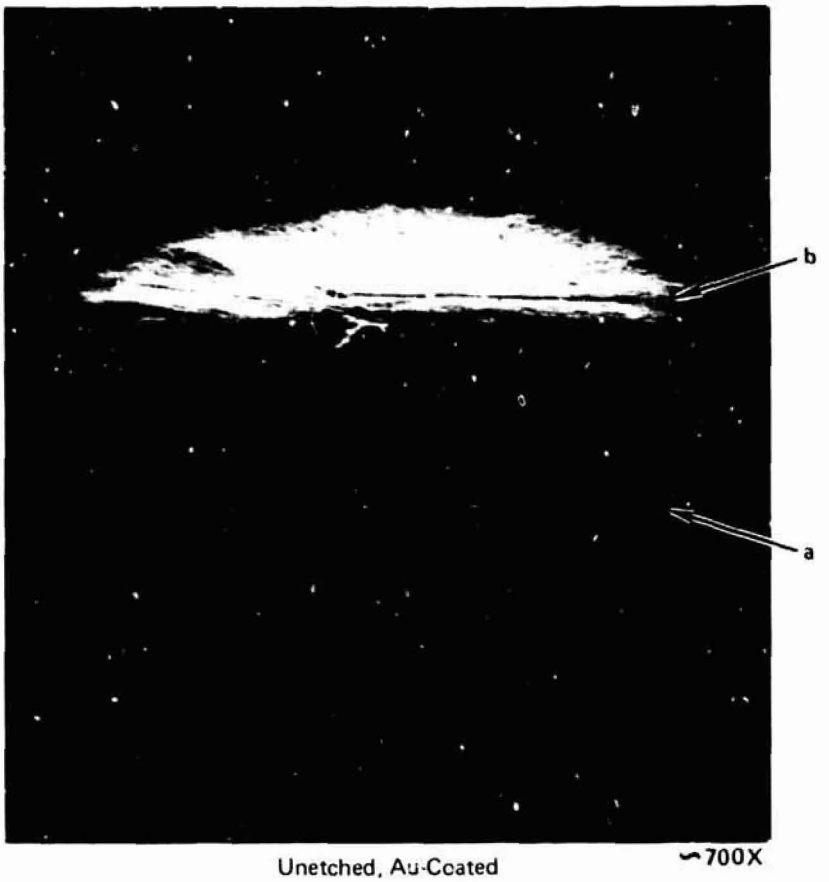

Figure 21. Scanning Electron Micrograph (SEM) of Typical Crystal Rosette on Surface of Flight Sample

The finding that platinum is most probably the nucleating agent for the crystals leads one to speculate about how the platinum got there. Four different mechanisms may be considered, as follows:

1. Migration of platinum by diffusion from the wire embedded in the molten flight sample over the surface.

2. Vapor transport from the platinum wire to the surface of the flight sample.

3. Migration by diffusion of the small amount of platinum dissolved in the glass from the terrestrial melting in platinum.

4. Mechanical transfer of platinum from the cage to the sample during early portions of the flight.

With respect to the fourth mechanism, the sample was apparently a rather loose fit in the cage. Vibration at launch could have caused it to rattle around between the inner and outer portions of the cage. Since the cage material is a platinum and 30 per cent rhodium alloy, one would expect the rhodium to be transferred along with the platinum. There are strong

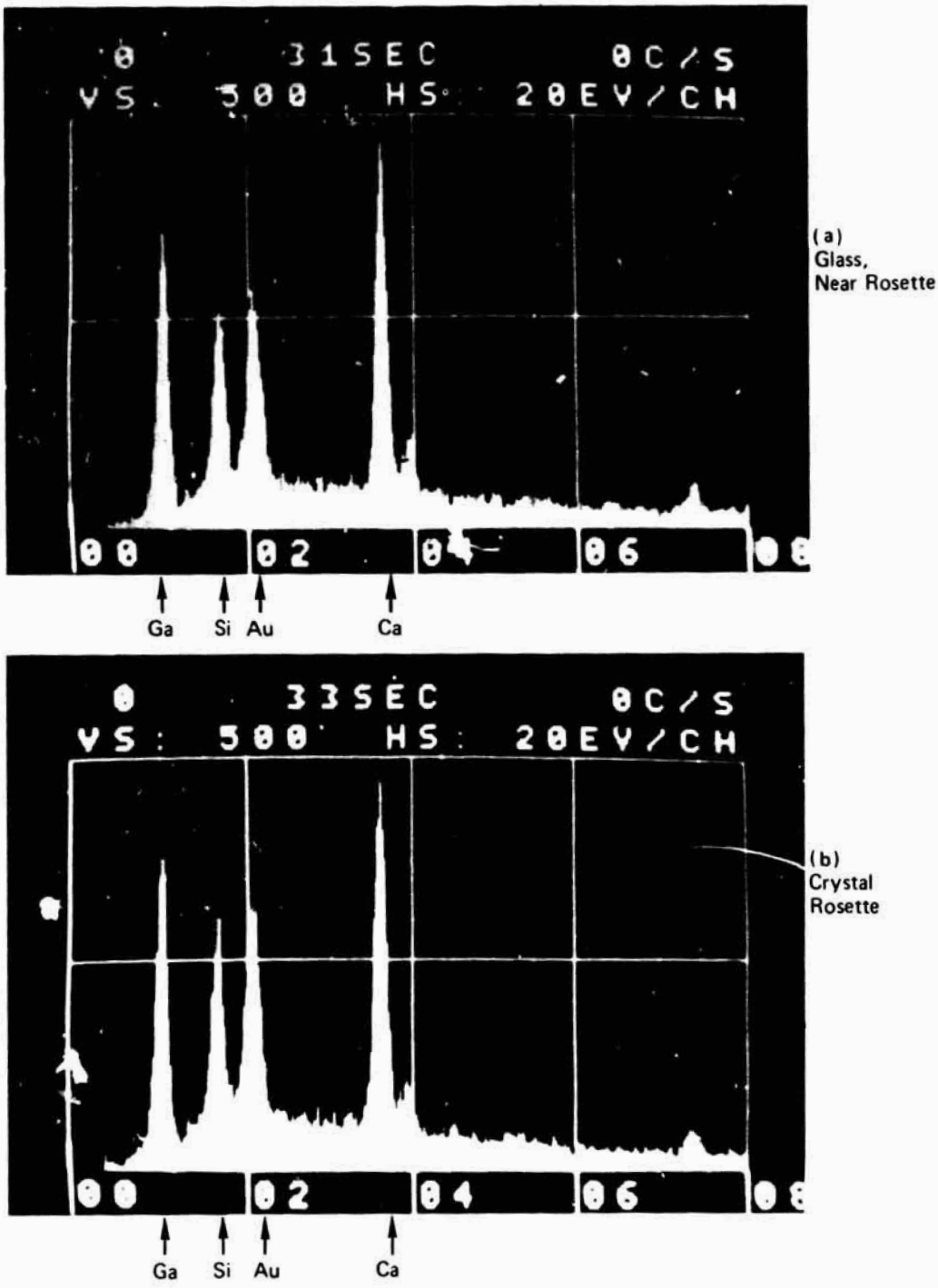

Figure 22. EDAX (Energy Dispersive Analysis by X Ray) of Glass of Figure 21, Near Rosette (Top) and Rosette Material (Bottom)

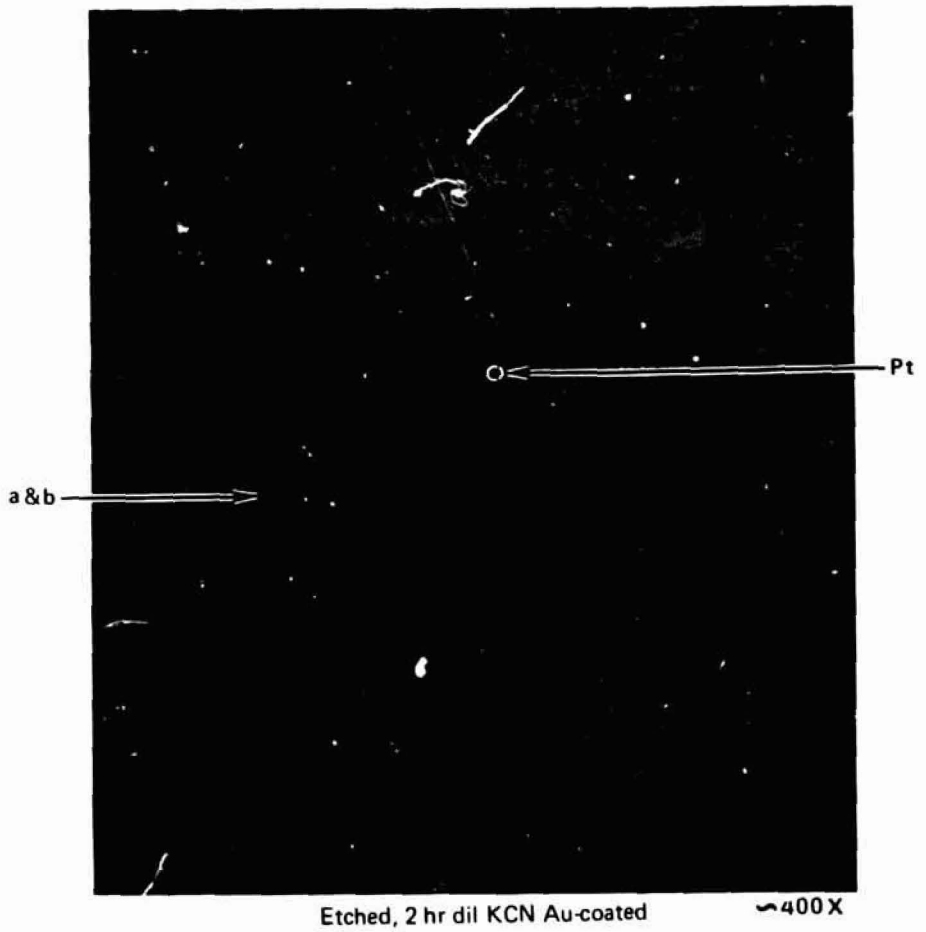

Figure 25. SEM Photograph of Rosette on Surface of Flight Sample

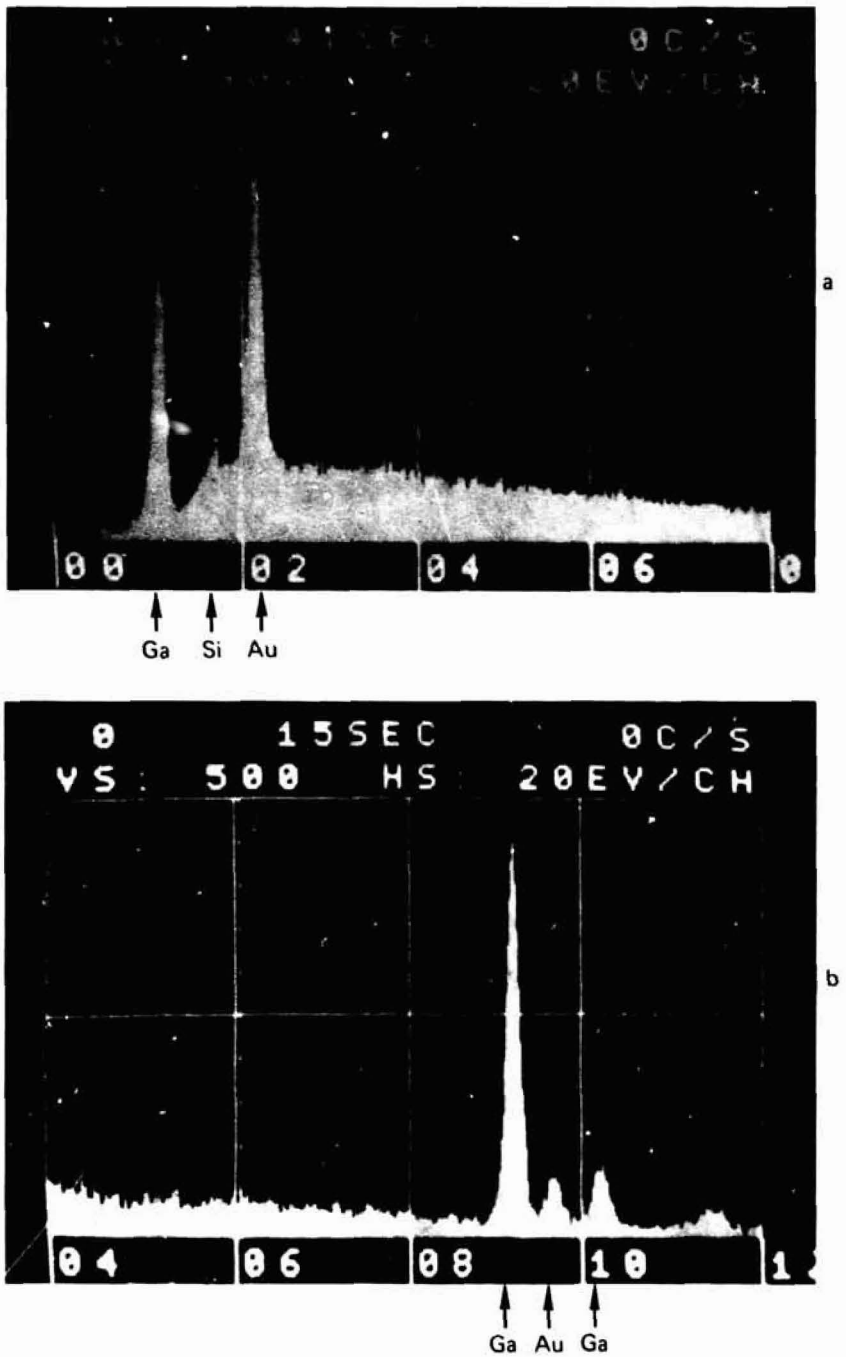

Figure 24. EDAX of Location a, b of Figure 23

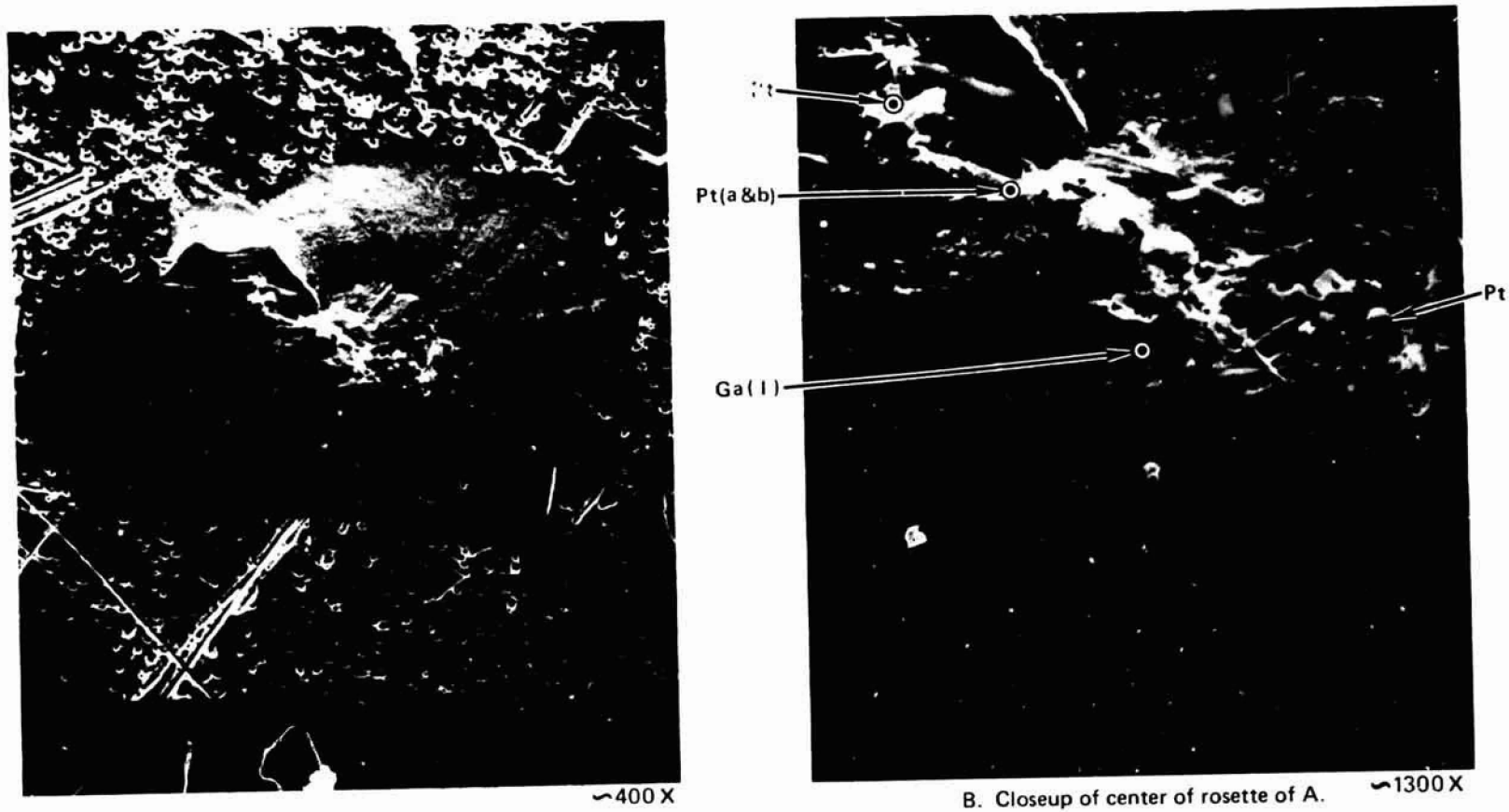

Etched 2 hours in dilute KCN, Au-coated

Figure 25. SEM Photographs of Rosette on Surface of Flight Sample

rhodium lines at 2.7 and 2.8 Kev. Examination of the EDAX of Figure 26b shows a small peak in this area, an indication that rhodium may well be present. The third mechanism would not appear to be likely since the laser-remelted sample did not contain surface crystals, as noted earlier.

The second mechanism cannot be positively eliminated at this time. However, a vapor transport mechanism would seem to require that, at the time of transport, the surface temperature of the glass sample be significantly lower than that of the platinum wire so that the platinum would condense there. There should have been only a small temperature difference between the two during the entire flight experiment schedule. If anything, during the heating phase the platinum would be expected to be at a lower temperature than the surface of the sample because it has a higher reflectivity (lower absorptivity). During cooling, the reverse should be the case because the glass has a much higher emissivity than the platinum. However, such a condition exists for only a few seconds of the total schedule. During the longest part of the schedule, i.e. the soak, the temperature of the glass and the platinum should be very nearly the same. If there is a difference, one would expect the platinum to be at a slightly lower temperature than the glass surface because it is in contact with much cooler portions of the hardware and is a relatively good thermal conductor.

It is the writer's opinion, lacking further evidence, that the first and fourth mechanisms are the strongest possibilities of the four. Dr. Housely of Rockwell's Science Center states that he has frequently encountered surface migration of platinum in contact with non-metallic melts of other compositions.

If the writer's reasoning is correct, the lack of physical contact with platinum during melting, which is planned for during the next SPAR experiment, should eliminate the possibility of transfer by surface diffusion.

Ensuring that the sample is held firmly in the cage before launch should substantially reduce the possibility of mechanical transfer. The next SPAR experiment, if it is carried out as planned, should cast further light on the subject.*

Returning to the SEM photographs, it was found that the roughly rectangular-shaped crystals are gallium oxide as is shown by the EDAX of Figures 26 (c) and 28 (c).

EDAX of the white rosettes on the surface of the loaf casting (Figures 27 (b) and 28 (b) showed them to be of approximately the same composition as those found on the flight sample. Accordingly some of the material was filed off and examined by X-ray diffraction. The diffraction pattern showed that the major constituent is $Ca_2Ga_2SiO_7$ ($2CaO : Ga_2O_3 : SiO_2$), Reference 7. This phase has a tetragonal structure and cannot therefore be isomorphous with those found in the binary gallia-calcia system, i.e.,

*At this writing, a decision has not been made whether to fly the binary gallia-calcia or the silica-modified composition on the next SPAR experiment. In the event the latter is chosen, it will be possible to check for platinum contamination if crystallites are found on the surface.

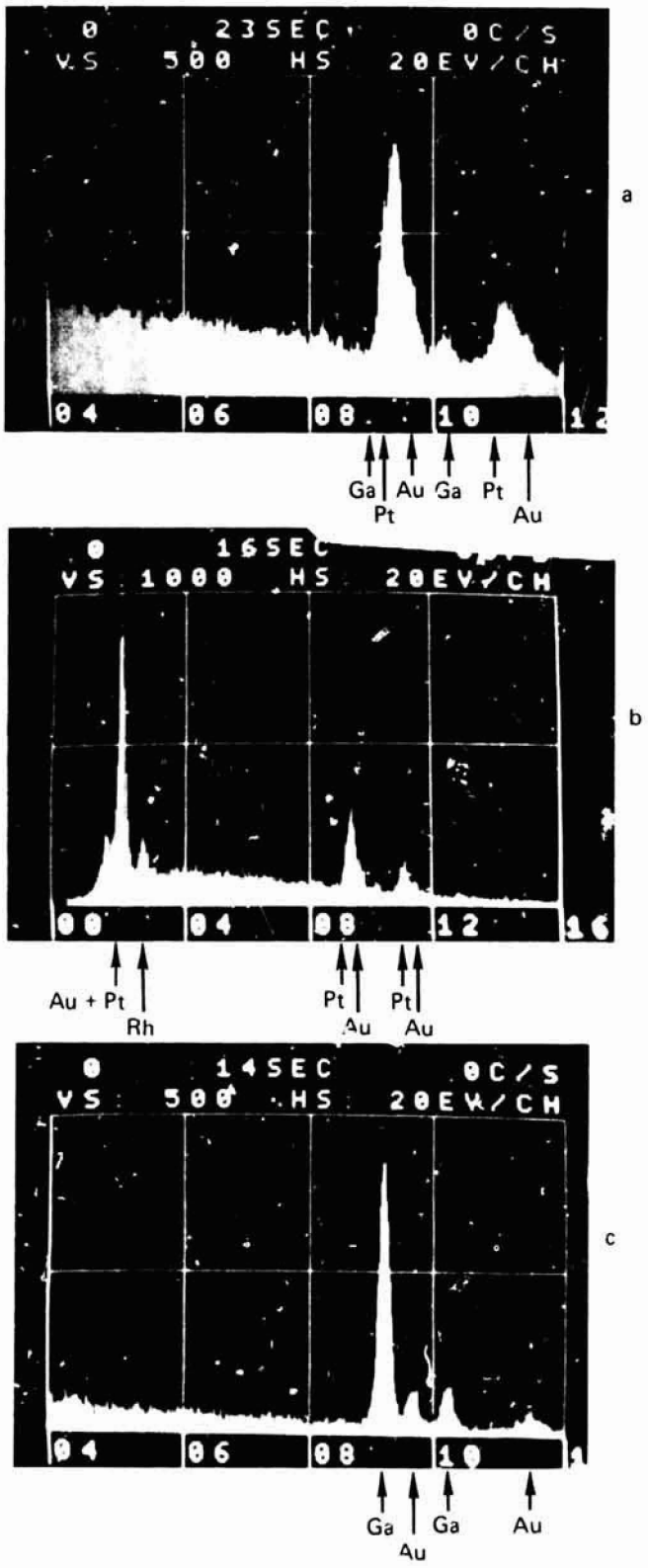

Figure 26. EDAX of Locations a, b, and c of Figure 25

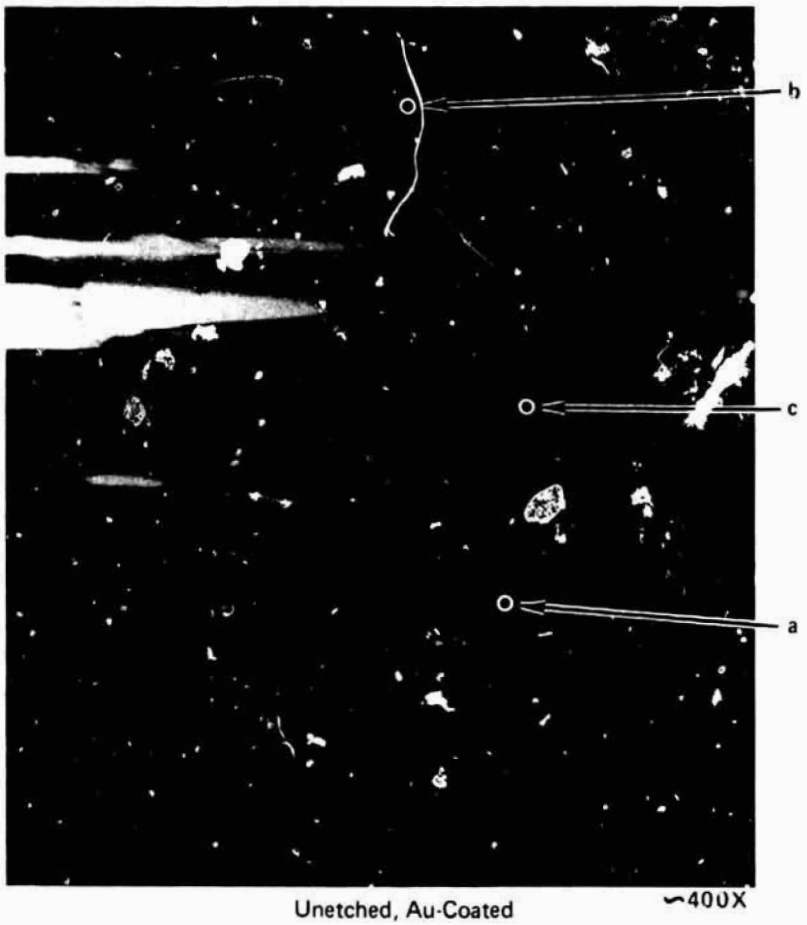

Figure 27. SEM of Top Surface of Terrestrially Prepared "Loaf" Casting

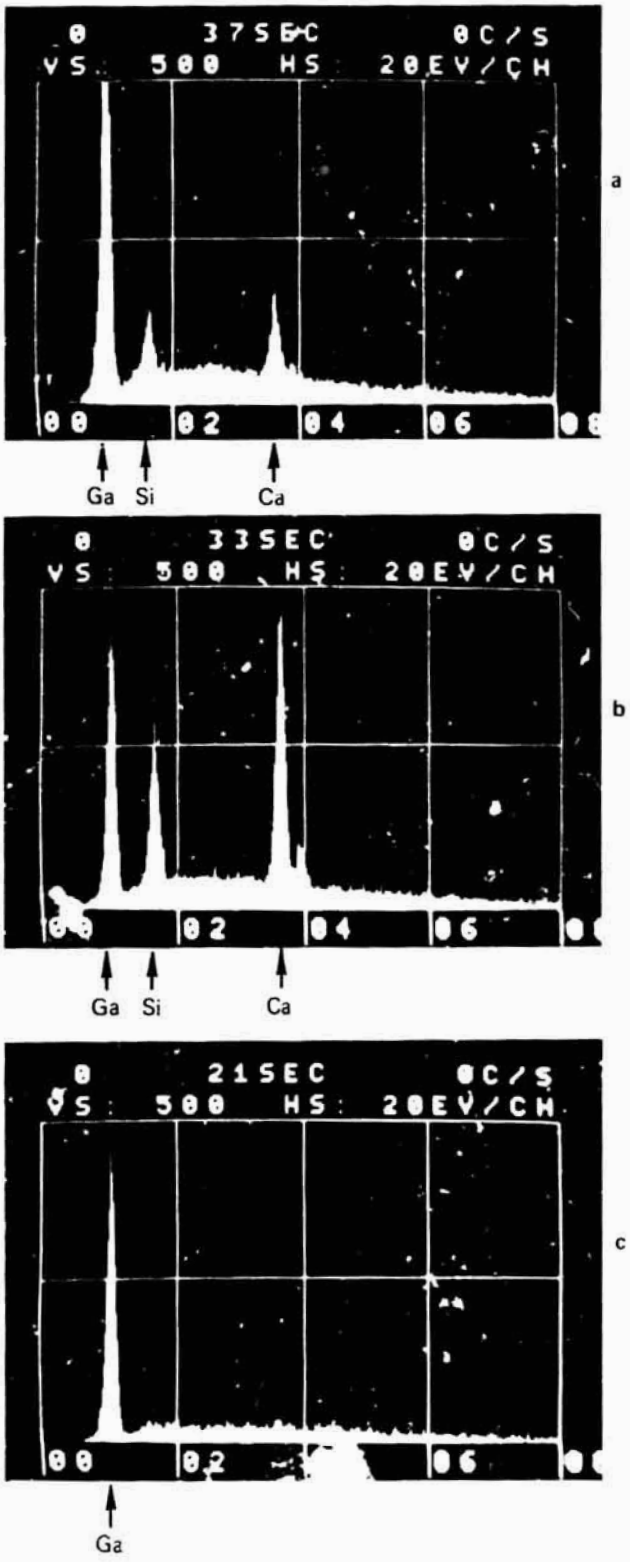

Figure 28. EDAX at Locations a, b, and c of Figure 27

CaO : Ga_2O_3 (orthorhombic) and CaO : 2 Ga_2O_3 (monoclinic, Reference 10). There is no 2CaO : Ga_2O_3 compound in the gallia-calcia system according to Reference 8 (refer also to Figure 2).

There are also five unidentified weak lines in the diffraction pattern which do not fit the $Ca_2Ga_2SiO_7$ pattern. This indicates that there are minor other constituent(s) present also.

In summary, the finding of the silicate phase, not isomorphous with any of the possible calcium gallates, indicates that the rosettes found on the surface of the flight sample are unique to the ternary system. The silicate cannot appear in the binary gallia-calcia glass planned for the next flight experiment.

CONCLUSIONS AND DISCUSSION

Despite the fact that the sonic positioning device did not prevent the sample from contacting solid objects within the furnace during the entire processing cycle as planned, the SPAR VI flight experiment may be considered a qualified success.

SCIENCE

The flight sample, which was returned in very good condition, had obviously been completely melted during the flight processing cycle. It therefore follows that the flight processing temperature-time cycle was adequate.

An unexpected development was the finding of numerous small crystallites of the compound $Ca_2Ga_2SiO_7$ which formed during cooling on the sample's surface. During the post-flight evaluation the crystals were identified and their presence almost certainly linked to the presence of platinum (and rhodium) on the surface of the glass sample. The platinum was found to be, with very little doubt, the nucleation sites for the crystallites. It was resulted either from (1) mechanical transfer from the loose-fitting platinum alloy injection cage during the highest vibration portion of the flight, i.e. during injection of the missile into its trajectory, or (2) surface diffusion of the platinum (and rhodium) from the platinum alloy wire impaling the specimen while it was molten.

FLIGHT HARDWARE

The flight experiment hardware functioned essentially as planned, with the exception that the sample contacted and wet the platinum alloy cage 36 seconds after sample injection into the hot zone of the furnace. Among the hardware functions that occurred successfully were:

1. The furnace and heating elements survived the launch environment and held to a nominal temperature during the entire processing cycle well enough to permit complete melting of the sample.

2. The acoustic positioning device was able to capture the sample, despite a rough injection. After several contacts with the cage during the first nine seconds, the acoustic positioner satisfactorily prevented contact of the sample with furnace components for 27 seconds before it contacted the cage wire.

3. The copper-rod cooling shroud was successfully deployed and cooled the sample approximately to the shroud temperature in the allotted time.

4. The flight motion picture camera functioned flawlessly, exposures were as planned, and the returned film, after development, was invaluable as an aid to understanding flight events.

While the writer, from his study of the flight motion pictures, is convinced that the sample must have been largely molten at the time of contact with the cage wire, there is room to argue that the successful suspension of a liquid glass has not yet been conclusively demonstrated. It has not been possible to demonstrate that the sample was completely molten at the time of contact. The first evidence that the sample appeared to have undergone a phase change occurred only six to twelve seconds before the sample contacted the wire. It is not known whether the, presumably, molten condition of the sample contributed to its escape from the sonic well. The fact that on its fifth and final contact with the platinum cage the sample stuck to the wire is strong evidence that the surface was molten at that time. The further observation that the sample essentially centered itself on the platinum wire only 2/10 of a second after making contact would appear to indicate that the surface melting must have extended to a depth of at least one-quarter diameter at the time of contact.

While the cooling shroud functioned as planned, the ability of the sonic system to prevent contact with the cage during and after deployment of the shroud was, of course, not demonstrated because the sample's wetting the platinum wire overrode the sonic positioning forces.

It is the writer's firm conviction that, despite the experiment's lack of total success, it was a valuable experience for all concerned and must be considered a major contribution to the technology of glass-making in space.

ACKNOWLEDGMENTS

The writer wishes to express his thanks to those in the Rockwell International organization who assisted in the post-flight evaluation portion of this investigation. Dr. L. E. Topol of the Environmental Monitoring and Service Center offered valuable suggestions in a consulting capacity. Dr. R. Housely of the Science Center performed the SEM work and is reponsible for the identification of the nucleation sites of the surface crystallites. Dr. M. D. Lind of the Electronics Research Center performed the X-ray diffraction analysis of the crystallite material. C. Parker did the still optical photography* of the specimen after removal from the injection cage. A. R. Sale was responsible for motion picture film processing and assisted the writer in analysis and interpretation of the flight motion pictures. C. N. Scully, the discoverer of the surface crystal rosettes, did the index of refraction measurements. The preceding three are all with the Space Operations and Satellite Systems Division of Rockwell.

In addition the writer held numerous valuable conversations with Intersonics personnel C. Ray, R. Whymark, and J. Yearnd.

Thanks are also extended to the members of the USRA Glass Committee, who have offered many valuable suggestions.

*All photography in the preflight sections and the flight samples with the injection cage was performed by the writer.

REFERENCES

1. Duwez, E. D. "Structure and Properties of Alloys Rapidly Quenched from the Liquid State." Trans. of the ASM 60 (1967) 606.

2. Neilson, G. F., and M. C. Weinberg. Development of Improved Amorphous Materials for Laser Systems - Final Report, Task Order RD-151, Contract 953846 under Contract NAS7-100, Owens Illinois, Inc. (November 1974).

3. Happe, R. A. Manufacturing Unique Glasses in Space - First Interim Report, Rockwell International Corporation, Space Division, SD 74-SA-0174 (November 1974).

4. Happe, R.A. Manufacturing Unique Glasses in Space - Second Interim Report, Rockwell International Corporation, Space Division, SD 76-SA-0029 (March 1976).

5. Rawson, H., Inorganic Glass-Forming Systems, Academic Press (1967).

6. Baynton, P.L., H. Rawson, and J. E. Stanworth, "Gallium Oxide Glasses," Nature (February 23, 1957).

7. Toropov, N.A. and Lin' Tszu-syan. "The Ca_2Al [$AlSiO_7$] - Ca_2Ga [$GaSiO_7$] System," Russian Journal of Inorganic Chemistry, Vol. 5, No. 11, (November 1960) p. 1194.

8. Jeevaratnam, J. and F. P. Glasser. "The System CaO-Ga_2O_3," Journal of American Ceramics Society. 44 (1961) 564.

9. Levin, M.L., C.R. Robbins, and H. F. McMurdie. Phase Diagrams for Ceramists, The American Ceramic Society, Inc. (1964, 1969,1975).

10. Deiseroth, H. J., and H. Muller-Buschbaum. Z anorg. Chem., 382, 149-156 (1971).

APPENDIX A

PRINCIPAL INVESTIGATOR'S "QUICK-LOOK" REPORT

National Aeronautics and Space Administration
George C. Marshall Space Flight Center
Marshall Space Flight Center, Alabama 35812

Attention: David Schaefer, LA11

Subject: Experiment 74-42, Principal Investigator's "Quick Look" Report - SPAR VI - NAS8-32023

Launch Information

SPAR VI Launched at 6:40 a.m., MST - White Sands Missile Range, New Mexico, October 17, 1979.

Payload returned to Missile Assembly Building at White Sands at approximately noon, October 17, 1979.

Flight experiment injection cage and specimen removed from the furnace - early afternoon, October 17, 1979.

Payload reported to have landed in a gully, toppled down-hill, slid over 30 feet into the gully before coming to rest. There was a large dent, with a fracture, in the casing surrounding the General Electric (G.E.) experiment at the upper and near the nose cone. Experiment 74-42 was the second from the nose cone. There were numerous scratches in the payload outer skin in the 74-42 section.

Flight Experiment Sample

The gallia-calcia-silica sample was found impaled on a fine platinum wire forming part of the wall of the outer injection cage of the flight hardware. The sample was clear, 100% glass, almost colorless, and appeared to be quite spherical in shape except for small projections caused by wetting the platinum wire at either end where it emerged from the sample. One or two small bubbles can be seen inside the glass sphere and in contact or close proximity with the platinum. Except for these, the sample appears entirely free from bubbles as determined by approximately 10X examination with a hand glass.

Flight Experiment Sample (cont'd)

The platinum wire appears to be very well centered in the sphere. The flight sample and the Pt cage, along with part of the injection mechanism, are in the possession of the writer.

Flight Motion Pictures

The flight film was signed over to the writer and returned to Los Angeles without exposing it to x-ray examination. It measured 159 feet in length. In order to cover the complete time line of the flight, the length would have to have been 149 feet. It was apparent, then, that the returned flight film contained all of the flight information, plus 10 feet of leader and ends.

The time line for the flight camera was as follows:

Event	Time, Sec.	Cumulative Time, Sec.
Camera on	0	0
Sample injection	5	5
Soak	155	160
Cooling shroud gate open		160
Cooling shroud insertion	10	170
Cooling	73	243
Sample retraction		243
Camera off		248

Camera Exposure Information:

-F/8, 140° shutter, 24 frames/second.

Flight Motion Picture Processing and Evaluation

A 21 foot section was cut from the film starting 42 feet (70 seconds) from the head end. The end of the cut was 45 seconds later. This piece is being stored for possible future image enhancement experiments. An additional length of the same type of film (EK Linagraph Shellburst 2476) was exposed outdoors using the manufacturer's ASA rating. This piece was developed along with the two pieces of flight film. Normal results were obtained.

Flight Motion Picture Processing and Evaluation (cont'd)

The flight film and a print were received on October 29, 1979, and examined using a photo-optical data analyzer.*

It was revealed that the specimen contacted the Pt wire, where it stuck, 860 frames (36 seconds) after sample injection. The specimen appeared to have centered itself on the wire 5 frames (0.21 seconds) later. The specimen touched the cage, while still solid, three times during the first 8.5 seconds after injection. It went through various motions without touching the cage for 27 seconds before touching and wetting the Pt wire. The sample appeared to be fully molten about 29 seconds after injection, or 7 seconds before it stuck to the wire.

When the cooling shroud gate opened near the tail end of the film the cage with the sample impaled on it could be seen clearly. It had cooled to a temperature where nothing more could be seen on the film (all black) 914 frames (38 seconds) after the cooling shroud gate opened.

Tentative Conclusions

Everything functioned as planned during the entire experiment with the exception that the specimen contacted and stuck to the platinum wire cage soon after it had melted. The following were accomplished successfully:

1. The furnace reached and held a high enough temperature to permit complete melting of the flight sample in the time available.

2. All mechanical functions appear to have been accomplished as planned. The only exception to this was that the specimen injection gate did not close completely (as shown by the telemetry data). This could have been caused by the failure of the injection cage to retract completely because of a clearance problem created by the specimen's projecting beyond the cage.

3. The flight specimen was recovered in excellent condition - was free of scratches and nicks and in good condition for completing the science evaluation.

---

* L-W Photo, Inc. - Type 224-A T-V.

Tentative Conclusions (cont'd)

4. Flight motion pictures were properly exposed according to the Principal Investigator's (P.I.) pre-planning. No camera jamming or other malfunction appeared to have occurred. Resolution is good enough to permit detailed study of the sample's behavior in the sound field.

5. The experiment exceeded the science minimum success criteria established before flight and met the science objectives.

Further Work Required

During the next few weeks, the following work needs to be done before the Final Post Flight Analysis Report is prepared:

1. Experiment Equipment Function

It is important that the exact cause of the specimen's contacting the platinum cage be understood so that corrective measures, if indicated, can be taken before the next flight experiment. This will involve:

a. Further detailed study of the flight film by Intersonics, Incorporated.

b. Careful comparison of the flight data obtained with accelerometer data to be provided by MSFC.

c. Analysis of pertinent results of other experimenters on the same flight; especially those of G.E. and J.P.L., and comparison with the 74-42 flight information.

2. Flight Sample Evaluation

The sample will be cut from the cage, after which the following is planed to be accomplished:

a. Sample dimensions and degree of sphericity will be measured using photographic techniques.

b. The index of refraction will be determined using immersion fluid techniques.

2. Flight Sample Evaluation (cont'd)

c. An immersion fluid with matching index of refraction will be prepared and the interior of the sample will be examined for:

1. Striae, and compared with pre-flight starting material.

2. Stress using polarized light.

d. Centering of the platinum wire will be measured using photographic techniques along with measurement of the wetting angles of the glass to the platinum.

If all of the above can be accomplished successfully, it will be unnecessary to cut or grind the sample and it can be preserved intact as a space artifact.

ROCKWELL INTERNATIONAL CORPORATION
Satellite Systems Division

R. A. Happe
Principal Investigator
Experiment 74-42
Contract NAS8-32023

gk

cc: Roy Whymark, Intersonics, Inc., Northbrook, Ill. 60062
W. B. Crandall, Alfred University, Alfred, N.Y. 14802
D. E. Day, Univ. of Missouri, Rolla, Missouri 65401
N. J. Kreidl, Santa Fe, New Mexico 87501
D. C. Larsen, ITT Res.Inst., Chicago, Illinois
G. E. Rindone, Penn. State Univ., University Park, Penn. 16802
E. Snitzer, United Tech. Res. Center, E. Hartford, Conn. 06108
D. R. Uhlman, Mass. Institute of Tech., Cambridge, Mass. 02139
M. C. Weinberg, JPL, Pasadena, CA. 91103

NASA

D. Schaefer, LA11	8 + Reproducible
AP29-F	1
AS21D	3
Mr. G. A. Abbott, NASA/MSFC, Downey	1
EH34/R. Nichols	1
EH23/L. H. Berge	1
AT01	1
ES74/J. Johnson	1

D2

National Aeronautics and
Space Administration

George C. Marshall Space Flight Center
Marshall Space Flight Center, Alabama 35812

CHAPTER IV

FINAL POST-FLIGHT REPORT

ON

SPAR VI

EXPERIMENT NO. 74-45

EPITAXIAL GROWTH OF SINGLE CRYSTAL FILMS

(CONTRACT NO. NAS8-31738)

TO

NATIONAL AERONAUTICS AND SPACE ADMINISTRATION

GEORGE C. MARSHALL SPACE FLIGHT CENTER

ALABAMA

MAY 31, 1980

PRINCIPAL INVESTIGATOR:

M. D. LIND, ROCKWELL INTERNATIONAL, THOUSAND OAKS, CA 91360

CO-INVESTIGATORS:

R. L. KROES, MARSHALL SPACE FLIGHT CENTER, AL 35812
A. A. IMMORLICA, JR., ROCKWELL INTERNATIONAL, THOUSAND OAKS, CA 91360

REPORT DOCUMENTATION PAGE	READ INSTRUCTIONS BEFORE COMPLETING FORM
1. REPORT NUMBER / 2. GOVT ACCESSION NO.	3. RECIPIENT'S CATALOG NUMBER
4. TITLE (and Subtitle) Epitaxial Growth of Single Crystal Films	5. TYPE OF REPORT & PERIOD COVERED Final Report 10/04/75 - 05/31/80
	6. PERFORMING ORG. REPORT NUMBER ERC41001.30FR
7. AUTHOR(s) M. D. Lind	8. CONTRACT OR GRANT NUMBER(s) NAS8-31733
9. PERFORMING ORGANIZATION NAME AND ADDRESS Electronics Research Center Rockwell International Corporation 1049 Camino Dos Rios, Thousand Oaks, CA 91360	10. PROGRAM ELEMENT, PROJECT, TASK AREA & WORK UNIT NUMBERS
11. CONTROLLING OFFICE NAME AND ADDRESS National Aeronautics & Space Administration Marshall Space Flight Center, AL 35812	12. REPORT DATE May 31, 1980 13. NUMBER OF PAGES 35
14. MONITORING AGENCY NAME & ADDRESS (if different from Controlling Office)	15. SECURITY CLASS. (of this report) Unclassified 15a. DECLASSIFICATION/DOWNGRADING SCHEDULE
16. DISTRIBUTION STATEMENT (of this Report)	
17. DISTRIBUTION STATEMENT (of the abstract entered in Block 20, if different from Report)	
18. SUPPLEMENTARY NOTES	
19. KEY WORDS (Continue on reverse side if necessary and identify by block number) liquid phase epitaxy, gallium arsenide, sounding rocket, SPAR program.	
20. ABSTRACT (Continue on reverse side if necessary and identify by block number) An experiment in gallium arsenide liquid phase epitaxy was performed successfully on the SPAR VI flight October 17, 1979. The design, fabrication, and testing of the experimental apparatus, and the performance and results of the experiment are discussed	

DD FORM 1 JAN 73 1473 EDITION OF 1 NOV 65 IS OBSOLETE

ABSTRACT

This report describes an experiment in gallium arsenide liquid phase epitaxy (LPE). This process appeared to be an appropriate subject for a SPAR experiment because (1) it is representative of crystal growth processes which are adversely affected by natural convection, and (2) the process variables, including temperatures and times, are within the capabilities of the SPAR flights. A general purpose LPE processor suitable for either SPAR or Space Transportation System flights was designed and built. For the SPAR flight the process was started before the launch, and only the final step, in which the epitaxial film is grown, was performed during the flight. The experiment achieved its objectives; epitaxial films of reasonably good quality and very nearly the thickness predicted for convection-free diffusion-limited growth were produced. The films have been examined by conventional analytical techniques and compared with films grown in normal gravity.

LIST OF FIGURES

TABLE OF CONTENTS

1.0 INTRODUCTION

A. Natural Convection in Crystal Growth Processes

In nearly all crystal growth processes, fluid density variations caused by variations in temperature or composition can result in fluid motion called natural convection. This can be a significant and even predominant factor in the transfer of material and heat in these processes. These flows can have adverse effects on growth rates, liquid-solid interface shapes, and distributions of impurities or dopants. In some cases, this is believed to contribute to the formation of excessive structural defects or compositional inhomogeneities in the crystals produced. These imperfections are likely to impair the performance of devices made from such materials, and can be a particularly acute problem in the production of large quantities of devices.

Natural convection occurs in a fluid when its Rayleigh or Grashof number exceeds a critical value. In the discussion which follows, we shall consider three cases: (1) For a vertical temperature difference, ΔT_V, across a fluid depth, d, the Rayleigh number

$$N_{Ra} = g \alpha \Delta T_V d^3/\kappa\nu \qquad (1)$$

is appropriate. Here g is the gravitational acceleration, α is the volume thermal expansion coefficient, κ is the thermal diffusivity, and ν is the kinematic viscosity of the fluid; (2) The equivalent Rayleigh number for a vertical solute concentration gradient, ΔC_V, is

$$N_{Ra} = g \beta \Delta C_V d^3/D\nu \qquad (2)$$

where β is the change in volume per unit change in solute concentration and D is the diffusion coefficient of the solute; (3) For a horizontal temperature difference, ΔT_H, across a fluid length, ℓ, the Grashof number

$$N_{Gr} = g \alpha \Delta T_H \ell^3/\nu^2 \qquad (3)$$

is appropriate. The critical values of the Rayleigh and Grashof numbers for natural convection in a particular crystal growth process depend on several factors, and can vary by an order of magnitude from one process to another. For the present discussion, it is not necessary to specify the critical values for any particular process, but only to note from the forms of the above three equations that to suppress natural convection in any given fluid, the Rayleigh or Grashof number can be reduced by reducing ΔT, ΔC, d, ℓ, or g. (In some special cases, natural convection can be suppressed by adding a substance to the fluid which increases its viscosity, ν, but this does not apply to the fluids to be discussed here).

Through the development of space flight in recent years, the investigation of crystal growth with reduced g has become possible. Several crystal growth experiments were performed during the Apollo, Skylab, and Apollo-Soyuz flights. During the interval between the Apollo-Soyuz flight (1975) and the first Space Transportation System flights (early '80's) the National Aeronautics and Space Administration is conducting a Space Processing Applications Rocket (SPAR) Project. This project utilizes Black Brant VC sounding rockets, which can carry payloads of several hundred pounds and provide durations of weightlessness of about five minutes.

B. Liquid Phase Epitaxy (LPE) of Gallium Arsenide

Gallium arsenide LPE appeared to be an appropriate process for investigation on a SPAR flight for the following reasons: (1) the process variables, including growth temperatures and rates, are compatible with the capabilities of the Black Brant VC flights; and (2) the numerous important technological applications of gallium arsenide LPE films have stimulated broad interest in this process and material, and therefore there was available

ample background information on which to base the design of a space flight experiment, and with which to compare results.

In most gallium arsenide LPE processes in normal gravity, the substrate is horizontal and a well of molten supersaturated solution of arsenic in excess gallium is slid horizontally over the substrate to cover it for a time long enough to grow the desired epitaxial film thickness, after which growth is terminated by sliding the solution away from the substrate (see Figure 1).

In solutions of arsenic in gallium, the diffusion coefficient, D, is much smaller than the thermal diffusivity, κ, and, therefore, solute concentration gradients predominate over temperature gradients in causing natural convection (see Equations 1 and 2, above). To suppress convection due to solute concentration gradients, it is necessary to limit the depth of solution, d, to 1-2 mm. Care must also be taken to minimize horizontal temperature gradients (ΔT_H in Equation 3) in order to suppress the convection that they would cause.

Until now, these ways of suppressing convection appear to have sufficed, and LPE processes routinely yield gallium arsenide and other compound semiconductor films adequate in quality for their applications. Therefore, the principal objective of the SPAR experiment was to improve our understanding of the process, and in particular, to confirm theoretical analyses of material transport and growth kinetics, rather than to achieve improved film quality. However, it is probable that natural convection is often not completely eliminated in conventional LPE processes in normal gravity, and that eventually the residual effects may be found to limit the usefulness of the films.

Furthermore, if future applications require larger wafer dimensions, the approach of reducing g may be the only one which can succeed. Thus, LPE processes in near-zero gravity may eventually turn out to be useful for producing superior films of gallium arsenide and other compound semiconductors.

For the process investigated, the epitaxial film thickness for the case of material transport by diffusion only is given by[1]

$$d_f = \frac{2\Delta T}{C_s m} \left(\frac{Dt}{\pi}\right)^{\frac{1}{2}} \qquad (4)$$

where ΔT = supercooling interval

C_s = concentration of arsenic in crystalline gallium arsenide

m = slope of the liquidus line[2]

$D = 5000e^{-20000/T}$, diffusion coefficient of arsenic in liquid gallium[3]

t = growth time

Evaluation of (4) with a growth temperature T = 990°K, ΔT = 10°K, and growth time t = 60 sec., all of which can be achieved on the Black Brant VC flights, results in $d_f \sim 1\mu m$. This is a desirable thickness for some gallium arsenide devices, such as field effect transistors.

II. Apparatus and Procedure for SPAR Experiment

A. Description of Apparatus

A self-contained LPE processor suitable for the Black Brant VC payload was designed and fabricated (see Figures 2-9). It is mounted in two adjacent rocket sections, 21.6 and 18.1 cm in length. The outside diameter of these sections is that of the rocket, 43.8 cm. The processor is composed of four major subsystems:

1. Furnace

The LPE processor has a specially designed tubular resistance heated furnace mounted in the upper rocket section (Fig. 6). Two doors in the section provide access for loading the furnace. The heating element is nichrome wire wound helically on a ceramic tube 2.5 cm in inside diameter and 9.5 cm long. The windings are spaced closer at each end to minimize axial temperature gradients. The insulation between the inner and outer tubes of the furnace is an asbestos based blanket. All other parts of the furnace are stainless steel. Its outermost shell is 10.2 cm in diameter and approximately 28 cm long. The maximum temperature of the furnace is approximately 1300°K.

2. Atmospheric Control

Provision is made for a flowing hydrogen atmosphere inside the furnace (see Figure 9). Hydrogen gas is always used to provide a reducing atmosphere so as not to allow any oxygen to be incorporated into the crystal. The presence of oxygen would have a serious adverse effect on the electronic properties of the crystals. The flow system includes the following components: (1) a 300 cm^3, 2000 psi supply cylinder, (2) pressure regulator, (3) flow-rate valve, (4) bubbler to prevent gas backstreaming, (5) non-propulsive exhaust, (6) two quick-release umbilical connectors used as inlet and exhaust during ground operation, and for loading the hydrogen supply, and (7) a solenoid valve for routing the exhaust through the umbilical connector during ground operation, and through the non-propulsive vents during the flight.

All components are stainless steel. The bubbler uses a magnetic fluid of very low vapor pressure held in place by a permanent magnet. The system is designed to operate at pressures up to 30 psig and flow rates up to a few hundred cm^3 per minute.

3. Slider

The slider is operated pneumatically with retraction by a spring when the gas pressure is released. It is enclosed in a cartridge (see Figure 7) which is removable through a door in the side of the rocket section to facilitate loading. A 50 cm^3 cylinder pressurized to 100 psig supplies gas for operating the slider. A solenoid valve applies the pressure and releases it, and a microswitch indicates the slider position. The slider accommodates two 1.1 x 1.3 cm substrates located on opposite sides of the solution cavity in an assembly fabricated from graphite (Figure 8). The depth of the solution cavity, 6.35 mm, was intentionally made great enough to result in natural convection in normal gravity. A spring-loaded volume compensator allows for expansion and contraction of the molten solution with temperature changes. Chromel-alumel thermocouples in alumina sheaths are located in grooves on either side of the graphite assembly adjacent to the solution cavity.

4. Electronic Controller

An electronic controller thermally isolated in the lower rocket section controls the entire process, including temperature control and operation of the two solenoid valves in the gas system. The

controller was provided by the Marshall Space Flight Center and is identical to that used in their General Purpose Rocket Furnace (GPRF). To simplify the adaptation of the controller to the LPE processor, the furnace heating element was made to match that of the heating elements in the GPRF, and the same type of thermocouple was used. The growth temperature set point, solenoid valve operation times, and power-off time are set by adjusting potentiometers. In addition to controlling the process, the controller provides readouts of the temperatures sensed by the two thermocouples, the actual times of substrate insertion and retraction, and the hydrogen supply pressure. These data are telemetered to the ground control facility at the launchsite during the flight. For ground and pre-launch operations, the temperature of the furnace and the operation of the slider are controlled manually, and the temperatures, slider position, and hydrogen pressure are indicated at the control panel.

The electrical power is provided by a 34 volt D.C. power supply during ground and prelaunch operations, and by batteries in a service module in the sounding rocket during the flight.

Besides the electrical control panel, the ground support equipment includes a gas control panel with valves, flow-rate meter, bubbler, and an oil-less vacuum pump for manual ground and pre-launch operation of the hydrogen system. It was designed to be used for evacuating the hydrogen system to a pressure of a few microns and back-filling with hydrogen to start the process.

The flow-rate meter is used to adjust the internal flow-rate valve. The external bubbler was provided in order that the system could be operated without filling the internal one. To ensure against spillage the internal bubbler was not filled until the rocket was in position in the launch tower.

The entire processor and ground support equipment were designed to be as multi-purpose as possible. The slider cartridge can readily be modified for different materials, and can be replaced by other kinds of sample cartridges. Gases other than hydrogen can be used for atmospheric control. The temperature-time program can readily be changed for other materials. Furthermore, the processor can be adapted to Space Transportation System flights with or without different packaging.

B. Procedure

For each pre-flight test of the apparatus and for the flight itself, the planned growth temperature was 990°K. For each, the solution was first saturated at a temperature in the range of 10-15°K above the planned growth temperature. The saturation step was performed in the flight apparatus, equipped with the same graphite slides to be used in the growth step. The slider was loaded with a fresh charge of pure gallium and two freshly cleaned gallium arsenide source wafers. The furnace temperature was raised to the desired saturation temperature, and the slider was operated to bring the wafers into contact with the gallium. The solution was allowed to equilibrate for one hour before the source wafers were retracted. The entire saturation step was performed with manual control of the temperature and slider position.

Two freshly cleaned substrate wafers cut perpendicular to the 100 direction were loaded in the slider for the growth step. The temperature-time profile of the growth step, shown in Figure 10, indicates the procedure followed in this step. Ninety minutes before the launch, the solution temperature was raised to 1050°K, and then beginning at the launch was lowered at a rate that allowed the growth temperature, 990°K, to be reached within the first four minutes of the flight. By this time, the near-zero gravity condition was well established, and the fluid motions induced by the launch were damped out. Growth was started at this time and terminated after one minute, well before the end of the near-zero gravity portion of the flight. Up to the time of the launch, the temperature was controlled manually. At the time of the launch, control of the process was transferred to the electronic controller.

Throughout the pre-flight tests of the apparatus and during the saturation step before the flight, the thermocouple outputs were monitored with a potentiometer giving much higher precision than the electronic readouts. This was necessary for sufficiently precise control of the supercooling interval, ΔT.

A hydrogen pressure of 5 psig and flow-rate of 100 cm^3 per minute were used for all pre-flight tests and for the flight. To provide adequate hydrogen for the flight, the hydrogen reservoir was pressurized to 600 psig before the launch.

III. Pre-Flight Testing

The LPE processor and its ground support equipment were subjected to three phases of pre-flight testing. The first was a series of engineering development tests to ensure that the apparatus could perform all its intended functions reliably and safely. These included vibrational, acceleration, and pressurization tests and repetitive functional tests. As may be expected for apparatus of the complexity of the LPE processor, the tests revealed the need for some modifications. The major modifications were (1) addition of a stainless steel fixture to support the graphite parts of the slider, which were found to be too fragile to withstand the mechanical loads to which they were subjected, (2) better electrical isolation of the thermocouples from the graphite parts, which was a requirement of the electronic control circuitry misunderstood at first, and (3) improved thermal isolation of the electronic controller to correct the problem of a small upward drift of the furnace temperature caused by heating of the controller by the adjacent hot furnace. After these modifications, the apparatus performed satisfactorily throughout the remainder of the pre-flight tests and the flight.

In the second phase of pre-flight testing, several epitaxial films were grown in the apparatus by simulating the pre-launch and flight procedures as closely as possible. The purposes of these tests were (1) to determine suitable temperatures for the process, (2) to verify the correctness of the pre-set slider operation and power-off times, hydrogen pressures, and hydrogen flow-rate, (3) to perform necessary

calibrations, and (4) to obtain experimental control samples for comparison with the flight samples. The test results indicated the growth temperature, 990°K, solution saturation temperature, 1000°K, and the pre-set times, pressures, and flow-rate to be suitable. The best epitaxial films were obtained in the last two tests, and are described in Section IV with the results of the flight eperiment.

The hydrogen flow-rate meter was calibrated by determining the times required to collect one liter of hydrogen for various flow-rate meter readings. The calibration data are shown in Figure 11, which indicates the correct readings for the desired rate of 100 cm^3 per minute.

The rate of hydrogen consumption was measured by recording the pressure in the hydrogen reservoir at five-minute intervals until depletion. This was done for several different initial pressures, with a flow-rate of 100 cm^3 per minute in each case. At the end of each test, the flow-rate fell from 100 cm^3 per minute to zero within a five-minute interval. Figure 12 shows the hydrogen pressure as a function of time for an initial pressure of 600 psig. These data agree with a simple calculation of the expansion of 300 cm^3 of gas under a pressure change from 600 psig to atmospheric pressure.

The pre-flight tests indicated that with power off the furnace cools from the growth temperature to about 300°K in two hours. An initial hydrogen pressure of 600 psig was chosen to provide for continued flow for this period and virtually complete depletion of the hydrogen at the end of the period.

C-2

The approximate power consumption of the processor was determined during the pre-flight tests. With the power limited to 300 watts, the furnace reaches 1050°K in fifteen minutes. Maintenance of this temperature requires approximately 200 watts, and of the growth temperature, 990°K, approximately 170 watts.

The third phase of pre-flight testing consisted of various full and partial functional tests at Marshall Space Flight Center, Goddard Space Flight Center, and White Sands Missile Range before and during the integration of the payload and rocket. During this phase, the electronic controller was modified by Marshall Space Flight Center personnel to improve its stability with variations in temperature, and thereby further ensure stability in the furnace temperature control.

IV. Results

The flight experiment was performed successfully on the SPAR VI flight on October 17, 1979. The processor functioned well throughout the flight. Epitaxial films of about the thickness expected were produced. They are shown along with pre-flight test results in Figure 13. Although the films grown during the flight are less smooth than the best films produced during pre-flight tests, they appear to be a satisfactory result for an initial space-flight experiment.

When the slider was removed from the furnace after the flight, it was in good condition, with the slides fully retracted. Later, after the slider had been returned to our laboratory and opened to remove the wafers, the solution cavity remained completely filled, confirming that there had been no leakage of solution dur-

ing the flight. On retraction of the slides, the solution had been swept from the wafers satisfactorily and the amount of gallium remaining on them was small.

Strip chart recordings of data telemetered to the ground during the flight also indicate satisfactory performance of the experiment. The recorded times of slider insertion and retraction were T + 262 sec. and T + 338 sec., respectively, both of which are within specifications. The recorded H_2 supply pressure was 640 psi at T + 0, and decreased uniformly to 620 psi at T + 700 sec., which also is within specifications. The recorded furnace temperatures are approximately as expected, but are relatively imprecise, as expected. They indicate that the furnace cooled significantly more slowly during the flight than in pre-flight tests. Presumably, this is because of the absence of convection as a mechanism to remove heat.

The recorded temperatures are not precise enough to confirm that the desired supercooling interval, $\Delta T = 10°K$, was achieved. The reliability of temperature control proven during the pre-flight tests is the only evidence available to show that it was. More reliable control of ΔT could be achieved if the slider were modified to accommodate both the source and substrate crystals simultaneously as in Figure 1, so the saturation and growth steps could be performed without cooling to ambient temperature and reloading the slider. This would eliminate variations (e.g., small changes in voltages, resistances, and thermocouple positions) which may result from reloading the slider and making electrical interconnections with the rest of the payload, and which can affect temperature control and measurement. The desirability of this modification was recognized early in the program but could not be implemented because of scheduling constraints. The change

should be made before the experiment is performed again on a future SPAR or Space Transportation System flight. Better control of ΔT may be an important key to producing smoother films.

When the wafers were removed from the slider, one was found to have some cracks (Figure 13f). With subsequent handling, it broke into five fragments, but each was suitable for analysis, and the breakage did not cause any serious problem. The reason for the cracks is unknown.

The returned flight samples and several films grown during the pre-flight tests have been examined by conventional analytical techniques for characterizing semiconductor materials. The thickness, structural perfection, compositional homogeneity, and electrical properties have been evaluated and are discussed in this section.

A. Film Thickness

The thickness of the epitaxial films was determined by cleaving a narrow sliver from each wafer, etching it with a solution known as an "A-B etch", which makes the interface between the film and the substrate visible, and making a photomicrograph of the cross-section of the cleaved wafer. The film thickness is measured on the photomicrograph and divided by the magnification factor. The results are shown in Figure 14. Only one flight sample is shown because of the difficulty in obtaining a suitable cleavage of the other. The thickness of the films grown during the sounding rocket flight, 1.5 microns, is very nearly that predicted (see Equation 4, Section I). The films grown in normal gravity are about twice as thick, a result that was expected because of the contribution of natural convection to transport of the arsenic in the solutions. Although natural convection

does not have a serious effect on the quality of the films of the order of three microns thick, it is known to cause non-uniformity of thickness and surface roughness in thicker films[4].

B. X-ray Diffraction Topography

X-ray diffraction topographs of four pre-flight samples and of the flight samples are shown in Figure 15. They were recorded by the Berg-Barrett reflection technique with CuKα radiation and the 422 diffraction maximum.

The topographs of the pre-flight samples were recorded after Hall effect measurements (see below) were completed and after the slivers had been removed for thickness measurements. The film coverage area is more easily visible in the topographs than in the photographs in Figure 13. The bright areas in these topographs are shadows cast by metallic indium contacts applied for the Hall effect measurements. These topographs show that the films are single crystals of fairly good quality and uniform composition. One topograph, Figure 15a shows some contrast near the center, probably caused by strain in the film or substrate.

Likewise, the topographs of the flight samples show that the films are single and of fairly good quality and uniform composition. The topographs in Figure 15f are for the two largest fragments of the broken wafer. The light areas in the topographs of both flight samples are shadows cast by high regions on the somewhat rough surfaces.

C. Electrical Measurements

The Hall coefficient and resistivity of the samples were measured by the Van der Pauw technique. This technique allows the use of rectangular samples. It requires that four metallic electrical contacts be formed on the sample. Measurements were made at 300°K and 77°K. The data, summarized in Table 1, are as expected for n-type films on semi-insulating substrates. The sign of the Hall coefficient indicates that the films are n-type. Knowledge of the Hall coefficient and resistivity allows calculation of the net carrier concentration and the mobility, which are given in Table 1. The carrier concentration is one or two orders of magnitude greater than desired, but this result is probably acceptable because of the early stage of development of the LPE processor. It may be related to impurities derived from the stainless steel components of the furnace or from the hydrogen supply. The hydrogen was not purified by diffusion through palladium as is the usual practice. Photoluminescence measurements made on several samples in an effort to identify the impurities have not succeeded so far. The photoluminescence peak at 8210Å, normally found for this kind of film, is much broader and more symmetrical than usual. No other peaks were found in the range 7800 to 8500Å.

Identification and removal of the sources of any impurities before the experiment is repeated is desirable. Replacement of some of the stainless steel furnace components by fused quartz components, and better purification of the hydrogen are reasonable approaches.

V. Conclusions

The following statements summarize the results of this experiment.

1. The experiment successfully produced single crystalline epitaxial films of gallium arsenide processed in the near zero-g environment provided by the SPAR VI flight. The crystal growth processor functioned properly throughout the flight and post-flight examination of the disassembled hardware showed no evidence of malfunctioning.

2. The experiment provided information concerning the effects of the near zero-g environment on the crystal growth process. The experimental results indicate that the growth process took place by diffusive mass transport. Solutal convection which is normally present and is the dominant mass transport mode in a one-g earth environment when a reservoir of this size is used was either eliminated or greatly reduced in the near zero-g environment. The justification for this conclusion comes from the fact that within experimental limits the film thickness of the flight samples was in agreement with the calculated prediction for diffusive mass transport controlled growth which is given by the relationship $d_f = \frac{2\ \Delta T}{C_s m}\left(\frac{Dt}{\pi}\right)^{\frac{1}{2}}$. Further evidence was gotten by a comparison of the growth rates of the flight and the earth processed samples. The presence of solutal convection during one-g earth processing would be expected to produce a significantly greater growth rate. A comparison of the flight and earth processed samples showed this to be the case.

3. A comparison was made of the properties of the flight samples with those of the ground processed samples. The ground processed samples were grown in the flight hardware under essentially identical conditions to the flight except for the presence of the one-g earth environment. Several ground processing runs were made and it was found that the quality of the flight samples was better than the worst but not as good as the best of the earth processed samples. Thus, with regard to the effects of space processing on the film quality, no definitive conclusions can be drawn from this experiment and further flights would be necessary to answer this question.

From the above statements, it is clear that the experiment was carried out successfully and achieved most of its intended objectives.

REFERENCES

1. J. J. Hsieh, J. Crystal Growth 27, 49 (1974).
2. C. D. Thurmond, J. Phys. Chem. Solids 26, 785 (1965).
3. D. L. Rode, J. Crystal Growth 20, 13 (1973).
4. S. I. Long, J. M. Ballantyne, and L. F. Eastman, J. Crystal Growth 26, 13 (1974).

TABLE 1. HALL EFFECT MEASUREMENTS

A. PREFLIGHT LABORATORY TESTS

	300°K	77°K
ρ,Ω cm	5.2×10^{-3}	5.4×10^{-3}
μ, $cm^2/Vsec$	2460	2290
n_D-n_A, cm^{-3}	4.9×10^{17}	5.1×10^{17}

B. SPAR FLIGHT

	300°K	77°K
ρ,Ω cm	2.1×10^{-3}	2.2×10^{-3}
μ, $cm^2/Vsec$	2140	2010
n_D-n_A, cm^{-3}	1.4×10^{18}	1.4×10^{18}

FIGURE CAPTIONS

1. Schematic drawing of apparatus for conventional gallium arsenide liquid phase epitaxy.

2. LPE processor, photographed after flight.

3. LPE processor with door open, showing end of furnace in which slider cartridge is inserted (furnace opening is covered with tape).

4. LPE processor with door open, showing other internal components.

5. LPE processor viewed from aft end with microprocessor section removed.

6. LPE processor, same view as Figure 5, but with insulation blanket removed.

7. Slider cartridge.

8. Graphite slider parts.

9. Schematic drawing of gas systems.

10. Temperature-time profile of film growth step.

11. Flow-rate meter calibration data.

12. Hydrogen consumption data.

13. Epitaxial films grown in LPE processor: a-d, pre-flight test samples; e-f, flight samples.

14. Microphotographs of cross-sections of LPE films: a-b, pre-flight test samples; c, flight sample.

15. X-ray diffraction topographs: a-d, pre-flight test samples; e-f, flight samples.

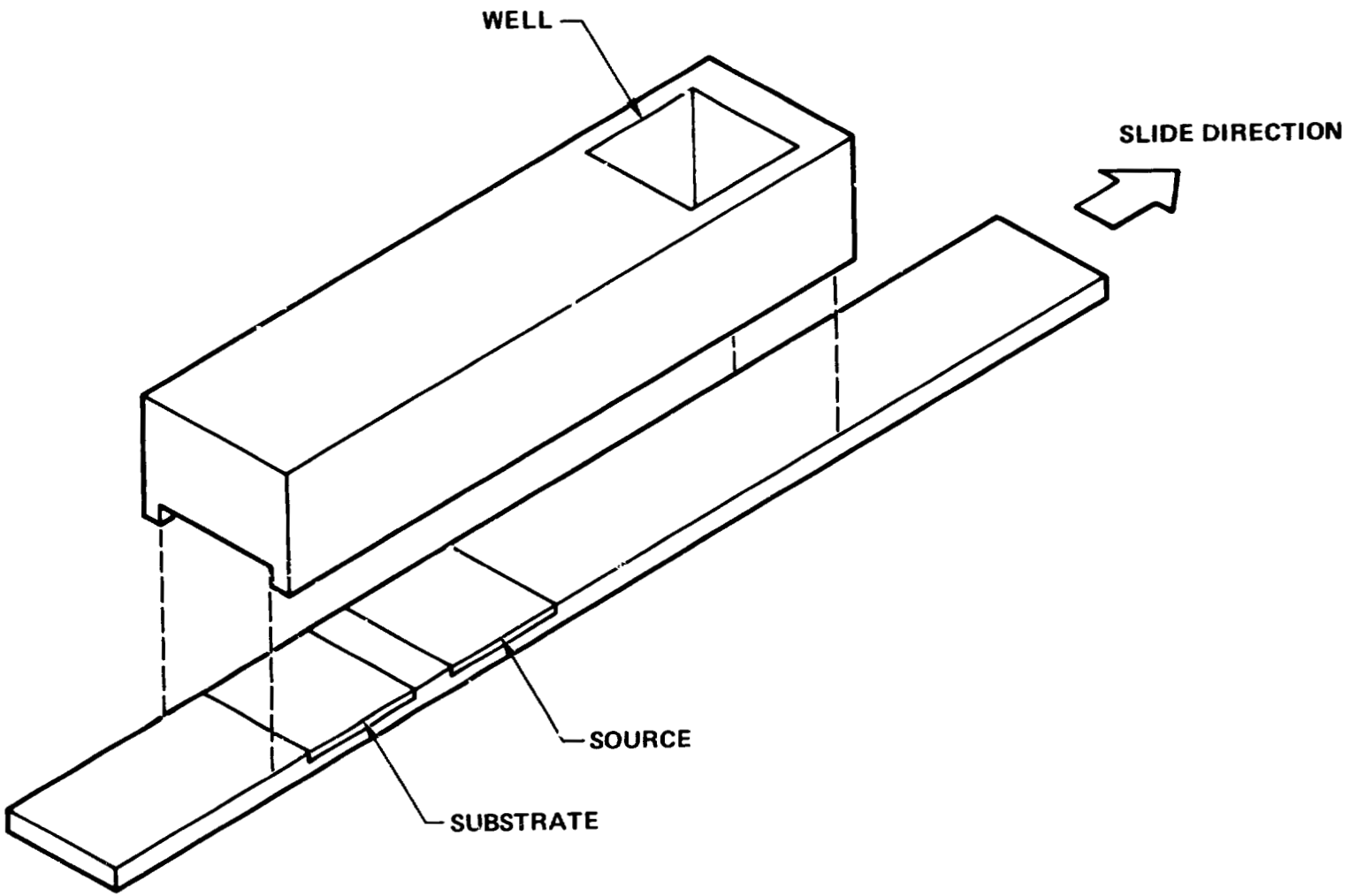

Fig. 1: Schematic drawing of apparatus for conventional gallium arsenide liquid phase epitaxy.

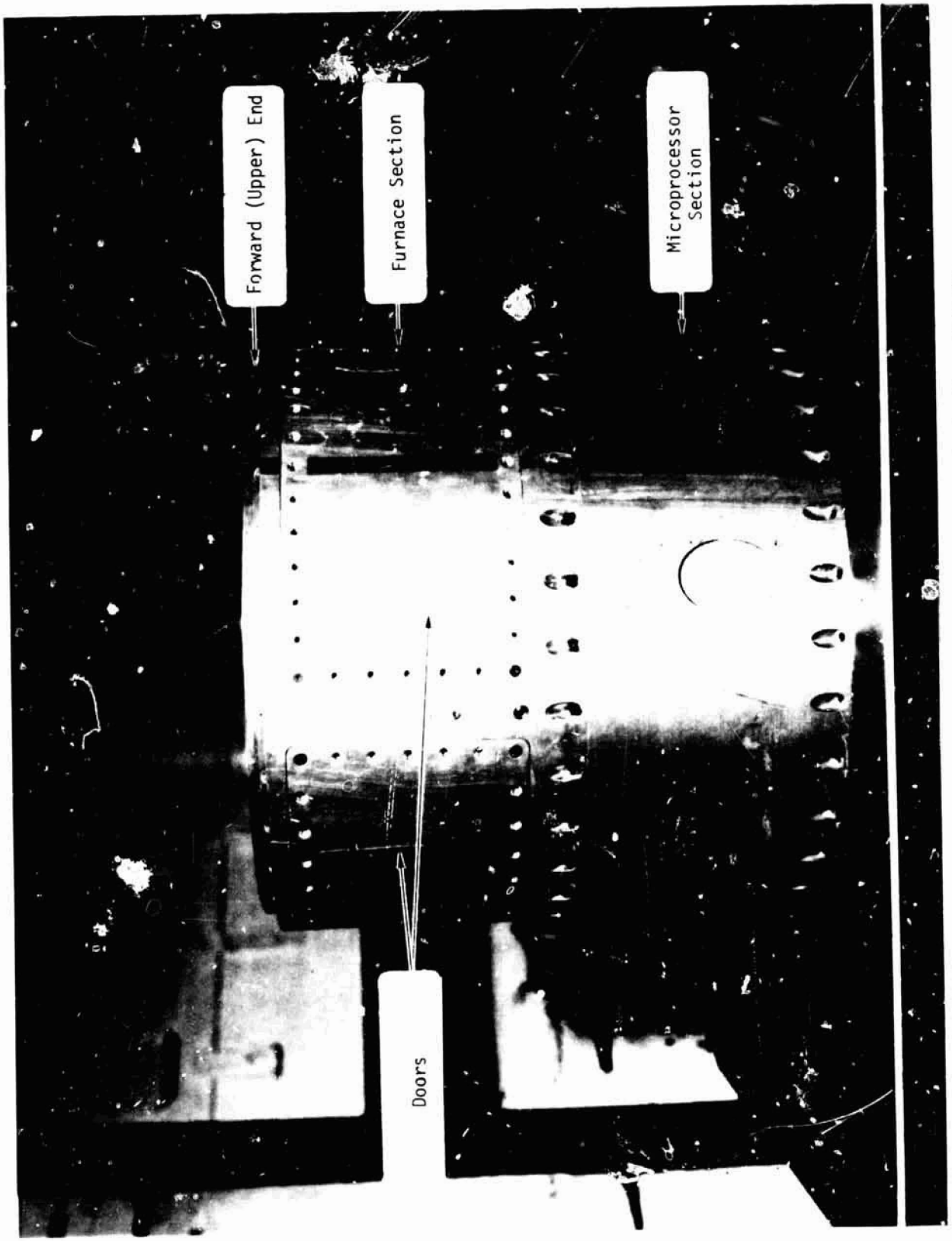

Fig. 2: LPE processor, photographed after flight.

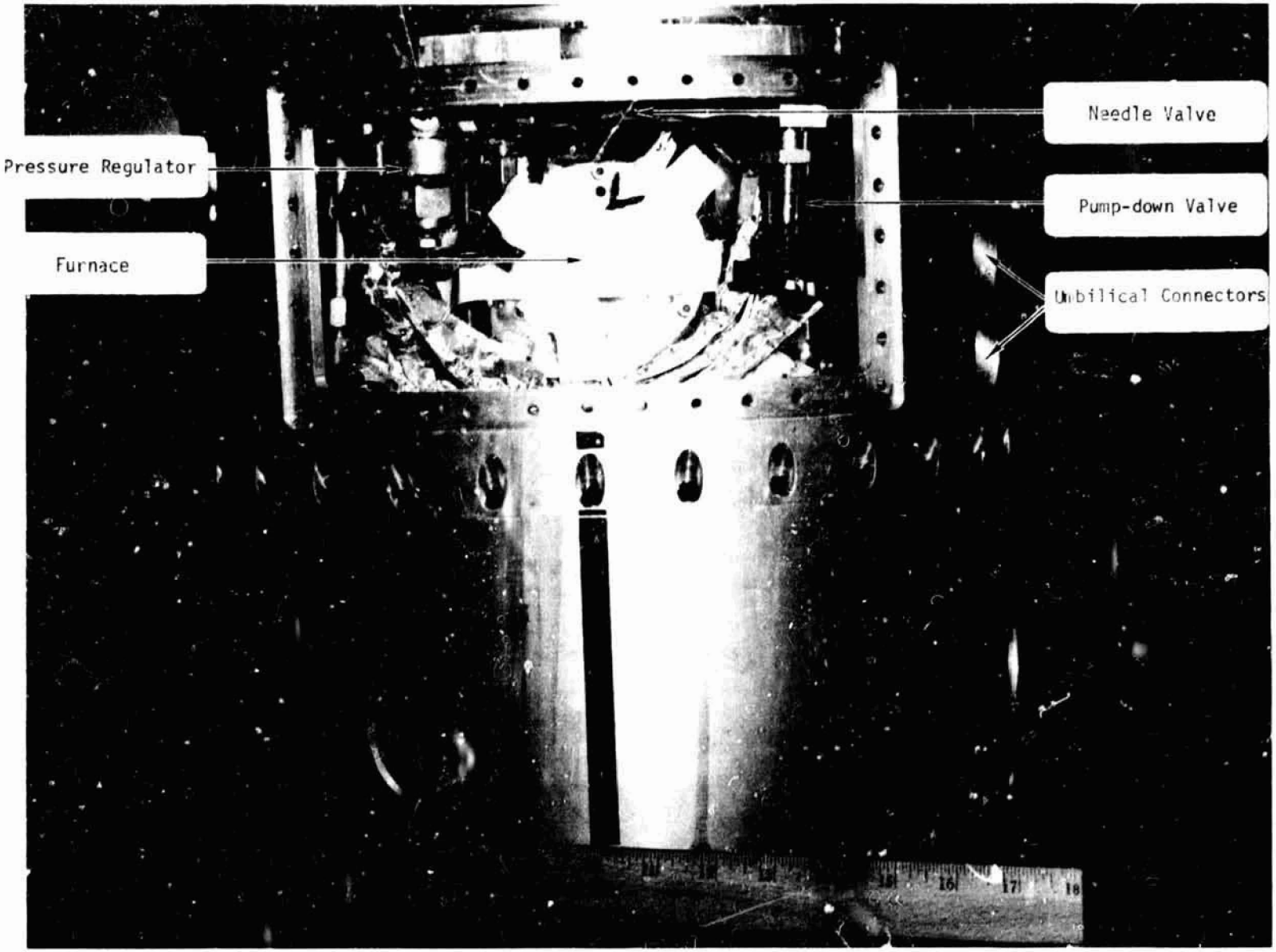

Fig. 3: LPE processor with door open, showing end of furnace in which slider cartridge is inserted (furnace opening is covered with tape).

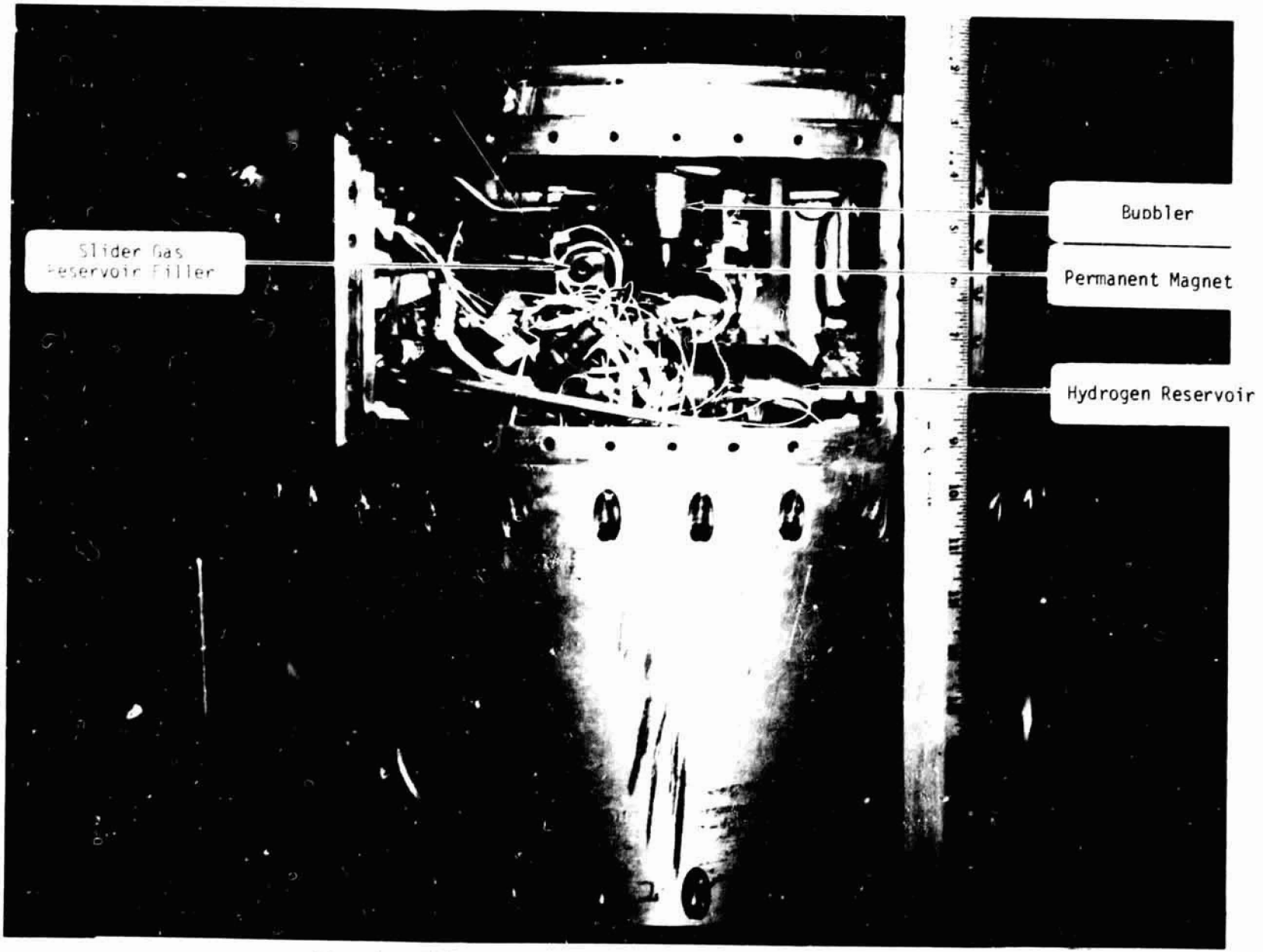

Fig. 4: LPE processor with door open, showing other internal components.

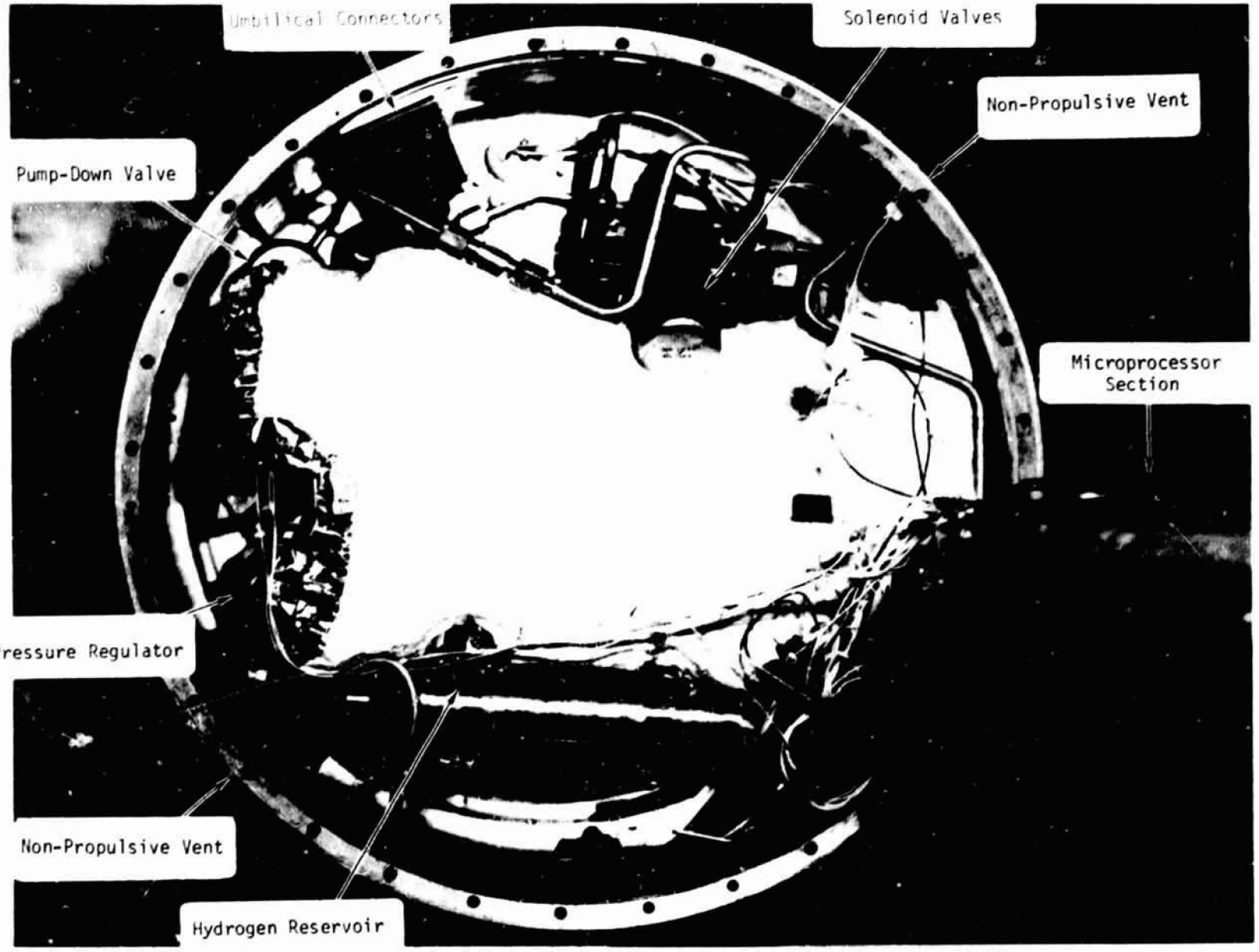

Fig. 5: LPE processor viewed from aft end with microprocessor section removed.

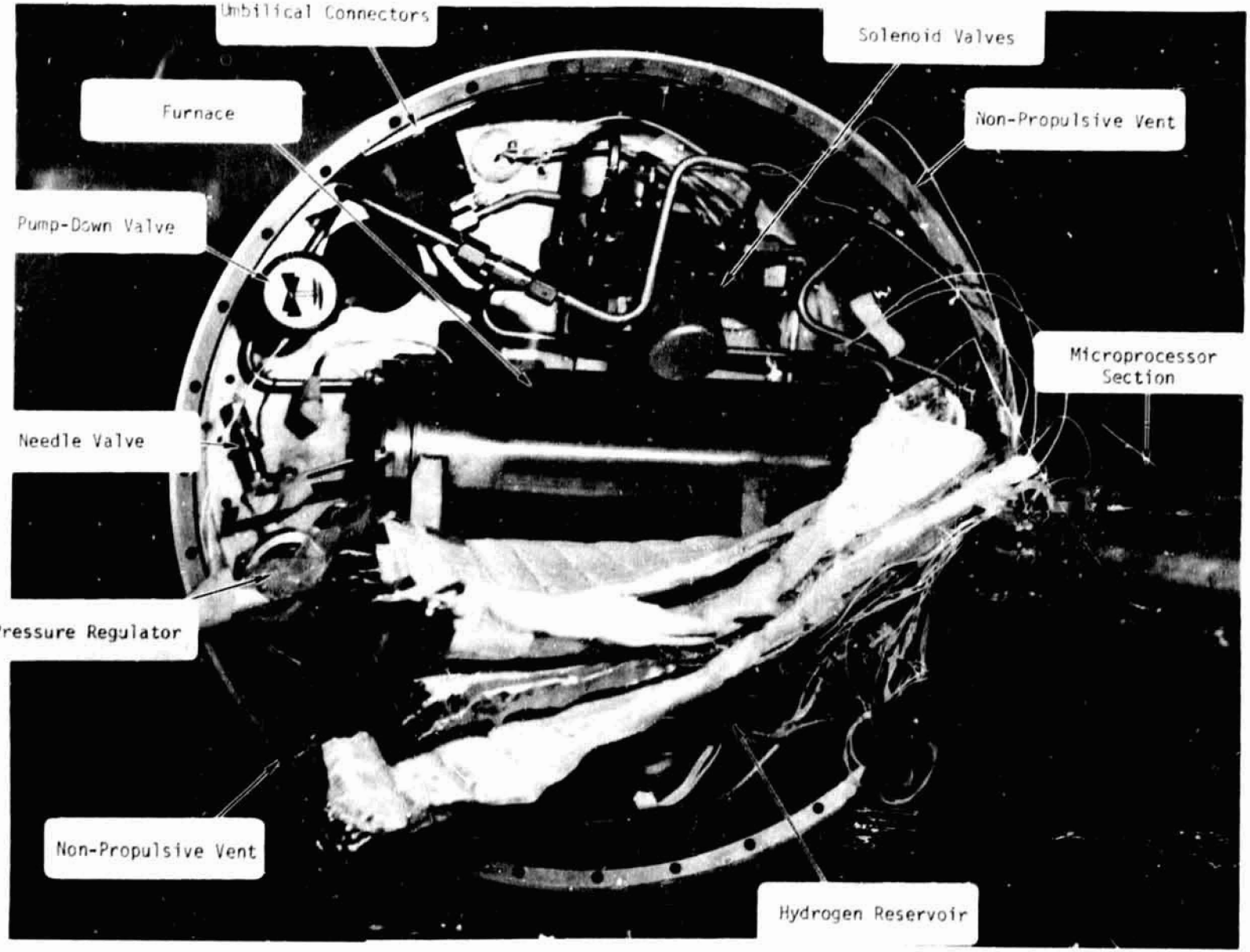

Fig. 6: LPE processor, same view as Figure 5, but with insulation blanket removed.

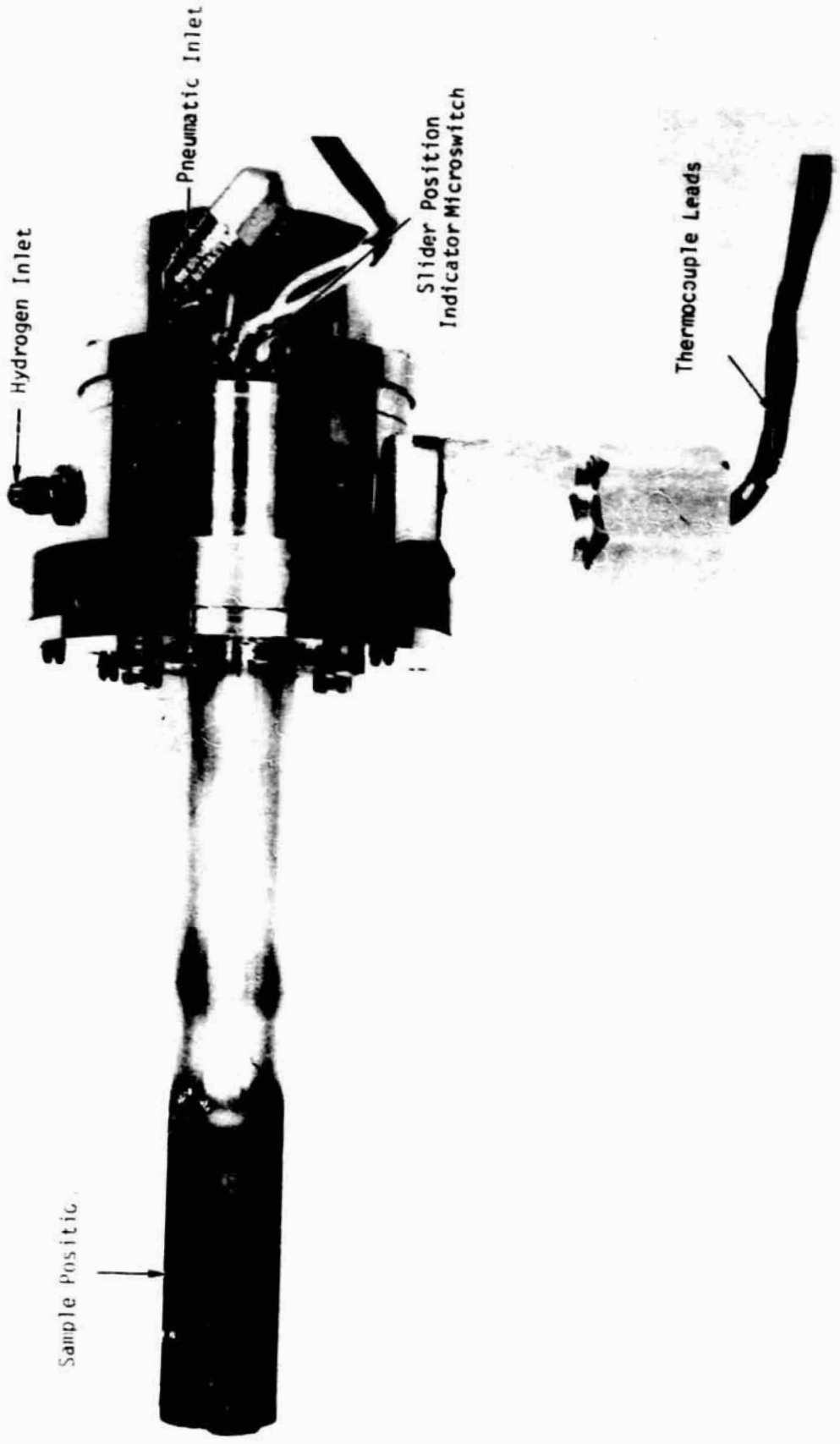

Fig. 7: Slider cartridge.

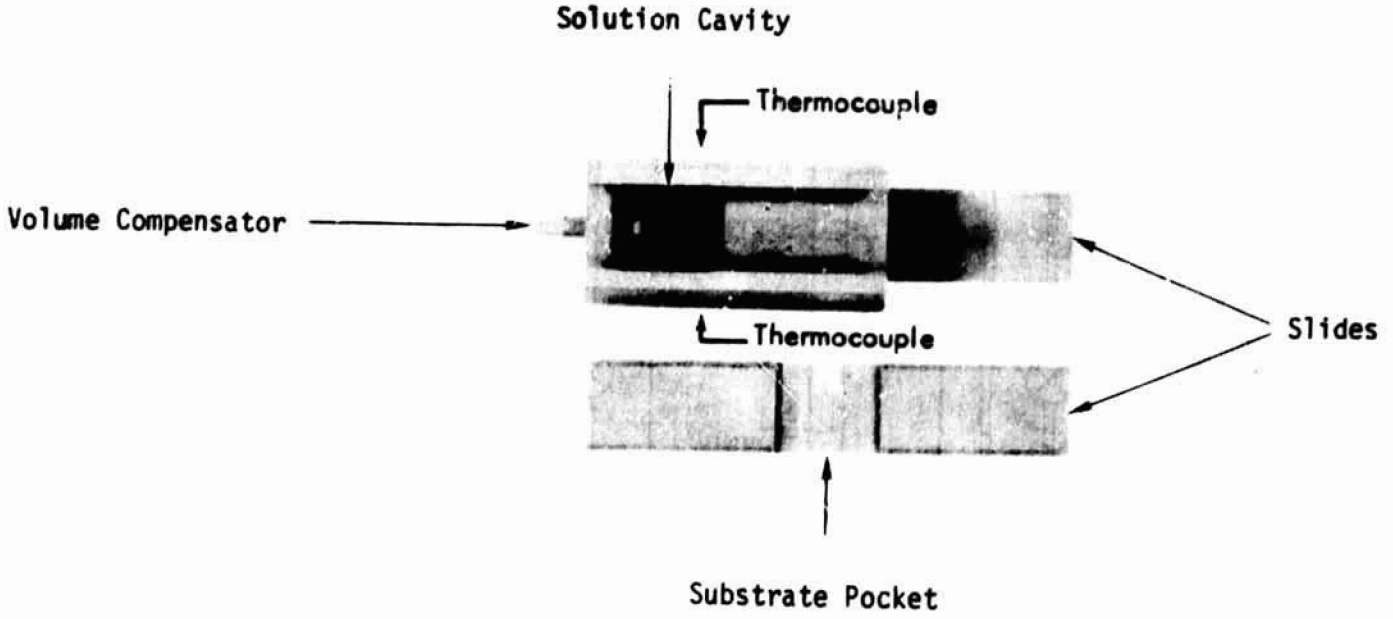

Fig. 8: Graphite slider parts.

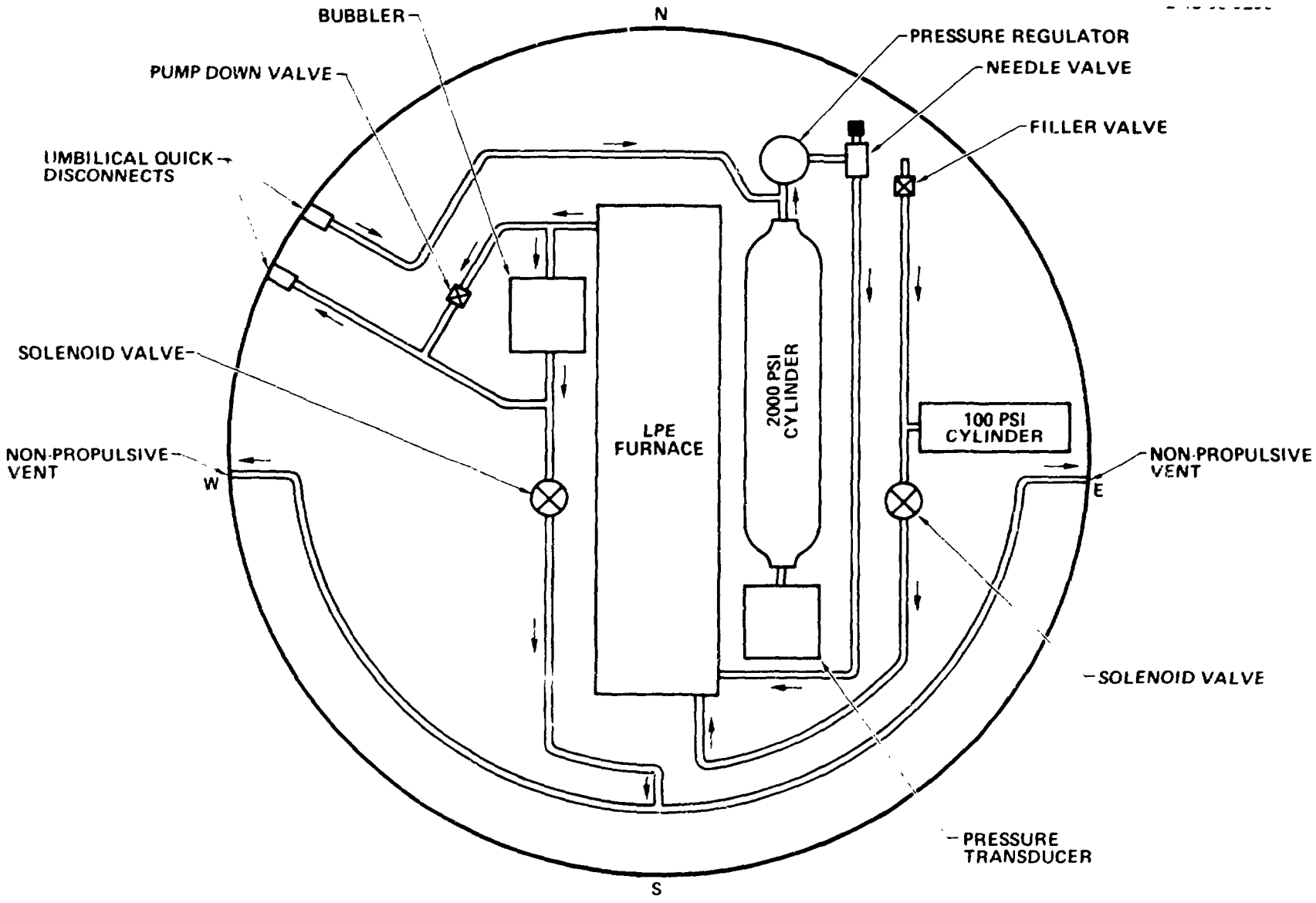

Fig. 9: Schematic drawing of gas systems.

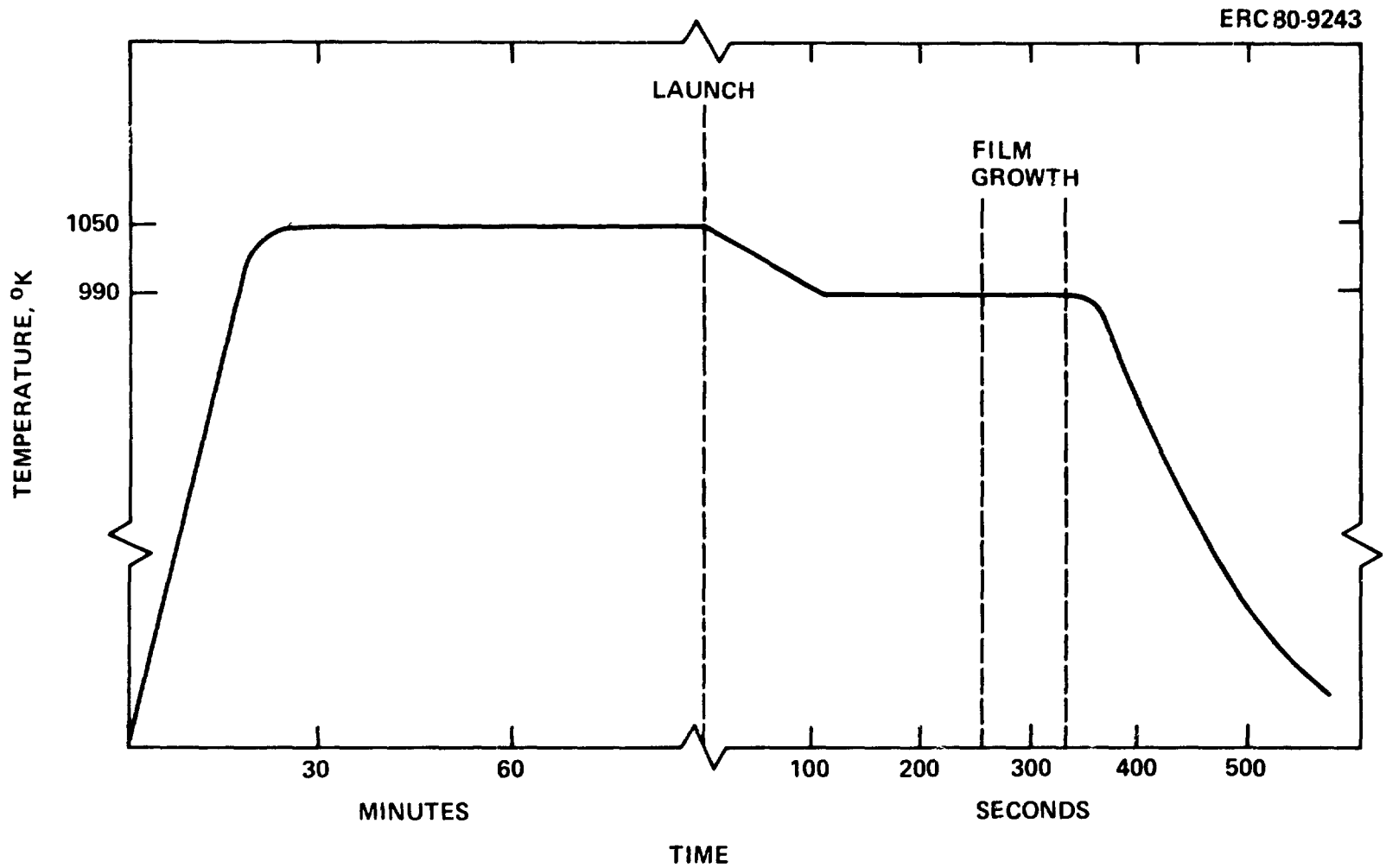

Fig. 10: Temperature-time profile of film growth step.

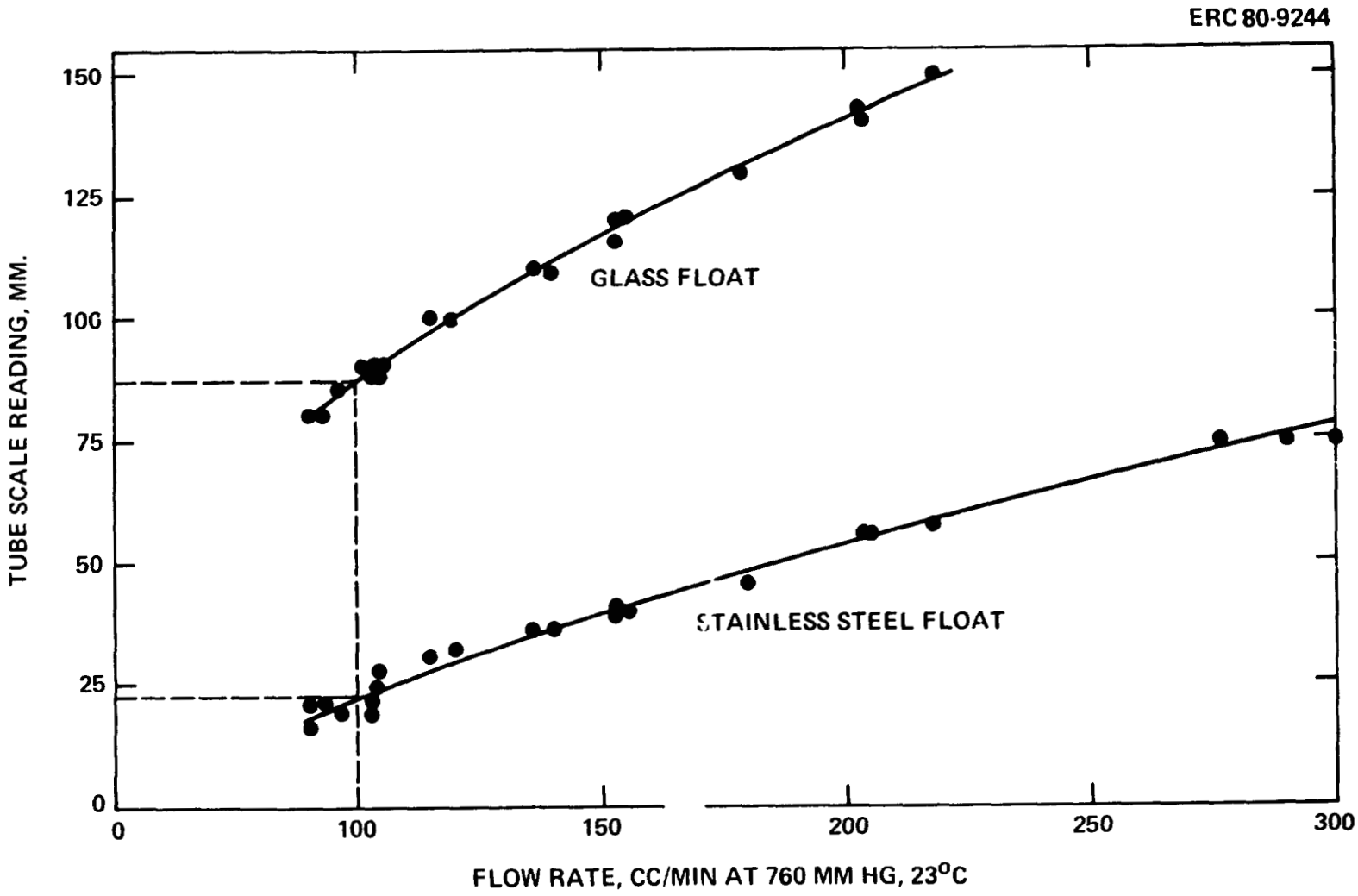

Fig. 11: Flow-rate meter calibration data.

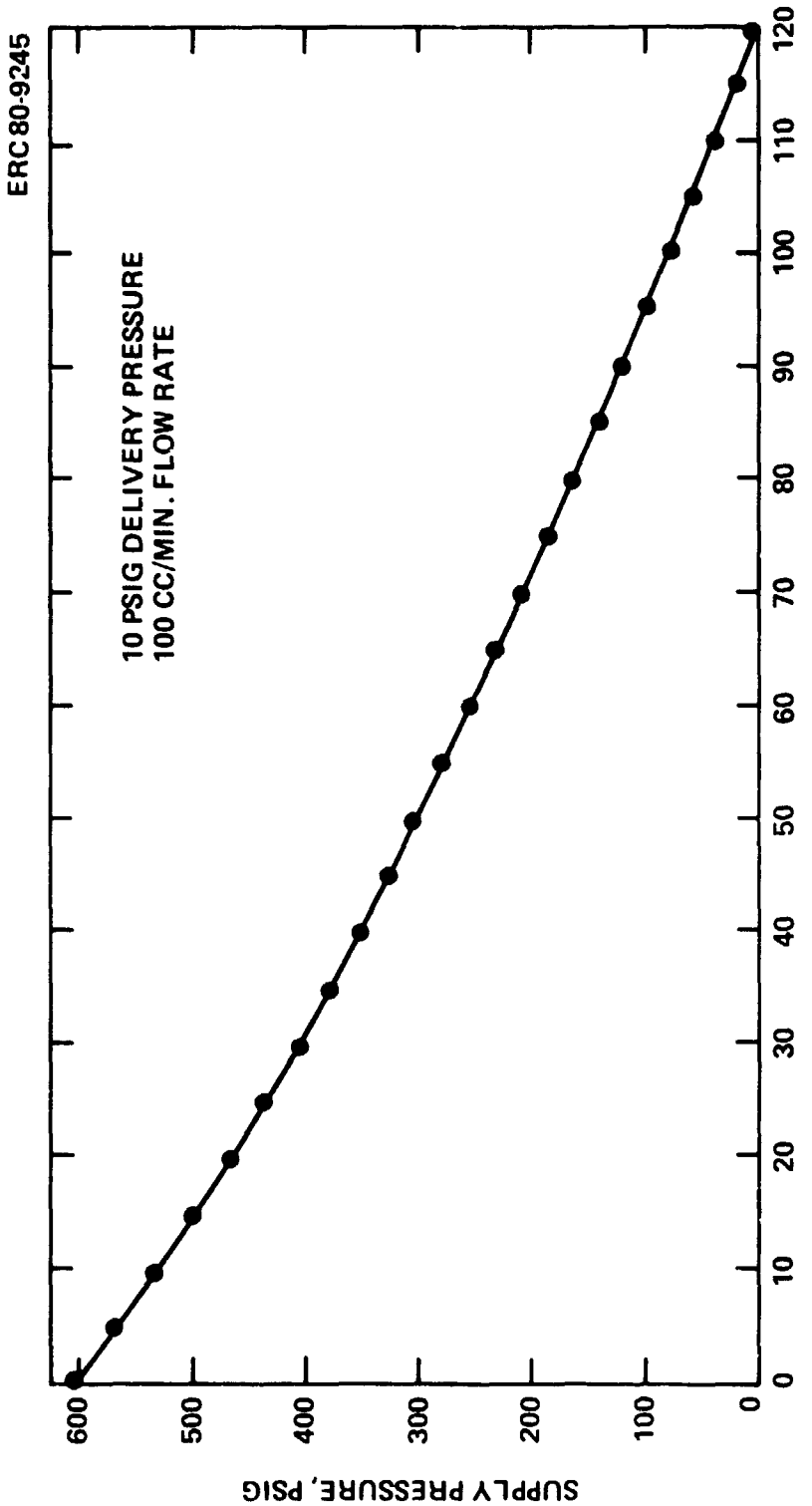

Fig. 12: Hydrogen consumption data.

Fig. 13: Epitaxial films grown in LPE processpr a-d, pre-flight test samples; e-f, flight samples.

(e)

(f)

Fig. 13 (Cont'd.)

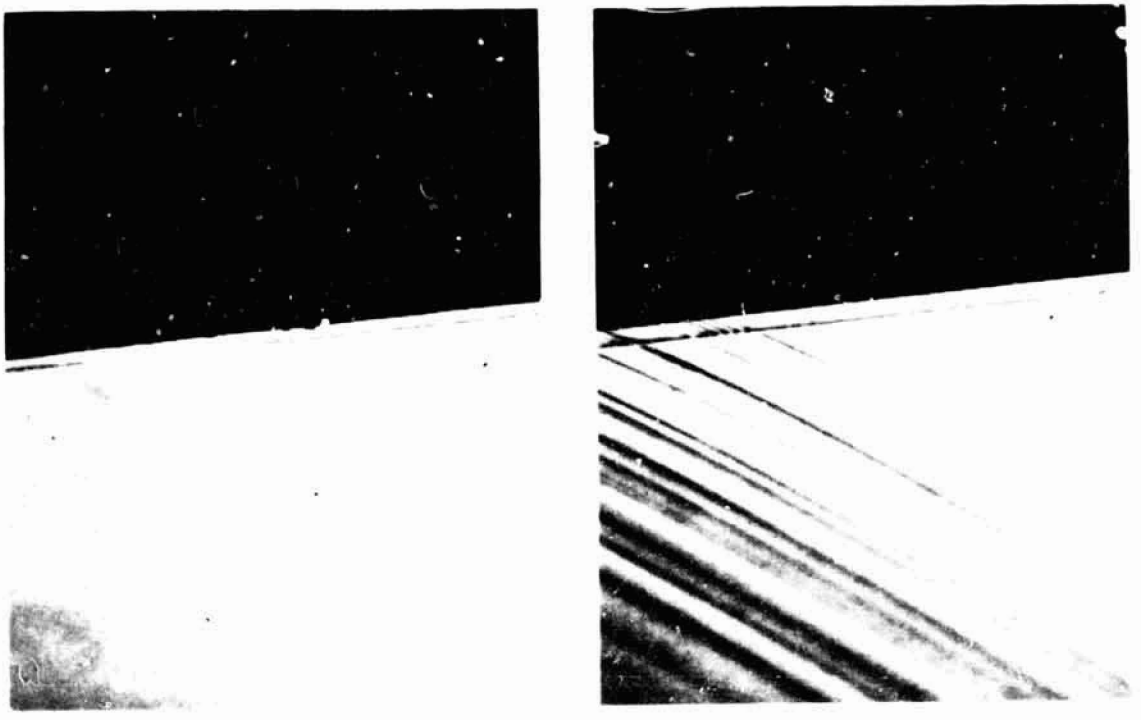

(a) (b)

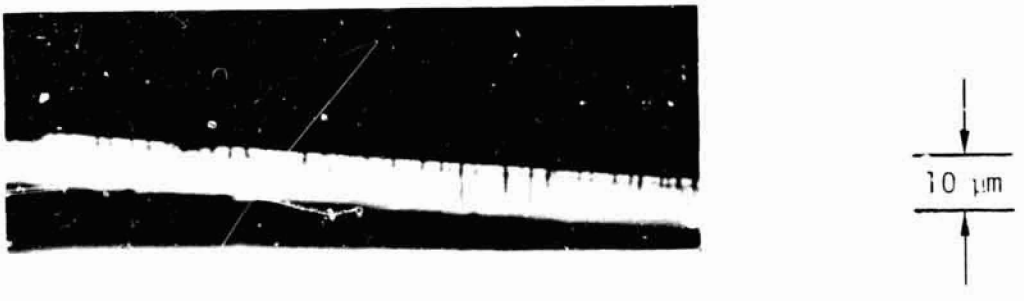

(c)

Fig. 14: Microphotographs of cross-section of LPE Films: a-b, pre-flight test samples; c, flight sample.

(a) (b)

(c) (d)

Fig. 15: X-ray diffraction topographs: a-d, pre-flight test samples; e-f, flight samples.

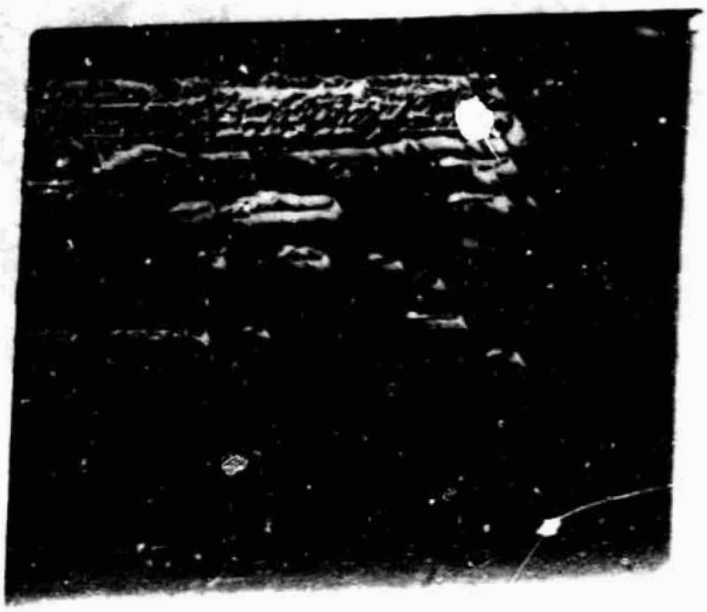

(e)

(f)

Fig. 15, Cont'd.

CHAPTER V

CONTAINERLESS PROCESSING TECHNOLOGY EXPERIMENT REPORT

SPAR VI EXPERIMENT 75-20

MAY, 1981

T. G. Wang, D. D. Elleman, N. Jacobi, and A. P. Croonquist

JET PROPULSION LABORATORY
California Institute of Technology
Pasadena, California

ACKNOWLEDGEMENTS

The authors are grateful to P. Rayerman and J. Brown for invaluable help in data processing and programming; to R. Selzer, D. Ledbetter and R. Ramage of the Image Processing Laboratory at JPL for digitizing the data; and to Dr. C. Lawson for enlightening discussions and suggestions that could not always be realised by us.

The authors also wish to thank R. Irigoyen, J. Conley, E. Olli, D. Kerrisk, L. Robinson, K. Tarver, and H. Press of JPL for their valuable assistance in all phases of this experiment. Dr. Wang wishes to thank R. Chassay, R. Fallen, and D. Schaefer of MSFC for their assistance and their patience in handling this experiment and the manuscript.

This paper presents the results of one phase of research carried out at the Jet Propulsion Laboratory, California Institute of Technology, under Contract No. NAS 7-100, sponsored by the National Aeronautics and Space Administration

CONTENTS

SECTION 1

INTRODUCTION

This report describes an experimental research program which will contribute to the understanding of containerless processing of materials in space. Study of the stability and manipulability of liquid drops is a useful and cost effective intermediate step in the development of a better understanding of the physics of liquid melts and the capability to manipulate them in a zero-G environment.

We will study three aspects of containerless processing technology in space: stability, oscillation, and rotation.

Stability studies will help us to determine the effect of residual G-jitter on the positioned sample. Also, stability of the sample will determine the focus requirement of the heat lamps, thus, impacting the thermal insulation requirements on the chamber.

Oscillation studies will enable us to better understand induced mixing currents within the melt and to define the maximum acoustic power required, thus impacting the total power, weight, and acoustic insulation requirements of the chamber.

Rotation studies will prove the feasibility of degassing the melt, which will increase the quality of the returned sample, and of shaping the melt, which will reduce waste of the returned sample, thus impacting the economical feasibility of containerless processing. In addition, a rotating sample requires only one heat lamp to raise the sample temperature uniformly, thus impacting the thermal design of the chamber.

The practical knowledge obtained in these studies will aid in the design of the Acoustic Containerless Experimental System. The study will take advantage of the laboratory work and zero-G aircraft tests already under way at JPL, as part of the overall Office of Applications Space Processing Program.

SECTION 2

OBJECTIVES

The broad objective of this task is to study the containerless processing of materials in space. In containerless processing, most of the steps are conducted in a liquid-melt state. Our knowledge of the physical properties of liquid melts today is qualitative, or at best, semiquantitative and empirical. The aim of this program is to gain a better understanding of the physics of liquid melts and the capabilities of manipulating them in a long-term, zero-G environment, thus aiding in the future design of a practical system for space processing.

The primary objectives of this flight, as stated in the proposal, were to:

(1) Study the center of mass motion in an acoustic chamber. The initial perturbation of the drop generated by the drop injection system will be allowed to damp down with the acoustical field on. The time required for a positioned liquid drop to approach its quiescent state can be determined from the film record.

(2) Determine the rotation capability of the acoustic chamber. The torque on the drop generated by the acoustic field will be gradually increased to slowly accelerate the drop up to 2 rps. The rate of spin-up as a function of the torque will establish the rotation capability of the chamber on a liquid drop.

(3) Study the natural resonant frequencies and damping mechanism of drop oscillation. The resonant frequencies and the damping mechanism have

been calculated. This experiment will allow comparison of observed and calculated values.

(4) Study the drop shape change due to rotation. The equilibrium shapes of near-rigid body rotation obtained in this experiment will be compared with existing equilibrium calculations. If rotation is to be used as a principle method of shaping liquid melts, it will be important to determine the deviation between calculated and observed shapes.

SECTION 3

APPARATUS AND OPERATION

1. APPARATUS

This study utilizes the existing acoustic levitation rocket instrument described in AO:0A-76-20 with minor modifications for this flight.

Figure 3-1 shows the rocket 76-20 payload and the housing. The heart of this apparatus is a triaxial acoustical levitation resonance chamber which is used to position and control large liquid drops in zero-g environments. The chamber itself is nearly cubical, with inside dimensions of 11.43 x 11.43 x 12.70 cm, which are the x, y, and z faces. respectively. Three acoustic drivers are fixed rigidly to the center of three mutually perpendicular faces of the chamber. During operation of the chamber, each driver excites the lowest-order standing wave along the direction that the driver faces. In a resonant mode, the ambient pressure is maximum at the nodes of the velocity wave (the walls) and minimum at the antinodes (the center). Consequently, there is a tendency for introduced liquids and particles to be driven toward the antinodes, where they collect and remain until excitation ceases.

Calculation of the acoustic pressure on the drop is simplified by the fact that the characteristic impedance of the liquid $\rho_d c_d$ is very much greater than that of the gas ρc: $\rho_d c_d$ ($\sim 10^5$ cgs) / ρc (~ 40 cgs) $\gg 10^3$ where the densities of the liquid and air are ρ_d and ρ, respectively, and c_d and c are the sound velocity of liquid and gas, respectively. Because of this impedance mismatch, the acoustic power transmitted into the drop is three orders of magnitude smaller than in the gas and is negligible.

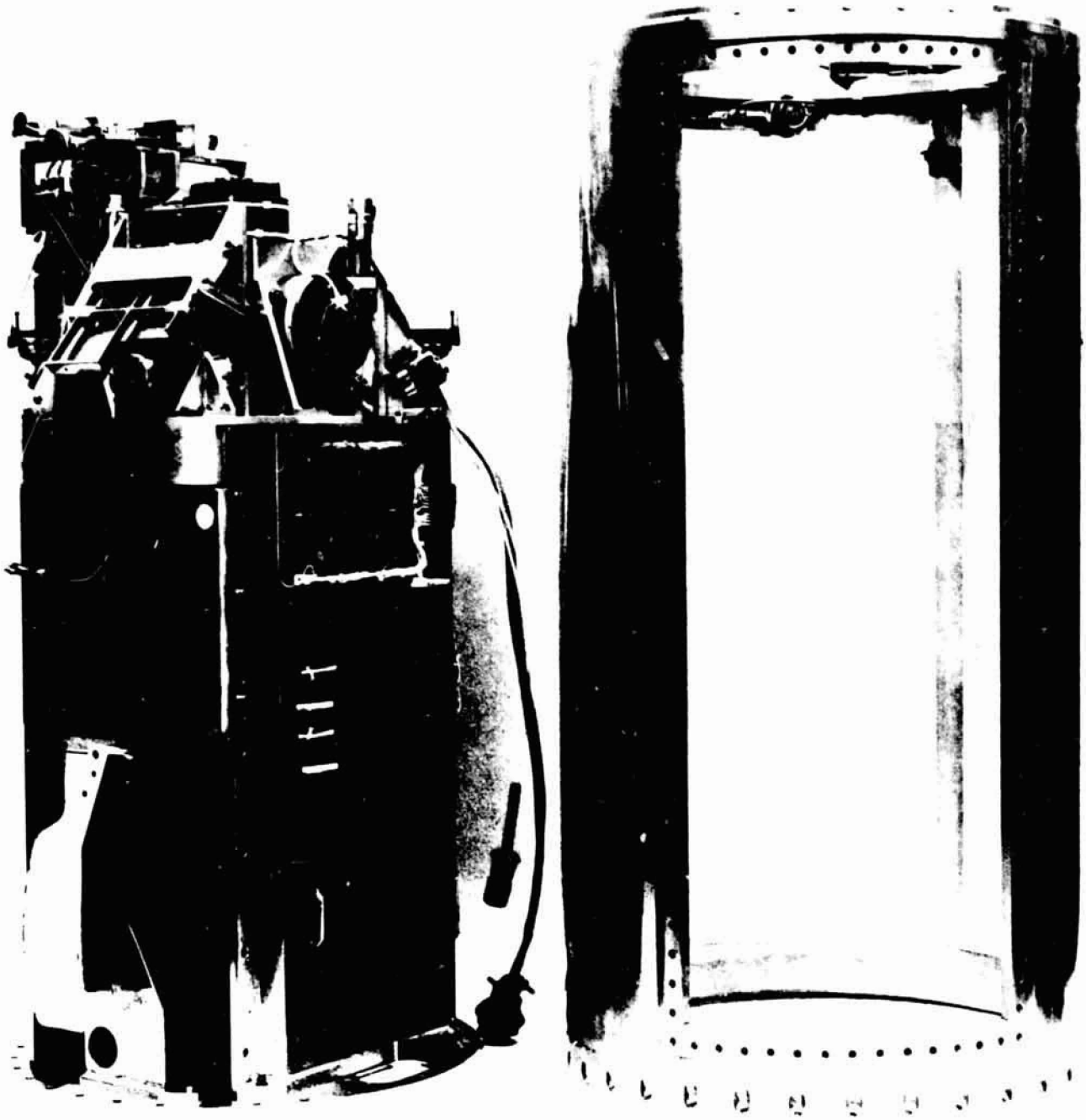

3-1. Triaxial Acoustical Levitation Resonance Chamber (with housing).

Rotation of the sample requires that two axes, the x and y, be of the same length and that they be driven at the same acoustic frequency shifted by 90^{o} (see section 4-5). For the non-rotation mode the two axes can be driven at 0^{o} or 180^{o} with respect to one another. However, at these phase shifts interference patterns are produced in the chamber that can severely distort the shape of the drop. In order to alleviate this problem the acoustic fields are turned on and off in a cyclic manner so that when the x axis acoustic field is on the y axis acoustic field is off and when the x is off the y is on. This complementary modulation of the x and y axes is done at a frequency that is high compared to the n = 2, 3, and 4 normal modes of the drop. Complementary modulation is discussed in Section 4.1.

The acoustic chamber was located in the rocket paylaod so that the z axis of the chamber was parallel to the center line of the rocket. Figure 3-2 shows the orientation of the payload with respect to the rocket.

The primary data from this experiment is obtained with a 16 mm cine camera. The camera was run at 48 frames per second. The camera is directed along the z axis (see Figure 3-2); in addition two mirrors give nearly othogonal views along the x and y axes. The view of the camera for each of the axes is from the positive axis to the negative axis of the accelerometer. In addition, the sound intensity at each wall, the deployment system condition, camera and lighting status, and the frequency of the z axis signal were monitored and recorded. This data was telemetered to the ground station in real time. The MSFC accelerometer data was supplied to aid in the data analysis. The x, y, and z axes of the accelerometer are coaxial with the x, y, and z axes of the acoustic chamber.

2. INSTRUMENT CALIBRATION

(a) Acoustic Calibration

The acoustic intensity calibration was difficult to accomplish because the instrument did not have calibrated microphones in the chamber. However, since the primary interest was not in the sound intensity itself but in the positioning force produced by the acoustic standing waves, the acoustic intensity was calibrated by measuring the acoustic positioning force itself. The force measurement was made by suspending a low density (styrofoam) sphere (1.25 cm radius and 0.229 g weight) 3.175 cm from the center of the chamber on a thin string 5.08 cm long (see Figure 3-3). The signal to each speaker was adjusted so that the acoustic force deflected the sphere 0.292 cm (0.115 in) toward the center of the chamber. This corresponded to a force of 12.9 dynes. This technique of acoustic calibration has been standardized for all of the SPAR flights that use the triaxial acoustic chamber.

It should be noted that the force measurements and calibration are made at the JPL site which is at a lower altitude than the White Sands Test Range where the system is hermetically sealed. This difference in atmospheric pressure between the two sites results in a small decrease in the acoustic force (see Section 5.3 for a detailed discussion).

(b) Liquid Volumetric Calibration and Surface Tension Measurements

The liquid deployment system was tested before the flight by taking repeated volumetric measurements of the deployed liquid. There was a variability of several percent in these measurements caused by backlash in the gear system that drove the fluid delivery system. The typical measured volume was 8.6 ± 0.2 cc water.

The liquid used in this experiment was distilled water with small quantities of dye added to provide optimum contrast in the cine film. The surface tension of the dyed water sample was measured before and after the flight and was found to be 71.0 $\pm$ 2.0 dynes/cm. The water was deployed into the center of the chamber through the two coaxial injectors. The 8.6 cc of water was deployed in 12 seconds. The slow liquid delivery was chosen so as to minimize unwanted flows within the drop. The injector tips were withdrawn from the drop while the acoustic field positioned the drop.

The tips of the injector tubes were treated with a small quantity of silicone oil so as to minimize the wetting of the tips by the water. This treatment facilitated the deployment of the drop when the injectors were withdrawn from the drop. Post-flight data analysis has shown that the silicone oil treatment of the tips has very little effect on the surface tension of the sample.

(c) Sequence and Time Line Calibration

The experiment control program had been run through the flight sequence over 100 times in pre-flight tests. No deviation from the programmed sequence was observed in these tests. In addition, flight telemetry confirmed the sequence operated as programmed during the flight and subsequent post flight tests of the system showed no anomaly. The instrument control function is shown in Table 3-1.

(d) Cine Camera and Lighting Calibration

Camera, lighting and film tests were run at JPL before the flight. The quality of the image was confirmed by the PI and CoI to be acceptable for data analysis. The camera was also run at White Sands just before the flight to confirm proper operation of the system.

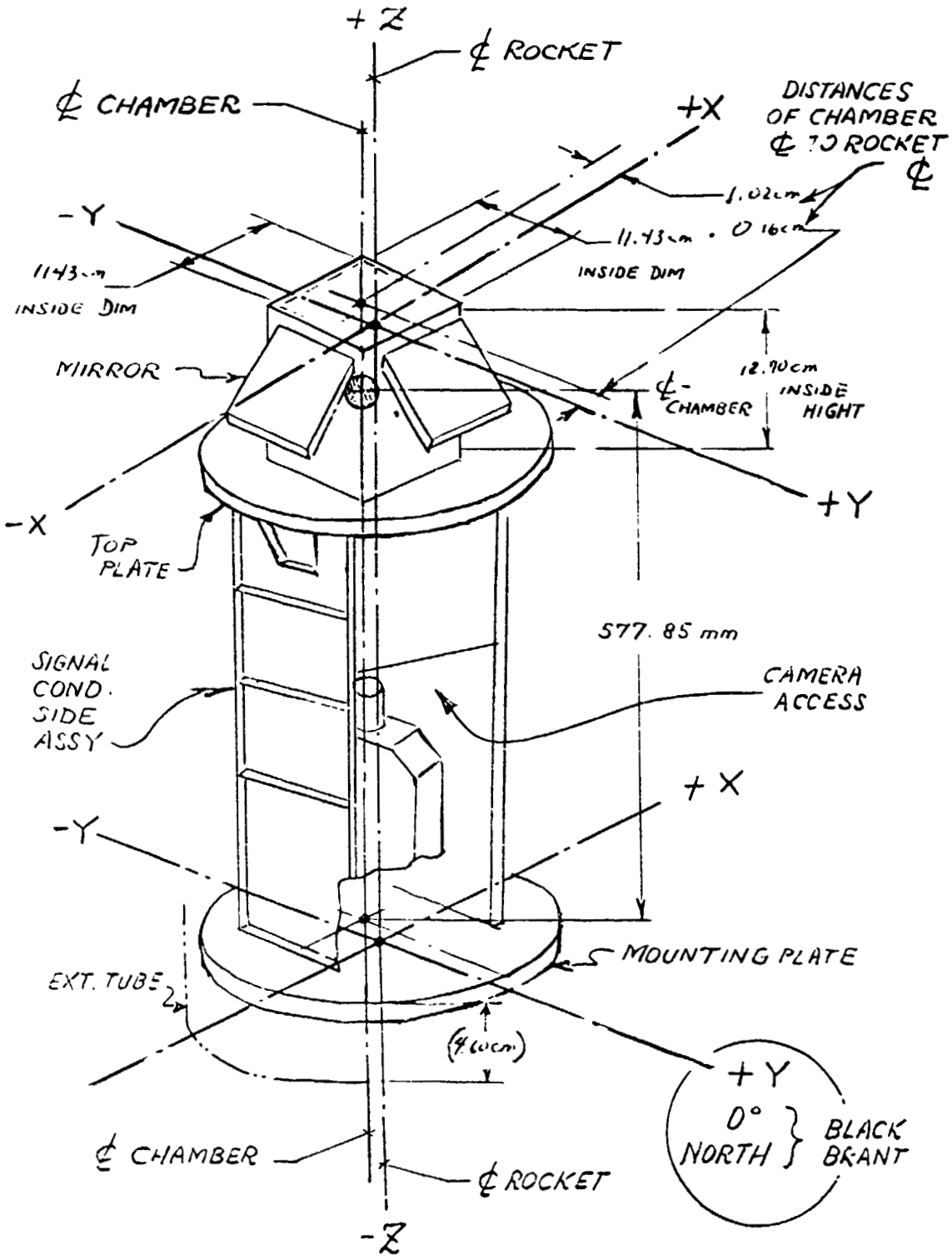

Figure 3-2. Schematic Drawing of the Payload

ACOUSTIC FORCE CALIBRATION

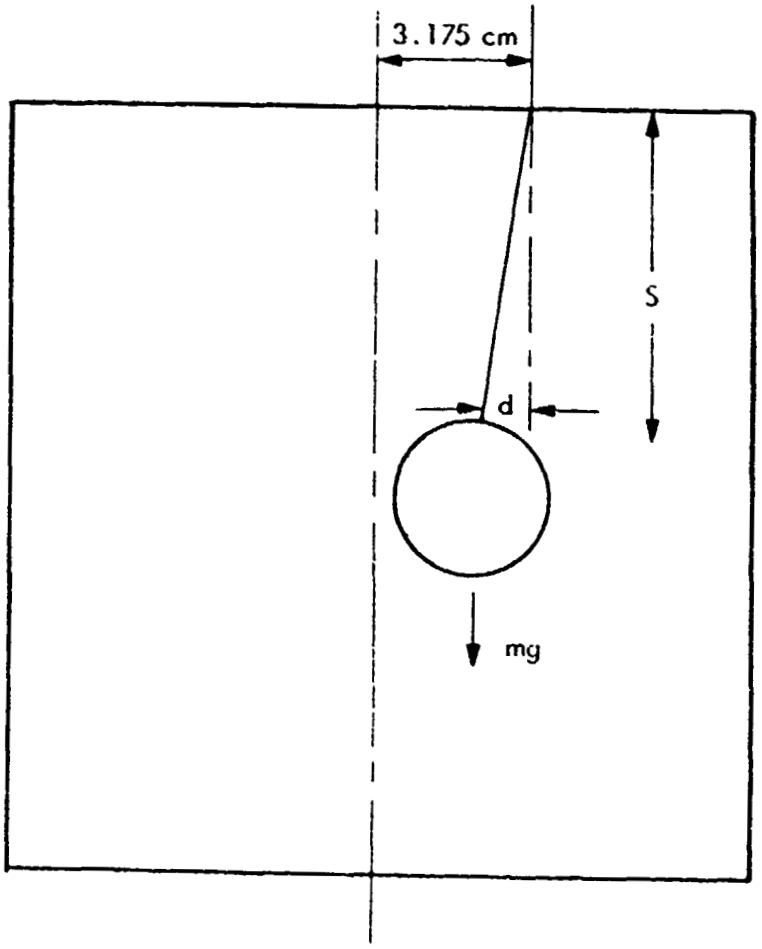

ACOUSTIC FORCE $F_A = mg \frac{d}{S}$

Figure 3-3. Method used to calibrate the sound pressure level inside the chamber. Each speaker was adjusted so that the centering force at 3.175 cm from the center was 12.9 dynes.

TABLE 3-1 INSTRUMENT CONTROL FUNCTIONS

28 VOLT CONTROLS

1. Injectors In--Level to move injectors in.
2. Injectors Out--Level to move injectors out.
3. Fluid Delivery--Level to cause the delivery of fluid to the injectors.
4. Fluid Reverse--Level to cause fluid motor to drive fluid in or out of injectors.
5. Fluid Continuous/Incremental--Level to cause fluid delivery to be continuous or to be defined as a preset amount by a 4-bit control.
6. Fluid Amount--4 bit control of the fluid delivered in the incremental mode.
7. Fluid Valve On/Off--Level to control a solenoid and allow the delivery of fluid.
8. Drop Removal--Level to control the drop removal mechanism.*
9. HV Probe In--Level to move the high voltage probe into the chamber.*
10. HV Probe Out--Level to move the HV probe out.*
11. HV On--Level to enable the HV power supply.*
12. HV Level--8 bits to control the output of the HV power supply.*
13. Camera On/Off--Level to enable the camera.
14. Camera Speed--3 bits to control the speed of the camera shutter.*

AUDIO CONTROLS

1. Audio On/Off--Level to enable the audio power.
2. Rotation--Level to enable X phase shift.
3. Sound Level--8 bits to control the sound power level.
4. Modulate--2 bits to enable the audio modulation on the x and y axes.
5. Modulation Select--2 bits to select modulation program.
6. Modulation Frequency--10 bits to control the frequency of the modulation.

*Function not implemented in Experiment 76-20.

SECTION 4

THEORETICAL BACKGROUND FOR THE SPAR DATA ANALYSIS

The data analysis required preliminary theoretical analysis of a number of situations arising in the various sequences of this experiment.

1. Two Dimensional Degenerate Pressure Profiles in the Acoustic Chamber.

The acoustic chamber used in the SPAR has two equal dimensions. This gives rise to a degeneracy of the transverse acoustic modes and to non-circular static pressure profiles at the center of the chamber. It is therefore important to analyze these pressure profiles in some detail. The velocity potential inside an empty chamber of dimension L, which is driven at its resonant frequency, ω, is

$$\phi = \frac{p_o}{\rho\omega} \{ \cos kx + \cos ky \} \cos\omega t \tag{1.1}$$

where $k = \pi/L = \omega/c$ is the wave number. The acoustic pressure is

$$p = -\rho \frac{\partial}{\partial t}\phi = p_o \{ \cos kx + \cos ky \} \sin\omega t \tag{1.2}$$

and the components of the particle velocity are

$$\begin{aligned} u_x &= \frac{\partial}{\partial x}\phi = \frac{p_o}{\rho c} \sin kx \cos\omega t \\ u_y &= \frac{\partial}{\partial x}\phi = \frac{p_o}{\rho c} \sin ky \cos\omega t \end{aligned} \tag{1.3}$$

The acoustic radiation pressure is given by (Landau and Lifshitz, 1959)

$$\langle \Delta p \rangle = \frac{\overline{p^2}}{2\rho c^2} - \frac{1}{2} \rho \overline{u^2} \tag{1.4}$$

Note that it is a second order effect. This radiation pressure does not exist in linear acoustics, it vanishes for travelling waves, and is small but

finite for standing waves. The acoustic radiation pressure gives rise to an acoustic potential well and to an acoustic force field in the chamber. The bars in Eq. (1.4) denote time averages over the high frequency component. Substituting the pressure and velocity into (1.4), we obtain

$$\langle \Delta p \rangle = \frac{p_0^2}{4\rho c^2} \{ \cos 2kx + \cos 2ky + 2\cos kx \cos ky \} \qquad (1.5)$$

This expression is for a coordinate system with its origin at the corner. Transfering to a coordinate system whose origin is at the center of the chamber, i.e.

$$x \longrightarrow x - L/2 \quad \text{and} \quad y \longrightarrow y - L/2$$

we have

$$\cos 2kx \longrightarrow -\cos 2kx \quad \text{and} \quad \cos kx \longrightarrow -\sin kx$$

resulting in

$$\langle \Delta p \rangle = -\frac{p_0^2}{4\rho c^2} \{ \cos 2kx + \cos 2ky - 2 \sin kx \sin ky \} \qquad (1.6)$$

The last term is the interference term due to mode degeneracy, which we will show gives rise to a non-spherical pressure profile near the center of the box. Expanding the trigonometric functions to $O(x^2)$, we obtain the following isobaric contours

$$x^2 + y^2 + xy = K = \frac{1 + \dfrac{\langle \Delta p \rangle}{p^2/4\rho c^2}}{2k_i} \qquad (1.7)$$

The last term on the left hand side comes from the interference term, and gives rise to the non-spherical pressure profile. The explicit isobaric contour is found by diagonalizing this quadratic form by the simple transformations

$$x = \frac{x' - y'}{\sqrt{2}} \quad \text{and} \quad y = \frac{x' + y'}{\sqrt{2}}$$

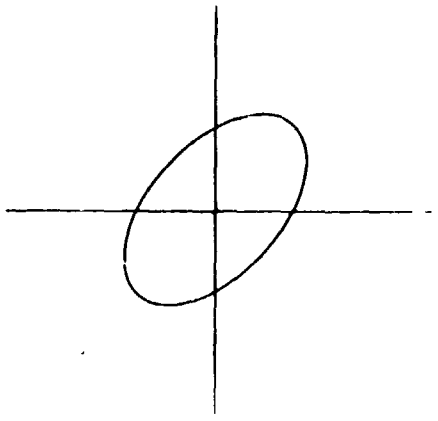

In terms of x' and y'
we obtain the following
isobaric contour

$$\frac{x'^2}{3K/2} + \frac{y'^2}{K/2} = 1 \tag{1.8}$$

This is an ellipse with an a/b ratio of $\sqrt{3}$. Indeed drop elongation was observed in KC-135 flights when both speakers were operated with 0° phase shift. This situation was remedied by complementary modulation, the arrangement in which the x and y speakers are operated on a mutually exclusive basis, i.e., when one is on and the other is off. We calculate the radiation pressure profile in this case using the simplest periodic representation of complementary modulation:

$$p = p_o \{ \cos kx \cos\omega_m t + \cos ky \sin\omega_m t \} \sin\omega t \tag{1.9}$$

where $\omega_m \ll \omega$ is the complementary modulation frequency. The preceeding geometric approach can be extended to this case. Equation (1.7) for the pressure profile near the center of the chamber is replaced by

$$x^2 (3/4 + 1/2 \cos 2\omega_m t) + y^2 (3/4 - 1/2 \cos 2\omega_m t) + xy (-1/2 \sin 2\omega_m t) = \frac{1}{2} - \frac{\langle \Delta p \rangle}{p_o^2/4\rho c^2} \tag{1.10}$$

This is a quadratic equation of the form

$$Ax^2 + 2Bxy + Cy^2 + F = 0$$

which is diagonalized by the transformation

$$x = x' \cos\alpha - y' \sin\alpha$$

$$y = x' \sin\alpha + y' \cos\alpha$$

with

$$\tan 2\alpha(t) = \frac{2B}{A-C} = \frac{1}{2} \tan 2\omega_m t \qquad (1.11)$$

The principal axis is no longer the diagonal, as was the case without complementary modulation; the new axes oscillate around the center with a frequency $2\omega_m$, which is chosen to be large in comparison with the drop oscillation frequencies. The isobaric contours are now

$$(A + B(t))x'^2 + (A - B(t))y'^2 + F = 0$$

This is again an equation of an ellipse, but its principal axes precess too quickly for the water drop to respond to. When this precession is averaged over a length of time comparable to a period of the n = 2 natural oscillation, the drop finds itself effectively in a spherical acoustic field, and its shape will not become distorted.

2. A Particle in a Static Acoustic Potential Well.

Consider now a drop moving in a 3-dimensional acoustic potential well

$$\langle \Delta p \rangle = -\frac{1}{4\rho c^2} \sum_{i=x,y,z} p_i^2 \cos 2k_i r_i \qquad (2.1)$$

If two dimensions happen to be equal, we assume that complementary modulation has been applied, so that this is the effective static pressure experienced by the drop. The force on a drop is approximately

$$\underset{\sim}{F} = -\iint \langle \Delta p \rangle \, \underset{\sim}{n} \, dS \qquad (2.2)$$

where $\underset{\sim}{n} = (\sin\theta\cos\phi, \sin\theta\sin\phi, \cos\theta)$ is the normal to the surface, and $dS = a^2 \sin\theta d\theta d\phi$ is the area element on the surface of a sphere. It is only an approximation because scattering effects have not been included. Comparison of laboratory measurements (Leung et al., 1979) with King's theory of acoustic forces leads to the conclusion that the effect of scattering is to enhance the acoustic force by 25% over the value indicated by Eq. (2.2). A further approximation is that the force was calculated for a rigid sphere, not on a deformable drop, thus neglecting the interaction of the acoustic field with the drop. This is a complicated problem which merits further analysis. With these restrictions the acoustic force is found to be

$$F_i = \frac{2\pi}{3\rho c^2} p_i^2 k_i^2 a^3 \Gamma(2k_i a) \sin 2k_i r_i \qquad (2.3)$$

where $$\Gamma(2k_i a) = \frac{\frac{\sin 2k_i a}{2k_i a} - \cos 2k_i a}{1/3(2k_i a)^2}$$

is the size factor, tending to 1 for $2k_i a \ll 1$. The calculation of (2.3)

required the evaluation of nine non-trivial surface integrals (Eqns. 2.2). It was found that each term in the pressure profile contributed to the force component in that direction only, as expected.

Consider now the motion of a particle in such a force field. Because near the center of the chamber we can replace sin $2k_i r_i$ by its argument, the object's motion is like that of a harmonic oscillator, described by

$$m\ddot{r}_i + K_i r_i = 0$$

with

$$K_i = \frac{4\pi}{3\rho c^2} p_i^2 k_i^2 a^3 \Gamma(2k_i a).$$

This gives rise to oscillation within the potential well at the frequency Ω, which is given by

$$\Omega_i^2 = \frac{K_i}{m} = \frac{p_f^2 k_f^2}{\rho_d \rho c^2} \Gamma(2k_i a) \qquad (2.4)$$

where ρ_d is the density of the scattering object. The oscillation frequency is proportional to the acoustic pressure in the chamber. Such behavior was seen on the SPAR film, where the frequency dropped with pressure, and was studied on the Vanguard Motion Film Analyzer (see Section 5.2).

3. A Drop's Response to Amplitude Modulation in the Acoustic Chamber.

Equations of motion are derived in this section for the boundary of a drop placed in a modulated acoustic potential well. The displacement from the equilibrium spherical shape is expanded in spherical harmonics and represented in the form

$$r(\Omega,t) = R + \varepsilon \sum_{\ell,m} a_{\ell m}(t)\, Y_{\ell m}(\Omega). \tag{3.1}$$

Equations of motion are to be derived for the boundary deformation coefficients $a_{\ell m}(t)$ from the Navier-Stokes equations of the system. In the potential flow approximation, in which viscosity effects are initially neglected, the velocity field $\underset{\sim}{v}$ is related to a scalar field ϕ via $\underset{\sim}{v} = \nabla\phi$, and the momentum (Navier-Stokes) and continuity equations are expressed in the form

$$\begin{aligned} &\frac{\partial \phi}{\partial t} + \frac{1}{2}(\nabla\phi)^2 + \frac{p}{\rho} = 0 \\ &\nabla^2\phi = 0 \end{aligned} \tag{3.2}$$

The boundary velocity is given, on one hand, by

$$\dot{r} = \varepsilon \sum \dot{a}_{\ell m}(t)\, Y_{\ell m}(\Omega) \tag{3.3}$$

and, on the other hand, by the solution of the Laplace equation (3.2) in the interior of the drop, namely,

$$\phi_{int} = \sum F_{\ell m} r^{\ell} Y_{\ell m}(\Omega).$$

Matching the boundary velocity in expression (3.3) with $v_r = \partial\phi/\partial r$ (the

kinematic boundary condition) results in

$$F_{\ell m} = \frac{\varepsilon \dot{a}_{\ell m}}{\ell a^{\ell-1}}$$

or

$$\frac{\partial \phi}{\partial t} = \varepsilon \sum_{\ell,m} \frac{\ddot{a}_{\ell m}}{\ell a^{\ell-1}} r^{\ell} Y_{\ell m}(\Omega)$$

and by Eq. (3.2) the pressure at the interior of the drop is, to lowest order of approximation

$$\frac{p_{int}}{\rho} = \frac{\partial \phi}{\partial t} = - \varepsilon \sum_{\ell,m} \frac{a_{\ell m}}{\ell a^{\ell-1}} r^{\ell} Y_{\ell m}(\Omega) \tag{3.4}$$

The pressure in the interior is related to the acoustic pressure of the exterior

$$p_{ext} = A_o e^{i\omega_o t} \sum p_{\ell m} Y_{\ell m}(\Omega) \tag{3.5}$$

by the Young-Laplace condition of pressure jump at a boundary (Landau and Lifshitz, 1959)

$$p_{int} - p_{ext} = \sigma \left(\frac{1}{R_I} + \frac{1}{R_{II}} \right) \tag{3.6}$$

where σ is the surface tension, and the expression in the parenthesis is the effective curvature. For not too drastic surface deformations the effective curvature can be expressed in the form

$$\frac{1}{R_I} + \frac{1}{R_{II}} = \frac{2}{R} + \frac{\varepsilon}{R^2} \sum_{\ell,m} (\ell-1)(\ell+2)\ a_{\ell m}(t)\ Y_{\ell m}(\Omega).$$

When this expression, as well as Eqs. (3.4) and (3.5), are substituted into

Eq. (3.6), we obtain the required equation of motion for the boundary deformation coefficient

$$\ddot{a}_{\ell m} + \omega^2 a_{\ell m} = A_o p_{\ell m} e^{i\omega_o t} , \tag{3.7}$$

where ω is the normal mode frequency of a water drop. With $p_{\ell m}$ being the component of the acoustic driving pressure at the surface of the drop, this mode obeys the equation of a forced harmonic oscillator. When viscosity effects are added, this equation is replaced by that of a forced, damped harmonic oscillator, being the basic expression for analyzing acoustically induced oscillations in the next section.

4. Acoustically Induced Oscillation.

To generate the characteristic oscillations of a liquid drop it is necessary to excite the drop surface at its normal mode oscillation frequencies. For a liquid sphere of surface tension σ, density ρ_d, and radius a, the normal mode frequencies are given by

$$\omega_n^2 = n(n-1)(n+2)\frac{\sigma}{\rho a^3} \tag{4.1}$$

The lowest order nonzero frequency corresponds to n = 2; n = 0 corresponds to a radial mode, which cannot exist in an incompressible fluid, and n = 1 describes the translational motion of the whole drop. The surface deformation for the n-th mode is

$$\delta r_n = \sum a_n P_n(\cos\theta) \tag{4.2}$$

where P_n is the Legendre polynominal of order n.

The simplest way to generate sample oscillations in a rectangular chamber is to modulate the scund pressure from one of the acoustic drivers. Introducing a sinusoidal amplitude modulation at frequency Ω_o in the x direction, or example, we have

$$\begin{aligned} p &= p_{xo} \cos k_x x \sin\omega_x t \cos\Omega_o t \\ &\quad + p_{yo} \cos k_y y \sin\omega_y t + p_{zo} \cos k_z z \sin\omega_z t \end{aligned} \tag{4.3}$$

These expressions and the associated components of the particle velocity lead to a radiation pressure (which includes scattering effects)

$$\begin{aligned} \langle \Delta p \rangle = -\frac{1}{24\rho c^2} & p_{xo}^2 (1 - 5/2 \cos 2k_x x (1 + \cos 2\Omega_o t)) \\ & + p_{yo}^2 (1 \quad 5\cos 2k_y y) + p_{zo}^2 (1 - 5\cos 2k_z z) \end{aligned} \tag{4.4}$$

We see that while the acoustic pressure is amplitude modulated at Ω_o, the radiation pressure, which drives the sample into oscillation and which is a second order effect, is modulated at $2\Omega_o$.

The amplitude of the normal modes of a drop driven by the modulated acoustic field may be calculated as follows. The expression for the surface of an axisymmetric drop is

$$r(\theta,t) = a + \sum_n a_n(t)\, P_n(\cos\theta) \tag{4.5}$$

An equation of motion for each mode $a_n(t)$ can be found by approximate solution of the momentum (Navier-Stokes) equation and incorporation of the Young-Laplace pressure jump condition at the surface. This results in a forced damped harmonic oscillator equation for $a_n(t)$

$$\frac{d^2}{dt^2} a_n + 2\beta_n \frac{d}{dt} a_n + \omega_n^2 a_n = \frac{n}{\rho a} F_n(t) \tag{4.6}$$

where ω_n^2 is given in Eq. (4.1), F_n is the forcing term, and the viscous damping β_n is (Lamb, 1932)

$$\beta_n = (n-1)(2n+1)\frac{\nu}{a^2} \tag{4.7}$$

where $\nu = \eta/\rho$ is the kinematic viscosity. Since in our case the sample is being driven at $2\Omega_o$, we assume a solution of the form $a_n(t) = A_n \exp(2i\Omega_o t)$ and substitute it into Eq. (4.6), giving amplitude coefficients:

$$|A_n| = \frac{n|F_n|}{a\rho\sqrt{\left((\omega_n^2 - 4\Omega_o^2)^2 + 16\beta_n^2\Omega_o^2 \right)}} \tag{4.8}$$

The amplitude of the n-th mode is not maximum when the sample is driven at

the normal mode resonance $2\Omega_o = \omega_n$, but at $2\Omega_o = \sqrt{\omega_n^2 - 2\beta_n^2}$. At the latter frequency the amplitude becomes

$$|A_n|_{max} = \frac{n|F_n|}{2a\rho \{\beta_n + \sqrt{\omega_n^2 - \beta_n^2}\}} \tag{4.9}$$

To evaluate $|A_n|_{max}$ we must know the magnitude of the forcing term F_n. This is obtained by integrating the radiation pressure, Eq. (4.4), over the surface of the sphere. This gives

$$|F_n| = \frac{p_{xo}^2}{8\rho c^2} \frac{2n+1}{4} I_n \tag{4.10}$$

where I_n is the integral

$$I_n (ka) = \int_{-1}^{1} \cos(2ka\mu) P_n(\mu) d\mu \tag{4.11}$$

It is seen that $I_n = 0$ for odd n, that is, one cannot excite the odd modes acoustically. This is a consequence of the fact that the pressure profile $\langle \Delta p \rangle$ is a symmetric function of the coordinates, and odd modes will only be observed as a result of asymmetries in the pressure profile. For even n the integral I_n has been evaluated analytically. An example of the normal mode amplitudes is given in Table 4-1 for some typical parameter values characterizing a 2.5 cm diameter drop of water.

Table 4-1. Amplitudes of The Normal Modes n=2 and n=4 for Various Values of the Acoustic Pressure.

A_2/a (%)	p_{xo} (dB)
1	138.6
2	141.6
5	145.6
10	148.6
25	152.6
50	155.6

A_4/a (%)	p_{xo} (dB)
1	153
2	156

Parameters (water drop in air):

L_x = 11 cm.
a = 1.25 cm.
ρ = 1.3 x 10^{-3} g/cc.
c = 3.5 x 10^4 cm./sec.
ν = 0.012 cm^2/sec.
σ = 70 dynes/cm.

The force exerted by a standing acoustic wave on a sphere was originally calculated by King (King, 1934). For the example considered here the minimum acoustic pressure required to position the drop is P ~ 10^3 dyne/cm^2 ~ 134 dB, relative to the reference pressure 2.0 x 10^{-4} dyne/cm^2. For a 50% efficient compression driver, less than 0.2 W of electrical power is needed to provide the required acoustic pressure. At this acoustic pressure level the surface tension force (F_s) that acts on the water drop is two orders of magnitude larger than the acoustic force (F_A): F_s/F_A ~ 100.

5. Acoustically Induced Rotation.

We consider the problem of the flow field in the neighborhood of an axisymmetric rigid body induced by periodic pressure fluctuations,

$$p_o = P(\underset{\sim}{r})\, e^{-i\omega t} \tag{5.1}$$

It is assumed that the pressure field (Equation 2.1) has been determined such that the boundary condition

$$\underset{\sim}{u}_o \cdot \underset{\sim}{n} = 0 \quad \text{on } \Sigma \tag{5.2}$$

is satisfied where $\underset{\sim}{n}$ is the normal unit vector on the surface Σ of the rigid body. Since we are restricting attention to small-amplitude motions in a nearly inviscid fluid, the velocity field $\underset{\sim}{u}_o$ is given by the linear ed inviscid equation of motion

$$-i\omega \underset{\sim}{u}_o = -\nabla \frac{p_o}{\rho} \tag{5.3}$$

where ρ is the mean density of the homogeneous fluid outside the surface Σ. The second problem is posed by the condition that the tangential velocity component must vanish on the surface Σ,

$$\underset{\sim}{n} \times \underset{\sim}{u} = 0, \tag{5.4}$$

where $\underset{\sim}{u}$ is the total velocity field.

In accordance with earlier work on acoustic streaming and damping, we assume that Equation (5.4) can be satisfied by a modification $\tilde{\underset{\sim}{u}}$ in a thin boundary layer of the solution $\overset{v}{\underset{\sim}{u}}$ of the inviscid equation of motion. The boundary layer has a thickness of the order $\sqrt{\nu/\omega}$ which we assume to be small compared to the typical wavelength $\lambda = 2\pi/k$ of the acoustic field as

well as the radius of curvature of Σ. Since the pressure is continuous across the boundary layer, the equations of motion for $\tilde{\underset{\sim}{u}}$ reduce to

$$\nabla \cdot \tilde{\underset{\sim}{u}} = 0 \tag{5.5a}$$

$$(\underset{\sim}{n} \cdot \nabla)^2 \, \tilde{\underset{\sim}{u}} = -i\omega \tilde{\underset{\sim}{u}} \tag{5.5b}$$

The solution for the total velocity field

$$\underset{\sim}{u} = \overset{\vee}{\underset{\sim}{u}} + \tilde{\underset{\sim}{u}}$$

proceeds by expanding both parts of the velocity field into a power series of of the small parameter ε, where $\varepsilon = k\sqrt{\nu/\omega}$,

$$\overset{\vee}{\underset{\sim}{u}} = \overset{\vee}{\underset{\sim}{u}}_o + \varepsilon \overset{\vee}{\underset{\sim}{u}}_1 + \ldots \tag{5.6a}$$

$$\tilde{\underset{\sim}{u}} = \tilde{\underset{\sim}{u}}_o + \varepsilon \tilde{\underset{\sim}{u}}_1 + \ldots \tag{5.6b}$$

We require that $\tilde{\underset{\sim}{u}}$ satisfies equation (5.5) and decays exponentially towards the outside, while $\overset{\vee}{\underset{\sim}{u}}$ satisfies equation (5.3) and remains constant on the scale of the boundary layer thickness. The two problems are coupled by the boundary conditions

$$(\overset{\vee}{\underset{\sim}{u}} + \tilde{\underset{\sim}{u}}) \cdot \underset{\sim}{n} = 0 \qquad \text{on } \Sigma \tag{5.7a}$$

$$(\overset{\vee}{\underset{\sim}{u}} + \tilde{\underset{\sim}{u}}) \cdot \underset{\sim}{n} = 0 \qquad \text{on } \Sigma \tag{5.7b}$$

Assuming that $\overset{\vee}{\underset{\sim}{u}}_o$ is given by equation (5.3) in terms of p_o, we find as solution of (5.5b)

$$\underset{\sim}{n} \times \tilde{\underset{\sim}{u}}_o = - \underset{\sim}{n} \times \nabla \frac{p_o}{i\omega\rho} \Big|_{\xi=0} \exp\{-\frac{(1-i)}{\sqrt{2}}\xi\} \tag{5.8}$$

The boundary layer coordinate ξ is defined by

$$\xi = \varepsilon^{-1} \underset{\sim}{n} \cdot (\underset{\sim}{r} - \underset{\sim}{r}_s)k \tag{5.9}$$

where $\underset{\sim}{r}_s$ denotes the position vector of a point at the surface Σ. While solution (5.8) satisfies the boundary condition (5.7b), it does not satisfy the continuity equation (5.5a). To the order ε^0, this equation can be written in the form

$$\frac{\partial}{\partial \xi} \underset{\sim}{\tilde{u}}_1 \cdot \underset{\sim}{n} + k^{-1} \underset{\sim}{n} \cdot \nabla \times (\underset{\sim}{n} \times \underset{\sim}{\tilde{u}}_0) = 0 \tag{5.10}$$

which yields the solution

$$\underset{\sim}{n} \cdot \underset{\sim}{\tilde{u}}_1 = - (\underset{\sim}{n} \times \nabla)^2 \frac{p_0}{\rho \omega k} \left| \frac{1-i}{\sqrt{2}} \exp \{-(1-i)\xi\} \right|_{\xi=0} \tag{5.11}$$

This solution decays towards the exterior, but it requires a perturbation of the exterior velocity field in order to satisfy boundary condition (5.7a)

$$\underset{\sim}{\tilde{u}}_1 \cdot \underset{\sim}{n} = (\underset{\sim}{n} \times \nabla)^2 \left| \frac{p_0}{\rho \omega k} \frac{1-i}{\sqrt{2}} \right|_{\xi=0} \tag{5.12}$$

A torque $\underset{\sim}{T}$ in the direction of the axis of an axisymmetric body can only be generated by viscous stresses exerted on the surface Σ. Using the unit vector $\underset{\sim}{a}$ in the direction of the axis, the torque $T = \underset{\sim}{a} \cdot \underset{\sim}{T}$ can be written as

$$T = \iint \rho \nu \, \underset{\sim}{a} \times \underset{\sim}{r} \cdot (\underset{\sim}{n} \cdot \nabla \underset{\sim}{\bar{u}}) \Big|_{\underset{\sim}{r}=\underset{\sim}{r}_s} d\Sigma \tag{5.13}$$

where $\underset{\sim}{\bar{u}}$ is the time average of the velocity field. A contribution to the time average $\underset{\sim}{\bar{u}}$ of the velocity field can only be generated by the nonlinear

terms of the equations of motion. Since the potential flow $\underset{\sim}{u}$ of the exterior does not generate a time-independent component of the velocity field, the mean flow must arise in the boundary layer. Denoting the time and the azimuthal average with a bar and noticing that only the azimuthal component $\bar{u}_\phi$ of $\bar{\underset{\sim}{u}}$ contributes in the integral (5.13), we obtain an equation for $\bar{u}_\phi$

$$(\underset{\sim}{n} \cdot \nabla)^2 \bar{u}_\phi = \underset{\sim}{n} \cdot \nabla \overline{(\underset{\sim}{u} \cdot \underset{\sim}{n}\, u_\phi)} \tag{5.14}$$

In principle, a second term corresponding to the derivative in the direction $(\underset{\sim}{a} \times \underset{\sim}{n}) \times \underset{\sim}{n}$ should be added to the right-hand side. But since, in general, it does not give a contribution to T, it has been neglected. By integrating equation (5.14) and using the condition $\underset{\sim}{n} \cdot \nabla \bar{u}_\phi \to 0$ for $\xi \to \infty$, we obtain

$$\nu \underset{\sim}{n} \cdot \nabla \bar{u}_\phi = \overline{\underset{\sim}{u} \cdot \underset{\sim}{n}\, u_\phi} - \overline{\underset{\sim}{u} \cdot \underset{\sim}{n}\, u_\phi}\Big|_{\xi=0} \tag{5.15}$$

Since we are interested in the stress generated by small amplitude motions, the velocity field derived earlier can be used as a first approximation on the right-hand side of (5.15) with the result

$$\nu \underset{\sim}{a} \times \underset{\sim}{r} \cdot (\underset{\sim}{n} \cdot \nabla) \underset{\sim}{u}\Big|_{r=r_s} = \varepsilon \overline{(\underset{\sim}{u}_1 \cdot \underset{\sim}{n})\, \underset{\sim}{u}_0}\Big|_{r=r_s} \cdot (\underset{\sim}{a} \times \underset{\sim}{r}) \tag{5.16}$$

Using expressions (5.3) and (5.12) and taking into account that only the real part (Re) of those expressions describes the physical velocity field, relationship (5.16) can be rewritten as

$$\nu(\underset{\sim}{a} \times \underset{\sim}{r}) \cdot [(\underset{\sim}{n} \cdot \nabla) \underset{\sim}{u}]\Big|_{r=r_s} = -\varepsilon \mathrm{Re}\left\{(\underset{\sim}{n} \times \nabla)^2 \frac{p_0}{\rho \omega k}\Big|_{r=r_s} \left(\frac{1-i}{2}\right)\right\} \quad \mathrm{Re}\left\{(\underset{\sim}{a} \times \underset{\sim}{r}) \cdot \nabla \frac{p_0}{i\omega\rho}\right\} \tag{5.17}$$

Restricting attention to the limit $|kr_s| \ll 1$, the pressure field generated by two standing waves of the same frequency can be written

$$p_o = p_x \sin(k\, r\sin\theta\cos\phi)e^{-i\omega t} + p_y \sin(k\, r\sin\theta\sin\phi)e^{-i\omega(t-t_o)} + p_{os} \tag{5.18}$$

$$= 3[j_1(kr) + \delta_1 y_1(kr)]\{p_x\, e^{-i\omega t}\, \sin\theta\cos\phi + p_y\, e^{-i\omega(t-t_o)}\, \sin\theta\sin\phi\}$$

where r, θ, and ϕ are spherical coordinates, $j_1(kr)$ and $y_1(kr)$ are the spherical Bessel functions of order 1, δ_1 is a phase angle due to scattering effects and ωt_o is the phase angle between the two signals. Evaluation of Equation (5.17) for the pressure given in (5.18) yields

$$\underset{\sim}{a} \times \underset{\sim}{r} \cdot \left(\frac{\partial \underset{\sim}{u}}{\partial r}\right) = \frac{9\varepsilon p_x p_y}{4(\omega\rho)^2}\, k \sin^2\theta\{\cos(\omega t+\pi/4)\sin(\omega[t-t_o])-\sin(\omega t)\cos(\omega[t-t_o]-\pi/4)\} \tag{5.19}$$

which gives rise to a torque about the polar axis with magnitude

$$T = \frac{3p_x p_y}{4\ \rho c^2} A\, l\ \sin(\omega t_o) \tag{5.20}$$

where A is the surface area of the sphere and l is defined as the viscous length, $l = \sqrt{2\nu/\omega}$. For a water drop 2.5 cm in diameter and a phase shift of 90° between the x and y signals, a torque of 2.0 dyne-cm is generated by an acoustic pressure of $p_x = p_y = 3 \times 10^3$ dynes/cm^2.

6. The Power Spectrum of a Freely Oscillating Drop.

The drop boundary can be represented in the form

$$r(\Omega,t) = a + \sum_{\ell,m} a_{\ell m}(t)\, Y_{\ell m}(\Omega) \tag{6.1}$$

On the movie film the boundaries seen are cross sections through the equatorial plane of the drop and along two orthogonal longitudinal planes, i.e., on three selected great circles. They can not completely characterize the surface of the drop. $Y_{\ell m}(\Omega)$ are the spherical harmonics, the normal modes of an oscillating drop; $a_{\ell m}(t)$, the coefficients of the normal modes, depend on time. Spectral information is derived from the $a_{\ell m}(t)$ by Fourier transforming them:

$$\begin{aligned} S_{\ell m}(\omega) &= \int dt\; e^{-i\omega t}\, a_{\ell m}(t) \\ &= \int dt\; e^{-i\omega t} \int d\Omega\; r(\Omega,t)\, Y_{\ell m}^{*}(\Omega) \end{aligned}$$

Taking into account that mode ℓ is $(2\ell+1)$-fold degenerate, the power spectrum associated with mode ℓ is

$$\begin{aligned} I_{\ell}(\omega) &= \sum_{m=-\ell}^{\ell} |S_{\ell m}(\omega)|^2 \\ &= \iint dt\,dt'\; e^{i\omega(t-t')} \iint d\Omega_1 d\Omega_2\; r(\Omega_1,t)\, r(\Omega_2,t') \sum_{m=-\ell}^{\ell} Y_{\ell m}^{*}(\Omega_1)\, Y_{\ell m}(\Omega_2) \end{aligned} \tag{6.2}$$

The addition theorem of spherical harmonics is

$$\sum_{m=-\ell}^{\ell} Y_{\ell m}^{*}(\Omega_1)\, Y_{\ell m}(\Omega_2) = \frac{2\ell+1}{4\pi} P_{\ell}(\cos\theta)$$

where θ is the angle between Ω_1, and Ω_2. This theorem is extremely important for the data analysis of the free oscillation sequence. Though the

individual $a_{\ell m}(t)$ depend on the particular choice of coordinate system used in analyzing the data, the total power spectrum is invariant to any particular choice. Equation (6.2) cannot be used as given, since the boundary is not given over the whole drop surface, but can be used in the version

$$I_\ell(\omega) = \iint dt\, dt'\, e^{i\omega(t-t')} \sum_{m=-\ell}^{\ell} a_{\ell m}(t)\, a_{\ell m}^*(t') \qquad (6.3)$$

The individual coefficients $a_{\ell m}(t)$ can be determined in an arbitrary coordinate system; the most convenient system has the polar axis in the z direction. But the total power spectrum will be independent of this particular choice. Note that the procedure outlined by Eq. (6.3) is far from trivial. The steps involved in evaluating the power spectrum are: 1) calculating $a_{\ell m}(t)$ by angular integration over each boundary, 2) calculating the correlation function between the various pairs of frames, 3) calculating the Fourier transform of the correlation function.

SECTION 5

DATA ANALYSIS

1. Introduction

Description of the Film Record

We surveyed the film to determine what kind of information was available from it. The main events occurring in the experiment are summarized in Table 5-1. Of these, the following five time sequences were identified for analysis.

(a) Free Oscillation (127-145 sec)

The fluid injectors are pulled out and the drop is held in position by the acoustic field. Free oscillations (excited by the retracting injectors) damp out, and the drop moves back and forth in the acoustic potential well. This part can be used to observe free oscillations, to measure the radius of the drop and to study its center of mass motion as a check upon theoretical predictions of motion in a potential well for a given pressure profile.

(b) Forced Oscillation (145-147 sec)

As the modulation of the acoustic pressure along the z axis is turned on, the resulting oscillations of the drop are very regular. This sequence requires detailed analysis and comparison with predictions of forced oscillation amplitudes.

(c) Combined Oscillation and Rotation (147-265 sec)

The regular behavior of the drop's response to the z axis modulation quickly developed an unexpected twist: to the large amplitude oscillations was added rotation of the drop. This portion is the most

Table 5-1. Sequence of Events

Clock Time (Sec after Liftoff)	Event
85	Camera on
90	Complementary modulation on
105	Fluid delivered through injector
117	Fluid delivery off
127	Fluid injector extracted
127-145	Free oscillation
145	z modulation on
145-265	Forced oscillation
265	z modulation off
265-300	Drop relaxation
300	Complementary modulation off
300	90^{o} phase shift on
300-330	Induced rotation
330	90^{o} phase shift off
330	Complementary Modulation on
330-360	Coasting
365.5	Drop hit wall

difficult and intriguing to interpret. The acoustic forces and torques on a strongly deformed drop at an arbitrary position are poorly understood.

(d) Relaxing Drop (265-300 sec)

With the complementary modulation of the x and y axes on, the drop relaxes prior to being spun up. The information in this sequence should be similar to that in sequence (1).

(e) Rotating Drop Spun Up from Rest (300-330 sec)

With a phase difference of 90° between the x and y pressure amplitudes a torque is generated on the drop causing it to rotate about the z axis. The time allotted is probably inadequate for reaching solid body rotation, and so some amount of differential rotation still takes place. The lack of tracer particles prevents the measurement of internal flows and rotation rates. Deformed shapes are observed, which can be compared with theoretical predictions of the equilibrium shape of a rotating liquid drop.

Procedure for Data Analysis

The strategy involved in processing and analyzing the SPAR VI data consisted of the following steps: (a) digitizing the drop boundary for selected frames, performed by the Image Processing Laboratory (IPL) of JPL, (b) transfer of the digitized data from magnetic tape, the output of IPL, to floppy disks, the input to an AODC microcomputer dedicated to the use of our group (this step was performed on a UNIVAC-1100 computer), (c) preliminary data analysis done directly from the film with the aid of a Vanguard film analyzer, and (d) analysis of the IPL-digitized data with the aid of the AODC microcomputer. The first two steps are briefly described here, while the latter ones containing the bulk of the data analysis, are discussed in detail in the remaining sections of this chapter.

IPL Activity

The digitization of the data was performed at JPL's Medical Image Analysis Facility. By making only a few changes in an existing routine to determine the volume of a ventricle from a sequence of 35 mm angiograms, their system was able to track the drop and produce as output digitized boundaries for each of the three views.

Using a Vanguard 35 mm film transport and a Spatial Data Systems vidicon/digitizer each of the selected frames was completely digitized into a 480 x 500 pixel grid with 256 possible levels of grey. An operator through interaction with a PDP 11/55 computer was able to stretch the contrast of the digitized frame to enhance the visibility of particular features.

The automated digitization required a rough boundary to initiate its search routine for the edge of the drop. The operator provided this line by locating five to ten points per boundary with a joystick-controlled cursor on the video monitor. The mini-VICAR programs (a minicomputer-based subset of JPL's Video Image Communication and Retrieval System) connected the points to form the first order edge. Looking within a window eighteen pixels wide perpendicular to this boundary, the program used the largest change in grey level to determine the edge. This is known as the slope or first derivative method of edge definition. The 'raw' values of the x and y coordinates obtained were smoothed averaged over nine points. This 'smoothed' set was used as the initial boundary for the next frame to be analyzed. The 'raw' set was used for the data analyses described below. After the initial input of points the operator was only required to monitor the progress of the routine on a video display.

A sample frame is shown in Fig. 5-1. Both a color and a black and white photograph are shown to illustrate the deterioration in contrast occurring in the conversion to black and white film. This transfer was made when the 16mm color film was blown up to the 35mm B/W, a format in which the Image Processing Lab could utilize its automated equipment. Figure 5-2 shows the computer-generated boundaries for the frame in the photographs, both the 'raw' data and a quadratically smoothed boundary are shown for each of the three views. It must be noted that despite the satisfactory appearance of the original photographs, some irregularities do appear in the digitized and smoothed versions. These may be due to overlap with the speaker ports, specular or back reflections, or to a peculiarity in the digitization algorithm. It is a persistent feature throughout the film.

When the activity of the drop was of small amplitude in space and time, this scheme worked very well. However, when the drop underwent large-scale motion or the density of frames digitized was low, the process was not quite as reliable, requiring the operator to intervene more often.

The following frame sequences were digitized at the given frame densities:

Time (sec)	Event	Low Resolution	High Resolution
127.1 - 130.4	Free Oscillation	1/1	1/1
130.4 - 144.6	Free Oscillation	1/3	
144.6 - 147.1	Forced Response: Regular	1/1	
147.1 - 170.4	Forced Response: Rotation	1/2	
263.7 - 300.4	Free Oscillation	1/4	
300.4 - 333.7	Rotation	1/5	

The total number of frames processed was 1826. In the low-resolution case the scanner viewed the whole frame (containing all three views), resulting in a reduced number of pixels (picture elements). This gave 90 to

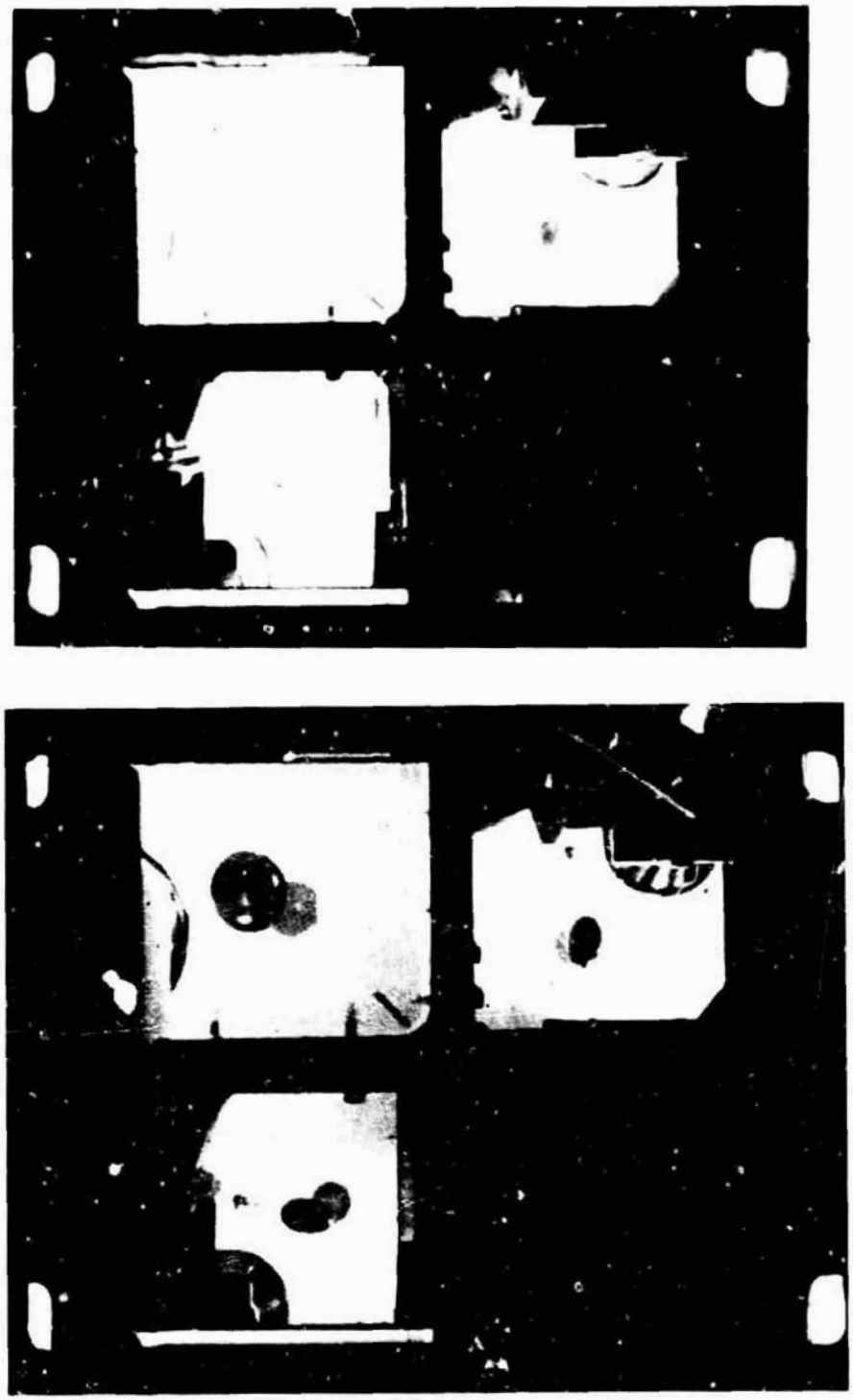

Figure 5-1. Photographs of a typical frame from the 16mm film record. The color and black and white pictures demonstrate the quality of the image which is to be digitized. They are frame #955 (t = 147.5 sec) from the forced oscillation sequence of the experiment.

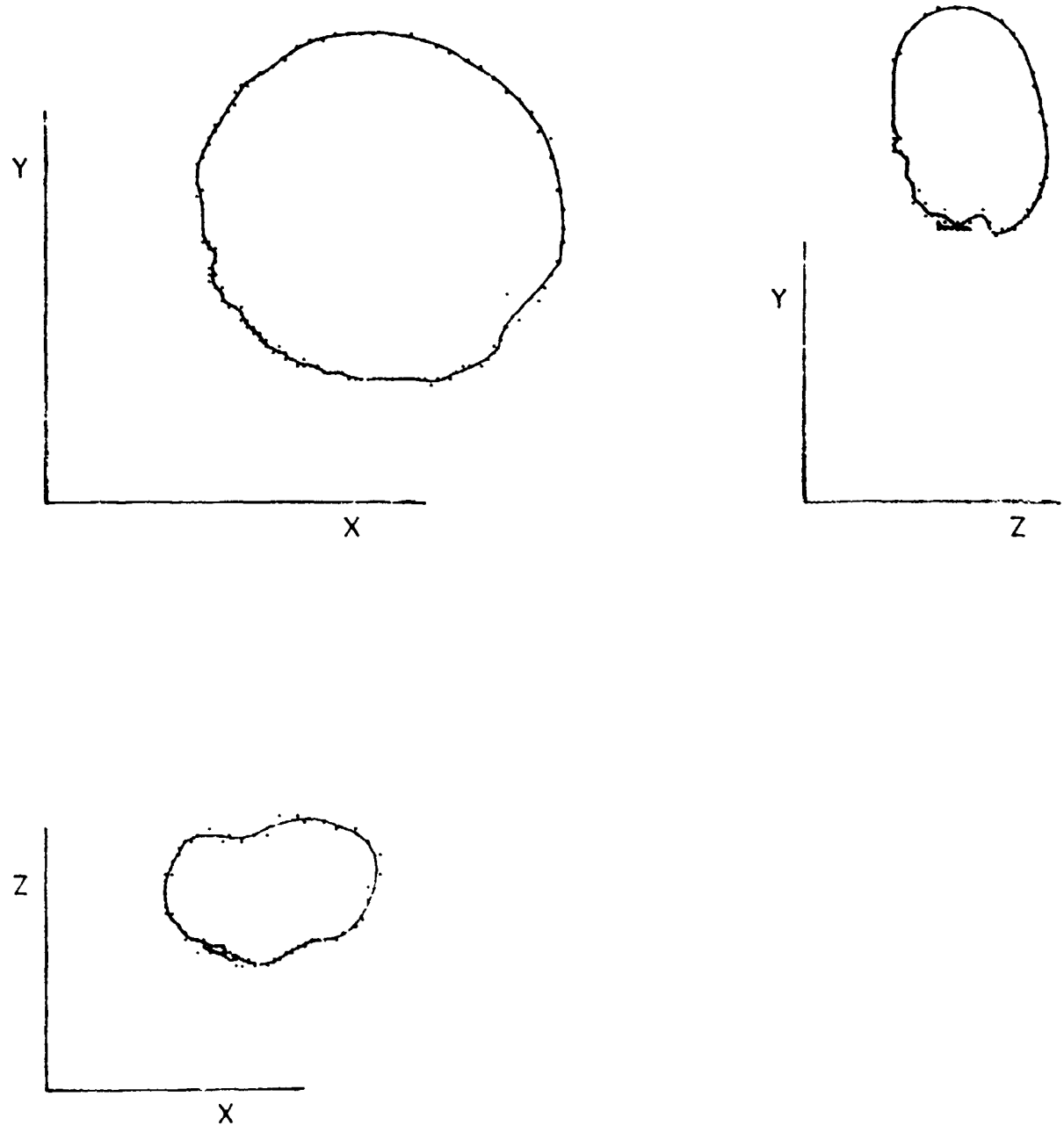

Figure 5-2. Digitized data: frame #955. The points are the 'raw' ata transferred from IPL and the lines are the quadratically smoothed description of them. Also shown are the axes corresponding to each view.

Figure 5-3. A magnified picture of the drop prior to release. This negative picture is the form of digitized image the Image Processing Laboratory of JPL generates from the cine film. The circle in the lower left is the port for the acoustic driver. Note the two spots on the drop. These are specular reflections from the photolamps. The scales for the axes are hundreds of pixels.

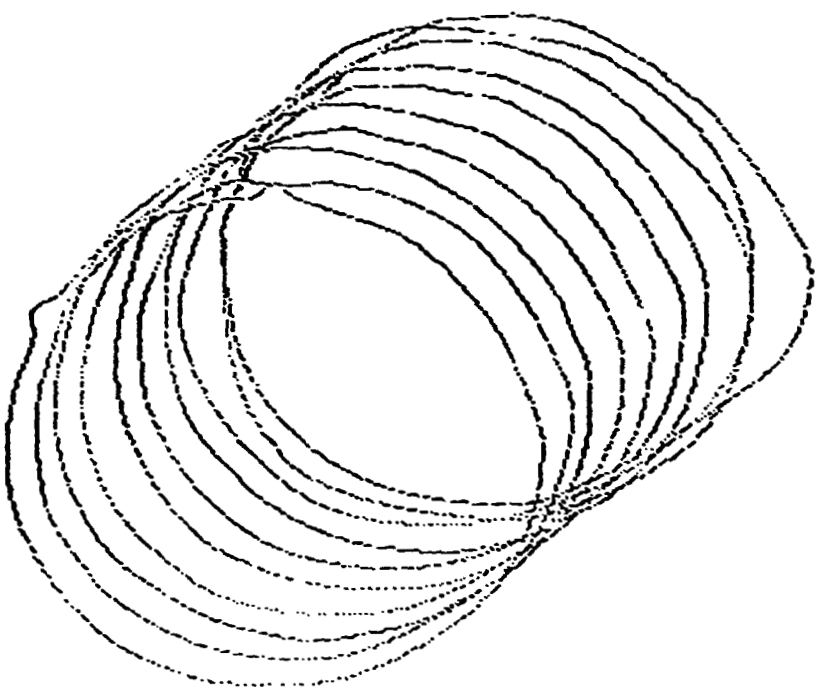

Figure 5-4. These ten boundaries show the digitized 'smoothed' version of the drop's boundary as the drop moves from the lower left to the upper right during the two second after its release. The scales are in hundreds of pixels.

150 points per boundary. In the few pictures taken at high resolution, the scanner viewed only the drop boundary of the main view, providing 450-500 points around the boundary. The boundary data were recorded in the form of 3-digit integers, thus placing a limit upon the resolution of the digitization. The data were stored on magnetic tape in the two versions: raw and smoothed. Figure 5-3 shows the fully digitized image of the drop just prior to release. It is taken from the main view and is at the high resolution. Samples of the digitized drop boundaries at the high resolution are shown in Fig. 5-4.

Data Processing

The next step was to transfer the digitized data supplied by IPL to floppy disks, the input to the AODC microcomputer. This was done through a UNIVAC-1100 general purpose computer. Though simple in principle, this step turned out to be quite laborious, due in part to frequent changes in development of the AODC system which was new at the time, and to the need to interact with several groups at three different computers. This stage of events is described in Appendix A.

The remainder of this chapter is arranged as follows: Section 2 describes the preliminary data analysis performed using a Vanguard film analyzer, designed to provide some insight into the nature and quality of data at hand. Section 3 discusses the slow periodic motion of the drop in the acoustic potential well. In the next section we discuss some computer-simulated experiments, in which typical situations are generated and studied under controlled conditions. In Sections 5 and 6 we discuss the analysis of acoustically induced oscillation and rotation.

2. Vanguard Analysis

It was felt that prior to automatic processing of relatively large amounts of data, it would be useful to investigate some of the interesting features manually on a Vanguard Motion Film Analyzer. These measurements, though sparse and of uncertain accuracy, provide some insight into what might be expected from a more detailed analysis. Three topics were handled: a) The drop moves periodically in the acoustic potential well. The frequency of this motion was measured and compared with a theoretical prediction approximating the acoustic potential well by an equivalent harmonic oscillator potential. These frequencies are correlated with the acoustic force and with the pressure level in the chamber. b) The two lowest normal mode frequencies, f_2 and f_3 were identified. With a knowledge of the surface tension, measured shortly before the flight, these measurements are used to infer the volume of the drop. c) The ratio of the minor to major axes was measured before, during, and after the rotational sequence. While there was significant scatter in the results, b/a is close to 1.0 prior to rotation, and shows a measurable change when the drop is spun up.

Center of Mass Motion.

The frequency with which the center of mass of an object moves in a potential well can be related to the restoring force the object feels. If the drop is neither too large nor moves too far from the center, the force it feels in the i-th direction (i = x, y, z) is

$$F_i = - m\Omega_i^2 d_i \qquad (1)$$

with m the mass of the drop, d_i the distance of its center of mass from the center of the box along the i-axis, and Ω_i the frequency with which it

oscillates in the acoustic field. This frequency can be related to other parameters as well

$$\Omega_i^2 = \frac{5\, k_i^2\, p_i^2}{4\, \rho_d\, \rho c^2} \qquad (2)$$

with wave number $k_i = 2\pi/2L_i$ along the i-axis (with chamber dimension L_i), and acoustic pressure, p_i for each of the axes and densities ρ_d for the drop and ρ for air.

Using the Vanguard Motion Analyzer, the times when the drop was at its furthest from the center for three axes were recorded. Three were chosen from the six available: the x and the y from the main view and the z from the lower left. The period was averaged over two cycles and from this the frequency was determined.

Fig. 5-5 is a plot of the frequency of oscillation in the potential well along the z axis as a function of time. Note that there are two regions: from deployment (at 127 sec.) to 265 sec., the frequency is roughly 0.163 Hz, from 265 sec. until the drop begins to move toward the wall at 361 sec. the frequency is 0.131 Hz. At 265 sec. the sound pressure level was decreased from 148 dB to 145 dB. This corresponds to a desrease by a fsctor of 2 in the force and of $\sqrt{2}$ in the frequency. The ratio of the observed frequencies along the z axis is 0.131 to 0.163 Hz or 0.81. The force determination requires an accurate radius which is not available at present. A similar change in frequency was reflected in the other two directions. In the x direction the average frequency changes from 0.143 Hz to 0.120 Hz (for a ratio of 0.84) and in the y direction from 0.149 Hz to 0.111 Hz (0.80).

The scatter of the points reflects the perturbations the chamber feels from the outside as well as errors due to the crude data reduction. A force

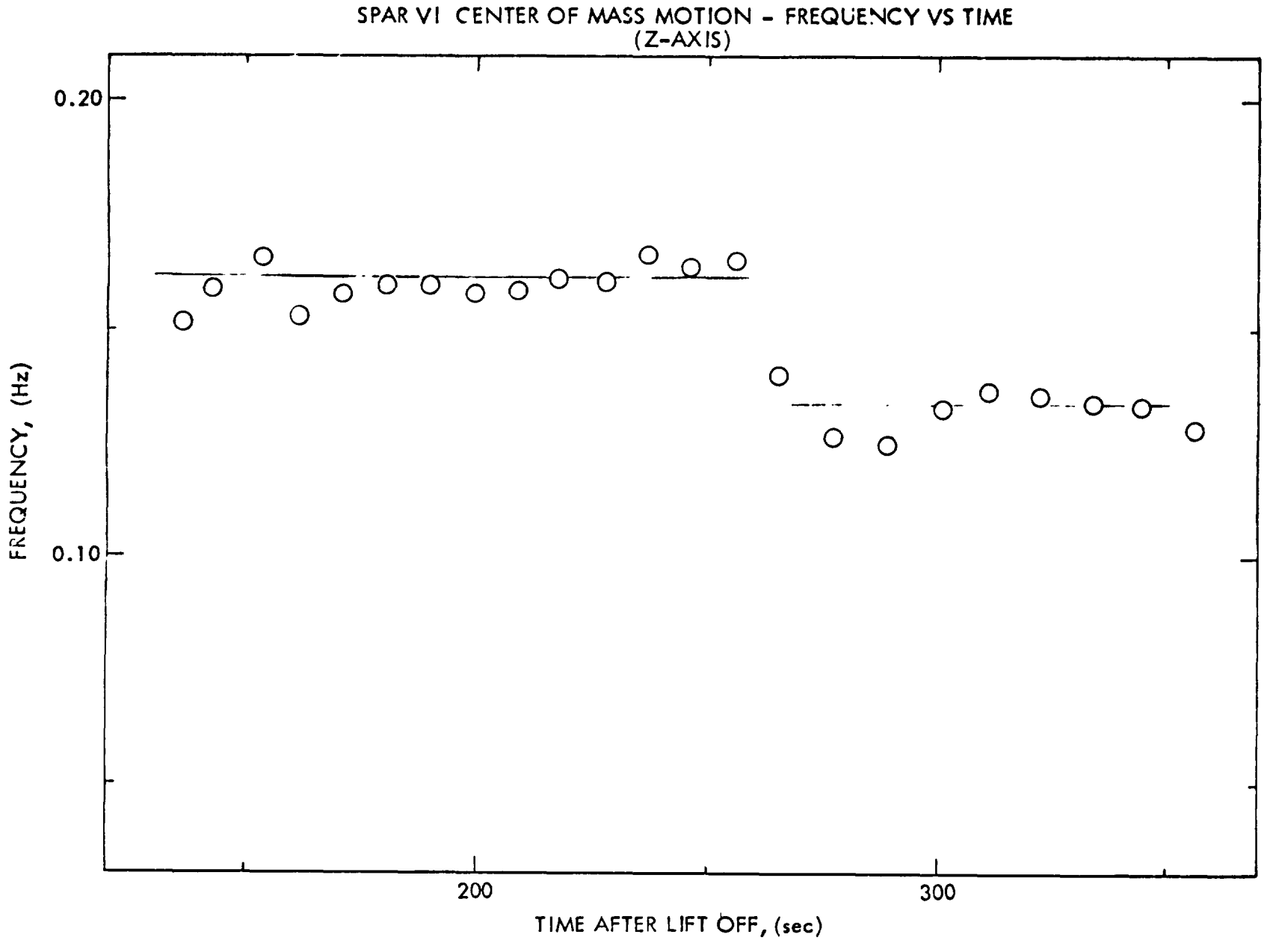
SPAR VI CENTER OF MASS MOTION - FREQUENCY VS TIME
(Z-AXIS)
0.20
0.10
FREQUENCY, (Hz)
200
300
TIME AFTER LIFT OFF, (sec)

of 0.9 dynes acting on a 9.2 gram drop corresponds to 10^{-4}g.

Natural Oscillations

For a simple liquid drop the frequencies of oscillation for small amplitude surface motion are

$$f_n^2 = \frac{n(n-1)(n+2)}{4\pi^2} \frac{\sigma}{\rho_d a^3} \tag{3}$$

where f_n is the frequency of the nth mode, σ the drop's surface tension, ρ_d its density and a its resting radius.

In this experiment when the drop oscillated the reflections of the photo lamps showed that motion. When the oscillations were regular, the motion of the reflection was too. Using the time information on the edge of the film and advancing the film through a certain number of cycles, a rough value of the frequency of these oscillations could be obtained. There were two periods of time during which the drop was merely positioned by the acoustics in the center of the chamber and not manipulated: the eighteen seconds after deployment (127 to 145 sec.) and the thirty-five seconds between z-axis modulation and the rotation sequence (265 to 300 sec). In the early segment the impulse provided by the probe retraction led to the detectable presence of higher modes (i.e. $n \geq 3$) which damped out very quickly. The second period permits study of the decay of the oscillations and motion generated during the modulation sequence.

The frequencies, $f_2 = 2.48 \pm .10$ Hz and $f_3 = 4.67 \pm .05$ Hz, were obtained from the early sequence and $f_2 = 2.54 \pm .03$ Hz from the later. $f_2 = 2.74$ Hz and $f_3 = 5.31$ Hz were the frequencies expected for an 8.6 cc water drop with a surface tension of 71.0 dynes/cm.

Using the experimental frequencies and the measured surface tension of 71.0 dynes/cm, the volume of the drop would be roughly 9.8cc. Because this is quite a bit higher than was expected, one suspects that the actual surface tension may have been lower than that measured several days before the launch. The final verdict must await the determination of the radius and volume from the film.

Rotation

At 300 seconds after lift-off the complementary modulation in the x and y axes was turned off and a 90 degree phase shift was introduced between the two signals. This generated a torque on the drop which tried to rotate it about the z axis.

Due to the large amplitude of the drop's response to the z-axis modulation (which stopped at 265 sec.), the drop was still strongly oscillating and rotating about the x axis when the rotation sequence began. As a result it was difficult to isolate the change of drop shape caused by the torque-induced rotation from that due to the modulation-induced motion. By averaging measurements of the greatest and least dimension of the drop for each view over a complete cycle of the oscillation, the effects of the latter were minimized somewhat. Fig. 5-6 shows the results of the attempt to separate the effects and to thereby determine the rate of rotation.

As the drop begins to rotate about the z axis, its profile in the x and y directions should flatten, leading to lover values of the ratio, b/a (i.e. least dimension/greatest dimension), while in the view along the z axis the drop should be circular (i.e. b/a ~ 1.0). The distortion due to rotation is most easily seen in the y axis data of Fig. 5-6: before 300 sec. the ratio is close to 1.00. Afterwards it decreased to 0.67. The z axis data also

demonstrate the effects of rotation: the ratio increases to 1.0 after the sequence begins and decreases when the phase shift is turned off.

If the drop rotated as a rigid body, then from studying its shape, a value of its rotation rate could be found. Fig. 5-7 illustrates the relation between b/a and the rotation rate. The observed ratio of axes of 0.67 corresponds to a value of the rotation parameter $\sum$ of 0.32 with

$$\sum = \frac{\omega^2 \rho_d a^3}{8\sigma} = \frac{\omega^2}{\omega_2^2} \tag{4}$$

and σ , ρ_d, and a being the drop's surface tension, density and radius and with ω being its angular velocity in radians/sec and ω_2 the frequency of oscillation of the n = 2 mode. This value of $\sum$ and the experimentally determined ω_2 would indicate a rotation rate of 8.92 radians/sec. (or 1.42 revolutions/sec.) if the drop were in solid body rotation. For purposes of comparison, the theoretical bifurcation point at which the equilibrium shape can either be axisymmetric or have two distinct lobes is located at $\sum$ = 0.313.

The assumption has been made in the foregoing analysis that the drop could be considered moving in solid body rotation, despite the presence of oscillation and absence of equilibrium. How far one can use this type of analysis must be critically examined.

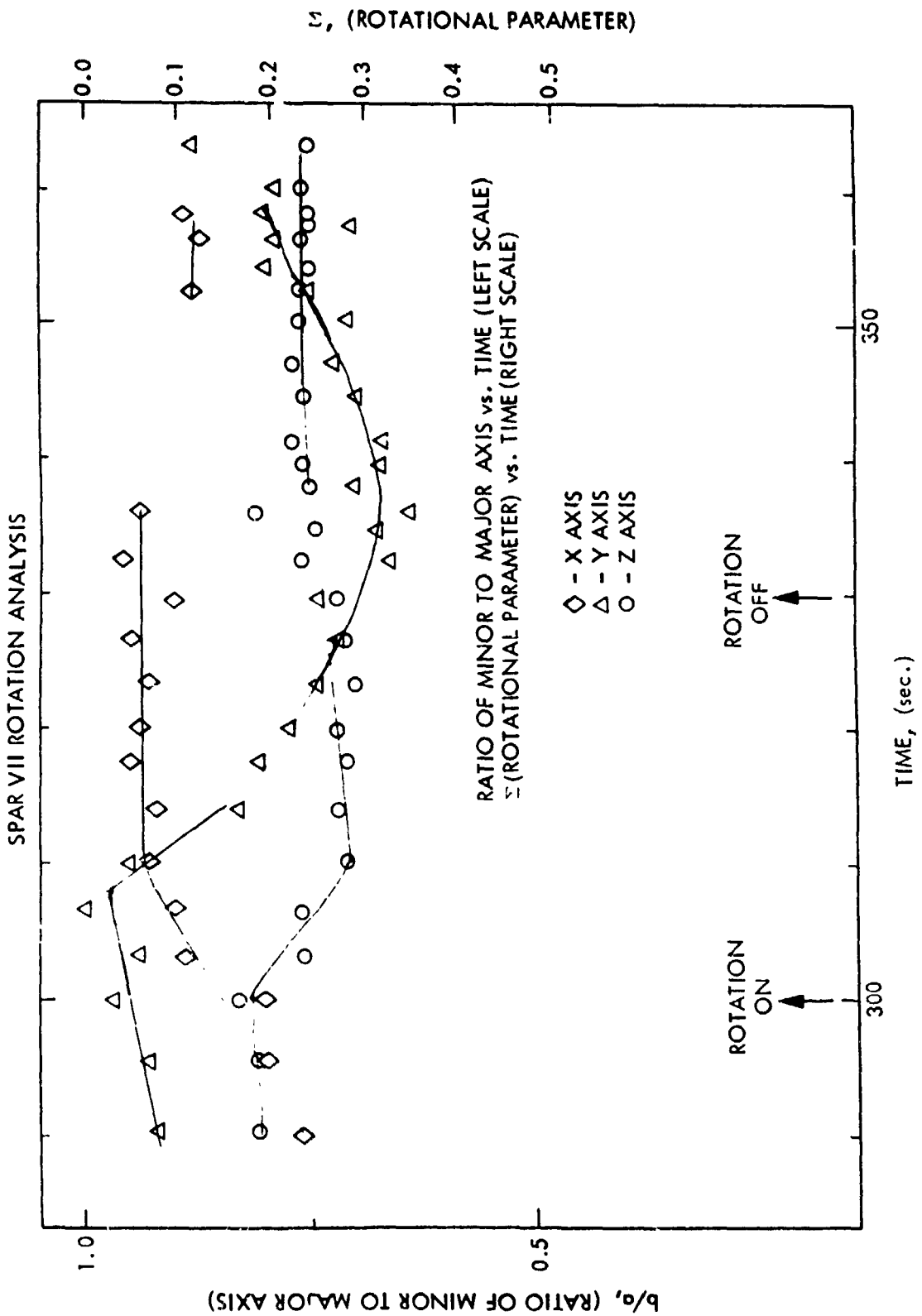

Figure 5.4. Rotational Analysis

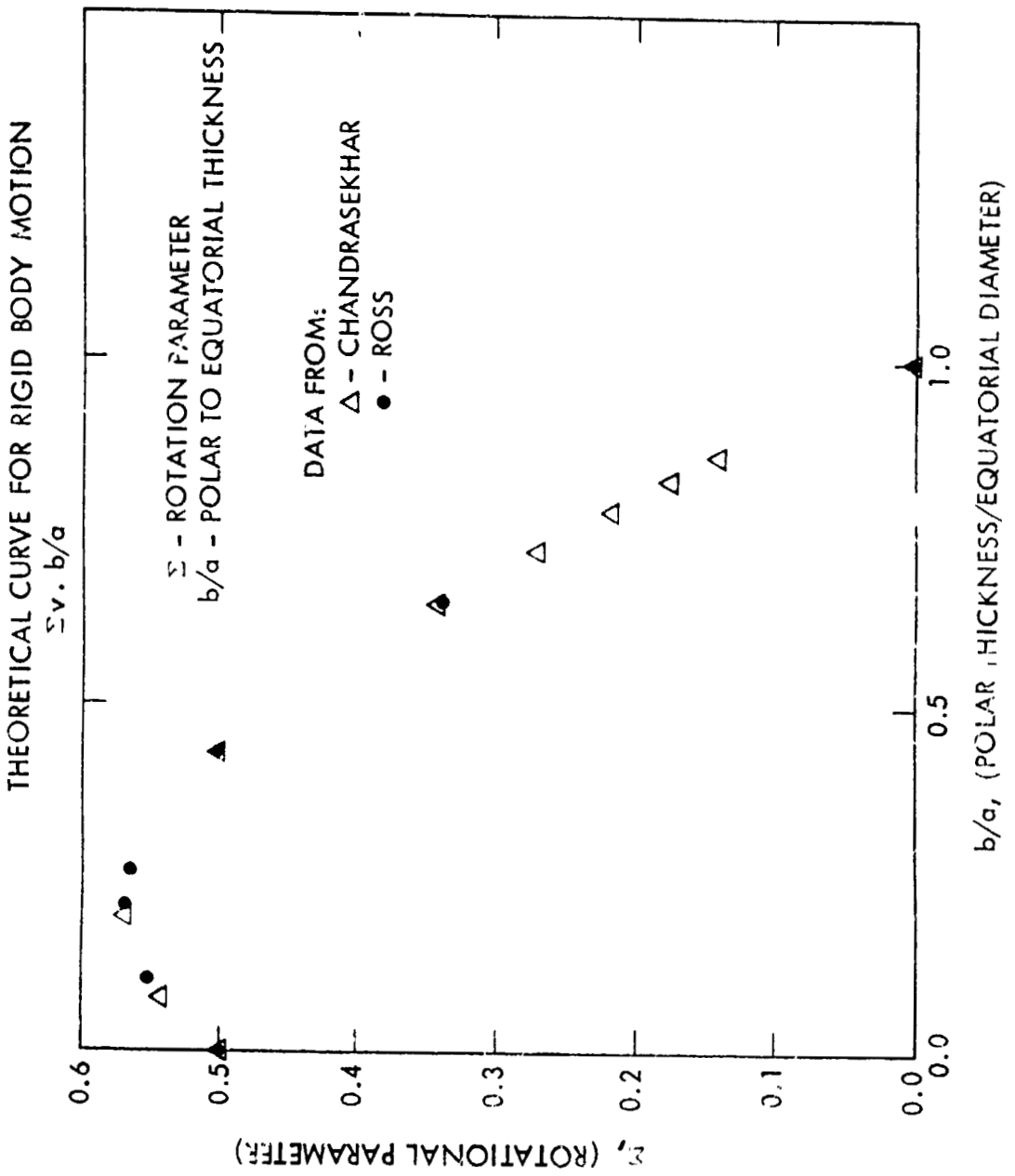

Fig 5.5. Theoretical calculation relating the ratio of axes to the rotation rate of a liquid drop in solid body rotation.

3. Center of Mass Motion

The acoustic pressure in the chamber was set so that an object displaced from the center by a certain distance along one of the axes would feel the same force for any of the three axes. Fig. 3-3 illustrates the method used to balance the acoustic forces. An acoustic force of 12.9 dynes at 2.883 cm from the center corresponds to a sound pressure level of 146 dB and a pressure amplitude of roughly 3×10^3 dynes/cm^2 at the walls.

The spatial dependence of the acoustic force has been shown both theoretically and experimentally to behave like $F_o \sin 2k_i r_i$ where r_i is zero at the center of the box (Leung, Jacobi, Wang, 1981). As long as the displacement of an object in the field is not too far from the center, the restoring force will be approximately $F_o 2k_i r_i$ which is the same form as the restoring force in a simple harmonic oscillator. In that case, the force on the mass m is given by $-m\omega_i^2 r_i$ when it is displaced a distance r_i, and ω_i is the frequency at which it will oscillate. If a dissipative mechanism is present the amplitude of the displacement will decrease with time.

From the film record it is easy to determine values of the frequencies with which the drop moves in the triaxial acoustic chamber. The results of a simple study of the period of the drop motion were presented in Section 5.2. It was hoped that using the more numerous and accurate digitized data any departure of the acoustic restoring force from the simple harmonic oscillator model would be indicated.

Because the drop was within the acoustic potential well the entire time the camera was on, any and all of the data digitized were suitable for this analysis. Primary interest focused on the time just after retraction of the probes (127 to 130 seconds) when the drop was not being manipulated and at

265 seconds which is when the sound pressure level was dropped by 3 dB and the acoustic restoring force decreased by a factor of 2.

Laboratory Calibration

As described in Section 3, the acoustic levels in the chamber were calibrated by balancing forces. Referring to Fig. 3-3 there is a balance between the tension of the string T, the weight of the ball, and the acoustic force F_{ac}:

$$F_{grav} = mg = T \cos \theta$$

$$F_{ac} = T \sin \theta$$

$$= mg \tan \theta$$

$$\text{where } \sin \theta = \frac{d}{S}$$

$$\text{or} \quad F_{ac} = \frac{mgd}{S\sqrt{1-(d/S)^2}} \sim \frac{mgd}{S}$$

A .229g ball with a radius of 1.27 cm which was suspended on a 5.08 cm string 3.175 cm from the center of of the chamber was deflected 0.292 cm by the acoustic field. This indicated an acoustic force of 12.9 dynes.

A sphere of radius a in an acoustic standing wave is subject to the force:

$$F_{ac} = \frac{\pi}{3\rho c^2} \eta_i p_i^2 a^2 \Gamma(\eta_i) \sin (2k_i r_i) \qquad (1)$$

where $\eta_i = 2k_i a$

$$\text{and } \Gamma(\eta_i) = \frac{(\sin \eta_i)/\eta_i - \cos \eta_i}{(1/3)(\eta_i)^2} \qquad (2)$$

is the correction (see Lee, Jacobi, Wang, 1981) due to the finite size of the sphere.

Using Eq. 1 and the calibration acoustic force of 12.9 dynes at r_i = 2.883 cm with the following parameters:

$$k_x = k_y = 0.275 \text{ cm}^{-1}$$

$$\eta_x = 2k_x a = 0.698$$

$$k_z = 0.247 \text{ cm}^{-1}$$

$$\eta_z = 2k_z a = 0.628$$

$$\rho = 0.001204 \text{ g/cm}^3$$

$$c = 34{,}075 \text{ cm/sec}$$

$$\text{and } \Gamma(\eta_x) = 0.952$$

$$\Gamma(\eta_z) = 0.961$$

we obtain the pressure amplitudes

$$p_x = p_y = 2.84 \times 10^3 \text{ dyne/cm}^2$$

$$p_z = 2.99 \times 10^3 \text{ dynes/cm}^2.$$

These pressures gave rise to an overall sound pressure level of 145.0 dB (re 0.0002 dynes/cm^2) at a corner of the chamber. When the acoustic calibration forces were doubled to 25.0 dynes, the resulting pressure amplitudes increased by a factor of 2 and the SPL became 148.0 dB.

These pressures can be related to the frequency of the oscillatory motion an object undergoes in the potential well. Applying the simple harmonic oscillator approximation to the potential well gives the relation

$$f_x^2 = \frac{k_i^2 p_i^2}{\rho (\rho c^2)} \Gamma(\eta_i)$$

For a water drop of any size

$$f_x = f_y = 0.145 \text{ Hz}$$

$$\text{and } f_z = 0.138 \text{ Hz}.$$

Because there is a change in elevation between JPL (where the package

was calibrated) and White Sands Test Range (where is was sealed prior to launch), there were changes in the acoustic parameters innvolved. Exactly how the acoustic pressure changes would be difficult to determine for any set of conditions, however the system was designed so that the acoustic pressure determined by a microphone in the chamber was held constant by adjusting the power to the drivers to maintain the pressure at the calibrated level. The other term in Eq. 1 which depends upon the ambient conditions of the gas is ρc^2, which is typically 1.40×10^6 dynes/cm^2 at JPL and 1.12×10^6 dynes/cm^2 at White Sands. The sound pressure level will not change as a result of the change in elevation but the acoustic force will increase from 12.9 to 13.6 dynes and similarly the observable frequency of the center of mass motion will increase by a factor of ρc^2 (i.e. by 1.07), giving

$$f_x = f_y = 0.162 \text{ Hz}$$

$$\text{and } f_z = 0.154 \text{ Hz}.$$

Data Analysis

The centers of mass of the digitized boundaries were determined for the drop in each view for each frame. This involved the average of approximately 90 points for the side views and 150 for the main view. The value of the center of the chamber for each of the six coordinates was subtracted These modified coordinates were Fourier transformed and the frequencies of the oscillation in the acoustic potential well were found from the resulting power spectra.

When the film was digitized by the Image Processing Lab the operator divided the data into blocks of 10, 20, 30, or 40 frames. Due to the methods used in the initialization of the digitization process, errors of a periodic nature were introduced. To minimize the effect of this problem a correction

function corresponding to the particular block size used was folded in with the data. Fig. 5-8 shows the results before this correction was incorporated. The peaks at integer multiple of 0.80 Hz are the results of data blocks twenty frames long: (48 fps/3)/(20 frames) = 0.80 Hz. Fig. 5-9 shows the corrected version. In both instances the desired signal (i.e. the peak at 0.15 Hz) is clearly present.

Table 5-2 lists the results of analyzing the experimental data. From Fourier analysis of the center of mass coordinates, spectra which are qualitatively identical to Fig. 5-9 are obtained; the observed frequencies of the oscillation in the chamber, f_{obs}, are taken from these spectra. Δf is the full width at half of the maximum value of the experimental peak located at f_{obs}. f_{th}(JPL) and f_{th}(WS) are the frequencies predicted by the simple harmonic oscillator approximation to the acoustic potential well for a water drop in the triaxial chamber at JPL and White Sands Test Range, respectively. It is apparant that the simple model used to describe the oscillation is an inadaquate description of the experimental situation. If one extended the approximation to the next higher order, Equation 1 would become

$$\begin{aligned} F_{ac} &= F_o \sin (2kr) \\ &\sim F_c (2kr) (1 - (2kr)^2/6). \end{aligned} \tag{3}$$

Inspecting this equation one would predict that the frequencies of oscillation, which are proportional to the square root of F_{ac}, to decrease slightly and to display some anharmonicity at the furthest distances from the center of the chamber. Even at the maximum excursions this effect on the force is only 6% of the magnitude of the simple harmonic oscillator prediction. The present level of anlysis has been unable to detect the

existence of this term.

Table 5-2: Center of Mass Motion Analysis

coordinate		f_{obs}	Δf	f_{th}(WS)	f_{th}(JPL)
view 1, coord.1	x	0.150Hz	0.076Hz	0.162Hz	0.146Hz
coord.2	z	0.146	0.084	0.154	0.137
view 2, coord.1	x	0.153	0.074	0.162	0.146
coord.2	y	0.144	0.082	0.162	0.146
view 3, coord.1	z	0.139	0.079	0.154	0.137
coord.2	y	0.146	0.085	0.162	0.146

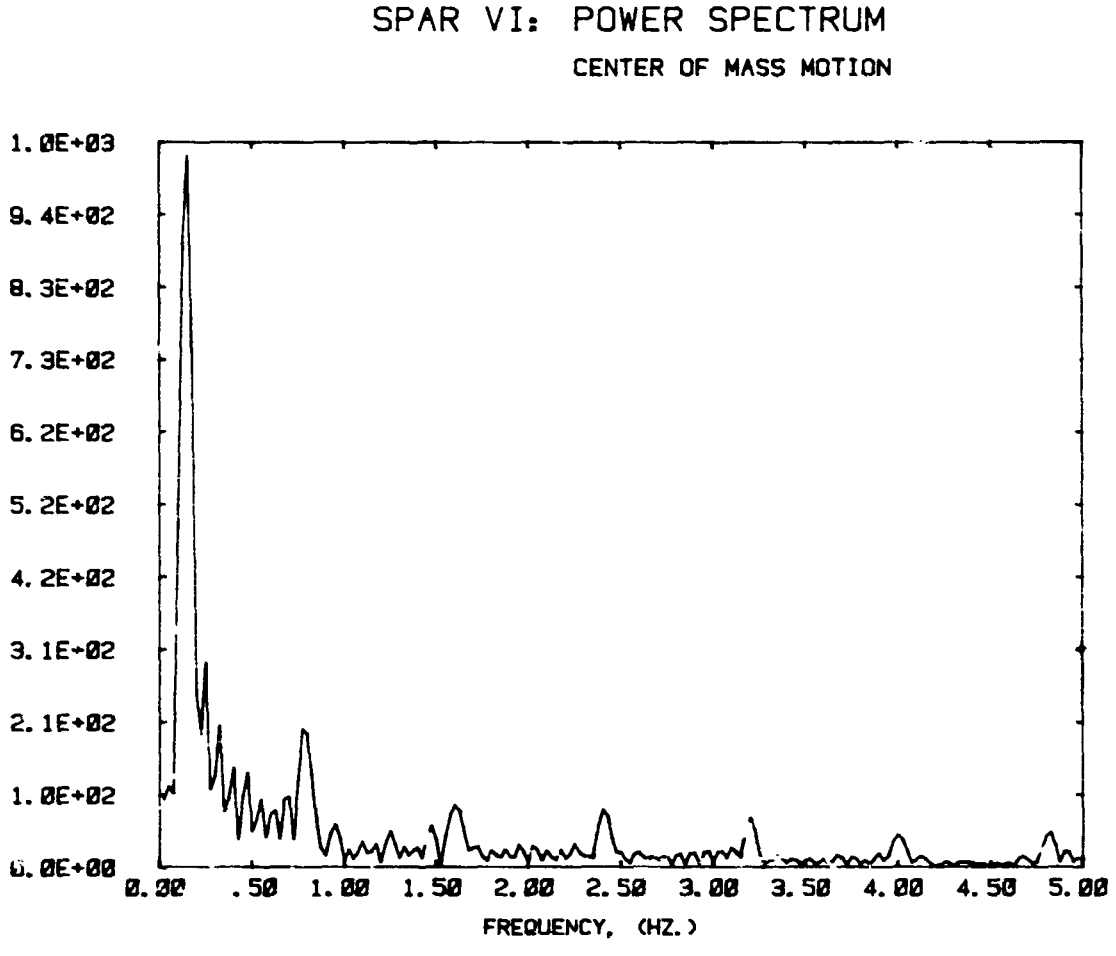

Figure 5-8. Center of Mass Motion in the y-direction. The peak at 0.146 Hz indicates the frequency of the drop's motion in the acoustic potential well. The peaks at integer multiples of 0.80 Hz are the results of the block size used in the data digitization.

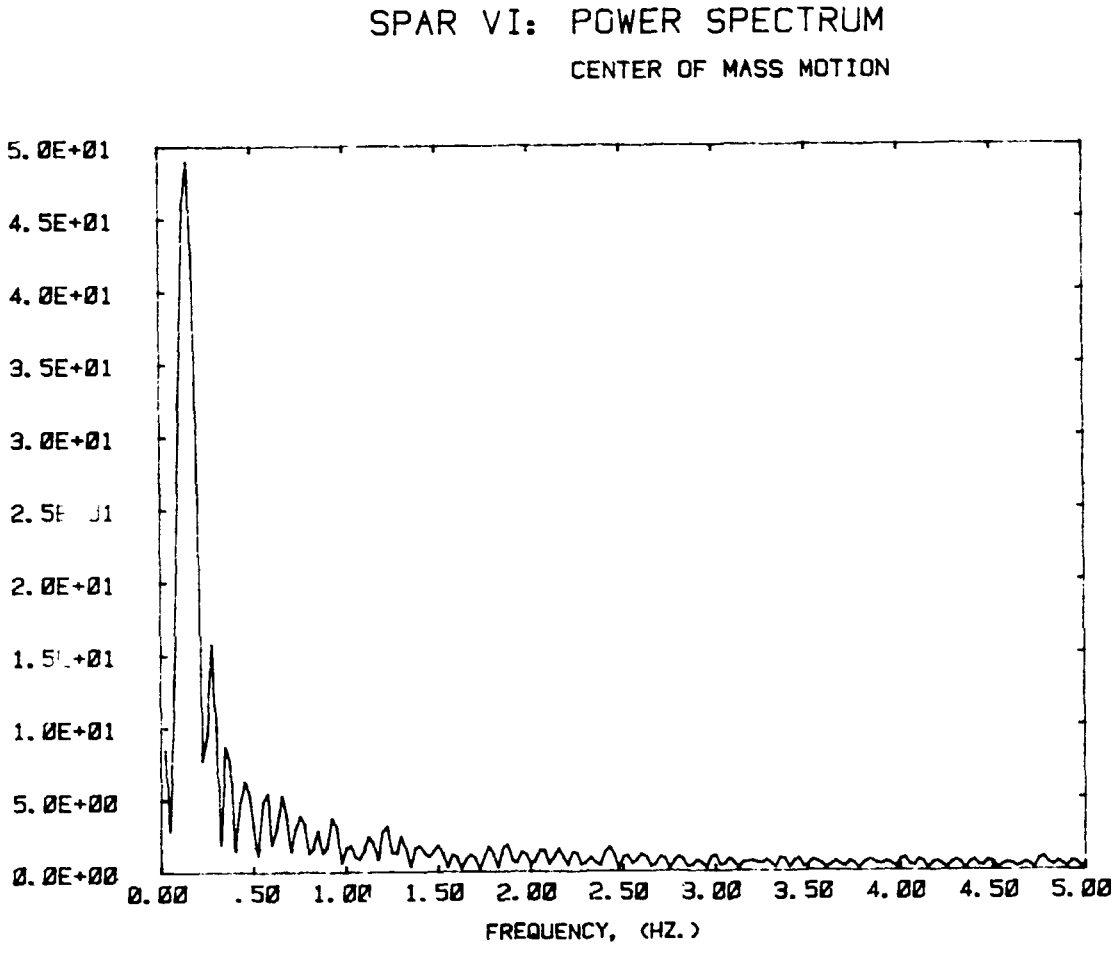

Figure 5-9. Center of Mass Motion in the y-direction. The peak at 0.146 Hz is the frequency at which the drop oscillated in the acoustic well. The effects of the block size have been reduced by incorporating a correction function.

4. Numerical Experiments

Some of the analysis required to study the behavior of the drop in this experiment, such as calculating the power spectrum of an oscillating drop from its digitized boundaries, was fairly complex and had not been handled before. For this reason it was decided to investigate numerical test cases involving the recovery of a known signal in the presence of various amounts of noise. Two such experiments were performed: the first was designed to recover the coefficients of the normal modes of a perturbed boundary, a situation encountered when analyzing the oscillatory motion of a drop. The second numerical experiment was designed to determine the ratio of the major to minor axis of a general perturbed ellipse, a situation encountered when the drop is either distorted by rotation or oscillation.

Normal Mode Analysis of an Axisymmetric Drop

Consider a one-dimensional description in which the drop boundaries are generated by

$$r(\theta) = R(1 + \sum a_n P_n(\cos\theta) + bN) \qquad (1)$$

where $P_n(\cos\theta)$ are the Legendre polynomials of order n, the normal modes of an axially symmetric oscillating drop, and N is a function simulating noise supplied by a random noise generator. In our calculations both uniform and Gaussian random number distributions were used, but only results with the Gaussian distribution are reported here because it is a better model of noise. The approach used was to generate the functions $r(\theta,t)$ for given coefficients a_n and b, and to calculate from these $r(\theta,t)$ the various a_n as functions of given amounts of noise. Fig. 5-8 shows both the component

normal modes used to build up $r(\theta,t)$ and the final outline, with and without noise.

The coefficients $a_n(t)$ were reconstructed in two ways. First, the orthogonality of the Legendre polynomials was used directly with the numerical integration

$$a_m = \int_0^{\pm\pi} r(\theta)\ P_m(\cos\theta)\ \sin\theta d\theta \qquad (2)$$

to recover the coefficients $a_n(t)$. This calculation has been done for a set of characteristic cases and is summarized in Table 5-3. It is seen that for the expected levels of noise (i.e. b $\leq$ 15% of radius) the recovered coefficients are reasonably close to the original values for a sufficient number of data points. When, however, the signal to noise ratio is comparable to 1.0 the input signal is only partially recovered, and other modes which originally had vanishing coefficients appear with nonzero amplitude.

A slightly more accurate approach, avoiding the approximation involved in the numerical integration, is to recover the coefficients of the normal modes a_n by a linear least squares procedure. This scheme generates a linear system of normal equations for the required coefficients a_n, the order being the number of basis functions or modes used in the calculations. The output for the same set of input parameters as used in Table 5-3 is shown in Table 5-4.

Comparison of both sets of data shows that on the whole both methods produce similar results, though the coefficients of the originally nonexistent modes ($n \geq 5$) are systematically smaller in the least squares approach than in the numerical integration method. It must be noted that the

numerical cases tested here are an idealized version of the real situation, and the quantitative estimates generated can only provide an upper limit on the expected accuracy when using a similar analysis for the real data.

An important ingredient in both the numerical work and the subsequent analysis of actual data is to have a substantial library of subroutines available which are capable of being used on the AODC. This required developing or adapting from other sources a number of specific routines, such as an extension of Simpson's integration rule for the case of nonequidistant points, generation of sets of random numbers with either uniform or Gaussian distributions, evaluation of the Legendre associated functions from recursion relations, development of linear least square programs which construct the normal equations and find their solutions, and development of adaquate normal and fast Fourier transforms. More details pertaining to software development can be found in Appendix B.

Ellipse Analysis

As a first approximation to a distorted drop, in which the distortion may be due to oscillation, rotation or a combination of both, we can take an ellipse. In the general situation the ellipse will have its principal axes oriented arbitrarily, and the center of the ellipse will be at some location which is not the origin. For these reasons we use the general form of an ellipse

$$Ax^2 + 2Bxy + cy^2 + 2Dx + 2Ey + F = 0 \qquad (3)$$

In addition, the actual data will also have noise due to the various stages of data digitizing and handling and imperfections in the instrumentation.

Given a set of points (x_i, y_i) describing an arbitrarily positioned noisy boundary, the least squares routine finds the best ellipse which describes them. This procedure involves minimizing the mean square deviation, S, where

$$\begin{aligned} S &= \sum \delta_i^2 \\ &= \sum (Ax_i^2 + 2Bx_iy_i + Cy_i^2 + 2Dx_i + 2Ey_i + F)^2 \end{aligned} \tag{4}$$

Only the ratios

$$a = A/F,\ b = B/F,\ c = C/F,\ d = D/F,\ e = E/F$$

can be determined, and the normal equations for them are

$$\begin{aligned}
(\sum x_i^4)a + (2\sum x_i^3y_i)b + (\sum x_i^2y_i^2)c + (2\sum x_i^3)d + (2\sum x_i^2y_i)e &= -\sum x_i^2 \\
(\sum x_i^3y_i)a + (2\sum x_i^2y_i^2)b + (\sum x_iy_i^3)c + (2\sum x_i^2y_i)d + (2\sum x_iy_i^2)e &= -\sum x_iy_i \\
(\sum x_i^2y_i^2)a + (2\sum x_iy_i^3)b + (\sum y_i^4)c + (2\sum x_iy_i^2)d + (2\sum y_i^3)e &= -\sum y_i^2 \\
(\sum x_i^3)a + (2\sum x_i^2y_i)b + (\sum x_iy_i^2)c + (2\sum x_i^2)d + (2\sum x_iy_i)e &= -\sum x_i \\
(\sum x_i^2y_i)a + (2\sum x_iy_i^2)b + (\sum y_i^3)c + (2\sum x_iy_i)d + (2\sum y_i^2)e &= -\sum y_i
\end{aligned} \tag{5}$$

Solving for a, b, c, d, e, it can be shown that α, the angle between the principal axis of the ellipse and the x-axis, is given by

$$\tan(2\alpha) = \frac{2b}{a-c} \tag{6}$$

and the ratio of the major to the minor axis is

$$\text{ratio} = \sqrt{\frac{a\sin^2\alpha + c\cos^2\alpha - b\sin 2\alpha}{a\cos^2\alpha + c\sin^2\alpha + b\sin 2\alpha}} \tag{7}$$

This procedure was used to study an ellipse which had been generated with various amounts of noise. The noise is simulated by random numbers with a

Gaussian distribution multiplied by a given distortion. The percentage of noise in a given run is given as 2x(maximum distortion)/(mean radius). In addition to the least squares procedure we also used a direct approach, called 'Min/Max', in which the minimum and maximum radius-vectors from an approximate center are found and used to obtain the ratio of the axes and the angle of orientation. While in the case of little or no noise both approaches should be equivalent, in the presence of appreciable noise it is expected that the least squares approach will be superior, as it uses all the data points rather than concentrating on a few selected directions, thus enhancing the signal/noise ratio.

Figure 5-11 illustrates the generation and analysis of an ellipse. Table 5-5 provides the computer outputs for various noise levels. The output consists of the coefficients a, b, and c, as reconstructed by the least squares analysis, and the ratio of axes and the angle of rotation as provided by both methods. Inspection of the results reveals that, as expected, when noisy data are involved the direct Min/Max approach can provide only crude results, and a more sophisticated procedure is required to obtain useful information whenever the level of noise cannot be assumed small.

SPAR VI Numerical Test Case: Normal Mode Analysis

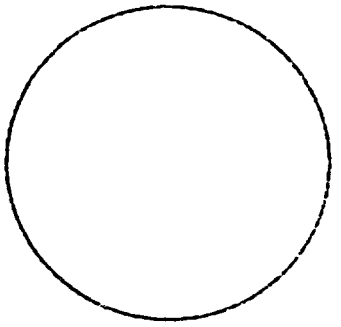

a) Circle

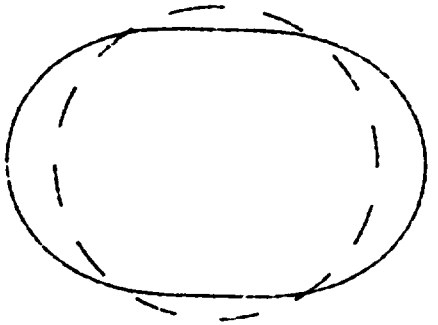

b) n = 2 node (30%)

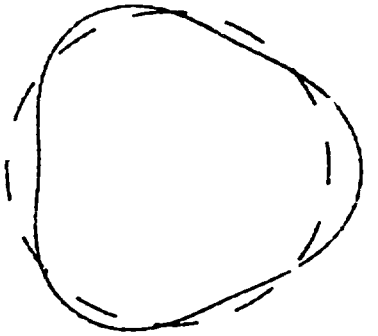

c) n - 3 node (20%)

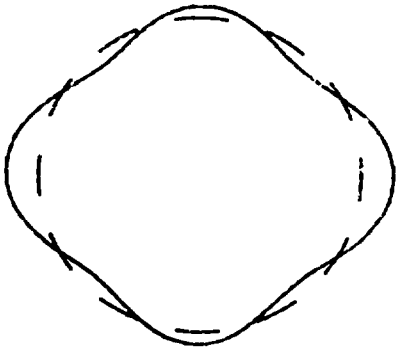

d) n = 4 node (10%)

e) sum of 2, 3, and 4

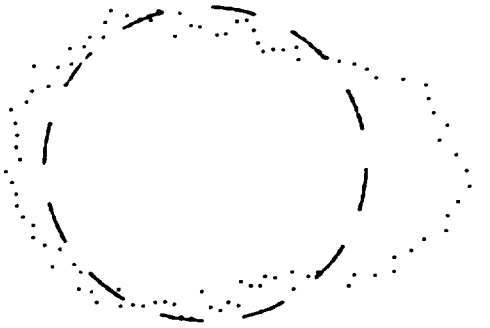

f) sum plus noise

BUILDUP OF NORMAL NODES

SPAR VI Numerical Test Case:
Analysis of a General Ellipse

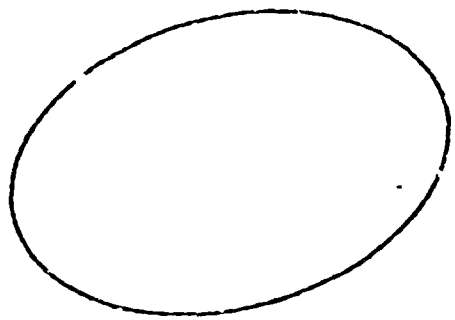

a) ellipse

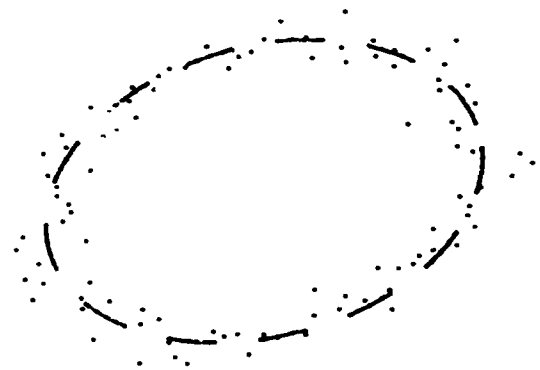

b) original ellipse plus noise

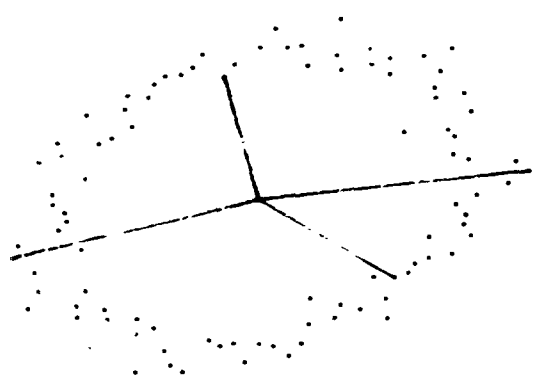

c) min/max method

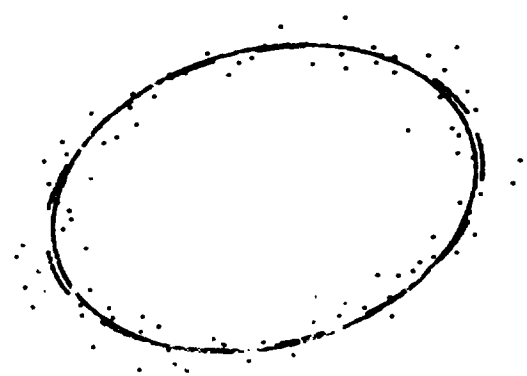

d) least square method

ELLIPSE ANALYSIS

TABLE 5-3. NUMERICAL TEST CASE:

STUDY OF NORMAL MODES BY NUMERICAL INTEGRATION

Input: $r(\theta) = R \left(1 + \sum a_n P_n (\cos \theta) + bN \right)$

Output: $a_m = 1/2 \int_0^{\pi} r(\theta) P_m(\cos \theta) \sin\theta \, d\theta + \int_0^{\pi} r(\theta) P_m(\cos\theta) \sin\theta \, d\theta$

Input Parameters:

$a_1 = 0.0$, $a_2 = 0.3$, $a_3 = 0.2$, $a_4 = 0.1$

$a_n = 0.0$ for $n \geq 5$

100 points

INPUT		RESULTS					
b	b/a_2	a_1	a_2	a_3	a_4	a_5	a_6
0.00	0%	0.000	0.299	0.200	0.099	-0.001	-0.002
0.05	17	0.008	0.302	0.200	0.098	-0.007	-0.015
0.10	33	-0.015	0.270	0.229	0.121	-0.005	-0.013
0.15	50	-0.044	0.275	0.220	0.114	0.012	0.038
0.20	67	0.007	0.314	0.150	0.062	0.091	-0.032
0.25	83	0.026	0.257	0.207	0.114	-0.036	0.062
0.30	100	0.024	0.294	0.138	0.170	0.066	-0.087
0.35	117	0.022	0.326	0.192	0.071	0.077	-0.038

C-3

TABLE 5-4. NUMERICAL TEST CASE:

STUDY OF NORMAL MODES BY LEAST SQUARES ANALYSIS

Input: $r(\theta) = R(1 + \sum a_n P_n(\cos\theta) + bN)$

Output: a_m, where $r(\theta) \sim \sum a_m P_m(\cos\theta)$

Input Parameters:

$a_1 = 0.0$, $a_2 = 0.3$, $a_3 = 0.2$, $a_4 = 0.1$

$a_n = 0.0$ for $n \geq 5$

100 points

INPUT		RESULTS					
b	b/a_2	a_1	a_2	a_3	a_4	a_5	a_6
0.00	0%	0.000	0.300	0.200	0.100	0.000	0.000
0.05	17	0.009	0.305	0.193	0.090	-0.002	0.017
0.10	33	-0.005	0.273	0.218	0.115	0.021	-0.003
0.15	50	-0.030	0.283	0.188	0.095	0.042	-0.003
0.20	67	0.012	0.302	0.128	0.081	0.054	-0.018
0.25	83	0.032	0.253	0.211	0.130	0.014	0.009
0.30	100	0.035	0.276	0.120	0.201	0.033	-0.053
0.35	117	0.021	0.297	0.179	0.093	0.025	-0.009

TABLE 5-5. NUMERICAL TEST CASE: ANALYSIS OF A GENERAL ELLIPSE

Input: $Ax^2 + 2Bxy + Cy^2 + 2Dx + 2Ey + F + \delta N = 0$

Output: 1. Least Squares Method: find a, b, c such that

$$ax^2 + 2bxy + cy^2 \sim 1$$

α_{ls}, orientation angle

β_{ls}, ratio of major to minor axis

2. 'Min/Max' method: α_{mm}, orientation angle

β_{mm}, ratio of major to minor axis

Input Parameters:

Axes: 30 and 20. Angle: 15^o. Offset: (250,66).

Number of points: 100

(these correspond to A=0.0048, B=0.0014, C=0.0096, D=0.1125)

INPUT	OUTPUT						
δ	a	b	c	α_{ls}	β_{ls}	α_{mm}	β_{mm}
0%	-0.0048	0.0014	-0.0096	15.000	1.500	15.000	1.500
12	-0.0048	0.0014	-0.0096	14.966	1.502	15.642	1.519
24	-0.0048	0.0014	-0.0096	15.109	1.511	15.776	1.553
36	-0.0048	0.0015	-0.0091	17.280	1.477	25.285	1.424
48	-0.0047	0.0011	-0.0089	14.038	1.449	15.309	1.507
60	-0.0046	0.0011	-0.0087	14.363	1.436	2.302	1.624

5. Acoustically Induced Oscillation

The amplitude modulation of the acoustic pressure field along the z axis was swept from 2.3 Hz to 2.9 Hz over a two minute period, so as to contain the expected resonance frequency, 2.6 Hz, with a sufficient safety margin. The drop began oscillating in the n = 2 normal mode during the first few seconds as intended. However, as the amplitude became very large very quickly the regularity deteriorated and rotation set in.

119 frames were digitized in this short period of regular response corresponding to 2.5 seconds. The sample frame shown in Figures 5-1 and 5-2 is from this sequence. This analysis attempted to characterize the development of the n=2 normal mode of oscillation as a function of time by studying the boundary of the drop, specifically the coefficient $a_2(t)$ where

$$a_2(t) = \frac{5}{2R} \int_0^{\pm\pi} r(\theta,t)\, P_2(\cos\theta)\, \sin\theta\, d\theta \ . \qquad (1)$$

This parameter can be obtained in one of the following ways:

1. Direct Numerical Integration. The z axis was used as the polar axis because the forcing modulation was in that direction. The boundary in each of the side views provides two values of a_2 one for the boundary between 0 and π and one between 0 and $-\pi$). The boundaries provided by the side views correspond to two orthogonal azimuthal angles. In the main view the angular dependence is that of the azimuthal angle. Figure 5-11 shows the digitized boundaries of frame #955 and the actual coordinate axes. This method encountered several nontrivial problems which had to be overcome before proceeding with the analysis. This entailed corrections when possible and alternative approaches for determining a_2 or related quantities when not.

2. General Ellipse Analysis. The dominant mode $P_2(\cos\theta)$ when superimposed upon an equilibrium circle can be loosely approximated by an ellipse (see Jacobi, Barmatz, 1979) with major and minor semi-axes a and b, having the ratio

$$\frac{a}{b} = \frac{R(1 + a_2 P_2(\cos 0))}{R(1 + a_2 P_2(\cos(\pm\pi/2)))} = \frac{1 + a_2}{1 - (a_2)/2} \qquad (2)$$

where we have used the relation $P_2(\cos(\pi/2)) = - P_2(\cos(0))/2 = - 1/2$ with $P_2(\cos\theta) = (3\cos^2\theta - 1)/2$. This relation can be inverted to express a_2 in terms of the observed a/b ratio

$$a_2 = \frac{(a/b)-1}{(a/b)/2 + 1} \qquad (3)$$

3. The VerHor Method. An approach similar to the Min/Max routine (discussed in Section 5.4) was employed as the lowest order method. In it the distances from the center of mass to the boundary along the vertical and horizontal axes are determined. As long as the drop's behavior remains regular this approach will indicate the growth of amplitude of the oscillation. To minimize the effects of noise from any source the data were smoothed quadratically over nine points before the distances were determined.

Analysis could stop here or if success with the other two procedures proved elusive the ratio (vertical distance)/(horizontal distance) could be related to a/b in a piecewise fashion and equation (3) used to find a value of a_2.

Results

Because apparantly good results were obtained with the integration routine, the other two approaches were used only to provide qualitatinve confirmation of the former's behavior.

The VerHor Method did provide information which illustrated the buildup of the amplitude of disortion of the drop boundary from a circle. Fig. 5-12 shows this clearly. Recall that the modulating frequency of the driver and hence the drop was being swept from 2.30 Hz at 145 seconds to 2.31 Hz at 147 seconds. Fig. 5-13 shows the same data analysed in the frequency domai. Because a constant block size was used in the digitization process, a signal with a period of twenty frames was generated; this corresponds to a frequency of 2.40 Hz. This is unfortunate because the drop's response should be the same as the forcing frequency i.e., 2.30 Hz. Because of the finite number of data the best resolution obtainable is that shown in Fig. 5-13, i.e., expanding the frequency scale does not help to seperate the peaks. Also because of the poor time/frequency resolution the anticipated buildup as the resonance was approached was observable on the film but has eluded quantitative description.

Results from the general ellipse analysis were similar in form to those of VerHor and so are not presented. Because of their determination of minimum and maximum semi-axes they are confusing to study because the axis of orientation of the major axis when the drop is elongated differs by 90° from that when the drop is flattened.

The numerical integration scheme provided direct evaluation of $a_2(t)$ and $a_0(t)$ from the data. There were four values of each per frame because the boundaries in the side views were integrated from 0 to both $\pm \pi$ (see Fig. 5-

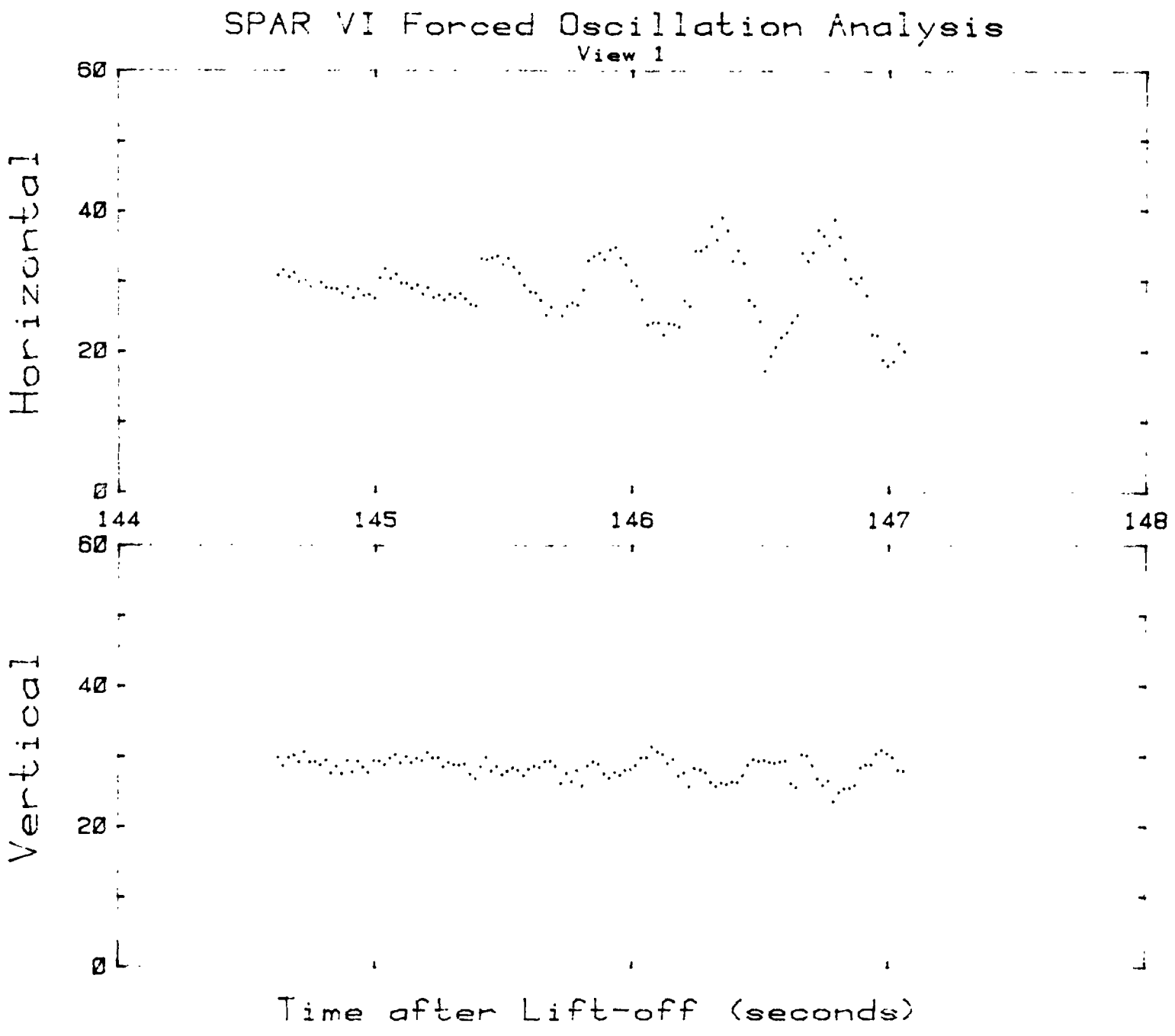
SPAR VI Forced Oscillation Analysis
View 1
Horizontal
60
40
20
0
144
145
146
147
148
Vertical
60
40
20
0
Time after Lift-off (seconds)

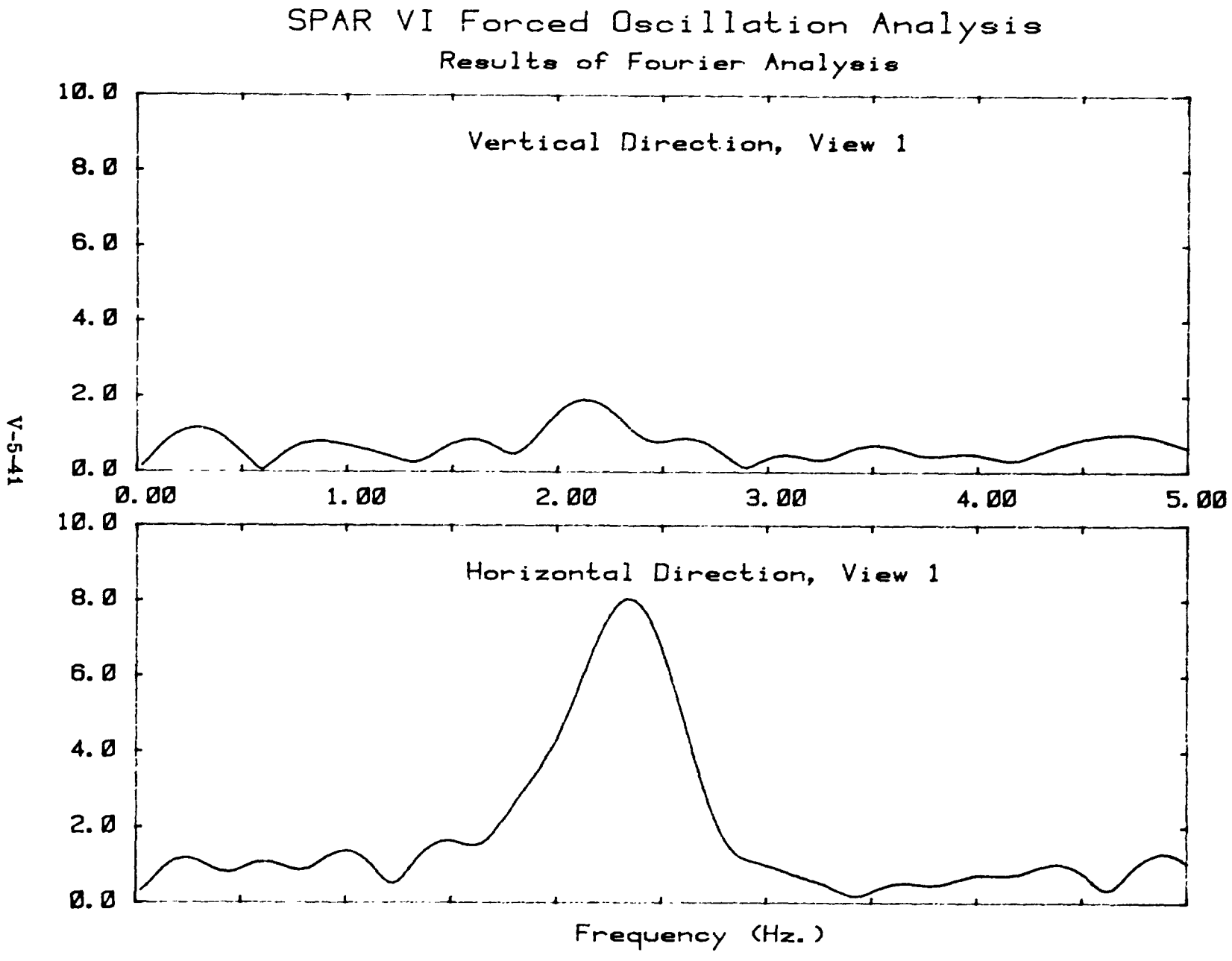
SPAR VI Forced Oscillation Analysis
Results of Fourier Analysis
Vertical Direction, View 1
10.0
8.0
6.0
4.0
2.0
0.0
0.00
1.00
2.00
3.00
4.00
5.00
Horizontal Direction, View 1
10.0
8.0
6.0
4.0
2.0
0.0
Frequency (Hz.)

14). The plot of a_0 in the time domain clearly shows the block behavior of the data; in the frequency domain this feature manifests itself as a peak at 2.4 Hz and a secondary peak at twice that frequency (see Fig. 5-15). As noted above, this behavior caused problems because the region of interest was centered about 2.3 Hz.

To minimize the block size problem, the $a_0(t)$ were used to normalize the $a_2(t)$ for the same view and appropriate half of the boundary. This was thought valid since both integrals were divided by the same radius factor R(t). As R(t) decreases from frame to frame within a given block, dividing a_2 by a_0 should help to cancel the effect and enhance the the desired signal. Figure 5-16 shows the results of this procedure. Similarly the vertical and horizontal dimensions found in the VerHor Method can be divided to eliminate the block size problem; the results are shown in Fig. 5-17. The large width of the peaks is due to the small number of data points.

The buildup was expected to be related to the damping coefficient, β_2, and to have the same order of magnitude. For the expected value of $\beta_2 \sim$ 0.036/sec the time constant of the response should have been roughly 28 seconds. This discrepancy can either be attributed to an underestimation of the force due to the acoustic modulation or to an unexpected interaction of the modulated acoustic fields with each other and the drop.

The cause of the rotational instability which developed 2 seconds onto the forced oscillation sequence is not understood very well at the present time. The acoustic field in which the drop finds itself is fairly complicated. Its components along each axis are modulated: there is amplitude modulation along the z axis, and complementary modulation along the x and y axes. In addition, the drop undergoes a continuous low-frequency

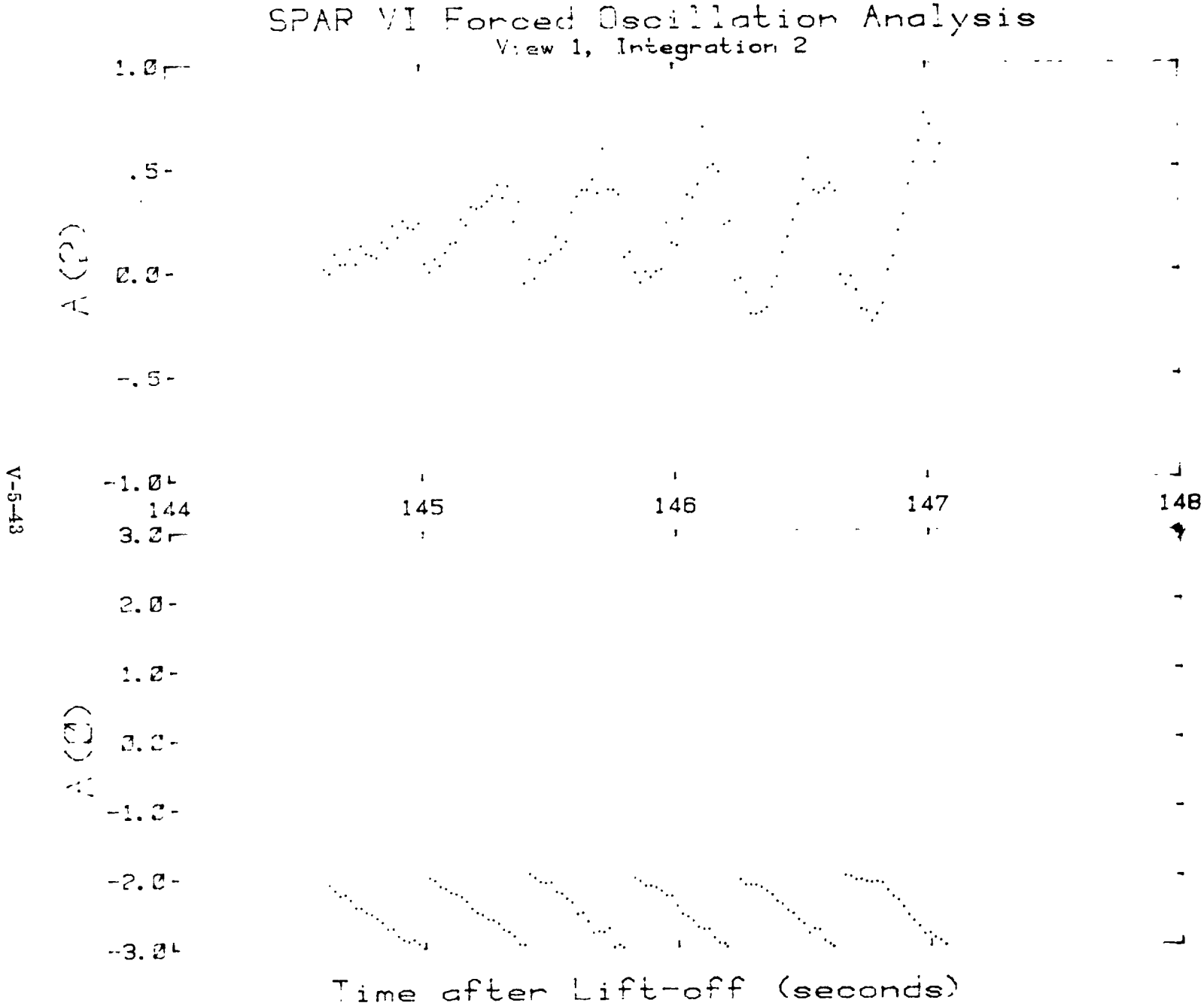
SPAR VI Forced Oscillation Analysis
View 1, Integration 2
1.0
.5
0.0
-.5
-1.0
144
145
146
147
148
3.0
2.0
1.0
0.0
-1.0
-2.0
-3.0
Time after Lift-off (seconds)

SPAR VI Forced Oscillation Analysis

Results of Fourier Analysis

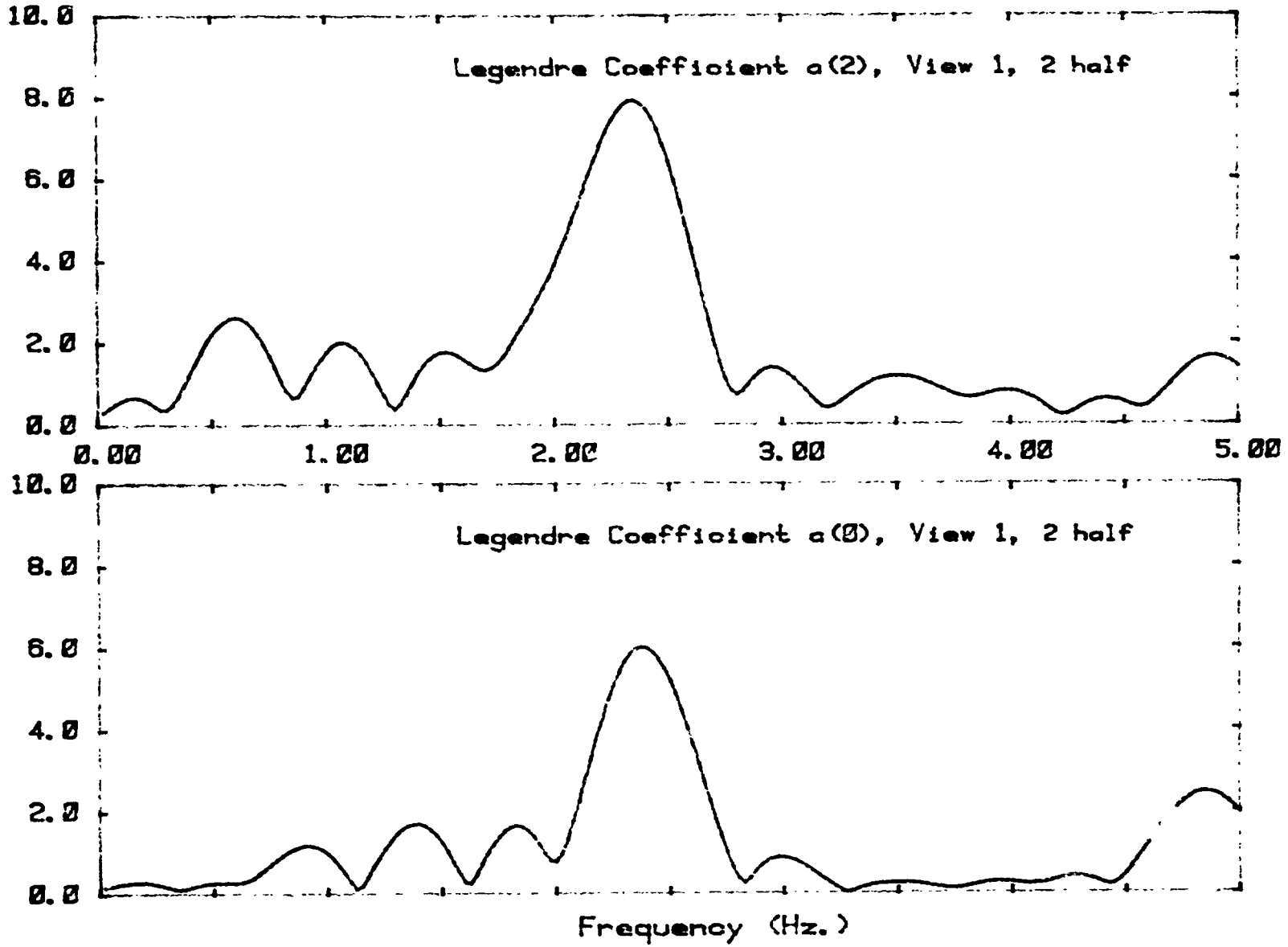

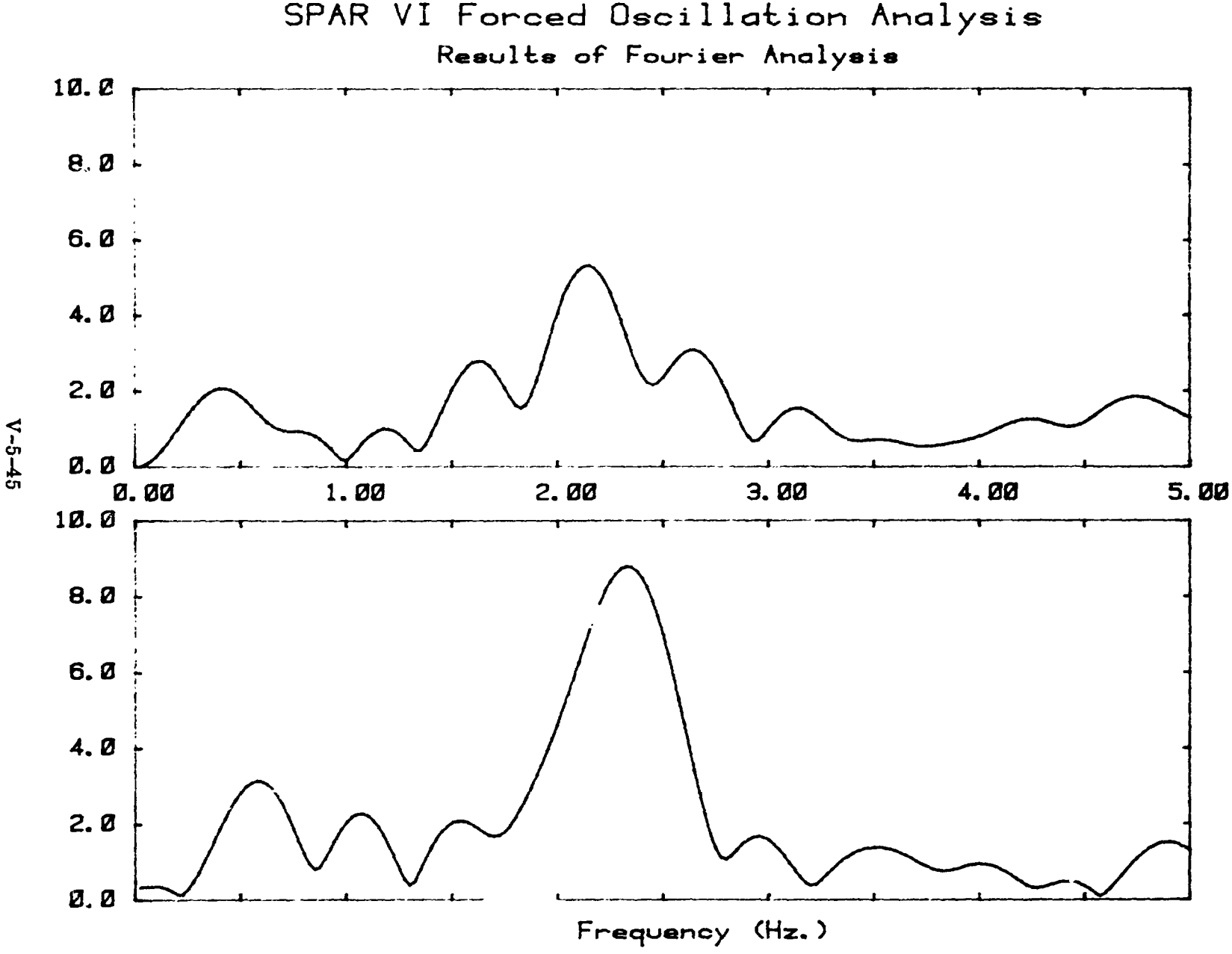
SPAR VI Forced Oscillation Analysis
Results of Fourier Analysis
10.0
8.0
6.0
4.0
2.0
0.0
0.00
1.00
2.00
3.00
4.00
5.00
10.0
8.0
6.0
4.0
2.0
0.0
Frequency (Hz.)

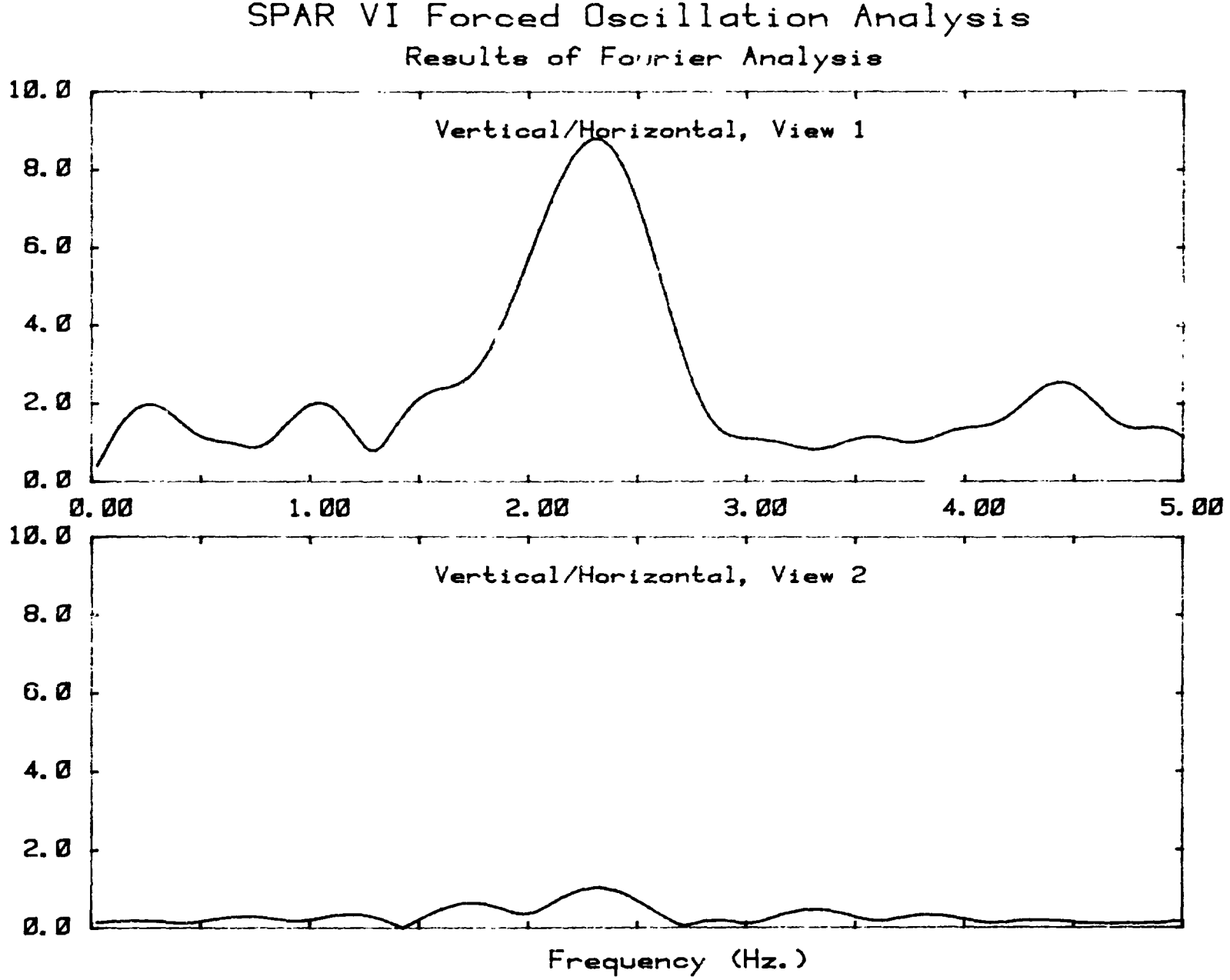
SPAR VI Forced Oscillation Analysis
Results of Fourier Analysis
Vertical/Horizontal, View 1
10.0
8.0
6.0
4.0
2.0
0.0
0.00
1.00
2.00
3.00
4.00
5.00
Vertical/Horizontal, View 2
10.0
8.0
6.0
4.0
2.0
0.0
Frequency (Hz.)

center-of-mass motion in this complex potential field. Solving the equations of motion for such a drop (see Section 4.3, in which a simple case was described) is not trivial, but must be attempted to provide some insight into the question of whether such an off-center drop will experience an effective torque in the given acoustic field. Another experimental investigation in which the drop is better stabilized and centered is obviously called for.

The onset of rotation can also be a result of the oscillation amplitude attaining a substantial value. Such a rotation has been observed in the laboratory (Trinh and Wang, 1981) during large amplitude steady-state oscillations, in which a running wave appeared on the drop surface and subsequently developed into solid-body rotation of the entire fluid.

The origin of this instability is not yet clear. It might be associated with the characteristics of large-amplitude oscillations, but it could also arise because of the asymmetry and misalignment of the drop in the acoustic field. Analysis reveals that such a destabilizing torque should arise when the drop response lags the oscillation drive in phase by an angle larger than 90°, a situation which would arise with a drive frequency larger than the drop resonance frequency. This is not the situation in the experiment at the onset of the rotation. At the present time it is not possible to tell what the phase relation was between the forcing modulation and the drop's response to it.

6. Acoustically Induced Rotation

For the thirty seconds of induced rotation (1600 frames on the film) every fifth frame was digitized, resulting in 320 frames to be analyzed. The expectation was that the drop's appearance in the main view, for which the line of view coincided with the axis of rotation, would be circular, while in the side views it would appear circular initially and become gradually more and more elliptical. All three views of the 320 frames were analyzed by the procedure which characterized a general ellipse outlined in the second half of Section 5.4. This was done both for the raw data and for quadratically smoothed data. In the smoothing procedure used (Hamming 1977) it was assumed that each set of points could be described approximately by a quadratic function (unlike averaging, which assumes a linear dependence and does not allow for curvature). In the calculations we used 9-point quadratic smoothing, in which the original boundary point x_n is replaced by

$$\bar{x}_n = \{59x_n+54(x_{n-1}+x_{n+1})+39(x_{n-2}+x_{n+2})+14(x_{n-3}+x_{n+3})-21(x_{n-4}+x_{n+4})\}/231 \quad (1)$$

The first study of the digitized rotation data was using the Min/Max routines described in Section 5.4, in which the greatest and least distances between the data and the center of mass were found for each half of the boundary. The ratio of the sums of the greatest to least distance is a crude indicator of the ratio of major to minor axes. Also, an angle was found from the four extreme points which characterized the orientation. The results of this analysis for one of the side views are contained in Figs. 5-18 and 5-19. Fig.5-18 is the result of the analysis performed on the raw data while Fig.5-19 shows the same for the smoothed data. The quality of the smoothed data is only slightly better than that of the raw data sets. Note the slow increase

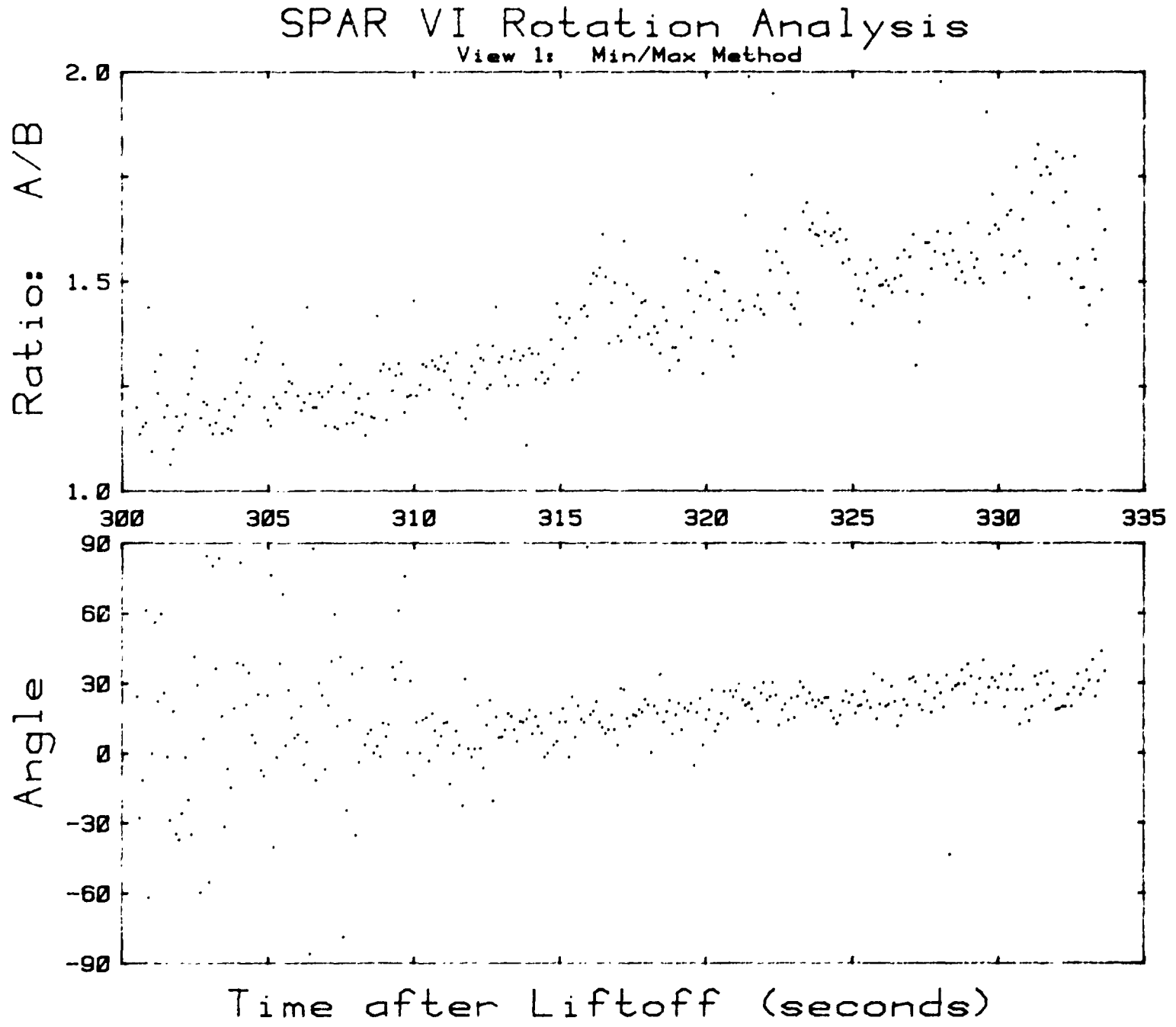
SPAR VI Rotation Analysis
View 1: Min/Max Method
Ratio: A/B
2.0
1.5
1.0
300
305
310
315
320
325
330
335
Angle
90
60
30
0
-30
-60
-90
Time after Liftoff (seconds)

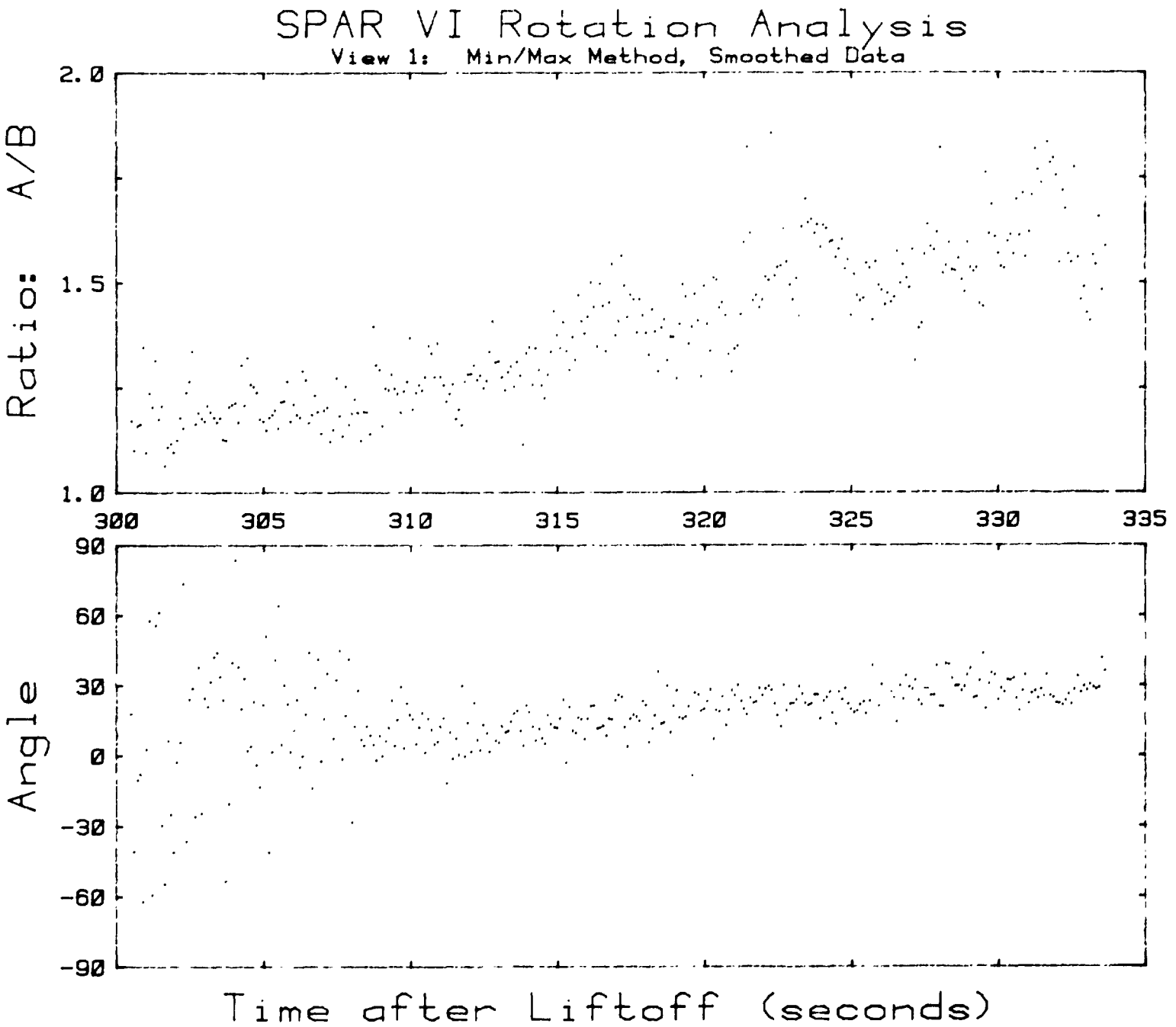
SPAR VI Rotation Analysis
View 1: Min/Max Method, Smoothed Data
Ratio: A/B
2.0
1.5
1.0
300
305
310
315
320
325
330
335
Angle
90
60
30
0
-30
-60
-90
Time after Liftoff (seconds)

in a/b in both. This corresponds to the flattening of the drop as the acoustic torque causes it to rotate faster. Before 310 seconds the wide scatter in the angle data reflects the fact that the drop was still oscillating as a result of the forced oscillation sequence.

The more accurate least squares method was also used. Examples of the results from it are shown in Figures 5-20,5-21 and 5-22. Fig. 5-20 shows the least squares results on the same boundaries as shown in Fig. 5-19. The basic features are the same, only the scatter of the points appears somewhat less for the least square analysis. For view 1 (Fig. 5-20) the a/b ratio starts from 1.0 and gradually builds up, reaching a level a/b ~ 1.5 at the end of the rotation sequence (330 sec). During the available few seconds of spin down there is a dramatic reduction of a/b, seeming to tend back to 1.0 rather quickly. The peak value of a/b is consistent with the result of the Vanguard analysis in Section 5.2, and comparison with the theoretical results of Chandrasekhar and Ross gives a rotational parameter $\Sigma \sim 0.3$, which is rather close to the value of the first bifurcation point. This suggests that spending a little longer on the spin up sequence, or applying a somewhat larger acoustic torque might produce non-axially symmetric equilibrium shapes. Though the general trend is proper, the data show an oscillatory structure, due to both the center of mass motion and the oscillations and tation caused by the previous sequence.

Fig. 5-21 illustrates the behavior along the intended axis of rotation. The ratio a/b is very close to 1.0 and decreases slowly towards that value. The fact that a/b is displaced from 1.0 could be the result of asymmetry between the x and y axes. The fact that there appears to be a definite angle of orientation further indicates a lack of circularity but the clustering of

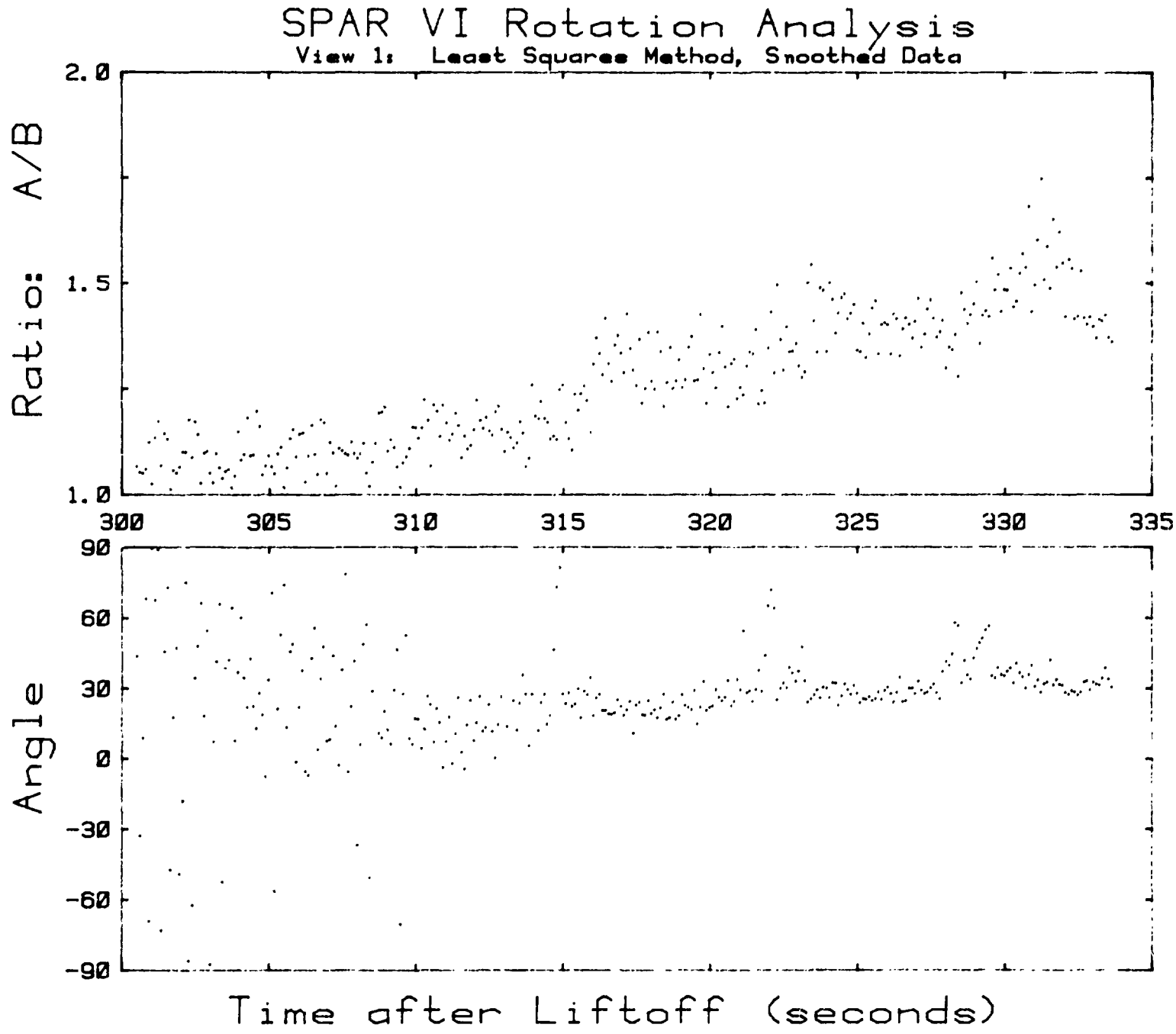
SPAR VI Rotation Analysis
View 1: Least Squares Method, Smoothed Data
Ratio: A/B
2.0
1.5
1.0
300
305
310
315
320
325
330
335
Angle
90
60
30
0
-30
-60
-90
Time after Liftoff (seconds)

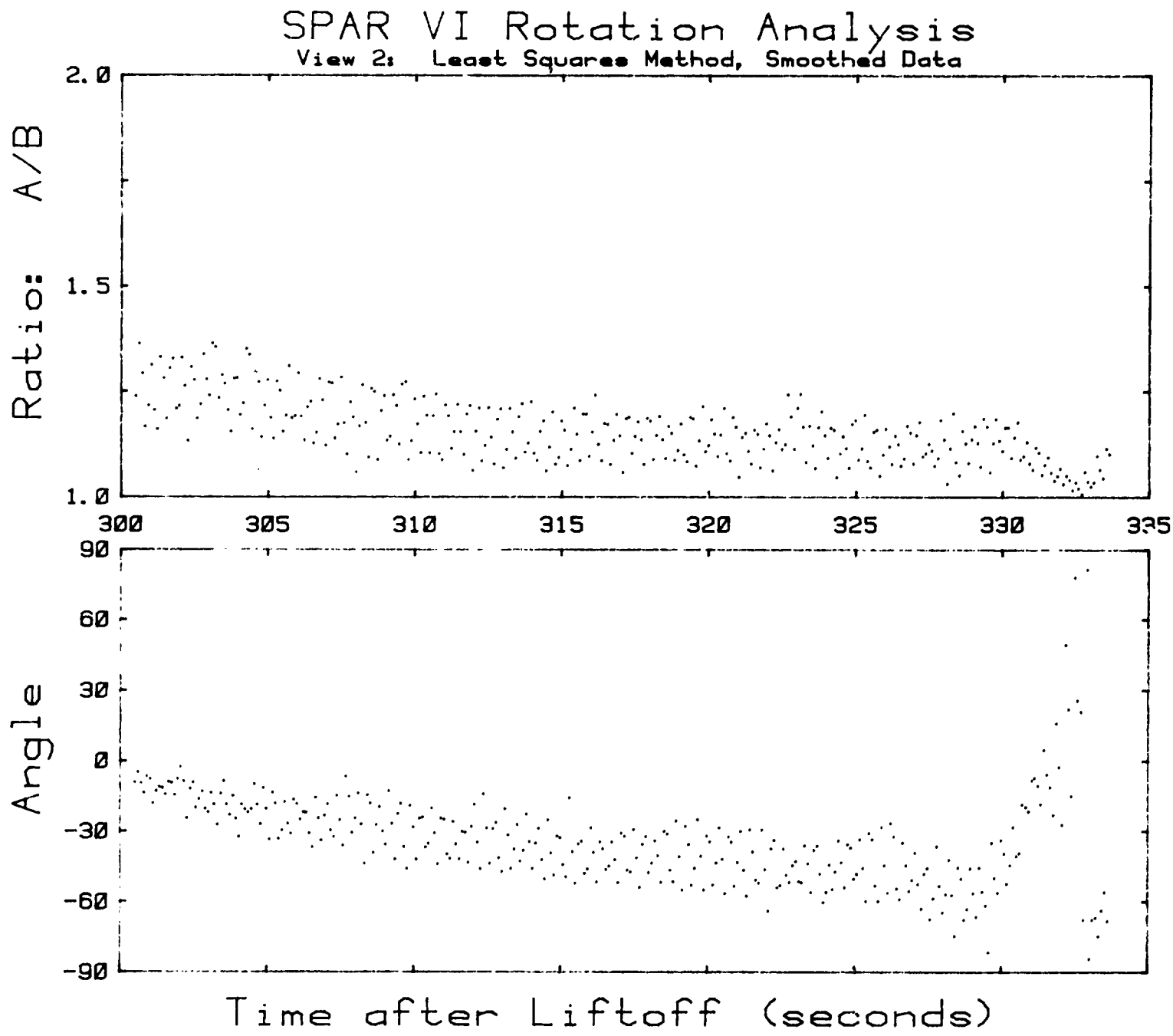
SPAR VI Rotation Analysis
View 2: Least Squares Method, Smoothed Data
Ratio: A/B
2.0
1.5
1.0
300
305
310
315
320
325
330
335
Angle
90
60
30
0
-30
-60
-90
Time after Liftoff (seconds)

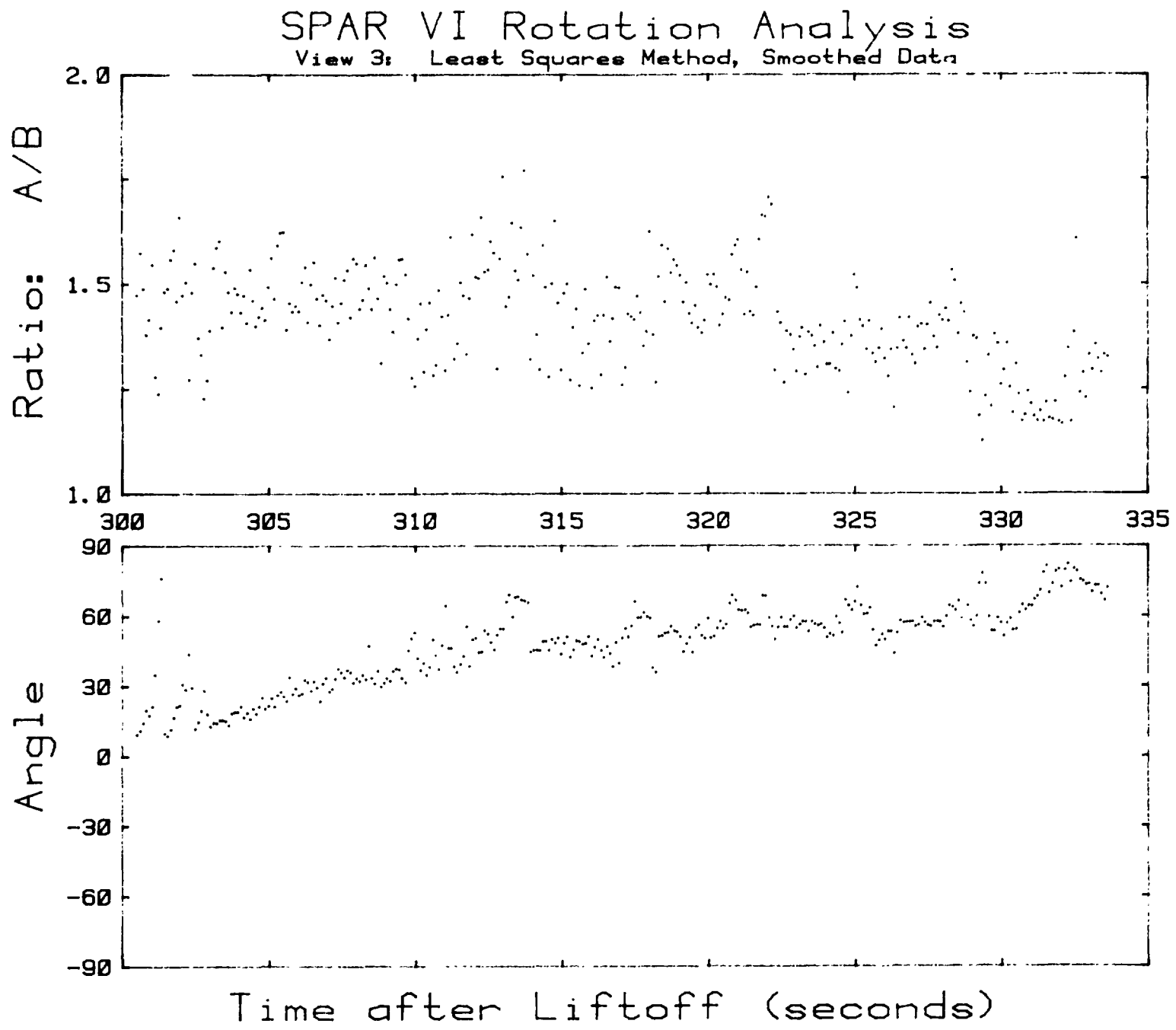
SPAR VI Rotation Analysis
View 3: Least Squares Method, Smoothed Data
Ratio: A/B
2.0
1.5
1.0
300
305
310
315
320
325
330
335
Angle
90
60
30
0
-30
-60
-90
Time after Liftoff (seconds)

the data is intriging because it is unexpected.

For completeness, Fig. 5-22, the results of the least squares analysis performed upon the third view is included. For some reason its patterns do not indicate the build up of rotation that the other two views did.

In views 1 and 3 the axes of orientation during rotation were roughly 20^{o} and 60^{o} respectively. The fact that they are not 0^{o} and 90^{o} is a result of the angle of viewing not being parallel to the appropriate chamber axes. The appearances of systematic spikes in the data of the several views is being investigated to check for correlation with digitization block size or g-jitter.

An attempt was made to push the analysis one step further. A drop held together by surface tension rotating as a solid body can be described by several parameters which can be related to parameters easily obtainable from the described data analysis: The rotation parameter, Σ, which is proportional to the square of the angular velocity can be obtained from the ratio a/b from the side views. A relative equatorial area can be found from the product ab from the main view. A curve relating these two parameters has been constructed from the theoretical results of Chandrasekhar (1965), Ross (1968), and Brown (1979). This curve has an axisymmetric trunk (in which the shape is symmetric about the polar axis) and two branches which correspond to lobed shapes. The bifurcation point for the two-lobed family occurs at $\Sigma = 0.313$ and for the three-lobed family at $\Sigma = 0.500$. Figure 5-23 reproduces their data. For the slower rotation rates

$$\Sigma = 0.674 - 0/178(a/b) - 0.522(a/b)^{2} \qquad (1)$$

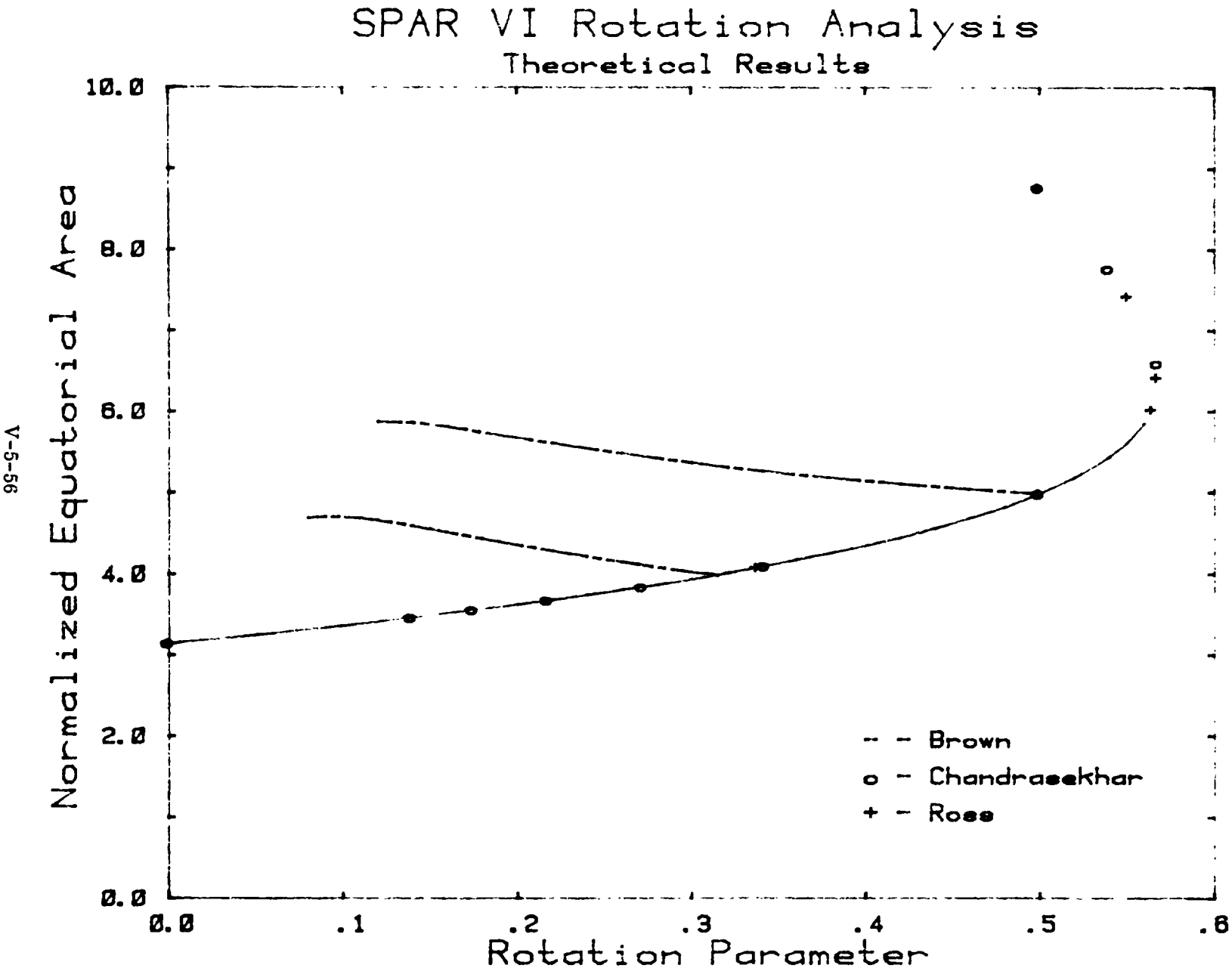
SPAR VI Rotation Analysis
Theoretical Results
Normalized Equatorial Area
10.0
8.0
6.0
4.0
2.0
0.0
0.0
.1
.2
.3
.4
.5
.6
Rotation Parameter
- - Brown
o - Chandrasekhar
+ - Ross

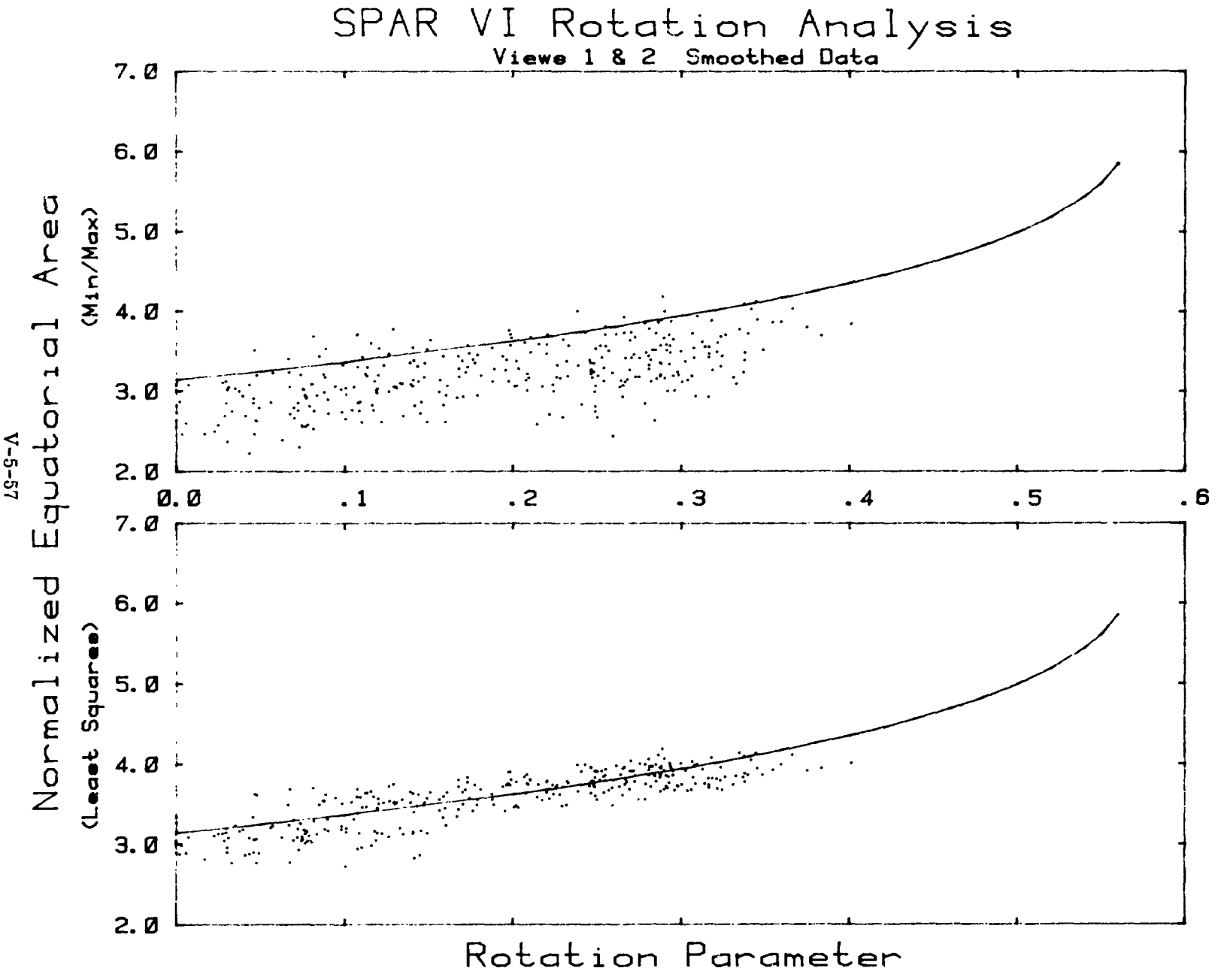
SPAR VI Rotation Analysis
Viewe 1 & 2 Smoothed Data
Normalized Equatorial Area
(Min/Max)
(Least Squares)
7.0
6.0
5.0
4.0
3.0
2.0
0.0
.1
.2
.3
.4
.5
.6
Rotation Parameter

Using the least squares routine on the data of view 2 to give a values of the product ab and and the view 1 data for the same frame to give a/b and hence Σ. Only qualtitative comparisons can be made as the resting radius and the center of mass motion have not be folded in. The results are shown in Fig. 5-24 along with part of the theoretical curve. The agreement between these measurements, performed for the first time under conditions similar to the standard theoretical assumptions, and theory is very encouraging. This calls for more study and experimentation in this direction.

SECTION 6

CONCLUDING REMARKS

Some conclusions can be drawn from the work described above; these conclusions both summarize the effort made so far and should have some impetus on future experiments.

We have achieved the objectives of this experiment successfully. The drop was deployed and acoustically manipulated as planned. Some more specific remarks are in order.

1. As to forced oscillations, there is no satisfactory qualitative understanding of the initially strong oscillation (at 2.3 Hz rather than 2.5 Hz) with the subsequent highly irregular motion which is a superposition of oscillation and rotation. One likely possibility is that an off-center drop in a complicated pressure field (all three axes are excited and modulated in different ways), accompanied by large amplitude motion, would experience an effective torque. In the present experiment the initial low-frequency center-of-mass motion persisted throughout the entire experiment, and most probably affected the complicated outcome. Obviously, this experiment should be repeated in a situation in which the drop is initially better stabilized.

2. As to rotation, the first bifurcation point was almost reached in only thrity seconds of rotation. Since equilibrium has not yet been reached, this means that spending more time on the rotation sequence or increasing the torque by using a higher sound pressure might take the drop beyond the first bifurcation point. In particular, such an experiment would show whether non-

axially symmetric equilibrium shapes are excited beyond the first bifurction point. We note the excellent agreement between the observations of the experiment, performed for the first time under conditions consistent with the assumptions made in the theoretical treatments of Chandrasekhar, Ross and Brown.

3. Concerning tthe IPL digitization, existing programs were used with very minor modifications. We feel that with some more software development IPL could supply us with more useful information from the same quality film. This activity will be pursued when it becomes necessary again to digitize whole drop boundaries.

4. Finally, the analysis presented here pertains to some key features in the film. Several sequences of the film have been processeed but not yet analyzed, and those that were must be compared in more detail with theory. These activities will be vigorously pursued in the near future. Results of these analyses will be presented in publications and meetings later this year and next year.

SECTION 7

REFERENCES

Brown, R., The Shape and Stability of Three-Dimensional Interfaces, Ph.D. Thesis, U. of Minnesota, 1979.

Busse, F., and Wang, T. G. , 'Torque Generated by Orthogonal Acoustic Waves - Theory,' (to be published, JASA 1981).

Carnahan B., Luther, H. A., and Wilkes, J. O., Applied Numerical Methods, Wiley, 1969.

Chandrasekhar, S., 'The Stability of a Rotating Liquid Drop,' Proc. Roy. Soc. 286A, 25 (1965).

Frost, R. T., Stockhoff, E. H., and Wouch, G., 'Electromagnetic Containerless Melting and Solidification,' Proceedings of the Third Space Processing Symposium (1974).

Goldberg, A. Z., 'Acoustic Radiation Pressure,' L. D. Rozenberg (ed.), High Intensity Ultrasonic Fields, Plenum Press, New York, 1971.

Hamming, Digital Filters, Prentice-Hall, New Jersey (1977).

Jacobi, N., Tagg, R. P., Kendall, J. M., Elleman, D. D., and Wang, T. G., 'Free Oscillations of a Large Drop in Space,' AIAA Paper 79-0225 (1979).

Jacobi, N., Barmatz, M., 'Equilibrium Shapes of Acoustically Levitated Liquid Drops,' Proceedings, IEEE Ultrasonics Symposium, 476 (1979).

King, L. V., 'On the Acoustic Radiation Pressure on a Sphere,' Proc. Roy. Soc. 147, 212 (1934).

Lamb, H., Hydrodynamics, 6th ed., Dover, 1932.

Landau, L. D., and Lifshitz, E. M., Fluid Mechanics, Pergamon Press, 1959.

Leung, E., Jacobi, N., Wang, T., 'Acoustic Radiation Force on a Sphere in a Resonance Chamber,' (to be published, JASA 1981).

Morse, P. M., Vibration and Sound, 2nd ed., McGraw-Hill: New York, Toronto, London, 1948.

Nyborg, W. L., 'Acoustic Stream. ,' in Physical Acoustics, vol. 11B, pp. 265-337 (W. P. Mason, ed.). Academic Press: New York and London, 1965.

Nyborg, W. L., 'Radiation Pressure on a Small Rigid Sphere,' J. Acous. Soc. Am. 25, 947 (1967).

Prosperetti, A., 'On the Oscillations of Drops and Bubbles in Viscous Liquids,' Proceedings Intern. Colloq. on Drops and Bubbles, Caltech - JPL, 357 (1974).

Ross, D. K., 'The Shape and Energy of a Revolving Liquid Mass Held Together by Surface Tension,' Aust. J. Phys., 21, 823 (1968).

Trinh E., Wang, T.,'Large Amplitude Shape Oscillations: An Experimental Approach,' (to be published, J.Fl.Mech. 1981)

Wang, T. G., Saffren, M. M., and Elleman, D. D., 'Acoustic Chamber for Weightless Positioning,' AIAA Paper 74-155, (1974).

Wang, T. G., Saffren, M. M., and Elleman, D. D., 'Drop Dynamics in Space,' Progress in Astronautics and Aeronautics, vol. 52 AIAA (1977).

Wang, T. G., and Kanber, H., 'Nonlinear Acoustic Torque in an Intense Sound Field,' J. Acous. Soc. Am., 64, S.14 (1977).

Wang, T. G., Kanber, H., and Rudnick, I., 'First Order Acoustic Torques and Spin Velocities of Solid Bodies in Intense Sound Fields,' Phys. Rev. Lett., 38, 128 (1977).

Wang, T. G., Kanber, H., and Olli, E., 'Fourth Order Acoustic Torque in Intense Sound Fields,' J. Acous. Soc. Am.,63, 5 (1978).

APPENDIX A

COMPUTER DATA TRANSLATION PROGRAM

In order to analyze the data prepared by JPL's Image Processing Laboratory (IPL), it was necessary to develop a program for use on the Univac 1100/81 computers at JPL which would correctly read the data provided on magnetic tape by IPL. This data was in the form of positive integers. This simplified the task of interpreting the data because the program to interpret IPL's data did not have to be designed to keep track of flags for negative signs, mantissas, or exponents. However, the task was complicated by IPL's choice to encode the data on the tapes in binary encoded octal as opposed to either a 7- or 9-bit ASCII format.

The major reason this choice was a problem is the difference between the way in which Digital Equipment Corporation (DEC) and Sperry-Rand have defined words of memory in their respective computers (PDP-11 and Univac). DEC uses 16-bit words divided into two eight-bit bytes and logically looks for the low-order byte to be written first (on the left) and the high order byte to be written second (on the right). (In other words, it reads its words in two halves, from right to left, and it reads the contents of each half from left to right.) Univac uses 36-bit words divided into 6 six-bit bytes and logically looks for the highest order bit to be written first and the lowest order bit to be written last. (In other words, it reads in six parts, and does so entirely as a human being would--from left to right.) Given the specified differences, the Univac computer sees only four words for each nine words it reads on the data tapes generated by IPL's DEC computer.

Advice was sought from a number of computer programmers at JPL, and it was finally determined that the simplest and most efficient way to handle the interpretation of the data would be simple bit-shifting: changing the position of bits within a word. The actual shifting was accomplished using the standard FLD function available in the Univac 1100 Series FORTRAN V. Four words and one nine-word array were established in a subroutine that was written to be used by the calling program each time bit-shifting (or interpretation of the data) was required.

IPL structured the data on the tapes in multiple files. Each file consisted of about twenty-one blocks of data. Each block represented one frame of the 16-mm movie film used to record the motions of the droplet and each block was 4096 DEC bytes or 911 Univac words in length. The main program, named DATXFR, which is short for Data Transfer, reads in one block (or frame) of data at a time. It then passes four UNIVAC words at a time to the bit-shifting subroutine, which is called BITS. The subroutine unpacks the nine words of data (data valves) and performs the necessary bit-shifting. It stores the results in its nine-word array, and passes the array back to the main program. The values in the array are then transferred to their appropriate array elements in one of the six arrays: X1, Y1, X2, Y2, X3, or Y3.

The six arrays correspond to the two axes, arbitrarily thought of as X and Y, for convenience, used to assign points along the boundary the droplet creates in the three orthogonal views present in each frame of the film. The main program automatically keeps track of when these arrays begin and end, to insure that only good data is processed.

Once the six arrays have been filled, the program enters its output

phase. During this phase, the data in the six arrays, plus some additional information, are written onto a magnetic tape. Also, the data may or may not be output in octal and decimal to a printer, for manual confirmation that the data is being properly interpreted. The actual manner in which the data is written onto the magnetic tape makes use of some JPL-developed routines designed for use in conjunction with the FORTRAN V used by the Univac 1100 series computers. These special routines are used so that the data are written onto the output magnetic tape not as numbers, but as character-encoded numbers. The character encoding used is Univac's field-data character set, although standard 7-bit ACSII could also have been used. The routines also write the data on the output tape in Univac's System Data Format (SDF).

The output of numbers is done in field data and SDF to facilitate the subsequent transfer of the data from the output magnetic tape to a JPL Automated Office Data Center (AODC), a minicomputer system developed by JPL for use as a word processor or computer. This transfer of data is required so that actual data analysis may be performed using the AODC.

The transfer of the data is accomplished via a software package available on the AODC which allows for file by file transfer of data from the Univac 1100/81 to the AODC. The software package, however, can only transfer files that are in Univac's System Data Format (SDF) and whose contents are encoded in either the field data or ASCII character sets. These required the use of the special output routines mentioned earlier.

One file at a time is read from the output created by DATXFR into the Univac 1100/81's main memory (or mass storage). The AODC is then hooked up to the Univac 1100/81 by telephone line, and the standard software package is

accessed from the AODC. The software then transfers the information present in the Univac mass storage file which one specifies to the AODC, where a new file is created to hold the data.

The first successful completion of this entire procedure occurred in September 1980, using sample data provided by the personnel of IPL.

APPENDIX B

COMPUTER GENERATED TEST CASES

While IPL continued to process the data, and concurrent with the development of the data translation program, sample or test cases consisting of computer simulations designed to study data similar to the anticipated film data were developed. These programs were developed using JPL's AODC, in part to build familiarity with the AODC and in part to determine if its limited computation and data memories would be sufficient to handle the entire data analysis.

Development of the test cases proceeded along two paths. One path led to an overall calling program with a set of routines to be used for generating sample sets of data. The other path concentrated on the development of a routine which would yield reasonably accurate values for integrals of functions using a numerical approximation of integration with unequal spacing. The latter routine was developed as a subroutine and was a generalization of Simpson's Rule of integration. The generalization made was one such that correct values for f(x) could be computed over an interval Δx using unequal increments of x along the interval Δx. The use of unequal increments in the routine was necessitated by the fact that the intervals between the real data points would not be equal.

The mathematics of the generalized Simpson's rule routine were straightforward, and the routine was not difficult to create. However, a few idiosyncracies in the FORTRAN supported by the AODC (Microsoft FORTRAN 80) had to be discovered and an alternative means of encoding certain steps had

to be worked out. Once ready, the routine gave excellent results, accurate to four or five digits, using single precision floating point numbers and variables. The original version of the routine would compute only one value of f(x) for one set of f(x') where x' represents the incremental values of x used to approximate the total interval Δx. Later versions of the routine could compute several f(x)'s for several sets of f(x')'s, via the use of a large DO loop.

Work continued on the development of the test cases, as additional personnel were asked to contribute to this effort. The calling program used by several test cases, DIGTST, which asked for the input of parameters and and then called the various routines which generated the boundary, continued to evolveμ the basic logic of DIGTST, however, remained the same.

At this point, only two test cases existed. One consisted of a calling program, TESTLP, and two subroutines, designed to generate the Legendre polynomials, their derivatives, and the assoociated Legendre functions. One subroutine, IBMLEP, was based on an IBM subroutine for computing Legendre polynomials. It calculated the Legendre polynomials $P_n(x)$ and their derivatives for a given value of x, for orders $n \leq L$. Values for the variables x and L were passed to the subroutine from the calling program. The second subroutine, ALEGFN, computed the associated Legendre functions $P_\eta^\mu(x)$ and was based upon the following recursion relation for varying order:

$$(\eta-\mu+1)P^{\mu}_{\eta+1}(x) = (2\eta+1)xP^{\mu}_{\eta}(x) - (\eta+\mu)P^{\mu}_{\eta-1}(x)$$

A few errors were discovered in the two above-mentioned subroutines. They were re-written. A new calling program was created. Sample or test runs were made. An additional program, with a separate subroutine which

performed all calculations, was created. It calculated the Legendre functions for each value of η and μ from explicit equations for each one. The results were compared to those generated by the subroutines making use of recurrence relations. All values were in excellent agreement. This portion of development was completed.

The second test case then in existence incorporated several steps. The calling program previously mentioned, DIGTST, was used to call a variety of subroutines which created and then analyzed the sample data. The test case proceeded as follows. First, DIGTST created default values for the parameters which define the test case. It then asked the person running it if these values were satisfactory. If not, the operator could input his special set of values for the parameters and then the program proceeded; otherwise, the program continued. It then called DIGCIR, a subroutine which created the points of a boundary, which in turn used the subroutines RANDOM, which generated random numbers to simulate noise, and IBMLEP, which perturbed the entire boundary (2π radians) by adding one or more Legendre polynomials to model drop oscillation. DIGCIR would also convert from polar to Cartesian coordinates, and would digitize either the values in polar or Cartesian coordinates, depending on the value assigned by the operator to specific parameters appearing in DIGTST.

DIGTST then called the routine generalized from Simpson's rule, SIMPS2, which was used to try to recover the coefficients of the Legendre functions used to perturb the boundary of the simulated drop. For some coefficients, the value should have been approximately zero; for others, values between 0.0 and 1.0 were expected, as these were the values of the coefficients used in DIGCIR.

In this form, the test case simply did not work. An effort was therefore begun to modify this test case and, in the process, discover if any false assumptions or errors in theory had been made.

First, the subroutine DIGCIR was divided into two subroutines: CIRGEN, which generated a circle boundary, in essentially the same manner as DIGCIR, and DIGTIZ, which digitized the data much as DIGCIR had. In the process, an alternative method of determining $\Delta\sigma$ between data points replaced the original method. In the original method, $\Delta\theta$ varied with radius; it was determined by a fixed incremental distance along the circle boundary. Now, $\Delta\theta$ was input directly by the operator and therefore became independent of radius. The number of data points for any size circle could be constant; before larger circles had a greater number of points. The formula used to create the f(x')'s which were passed to the integration routine was found to be in error. It was corrected. The Simpson's rule routine was also modified, to expand its capabilities.

With these modifications, the test case was tried again. It still did not yield the proper values for the coefficients of the Legendre polynomials. Possible reasons were discussed, and a suggestion was made that the problem might lie in the fact that we were integrating Legendre polynomials over the entire boundary of the circle, or 2π radians. When using these functions is a polar angle varying from 0 to 2π radians. Although this suggestion was only tentative, a quick modification was made in the program so that only half of the circle boundary was perturbed and integrated over. The results were immediately rewarding. The correct values for the coefficients of the Legendre polynomials were returned from the integration routine, within about 10%, if the noise level was less than the coefficient of the Legendre

polynomial.

Work then began on a modified test case. To distinguish the new case, DIGTST was renamed to SMOOTH, which stood for the fact that before being integrated, the data would now be sent to a new routine, called ARITH, which would take the arithmetic mean of nine data points as the new or smoothed value of the fifth or middle data point. The smoothed data would then be passed to the integrating routine, to determine if smoothing of this nature would enhance the recovery of the coefficients of the Legendre polynomials by eliminating some of the background noise. The reason for developing this test case was that IPL was not only providing us with digitized data, but also with a set of smooth digitized data, the smoothing being the arithmetic mean of nine equally weighted data points. This test case would demonstrate whether the smoothing decreased the background noise or buried the higher frequency natural oscillations.

During the development of this new routine, it was realized that all data coming from IPL would be digitized, since IPL was limited in its resolution of the circle boundary by the size of the picture elements (pixels) used. A pixel is a unit, like the unit integer one. Neither can be sub-divided. Therefore, the results of the previous test case, DIGTST, were not entirely valid, as the data was digitized as an exercise only; the digitized values were not used. Instead real number values were passed to the integration routine, and therefore the accuracy of the coefficients computed by the routine was probably enhanced, as real numbers can represent the location or value of a point more accurately than can integers.

So the logic of SMOOTH was altered a little from that of DIGTST. In SMOOTH, the simulated data passed from CIRGEN to DIGTIZ. The digitized

values were then sent to a new routine, PRDGEN, which converted the digitized Cartesian coordinates which were produced by DIGTIZ (and, in the future, would be provided by IPL) into real-valued polar coordinates. PRDGEN then generated PROD, which is an array of the f(x')'s which, when multiplied by $r(\Omega,t)$ and integrated over the boundary, should yield the values of the coefficients of the Legendre polynomials.

The values returned by SMOOTH from the unsmoothed digitized coordinates were in good agreement with their correct values, but not as good as the better-than-possible values returned in the original DIGTST test case.

An option in the calling program, SMOOTH, allowed the operator to tell the program to use the actual smoothing routine, ARITH, between the routines DIGTIZ and PRDGEN, in order to simulate the receipt of smoothed data from IPL. After the smoothed digitized Cartesian data was converted to real-valued polar data, and the array PROD of f(x')'s created from the latter, integrations could be performed. The results were not promising. The values returned for the coefficients of the Legendre polynomials were no more accurate, and in some cases less so, than the values obtained for the unsmoothed digitized data. At present, a least squares approach is being investigated as a potentially more powerful tool for the recovery of the Legendre coefficients from the boundaries.

CHAPTER VI

Grumman Research Department Report RE-602

SPAR VI TECHNICAL REPORT FOR EXPERIMENT 76-22 - DIRECTIONAL SOLIDIFICATION OF MAGNETIC COMPOSITES

by

Ron G. Pirich and David J. Larson, Jr

Research Department
Grumman Aerospace Corporation
Bethpage, New York 11714

Post-Flight Technical Report on Contract NAS 8-32219

for

George C. Marshall Space Flight Center
National Aeronautics and Space Administration
Marshall Space Flight Center, Alabama 35812

July 1980

Approved by:

Richard A. Scheuing
Director of Research

ABSTRACT

Three samples of eutectic Bi/MnBi were directionally solidified during a low-$\bar{g}$ interval (10^{-4} $\bar{g}$) aboard the SPAR VI flight. Comparison samples were solidified in a 1-$\bar{g}$ environment under identical furnace velocity and thermal conditions. In addition, eutectic Bi/MnBi composites were plane-front directionally solidified in 1-$\bar{g}$ over a range of growth velocities, thermal gradients, and solidification orientations with respect to the gravity vector. The Bi/MnBi eutectic was chosen for this investigation because its microstructure is characterized by a regular rod eutectic whose morphology may be sensitive to thermo-solutal convection and because one of its components, MnBi, is ferromagnetic. Therefore, the magnetic properties can be used to provide an efficient and sensitive measurement of the effect of convection on solidification processing.

Morphological analyses on samples that were directionally solidified during the 240-s low-$\bar{g}$ interval of the SPAR VI flight experiment show statistically smaller interrod spacings and rod diameters with respect to samples grown under identical solidification furnace conditions, in the same apparatus, in 1-$\bar{g}$. The magnetic property measurements indicate that the flight samples contain $\sim$ 7 v/o less dispersed MnBi than similarly processed 1-$\bar{g}$ samples of the same starting composition. Convectively driven temperature fluctuations in the melt, which result in unsteady liquid-solid interface movement in 1-$\bar{g}$, are suggested to explain the morphological change between low-$\bar{g}$ and 1-$\bar{g}$ solidification. As a result of these fluctuations, an adjustment between the interrod spacing, growth velocity, and total undercooling at the solidification interface is proposed to account for the observed change in volume fraction of dispersed MnBi.

Morphological analyses on samples grown in 1-$\bar{g}$ indicate little difference between results for different growth orientations with respect to the gravity vector, i.e., growth up (antiparallel), down (parallel), and horizontal (perpendicular). The magnetic properties are significantly affected, however, by the presence of a nonequilibrium magnetic phase. The amount of this phase is a sensitive function of the growth velocity, thermal gradient, and gravity vector orientation. The nonequilibrium phase transforms to the equilibrium ferromagnetic phase during isothermal heat treatment.

CONTENTS

INTRODUCTION

To assess the role of convection and coupled convective-diffusive transport on the crystal growth of eutectic alloys, the plane-front solidification of eutectic Bi/MnBi was investigated during both low-$\bar{g}$ and 1-$\bar{g}$ experiments. The Bi/MnBi eutectic was chosen because its microstructure is characterized by a regular rod eutectic morphology when grown by plane-front solidification with cooperative growth. One of the phases, MnBi, appears faceted while the other, Bi terminal solid solution, may be unfaceted. Therefore, the soldification of Bi/MnBi represents a candidate system thay may be sensitive to thermal and solutal instabilities produced by convective flows. In addition, the equilibrium MnBi phase is highly ferromagnetic and its magnetic properties can be used to characterize the effect of solidification processing and convection on rod size, shape, and alignment.

Since about 1960, considerable study has focused on the plane-front solidification of eutectic alloys (Ref 1), and more recently on thermo-solutal convection (Ref 2 and 3) that occurs when the fluid density depends on variables such as temperature and solute concentration. Theoretically, free convection might cause, for example, fluctuations in the rate of solidification (Ref 4), which would lead to microstructural variations along the growth direction. In a rodlike eutectic, these variations could lead to changes in volume fraction, rod diameter, interrod spacing, and electronic properties, e.g., magnetic properties, associated with these microstructural characteristics.

In the high furnace rate and thermal gradient regime of $V \sim 30$ cm/h and $G_L \sim 100°C/cm$, the mass transfer film thickness, δ_m, is expected to be on the order of 50 μm in 1-$\bar{g}$ and 500 μm in a 10^{-4} $\bar{g}$ environment, while the solute boundary layer, or Stefan length, p^{-1}, is on the order of 25 μm for V = 30 cm/h for eutectic Bi/MnBi (Ref 5). The ratio δ_m/p^{-1} or $p\,\delta_m$ is, therefore, ~ 2 in 1-$\bar{g}$ and ~ 20 in 10^{-4} $\bar{g}$ suggesting a possible convective interaction in 1-$\bar{g}$ even at this high growth velocity and near diffusion control in 10^{-4} $\bar{g}$ environment.

Samples were grown up, down, and horizontal to the gravity field in an effort to change the degree of thermal and solutal convection present. Ground base

experiments ($1\text{-}\bar{g}$), were performed over a range of furnace velocities, V, $0.5 \leq V \leq 50$ cm/h, and thermal gradients in the liquid at the solidification interface, G_L, $20 \leq G_L \leq 150°C/cm$. Therefore, $p\,\delta_m$, $0.2 \leq p\,\delta_m \leq 3.5$. For example, a statically stable fluid (net fluid density < 0) might be expected for eutectic Bi/MnBi in a growth up configuration with sufficiently large temperature gradient since the fluid density of Mn is less than Bi, thereby minimizing convective effects in the absence of sufficiently large radial temperature gradients near the solidification interface. Similarly, convective flow should be maximum when the growth is horizontal because both thermal and solutal convection are present. However, definitive analytic analysis or experimental evidence for a priori prediction of the effects of these levels of $p\,\delta_m$ on microstructure and associated electronic properties of directionally solidified eutectics have not yet been developed or determined. The objective of this investigation was, therefore, twofold:

(1) Determine the effect of a reduction in gravity for samples grown in the same apparatus under identical furnace conditions except for the suppression of the magnitude of the gravitational force; and

(2) Attempt to alter the degree of thermosolutal convection in $1\text{-}\bar{g}$ by changing the solidification direction with respect to the gravity vector over a range of V, G_L and, therefore, $p\,\delta_m$.

EXPERIMENTAL PROCEDURE

SAMPLE PREPARATION

Bi/MnBi samples were prepared using commercially pure Mn (99.9 w/o) and high purity Bi (99.999 w/o). Both were melted together in an evacuated ($\sim 10^{-5}$ torr) high purity quartz crucible (1.0-cm inner diameter) above 446°C, the temperature at which the stoichiometeic MnBi compound forms (Ref 6). The melt was electromagnetically stirred for a period of 16 h to ensure homogenization. The Bi-Mn phase diagram (see Fig. 1) was determined in the vicinity of the eutectic composition by means of differential scanning calorimetry and chemical spectrohotometric absorbance (Ref 7). The eutectic composition was found to be 0.72 $\pm$ 0.03 w/o Mn (2.69 $\pm$ 0.08 a/o Mn), which results in an MnBi volume fraction of 3.18 $\pm$ 0.09 v/o. Portions of these eutectic starting boules were then encapsulated in a specially designed, evacuated quartz ampoule (0.4-cm inner diameter), illustrated in Fig. 2. The eutectic Bi/MnBi sample was localized by means of tight-fitting, high purity graphite spacers and quartz wool "O" rings at the appropriate position for solidification. A melt back interface was used to minimize leak-by of the melt. The ampoules were instrumented with very fine chromel-alumel thermocouples (0.0015-in. bead diameter) sheathed in MgO insulation with a 0.010-in diameter 304 stainless steel outer tube. The preflight and postflight ground base experiments consisted of four ampoules: two directionally solidified growth up and instrumented with four equally spaced thermocouples, and two directionally solidified growth down and instrumented with one thermoucouple per ampoule. A similar arrangement was used for the flight experiment. Those samples investigated in other ground base experiments, i.e., grown at velocities and thermal gradients other than the SPAR VI flight conditions, were instrumented with one thermocouple. The presence of these thermocouples did not appear to perturb significantly the solidification processing either through chemical contamination or heat transfer. In fact, the thermal conductivity of the thermocouple probes was found to be very near the thermal conductivity of liquid eutectic Bi/MnBi.

DIRECTIONAL SOLIDIFICTAION PROCESSING

The preflight, flight, and postflight experiments were performed using the Bridgman-Stockbarger method in an automatic directional solidification system

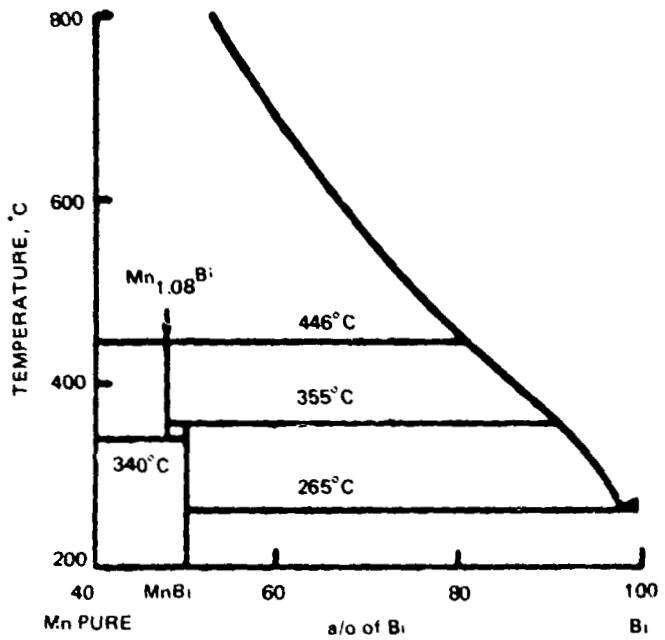

a) As Determined by Chen

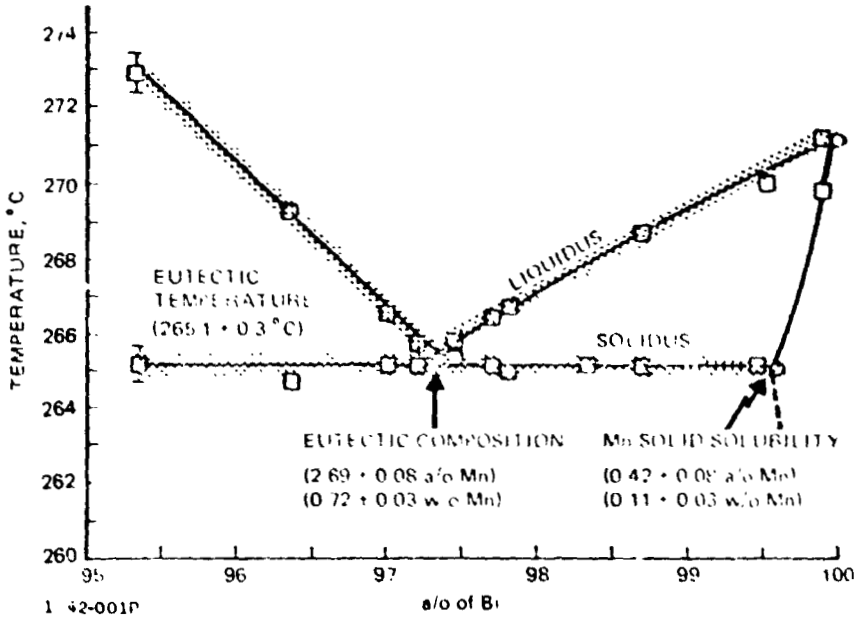

(b) In the Vicinity of Eutectic as Determined in This Work

Fig. 1 Bi-Mn Phase Diagram

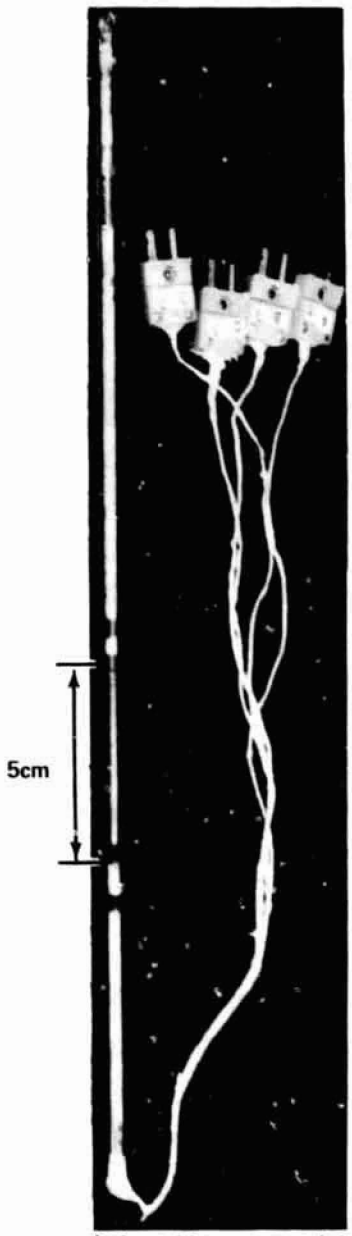

a) Actual Instrumented Ampoule Used for Solidification Processing

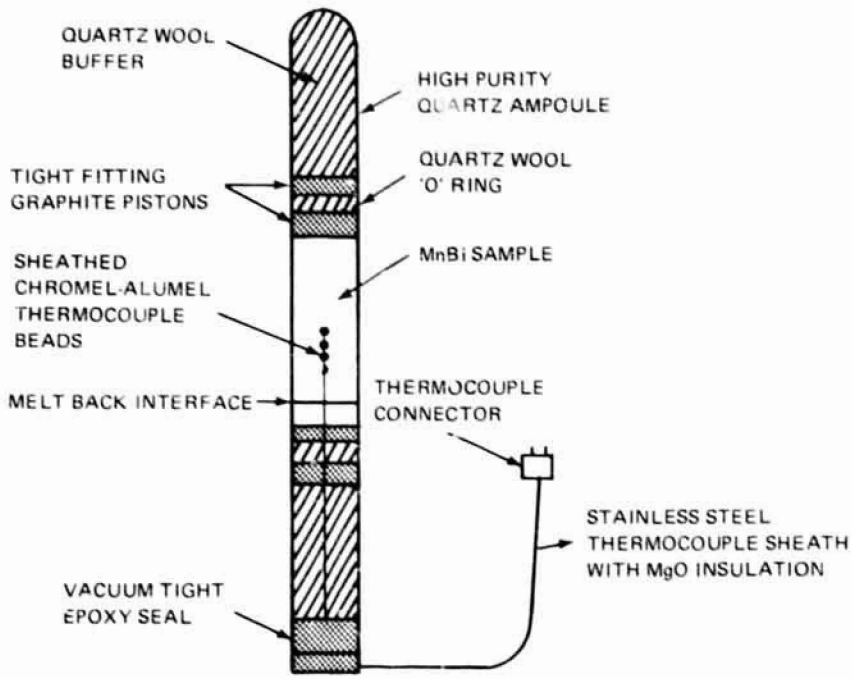

b) Representative Schematic

1342-002P
0868-007P

Fig. 2 Eutectic Bi/MnBi Ampoule Configuration

(ADSS) built by General Electric (Ref 8). The ADSS apparatus consists of four symmetrically mounted furnace assemblies, each completely independent with respect to temperature and linear velocity of movement. Schematics of the furnace assembly and actual apparatus are shown in Fig. 3 and 4, respectively. For the preflight, flight, and postflight experiments, each furnace produced about the same gradient (~100°C/cm) and moved at the same linear speed (~30 cm/h). In addition, furnaces mounted in opposition with respect to the assembly mounting plates moved in the same direction so that the total ADSS momentum was zero. The apparatus also underwent intrinsic vibrational testing so as to monitor the level of external force produced by furnace movement at the location of the ampoule. This level was found to be $< 10^{-5}$ $\bar{g}$. Each ADSS furnace assembly produced a well controlled unidirectional thermal gradient near the solidification temperature of eutectic Bi/MnBi at 265.1 $\pm$ 0.3°C. This gradient can be varied from 10°C/cm to 200°C/cm by adjusting the temperature of the furnace nichrome heating elements and the fluid cooled copper quench block. The linear furnace velocity can be varied from 0.1 to 100 cm/h. A similar furnace unit was used for the other ground base investigations.

PREFLIGHT, FLIGHT, & POSTFLIGHT EXPERIMENTS

Two preflight experiments were conducted in the ADSS apparatus at Marshall Space Flight Center in accordance with the SPAR VI flight operational timeline. One of these tests - the Pre-Installation Acceptance Test (PIAT) - was conducted with the ADSS unit separated from the other flight experiments, in ambient atmosphere and temperature, and in a vertical geometry (growth up and down). The purpose of the PIAT was to ensure that plane-front solidification occurred at the SPAR VI solidification conditions, and to establish baseline criteria for the flight experiment. In the other preflight experiment (All-Systems Test), the entire apparatus was placed in a sealed cannister filled with dry N_2 gas and run in conjunction with the other flight experiments. All conditions were identical with the flight experiment except for the presence of the vertical gravity vector. The All-Systems Test provided 1-$\bar{g}$ samples to be used for direct comparison with the SPAR VI flight samples.

The SPAR VI flight experiment began with initiation of furnace heating 90 min before launch. At 5 min before launch, each in situ sample thermocouple temperature was monitored and compared against the baseline criteria established

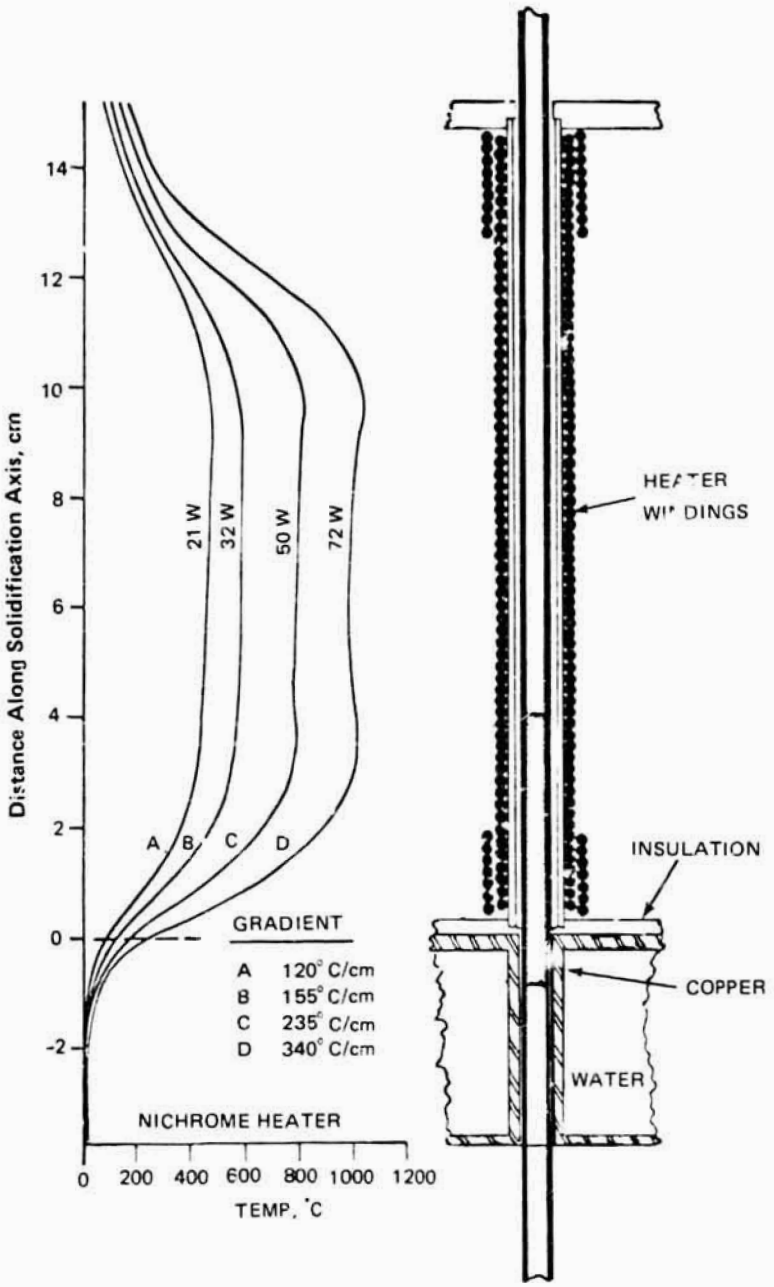

1342-003P
0868-006P

Fig. 3 Schematic Representation of ADSS Furnace Assembly and Representative Thermal Profiles

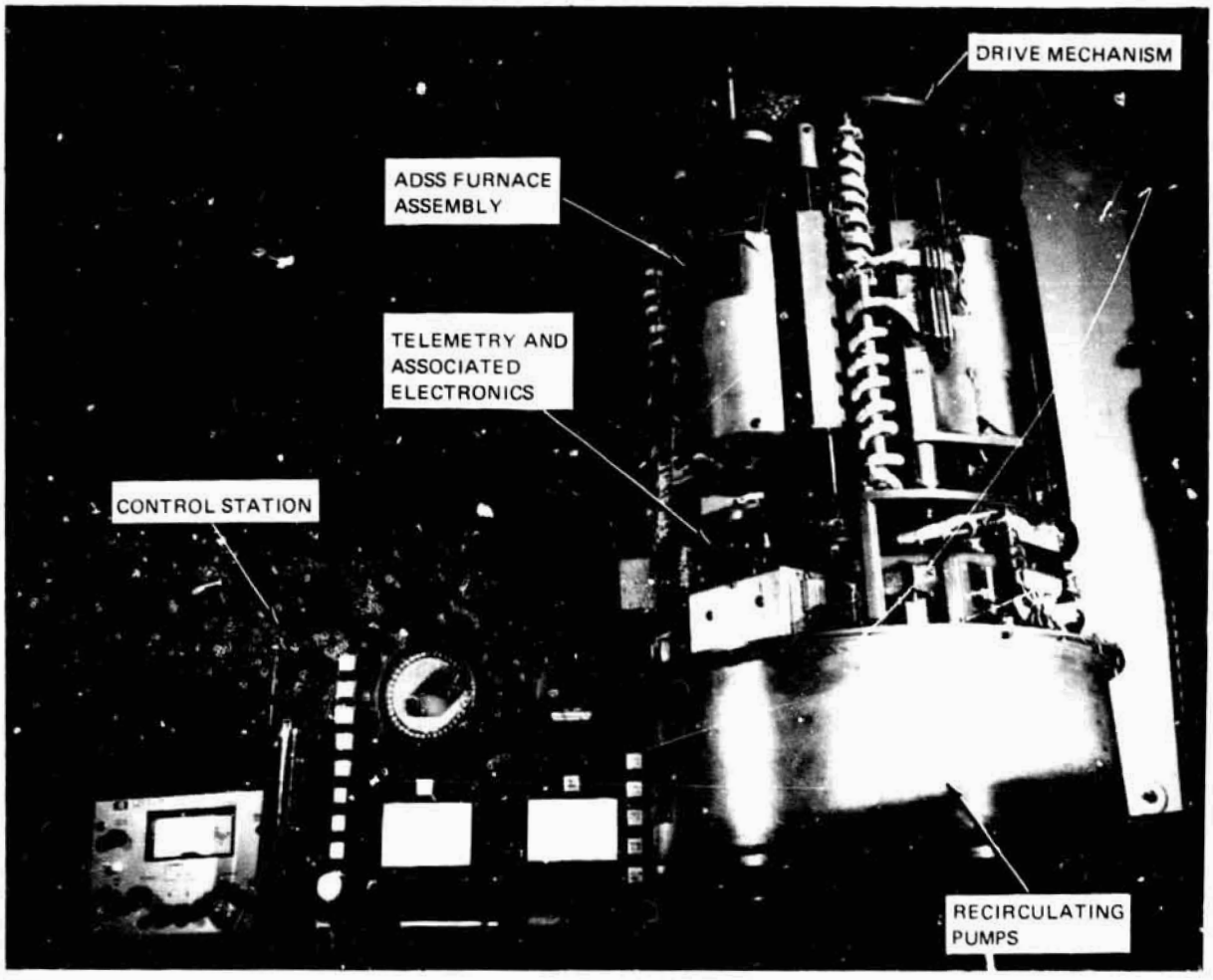

1342-004P

Fig. 4 Actual ADSS Flight Apparatus With Ground Base Control Station

following the PIAT test. After launch, directional solidification commenced ~ 30 s after low-$\bar{g}$ had been attained or ~120 s after launch. Directional solidification proceeded through the low-$\bar{g}$ interval (~240 s) and continued even after deployment of the drop parachute, terminating ~ 728 s after launch. By this time, the entire length of each Bi/MnBi sample (~ 5 cm) had been directionally solidified with ~ 1.8 cm plane-front directionally solidified in low $\bar{g}$.

A PIAT type test was also conducted after the flight experiment to ensure that no systematic apparatus anomalies had occurred as a result of the launch.

FLIGHT (Low-$\bar{g}$) & ALL-SYSTEMS TEST (1-$\bar{g}$) COMPARISON

Each SPAR VI flight (low-$\bar{g}$) and All-Systems Test (1-$\bar{g}$) sample was partitioned, as shown in Fig. 5, at the axis of solidification as well as at three fraction solidified locations by means of a diamond impregnated string saw. The string saw was used to avoid unnecessary stress during the sectioning process.

The top half (containing no thermocouple remanant) of each axial section was used for both magnetic and morphological analysis. The remaining half was used only for morphological study. Comparison between flight and ground base samples was made at the same fraction solidified or fraction solidified interval for samples grown in the identical furnace assembly so as not to skew the results systematically. All comparisons were made in the low-$\bar{g}$ interval of solidification.

GROUND BASE (1-$\bar{g}$) MATRIX EXPERIMENT

In a series of ground base investigations, samples were grown parallel, anti-parallel, and perpendicular to the gravity field at growth velocities between V = 3 and 30 cm/h and thermal gradients, G_L = 20 and 150°C/cm. The hot zone was adjusted, regardless of growth orientation with respect to the gravity field, to maintain a constant thermal gradient in the liquid in both the high and low thermal gradient regimes. One transverse fraction solidified location, near the thermocouple bead, was used for morphological study. Several longitudinal locations were observed to ensure that cooperative growth had occurred as a function of fraction solidified. In addition, two fraction solidified sections per growth condition were used for magnetic property analysis. For two ampoules, the

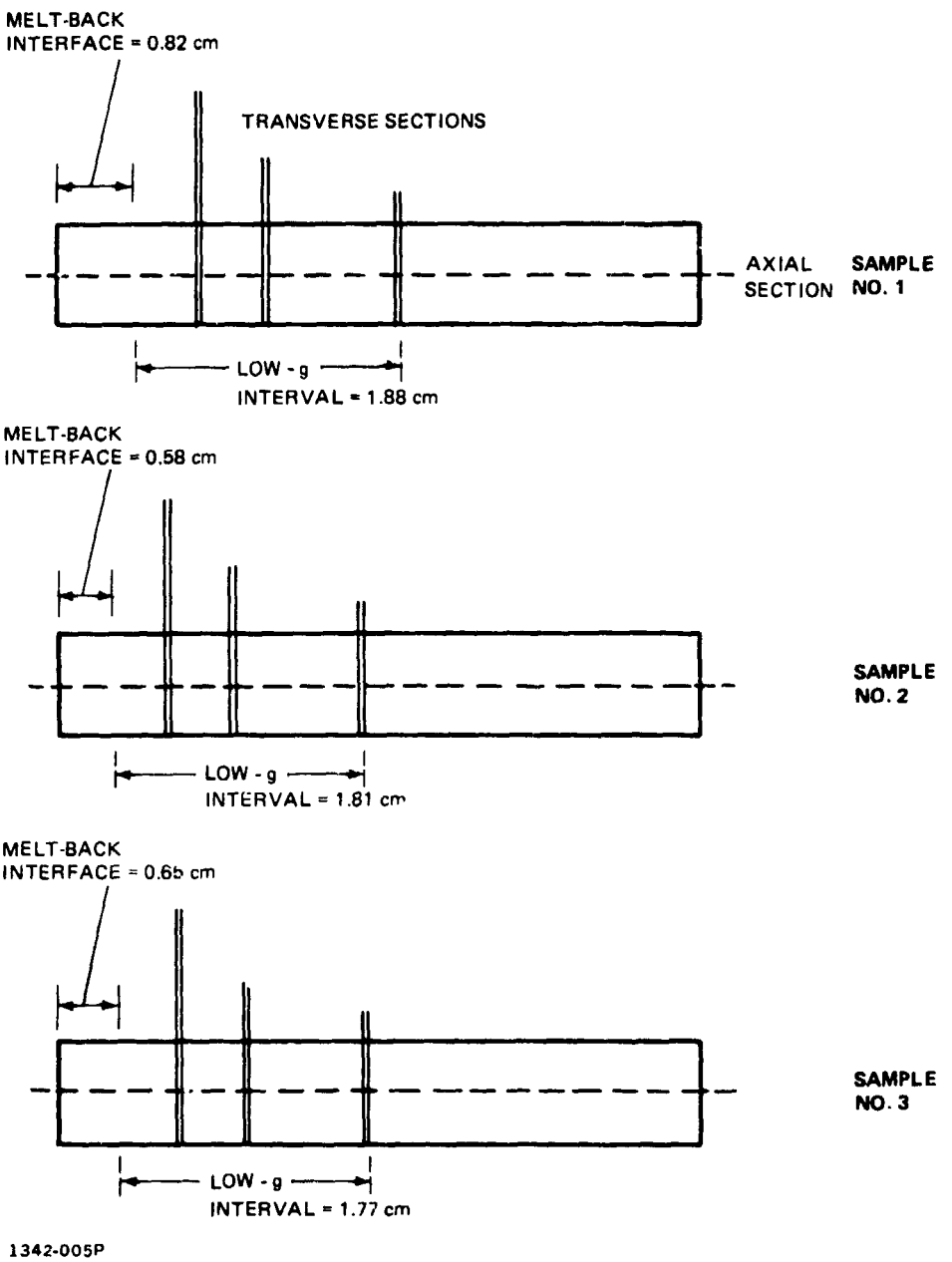

Fig. 5 Schematic Representation of Sample Partitioning of All Systems Test and Flight Experiment Samples

entire length was equipartitioned and the magnetic properties determined as a function of fraction solidified.

MICROSTRUCTURAL, THERMAL, & MAGNETIC PROPERTY ANALYSIS

Sample morphology (dispersed MnBi rod size, volume fraction, and rod alignment) was determined from optical micrographs of mechanically polished surfaces both parallel and perpendicular to the solidification direction. Fifteen micrographs of a mechanically polished surface at each tranverse fraction solidified location were analyzed as to MnBi rod area, interrod spacing, and volume fraction. Analysis was performed using a computer aided Leitz particle analyzer system.

For the preflight and flight experiment, each in situ thermocouple, four furnace control thermocouples, and two reference thermistors were monitored at about one reading per second for each furnace assembly. These measurements were transmitted via telemetry and recorded both in digital and analog format. The subsequent analog voltages were converted to temperature in degrees centigrade by assuming a quadratic relationship between voltage and temperature. Due to the lack of point to point grounding in the ADSS apparatus, resolution of the in situ thermocouple measurements was limited to $\pm$ 0.08 mV($\pm$2.0°C). For the remaining ground base testing, in situ thermocouple measurements were monitored using a Digitec Thermocouple acquisition system with a temperature resolution of $\pm$0.2°C.

Magnetic properties were determined from magnetization measurements of cylindrically shaped samples. Magnetization was measured parallel and perpendicular to the solidification direction at 290,77, and 4.2 K in applied fields up to 230 kOe at the Francis Bitter National Magnet Laboratory, using a low frequency vibrating sample magnetometer. A Princeton Applied Research high frequency vibrating sample magnetometer was used at Grumman to measure magnetization as a function of angle with respect to solidification direction, applied field up to 17 kOe over a temperature from 290 K to the eutectic melting temperature of 538 K. A portion of the magnetic characterization facility used at Grumman is shown in Figure 6.

It had been anticipated that because the equilibrium MnBi phase is ferromagnetic at and below room temperature, its magnetic properties could be used to measure the effect of particle morphology (e.g., average rod size and particle alignment) and the effect of solidification processing and convection on the

1342-006P

Fig. 6 Part of Magnetic Characterization Facility at Grumman

morphology. For example, the intrinsic coercivity, $_mH_c$, of ferromagnetic materials should increase with decreasing particle size and approach the theoretical maximum when the particle contains only one magnetic domain (single domain behavior). It was observed, however, that plane-front directionally solidified eutectic Bi/MnBi with comparable morphologies differed dramatically in magnetic properties depending on solidification processing conditions and heat treatment after solidification (Ref 9-12). As is seen in Fig. 7, the room temperature (300 K) intrinsic coercivity for samples processed only by directional solidification (as-grown state) appears to be a weakly dependent function of the average dispersed MnBi particle size except for higher growth velocities where the samples become almost paramagnetic in character. This behavior is supported by the decrease in remanent magnetization shown by samples in the as-grown state. For the same samples sufficiently heat treated (at 250°C for periods greater than 24 h), a dramatic increase is observed not only in room temperature remanent magnetization but also in intrinsic coercivity. Another magnetic phase, other than the expected equilibrium (so-called LTP) MnBi, which occurs in directionally-solidified material, has been identified as the origin of these differences. This new magnetic phase, termed the high coercivity or HC phase, is found to coexist with the LTP phase. The HC phase is paramagnetic at room temperature and orders ferrimagnetically (Ref 10) near 250 K with an intrinsic coercivity ~110 kOe at 77 K, measured parallel to the solidification direction. With the applied field parallel to the solidification direction, the hysteresis curves corresponding to the LTP and HC phases are distinct and separate both at room temperature and 77 K (Fig. 8) so that determining the amount of each phase present is straightforward (Ref 9-13). The magnetization can be measured with an uncertainty of $\pm 10^{-3}$ emu. Since eutectic samples used for magnetization studies have moments between ~0.75 emu for 100% HC phase and ~1.70 emu for 100% LTP phase, for an applied field of 150 kOe at room temperature, the uncertainty in determining the amount of each magnetic phase (and the volume fraction of MnBi) varies from ± 0.3 % for 100% LTP phase to ± 1.0% for a 30/70% combination of LTP/HC phases at the eutectic Bi/MnBi composition.

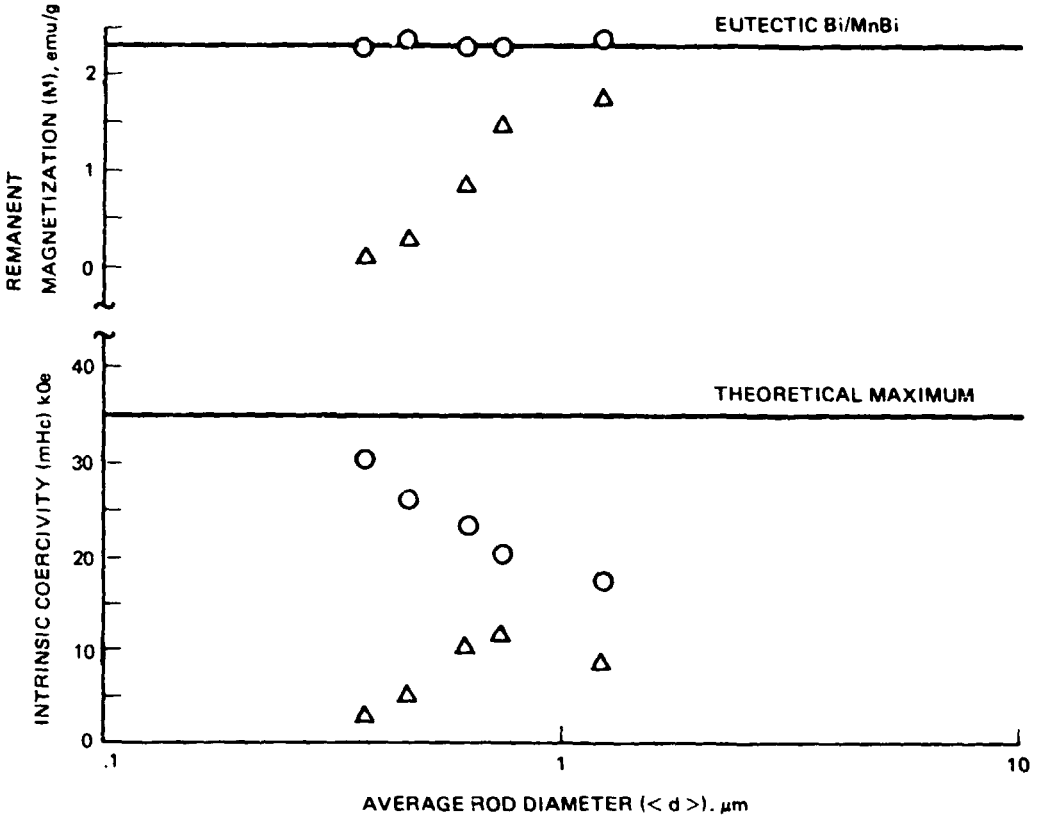

1342-007P

Fig. 7 Dependence of Room Temperature Remanent Magnetization and Intrinsic Coercivity on Mean MnBi Rod Diameter in As-Grown (Δ) and Heat-Treated States (o)

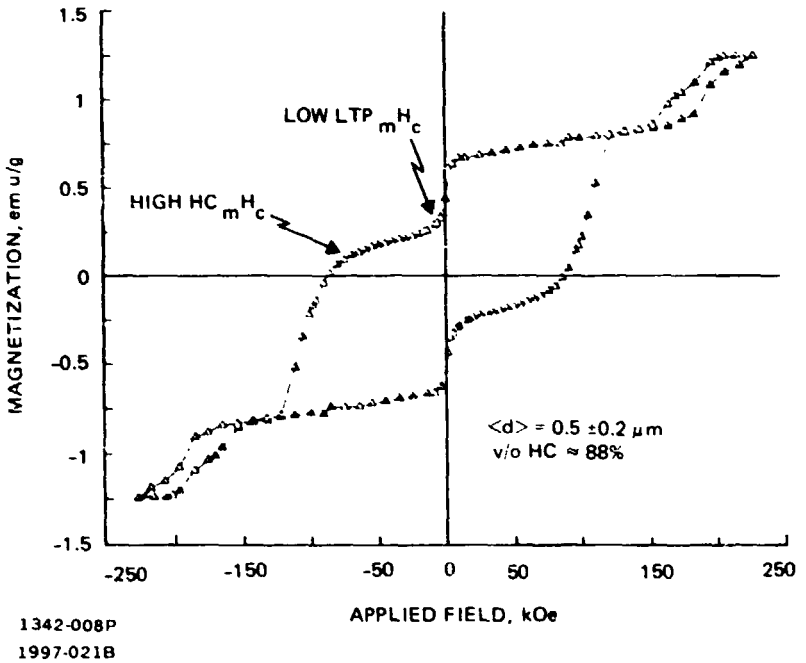

Fig. 8 Hysteresis Curve Measured Parallel to the Solidification Direction at 77 K for Sample Containing Combinations of HC and LTP MnBi Phases

RESULTS

LOW-$\bar{g}$ EXPERIMENT - GENERAL OBSERVATIONS

On October 17, 1979, SPAR VI was flown successfully. The flight ampoules were removed the same day, and were returned to Grumman on October 19. As shown in Fig. 9, ampoule No. 1 and 3 were completely intact; their in situ themocouples (four in each ampoule) were still functioning properly. Ampoule No. 2 had been broken near the top retaining washer of the ADSS furnace No. 2 assembly, but the fracture was located sufficiently far away from the Bi/MnBi sample so that the sample was not affected. Fracture most probably occurred at impact, i.e., after the sample had completely solidified. This probability is supported by the recovery team which reported a large gash in the outer payload skin near the 76-22 apparatus (see Fig. 10), apparently caused by the payload being dragged over rough terrain at the impact site. Ampoule No. 2 was singly instrumented, and its thermocouple was also still functioning properly. Ampoule No. 4, also singly instrumented, was broken at launch. This is confirmed by a sudden disturbance in thermocouple output as observed from the telemetry data at launch. Ampoule breakage may have been caused by the rather severe vibration of the rocket bumping against the gantry. Fortunately, the molten Bi-Mn quickly quenched on the lower ADSS base plate and did not interfere with any other furnace assembly.

Evaluation of the telemetry data indicates that all in situ and furnace thermocouples, reference transistors, and furnace assemblies operated properly. The telemetry data also indicate that one of the recirculating pumps malfunctioned, but because of the large thermal mass of each furnace, and since the ADSS has two such pumps, no noticeable effect on the temperature of the fluid cooled furnace assembly quench blocks was discernable.

Several x-ray radiographs and macrophotographs of the ampoules were taken, as shown in Fig. 11 and 12. They indicated no unusual porosity except for ampoule No. 2 in which the volume made available by a slight leak-by of molten Bi-Mn at launch (furnace was above quench block) caused separation of the sample into four distinct parts. This did not have any adverse effects on evaluation of sample thermal data since the first separation occurred below the termination of the in situ thermocouple and after solidification during the low-$\bar{g}$ interval.

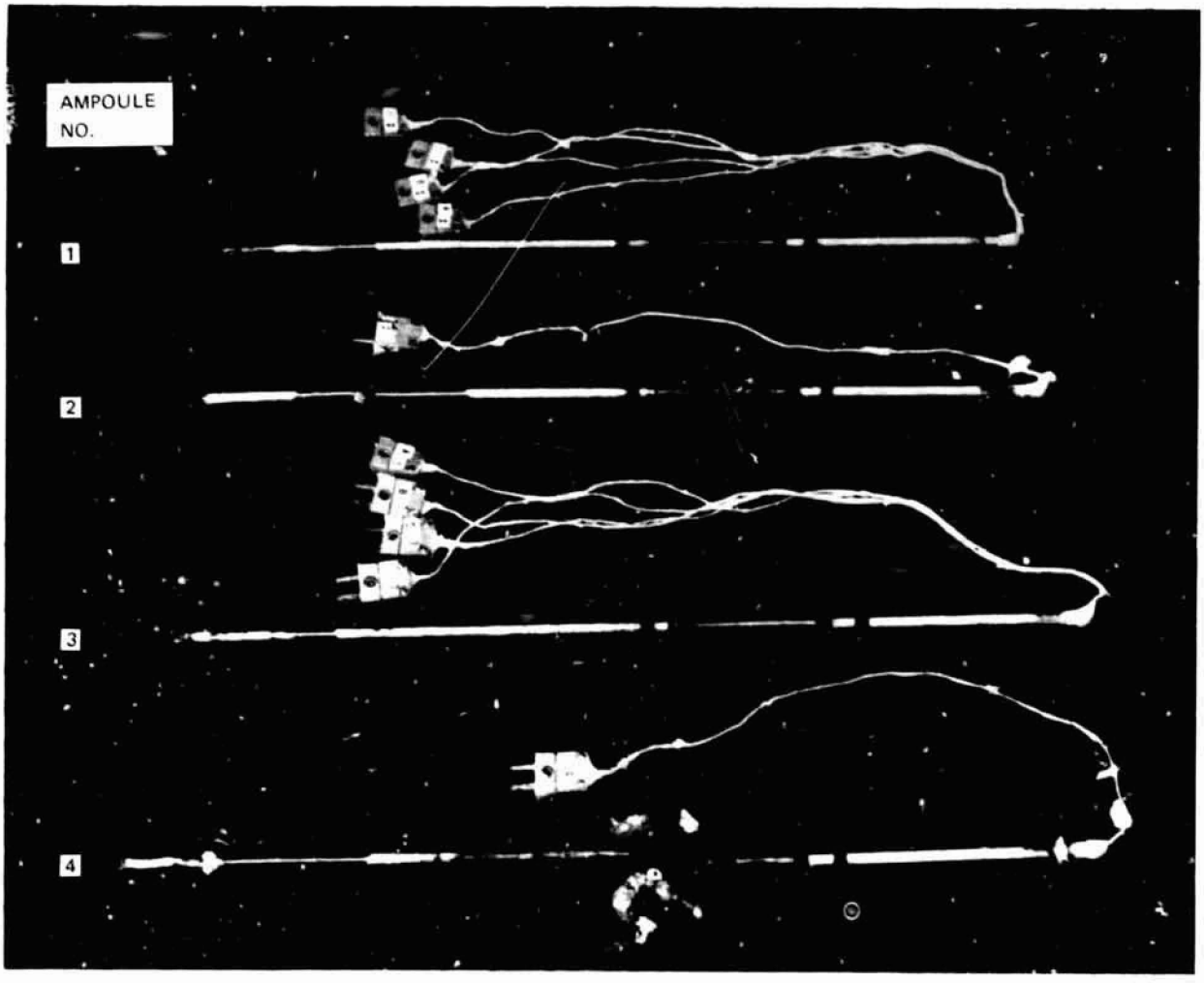

1342-009P

Fig. 9 SPAR VI Flight Ampoules as Received After the Flight Experiment

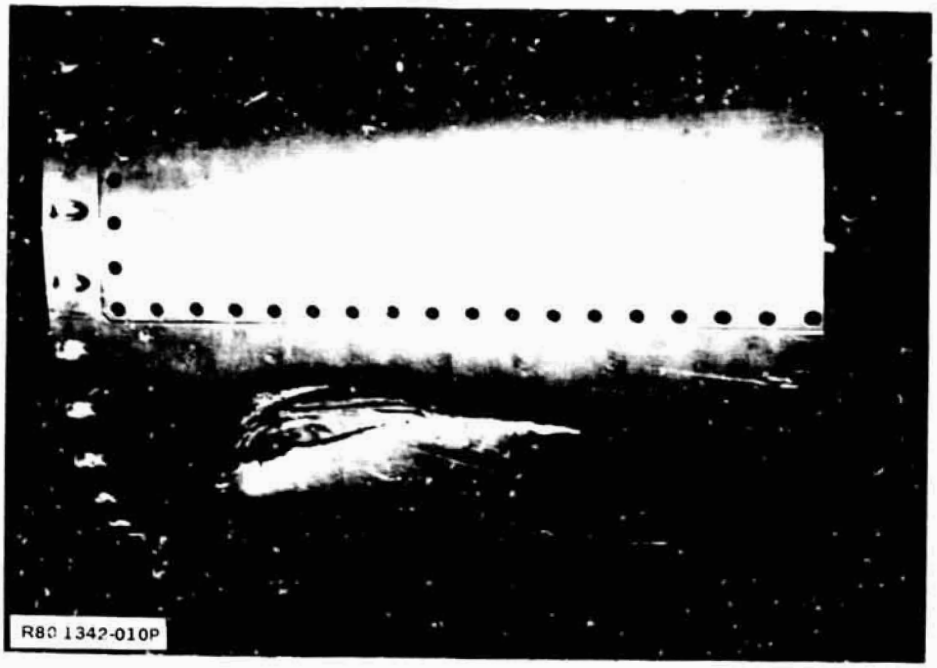

Fig. 10 Photograph After SPAR VI Flight Showing Gash in Outer Payload Skin Near the 76-22 Apparatus

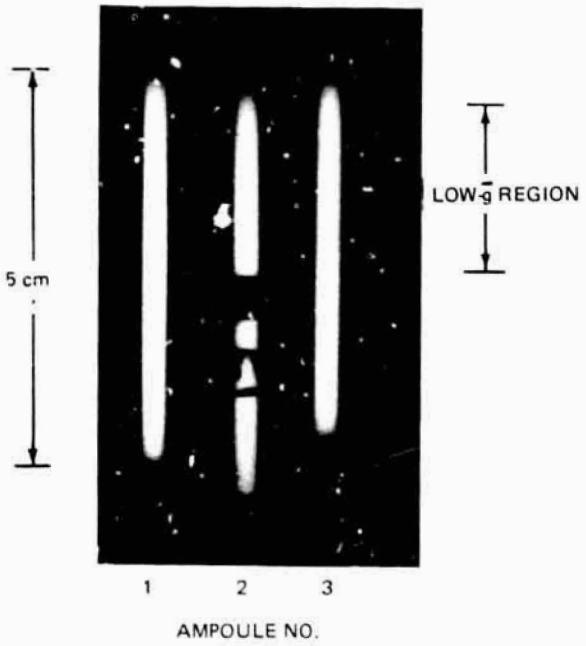

Fig. 11 X-Ray Radiograph of Flight Ampoules No. 1, 2 & 3 After SPAR VI Flight

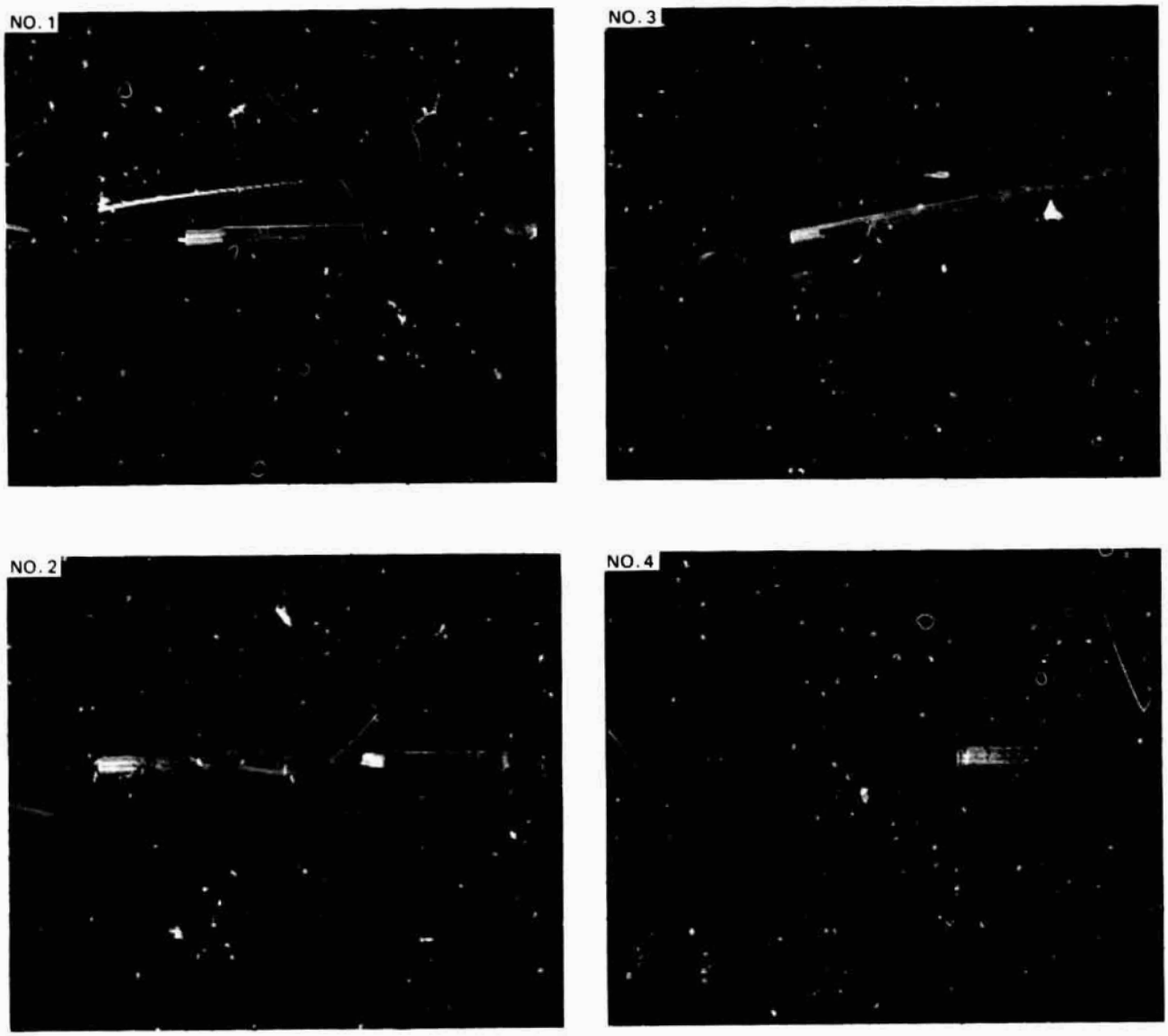

1342-012P

Fig. 12 Photographs of Flight Samples After Removal From Ampoules

FLIGHT (Low-$\bar{g}$) AND ALL-SYSTEMS TEST (One-$\bar{g}$) COMPARISON

Morphology

Plane-front solidification with cooperative growth of eutectic Bi/MnBi results in an aligned ensemble of MnBi rods, with length to diameter ratios on the order of 100, dispersed in a Bi-terminal solution matrix on the order of 0.1 w/o Mn. Typical Transverse and longitudinal microstructures are shown in Fig 11. The long axis of the rods is parallel to the solidification direction. The morphology of the rod cross-sections is degenerate-faceted and chevron-shaped at the lower furnace velocities ($V < 3.0$ cm/h) as shown in Fig 13, and more circular-like at higher furnace velocities ($V > 20$ cm/h) as shown in Fig. 14. Mean rod diameters $\langle d \rangle$, and interrod spacings, $\langle \lambda \rangle$, as determined by fitting the measured rod diameter and interrod spacing distributions with a Poisson distribution function and minimizing the x^2, were found to vary in the expected manner (Ref 1) with growth velocity, V, i.e.,

$$\langle d \rangle, \langle \lambda \rangle \sim V^{-1/2} \qquad (1)$$

Very uniform, cooperative growth was observed from the beginning of solidification, through the low-$\bar{g}$ interval until the deployment of the SPAR VI flight parachute (Fig. 15). The deployment of the parachute resulted in a large perturbation to the solidification processing with an abrupt termination of cooperative growth see Fig. 16, and in a melting back of the solidification interface as determined by the in situ thermocouple data.

Morphological measurements of MnBi rod diameter and interrod spacing distributions on all three flight samples solidified during the low-$\bar{g}$ interval show a statistically significant difference with respect to the same fraction solidified regions of samples grown under identical furnace conditions, in the same furnace assembly, in 1-$\bar{g}$ (as seen in Table 1). This is shown in Fig. 17 for samples grown in furnace assembly No. 1. Both the MnBi rod diameter and interrod spacing distributions have smaller values for the low-$\bar{g}$ grown samples, with mean rod diameters and mean interrod spacings $30 \pm 9\%$ and $35 \pm 12\%$ smaller, respectively (Fig. 18 and Table 1). This behavior was similar at each fraction-solidified location measured and for each sample solidified. The measured MnBi volume fraction of the flight samples (2.96 ± 0.38 v/o), as determined from quantitative morphological analysis, was statistically equivalent to the All-Systems Test

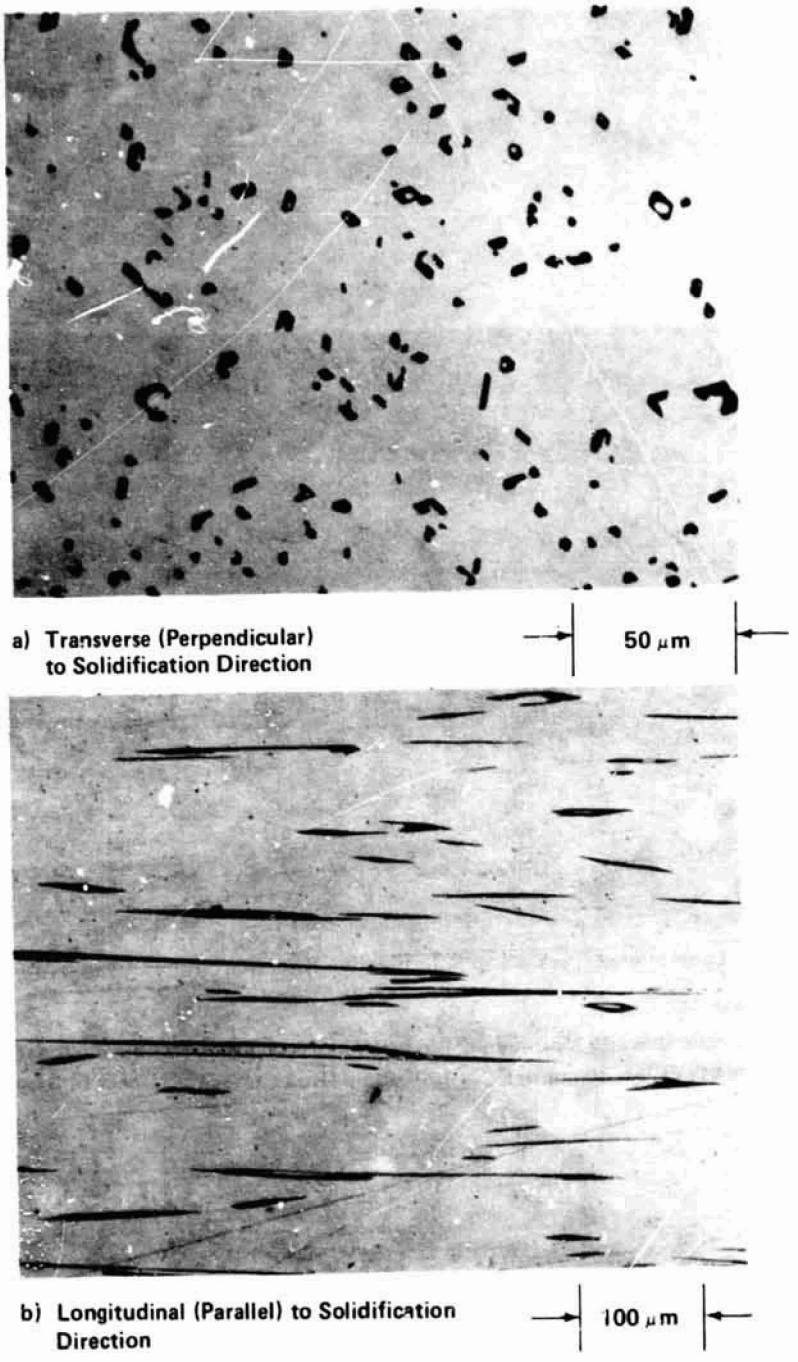

Fig. 13 Eutectic Bi/MnBi Cooperative Growth Morphology at V = 0.8 cm/h and G_L = 150° C/cm

a) Transverse (Perpendicular) to Solidification Direction → 5 μm ←

b) Longitudinal (Parallel) to Solidification Direction → 5 μm ←

1342-014P

Fig. 14 Eutectic Bi/MnBi Morphology Produced by Plane-Front Solidification with Cooperative Growth at V = 30 cm/h, G_L = 100° C/cm Grown up with Respect to Gravity Vector

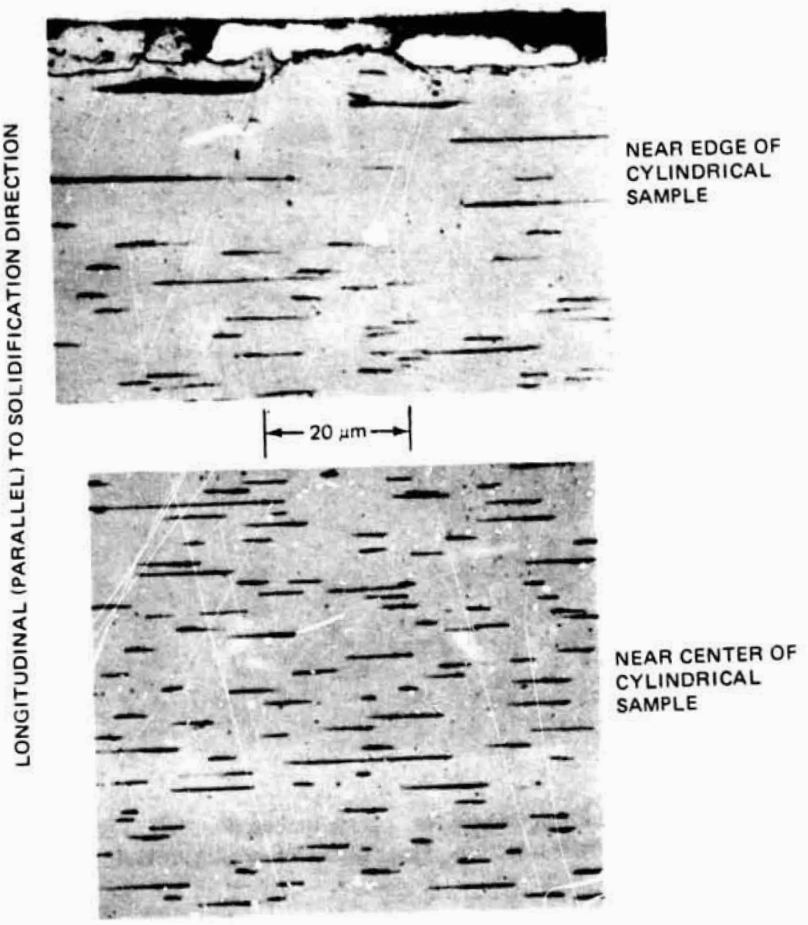

1342-015P

Fig. 15 SPAR VI Flight Sample No. 1 Morphology in Low-$\bar{g}$ Interval Longitudinal (Parallel) to Solidification Direction

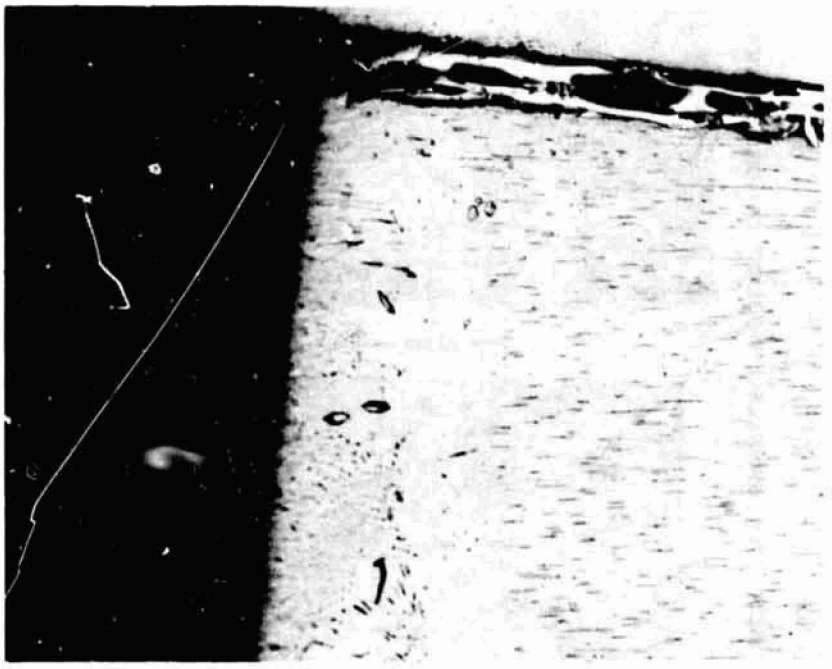

1342-016P

Fig. 16 Microstructure of Flight Sample No. 2 Longitudinal (Parallel) to Solidification Direction Near Region of First Separation. This region corresponds to deployment of drop parachute.

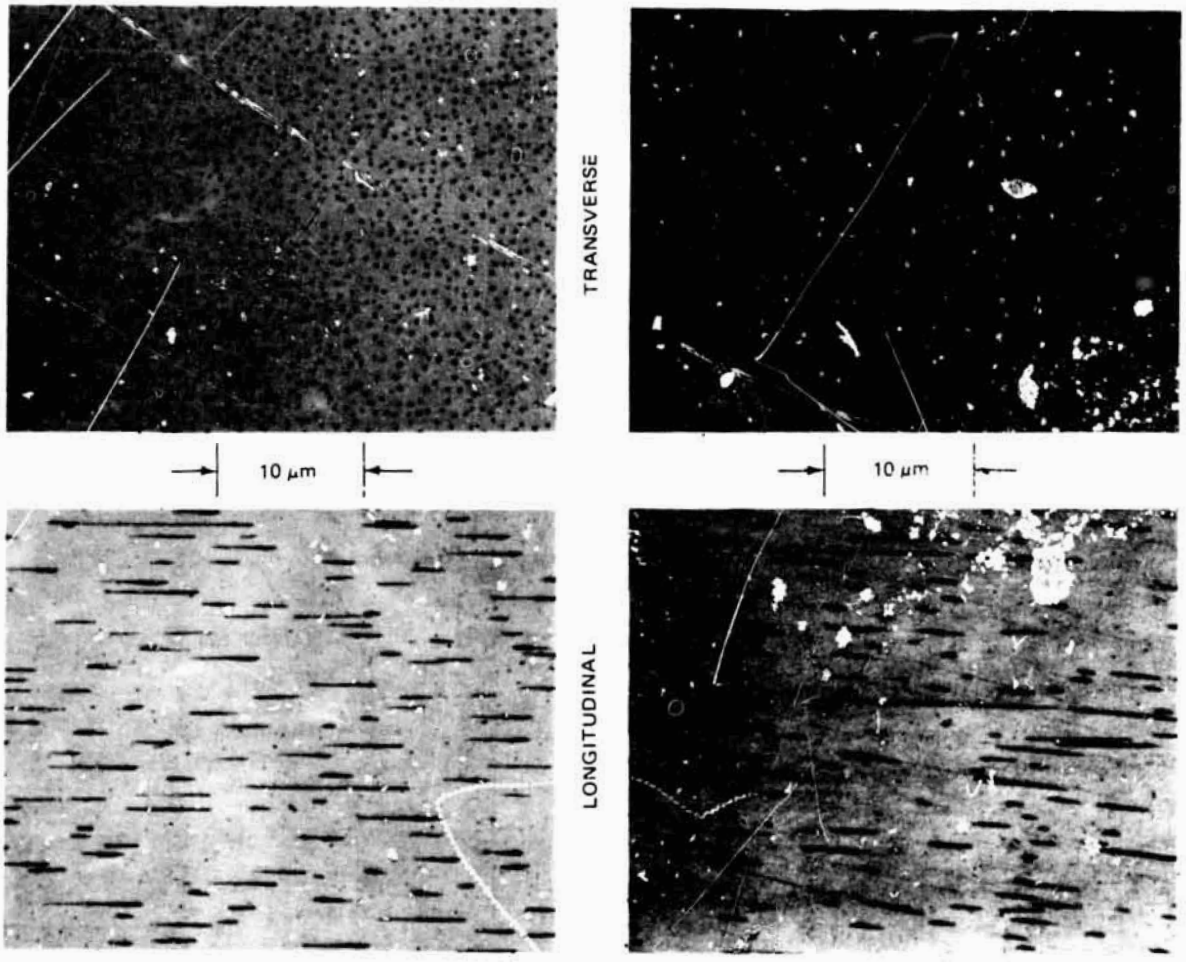

1342-017P

Fig. 17 Comparison of Flight and All-Systems Test Microstructures for Samples Processed in Furnace Assembly No. 1 at Same Fraction Solidified Location During Corresponding Interval of Low-$\bar{g}$ Solidification

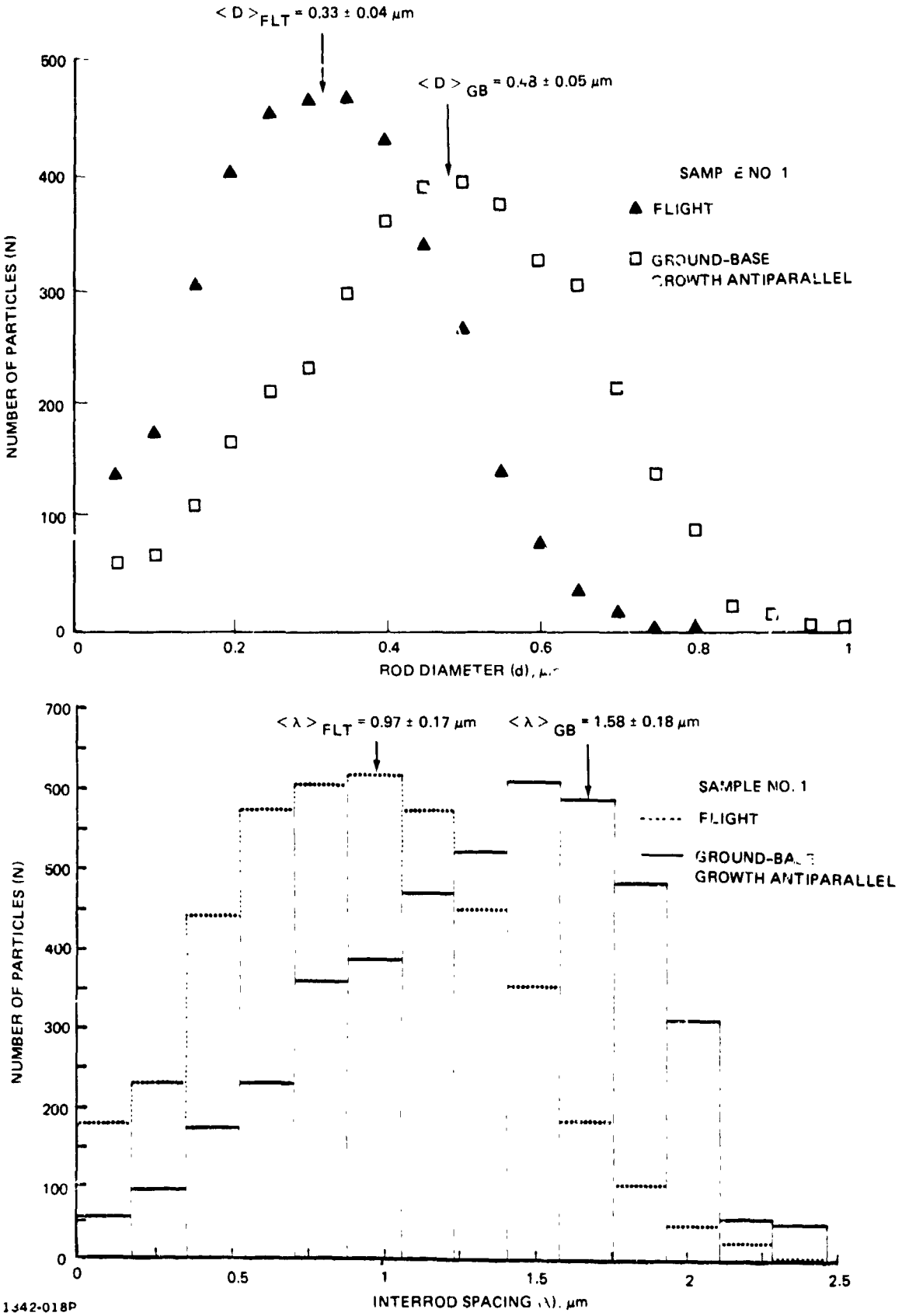

Fig. 18 Comparison of All-Systems Test & Flight MnBi Rod Diameter & Interrod Spacing Distributions for Samples Grown in Furnace Assembly No . 1 Including Statistics From All Transverse, Low-$\bar{g}$ Sections

Table 1 Comparison of Thermal, Morphological, & Magnetic Properties for Samples Grown During All-Systems Test 1-$\bar{g}$ & SPAR VI Flight (Low-$\bar{g}$) in Identical Furnace Assembly Apparatus. Comparison is Normalized to Low-$\bar{g}$ Regions of Solidification.

EXPERIMENTAL MEASUREMENT	All-Systems Test (1-$\bar{g}$) Furnace Assembly No.			SPAR VI Flight (10^{-4} $\bar{g}$) Furnace Assembly No.		
	1	2	3	1	2	3
Bulk starting composition, (w/o Mn)	0.71 ±0.03	0.72 ±0.03	0.72 ±0.03	0.72 ±0.03	0.71 ±0.03	0.72 ±0.03
Furnace assembly velocity, x 10^{-3} cm/s	8.0 ±0.6	7.8 ±0.3	7.7 ±0.3	7.8 ±0.5	7.5 ±0.3	7.3 ±0.3
Furnace hot zone temperature, °C	451 ± 5	462 ± 5	451 ± 5	446 ± 5	460 ± 5	446 ± 5
Furnace quench block temperature, °C	48.5 ± 1.2	47.5 ± 1.2	48.5 ± 1.2	48.0 ± 1.2	48.0 ± 1.2	48.0 ± 1.2
Solidification temperature, °C	265.3 ± 2.0	---	265.1 ± 2.0	262.4 ± 2.0	---	262.6 ± 2.0
Thermal gradient at interface/liquid, °C/cm	102.6 ± 8.6	---	108.1 ± 8.8	105.1 ± 6.7	---	107.8 ± 6.9
Thermal gradient at interface/solid, °C/cm	179.9 ±15.0	---	177.1 ±14.3	162.5 ±10.4	---	173.4 ±11.7
Mean MnBi interrod spacing (λ), μm	1.58 ±0.18	1.60 ±0.19	1.43 ±0.19	0.97 ±0.17	0.98 ±0.17	1.05 ±0.16
Mean MnBi rod diameter (D), μm	0.48 ±0.05	0.46 ±0.05	0.48 ±0.05	0.33 ±0.04	0.32 ±0.04	0.35 ±0.04
Volume percent HC MnBi phase normalized to v/o MnBi, %	95.3 ± 0.1	95.1 ± 0.1	95.2 ± 0.1	95.3 ± 0.1	95.2 ± 0.1	95.3 ± 0.1
Volume percent MnBi from magnetic property measurements, %	3.18 ±0.03	3.16 ±0.03	3.19 ±0.03	2.96 ±0.03	2.93 ±0.03	2.98 ±0.03
Resistance to demagnetization (intrinsic coercivity) for partially annealed 50% equilibrium/nonequilibrium MnBi magnetic phases, kOe	25.6 ± 0.5	---	---	30.0 0.5	---	---

R80-1342-038P

samples (3.18 ± 0.47 v/o). The local inhomogenity in volume fraction noted in ground base samples was also present in the flight samples and tended to increase significantly the width of volume fraction distributions observed by morphological measurements.

Thermal Properties

Comparison of thermal data through the solidification temperature was limited to samples in furnace assemblies No. 1 and No. 3 (each sample instrumented with four in situ thermocouples) since these samples had at least one thermocouple terminate within the low-$\bar{g}$ fraction solidified region. The sample in furnace assembly No. 2 was instrumented with only one thermocouple, which terminated beyond the low-$\bar{g}$ interval of solidification.

The thermal profiles of each sample solidified in low-$\bar{g}$ are quite similar to those observed in the 1-$\bar{g}$ comparision experiment. This is shown in Fig. 19 for samples solidified in furnace assembly No. 1; the temperature profile as a function of distance from the solidification interface, as well as the thermal gradients near the solidification interface, are statistically equivalent for all samples, as is shown in Table 1. This distance from the solidification interface was deduced from the time of solidification and furnace velocity, assuming that the location of the interface coincides with the discontinuity in the thermal profile.

Magnetic Properties

The magnetic properties of both the low-$\bar{g}$ flight and 1-$\bar{g}$ All-Systems Test samples were also very similar in that both were dominated by the HC (high coercivity) phase. As shown in Fig. 20 for samples grown in furnace assembly No. 1, the first quadrant demagnetization curves at room temperature (samples first exposed to an applied magnetic field of 150 kOe) indicate a remanent magnetization of 0.1 emu/g of Bi/MnBi. The remanent magnetization data suggest that both the low-$\bar{g}$ and 1-$\bar{g}$ samples contain > 95 v/o HC phase. By deconvoluting the magnetization into HC phase and LTP phase components (Ref 9-12) and normalizing to equivalent /o of dispersed MnBi using correlations established during ground base experiments, we found that the low-$\bar{g}$ samples contained 7 ± 1% less v/o MnBi than the 1-$\bar{g}$ samples as seen in Table 1. The mean 1-$\bar{g}$ value of 3.18 v/o MnBi corresponds to the anticipated nominal value determined for eutectic Bi/MnBi (Ref 7).

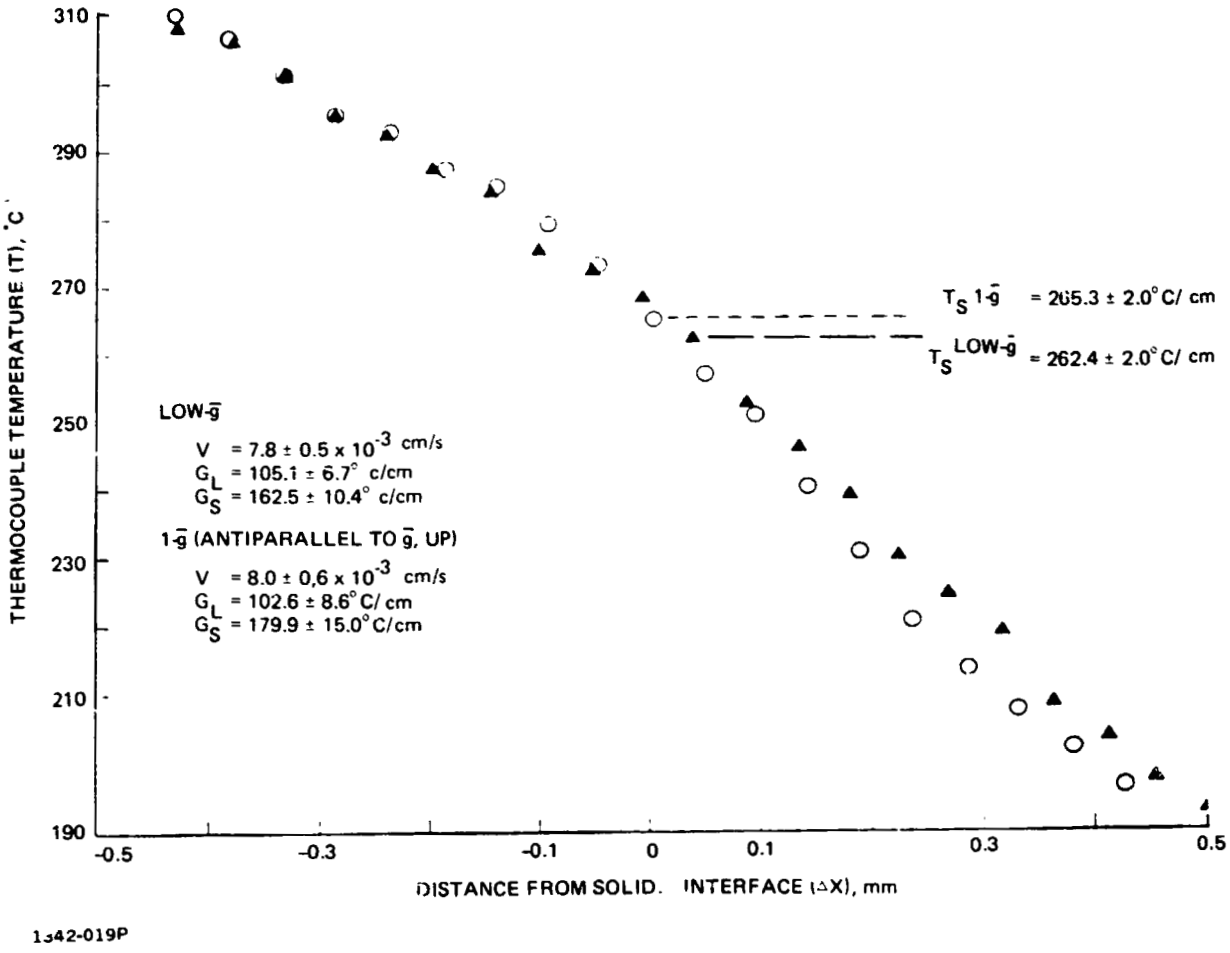

1342-019P

Fig. 19 Comparison of Flight and All Systems Test Thermal Profiles Near Solidification Temperature for Samples Solidified in Furnace Assembly No. 1

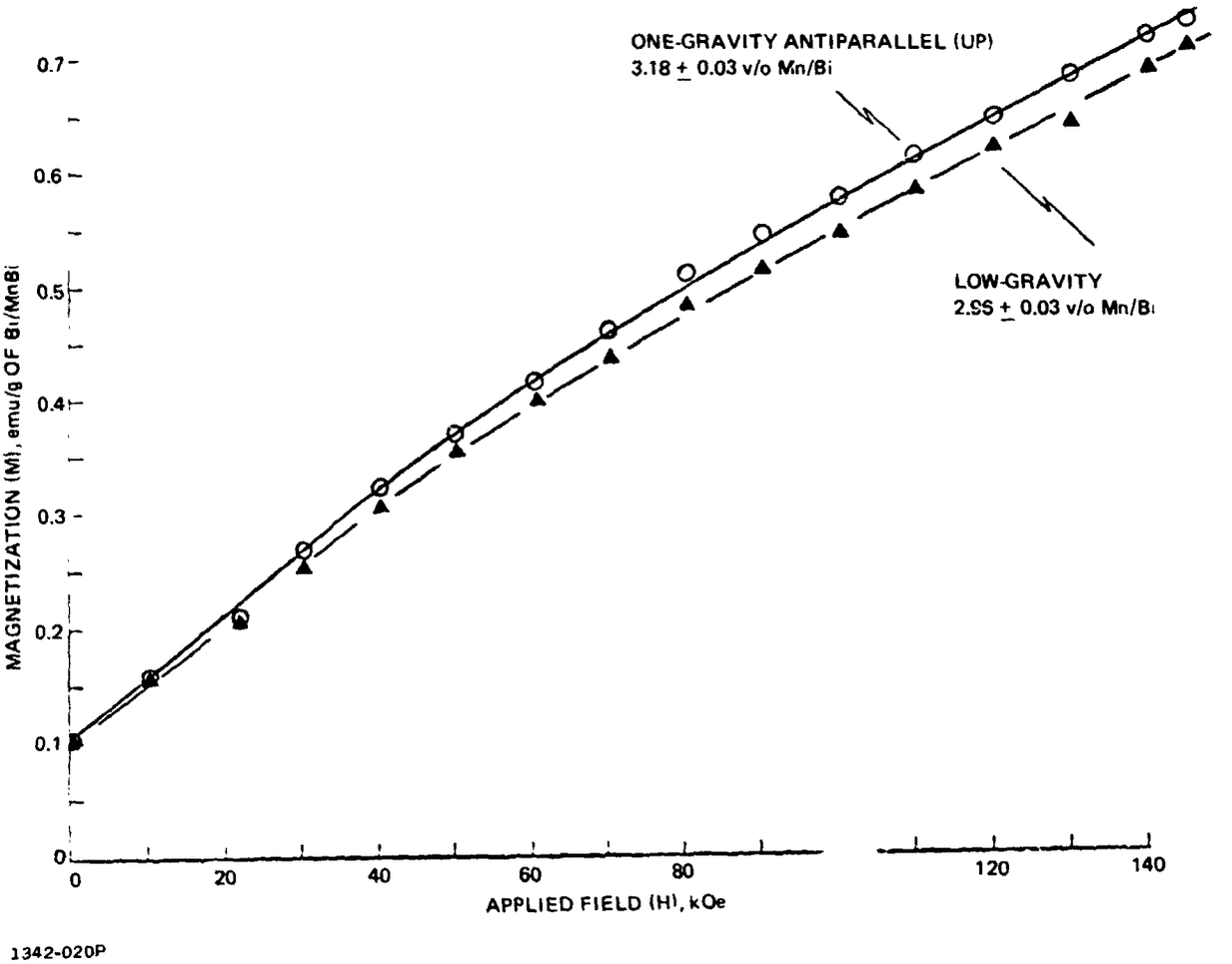

Fig. 20 First Quadrant Demagnetization of Flight vs All Systems Test Samples Solidified During Low-$\bar{g}$ Interval in Furnace Assembly No. 1 Indicating Lower v/o Dispersed MnBi for Low-$\bar{g}$ Sample

In addition, selected flight and ground base comparison samples were isothermally heat treated and their room temperature hysteresis measured after each anneal cycle. Identical fraction solidified segments, corresponding to the low-$\bar{g}$ interval of solidification, were heat treated together in the same apparatus and allowed to cool slowly from the anneal temperature of 220°C. The v/o of dispersed MnBi of both low-$\bar{g}$ and 1-$\bar{g}$ samples remains essentially unchanged from the as-grown state while the intrinsic coercivity of the low-$\bar{g}$ samples, as seen in Fig. 21, is consistently larger with respect to the 1-$\bar{g}$ comparison sample. Also shown in Fig. 21 is a similar study of samples grown in the PIAT test. The higher intrinsic coercivity obtained from the same time at temperature anneal in the low-$\bar{g}$ samples supports the smaller particle size or rod diameter distributions observed in the morphology studies.

A set of postflight samples were also grown in the SPAR VI flight apparatus at General Electric/Valley Forge under PIAT conditions. Those samples were identical in morphology, thermal, and magnetic properties with respect to the preflight All-Systems Test samples, indicating that no anomalies had occurred in the ADSS apparatus as a result of the launch or flight experiment.

Laboratory (1-$\bar{g}$) Experiments - Morphology & Thermal Properties

In the high furnace rate regime of V $\sim$30 cm/h, comparable to the SPAR VI flight, samples were grown up, down, and horizontal to the gravity field in an effort to change the degree of thermal and solutal convection present. However, as pointed out by Coriell (Ref 14), the interaction of the solute and temperature gradients is complex and a priori effects are difficult to estimate. For example, a statically unstable density profile (growth down) without convection, as well as a statically stable density profile (growth up) with convection, can occur.

The first observation is that, regardless of growth orientation, at V $\sim$30 cm/h and G_L $\sim$100°C/cm, there exists significant nonhomogeniety, on a small microscopic scale, in the measured volume fraction of MnBi from region to region, even at the same fraction solidified. The size of each areal region measured was typically $\sim$2500 μm^2 with an average population of 375 $\pm$ 50 particles. This inhomogeniety is shown in Fig. 22 for samples grown up and down during the All-Systems Test. If a suitable number of regions were considered or, conversely, one large-encugh region monitored, the variance in bulk volume fraction was small ($\pm$5% v/o MnBi) compared with a variance in volume fraction as large as $\pm$ 25% for

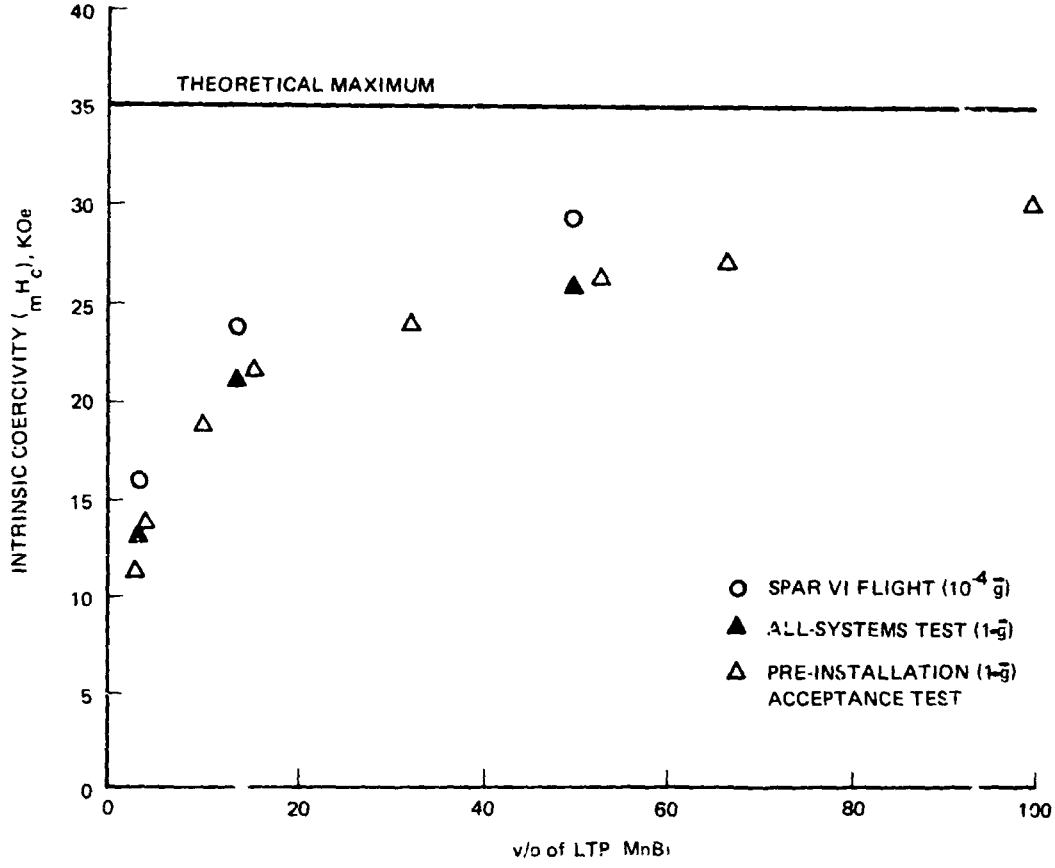

1342-021P

Fig. 21 Effect of Isothermal Annealing of PIAT (Growth up to $\bar{g}$), All-Systems Test (Growth up to $\bar{g}$) and Flight Sample No. 1 on Magnetic Intrinsic Coercivity as a Function of v/o LTP MnBi Transformed. Faster rate of increase in flight sample suggests smaller rod diameter distribution for sample solidified in low $\bar{g}$.

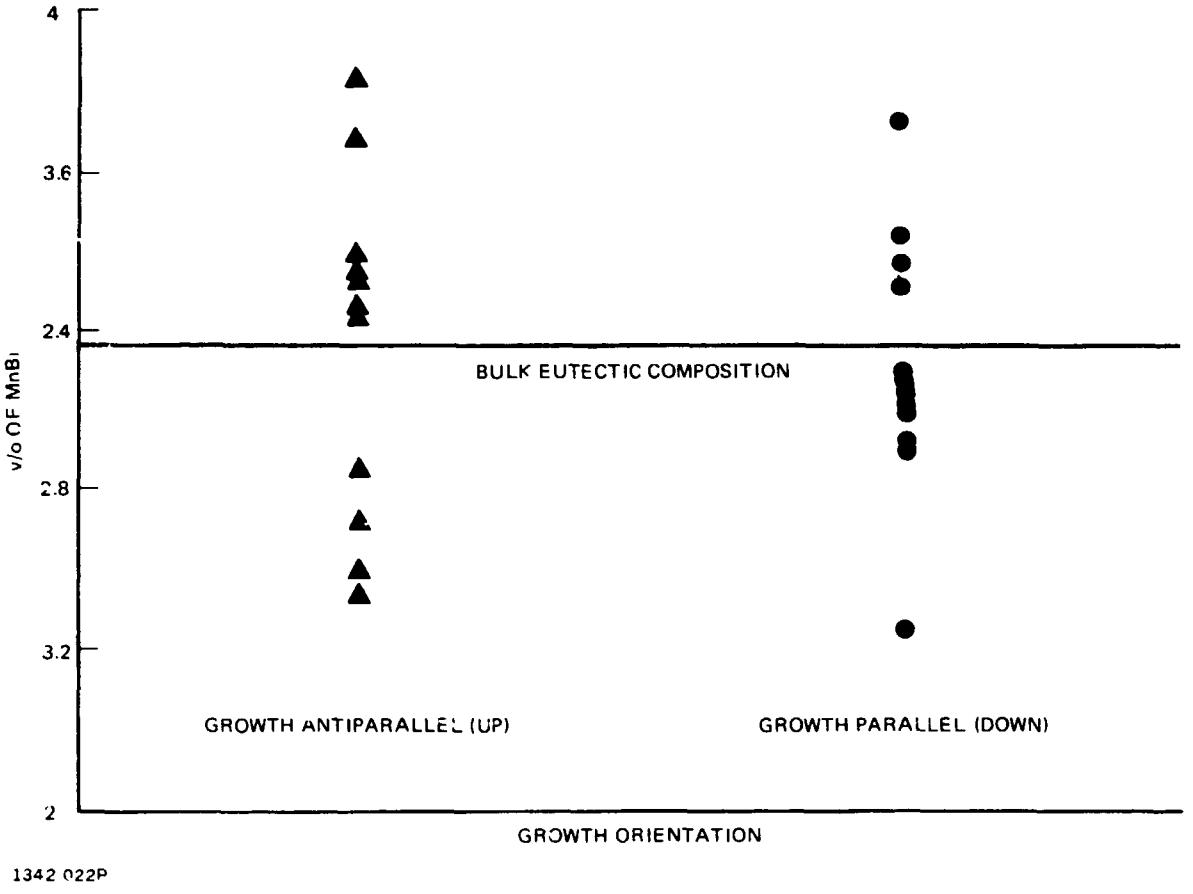

Fig. 22 Local Volume Fraction Measured by Computed-Aided Particle Analysis for Growth Up and Down at V = 30 cm/hr and $G_L = 100^{o}$ C/cm

each areal region. In any case, the mean volume fraction corresponded to the bulk eutectic composition of 3.18 v/o MnBi. Both the rod diameter and interrod spacing distributions were also rather insensitive to growth orientation. As is shown in Fig. 23 and 24, the shape and mean of both the rod diameter and interrod spacings are quite similar in each orientation even though growth down has a larger median and asymmetry than growth up or horizontal Statistically, the distributions are equivalent. The thermal profiles for each growth orientation were also very similar at these high furnace rate and thermal gradient conditions.

Samples were also grown at one order of magnitude lower furnace velocity ($V \sim 3$ cm/h) in both high ($G_L \sim 150°C/cm$) and low ($G_L \sim 20°C/cm$) thermal gradients. It was anticipated that, at the lower growth velocity, the solute boundary layer or Stefan length, p^{-1}, would be increased from ~ 25 μm at $V = 30$ cm/h to 250 μm at $V = 3$ cm/h where

$$p^{-1} = D_L/V \qquad (2)$$

and V is the interface or growth velocity, and D_L is the diffusion coefficient in the liquid at the eutectic composition, taken to be 2×10^{-5} cm^2/s. The calculated mass transfer film thickness, δ_m, however, assuming that a vertical flat plate-type model is appropriate (Ref 5), is expected to be on the order of 50 μm for $G_L = 150°C/cm$ and 80 μm for $G_L = 20°C/cm$, where

$$\delta_m = (Pr/2.41\ Sc)^{1/3}\ L \left\{(1 + [0.95/Pr])/Pr(\bar{g}\,\alpha\,\Delta T L^3/\gamma^2)\right\}^{1/4}$$

and Pr = Prandtl number

Sc = Schmidt number

L = characteristic length or diameter of the ampoule

$\bar{g}$ = magnitude of the gravitational force

α = percent change in liquid density with temperature

ΔT = temperature difference in the system

γ = kinematic viscosity.

Notice that δ_m is not a function of V and varies with $\bar{g}^{1/4}$. For $G_L = 150°C/cm$, the ratio δ_m/p^{-1} or $p\,\delta_m$ would be expected to vary from 2 at $V = 30$ cm/h to 0.2 at $V = 3$ cm/h and we would, therefore, expect convection to have a greater influence at the lower growth velocity since convection should become increasingly more important as a mass transport mechanism as $p\,\delta_m \longrightarrow 0$ while diffusion dominates for $p\,\delta_m >> 1$.

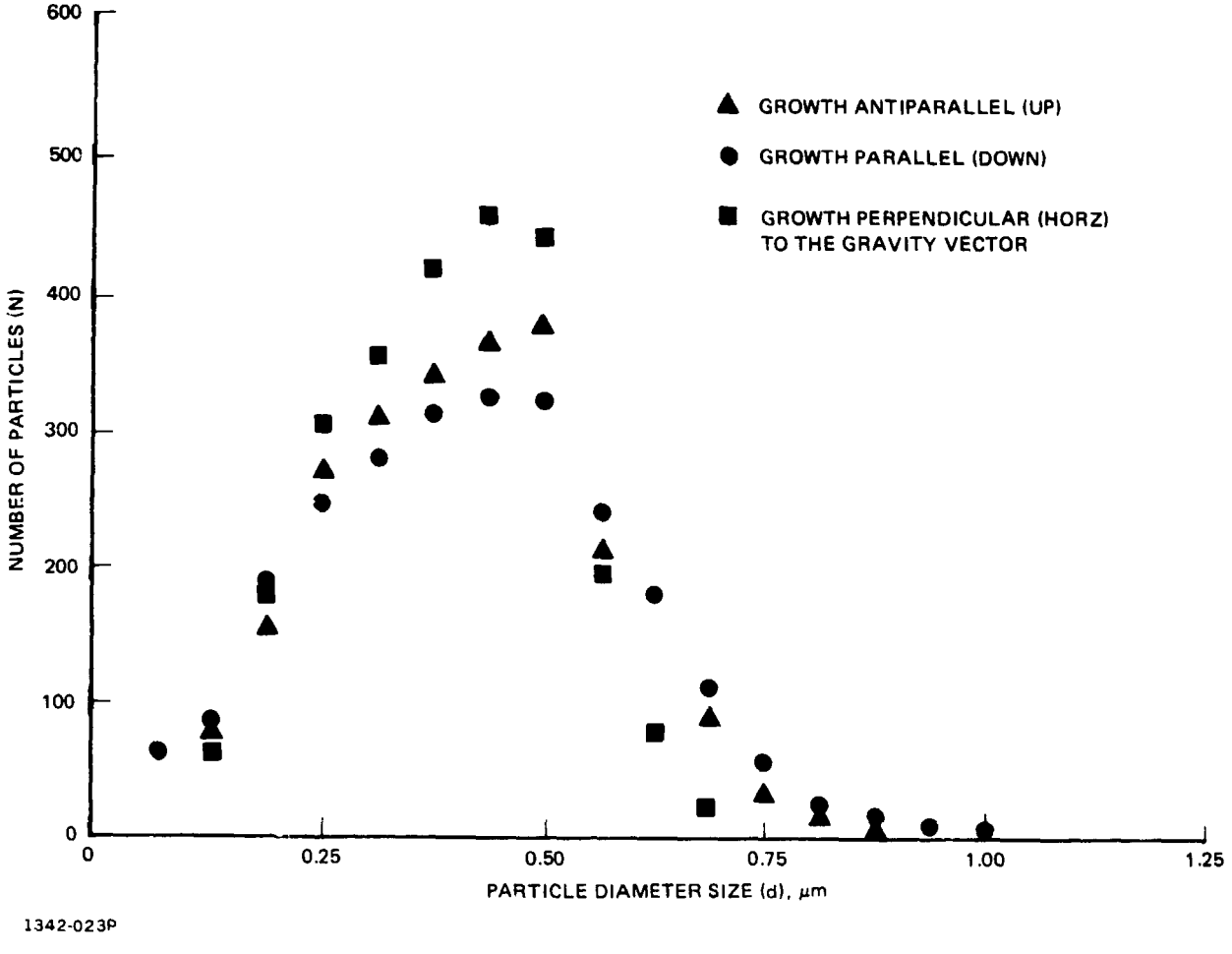

Fig. 23 Dispersed MnBi Rod Diameter Distributions as a Function of Solidification Orientation Axis in 1-$\tilde{g}$ at V=30 cm/hr and $G_L = 100^o$ C/cm

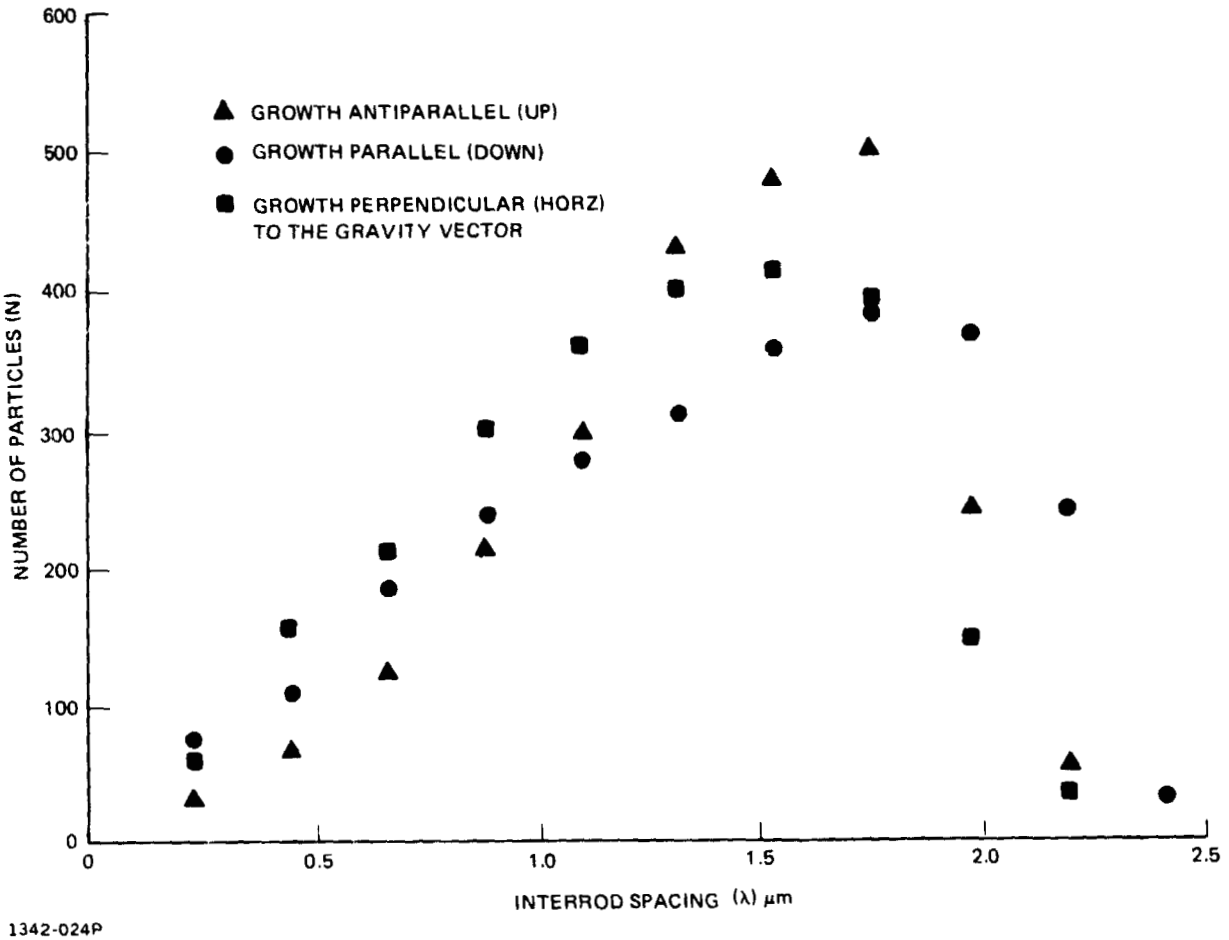

Fig. 24 Interrod Distributions of Dispersed MnBi Rods Measured Transverse to Solidification Direction as a Function of Growth Orientation at V=3 0 cm/h and G_L = 100° C/cm

The morphology of the lower growth velocity samples, however, also showed no dependence on growth orientation with respect to the gravity vector. As is shown in Fig. 25, the interrod spacing distributions are statistically equivalent for growth up, down, and horizontal. In addition, no change in either rod diameter or interparticle spacing (Fig. 26) was noted on decreasing the thermal gradient in the liquid by nearly an order of magnitude ($G_L \sim 150°$ to 20°/cm). Similar studies on directionally solidified eutectic Bi/MnBi grown in larger diameter (0.7 cm inner diameter) quartz ampoules (Ref 15) have also shown no dependence of interrod spacing on thermal gradient. In addition, the inhomogeniety in local volume fraction was noted as well for $V \sim 3$ cm/h (Fig. 27).

In situ thermal measurements as a function of solidification time for $V \sim 3$ cm/h and $G_L \sim 20°C/cm$ for growth up, down, and horizontal orientations were also investigated. A typical temperature vs time profile for a growth up orientation is shown in Fig. 28. The discontinuous change in slope or thermal gradient observed in the thermogram occurs at the solidification or eutectic melting temperature and is the result of a discontinuous change in thermal conductivities between liquid ($K_L = 0.12$ $Wcm^{-1}K^{-1}$) and solid ($K_S = 0.06$ $Wcm^{-1}K^{-1}$) Bi/MnBi. The thermal gradients were deduced from the thermocouple thermograms by calculating the instantaneous slope for each temperature interval and averaging in a stepwise fashion over six consecutive measurements. The effect of varying the growth orientation on the resultant gradients with respect to the position of the solidification interface is displayed in Fig. 29. The experiment was conducted so as to maintain a similar gradient in the liquid near the solidification interface, regardless of orientation, by adjusting the temperature of the hot zone of the furnace. Hence, any effect of orientation of $\bar{g}$ would occur in the observed gradient of the solid. In fact, such an effect is observed with a steeper gradient for growth down (thermally unstable) compared with growth up (thermally stable).

Laboratory (One-Cravity) Experiments - Magnetic Properties

The volume percent of HC phase formed (normalized to v/o of dispersed MnBi) is a sensitive function of solidification processing conditions. By varying the furnace velocity over approximately two orders of magnitude, the amount of HC varies from ~10 to ~100 v/o as shown in Fig. 30. The amount of HC phase also

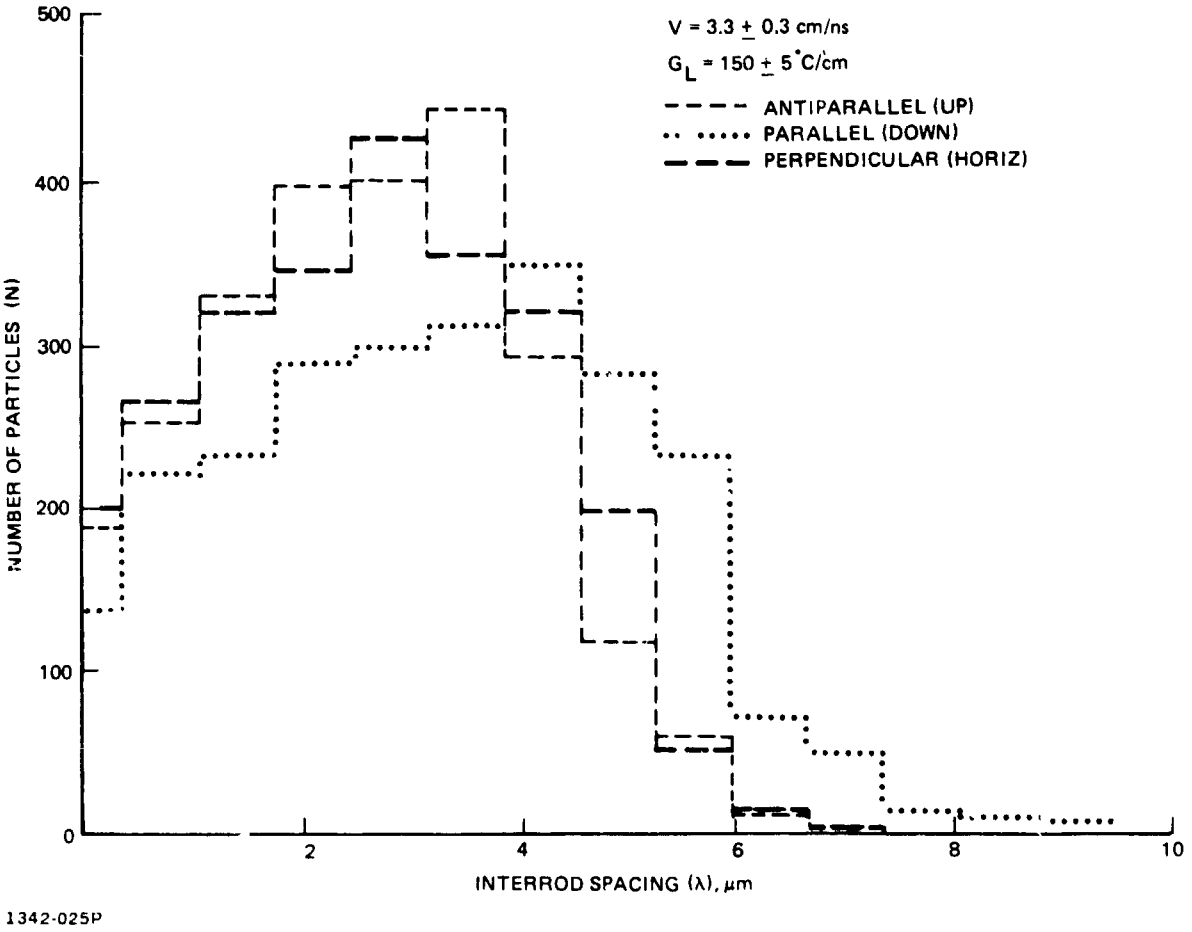

Fig. 25 Interrod Spacing Distributions as a Fu :tion of Solidification Direction in 1-$\bar{g}$ at V=3 cm/h, G_L = 150° C/cm

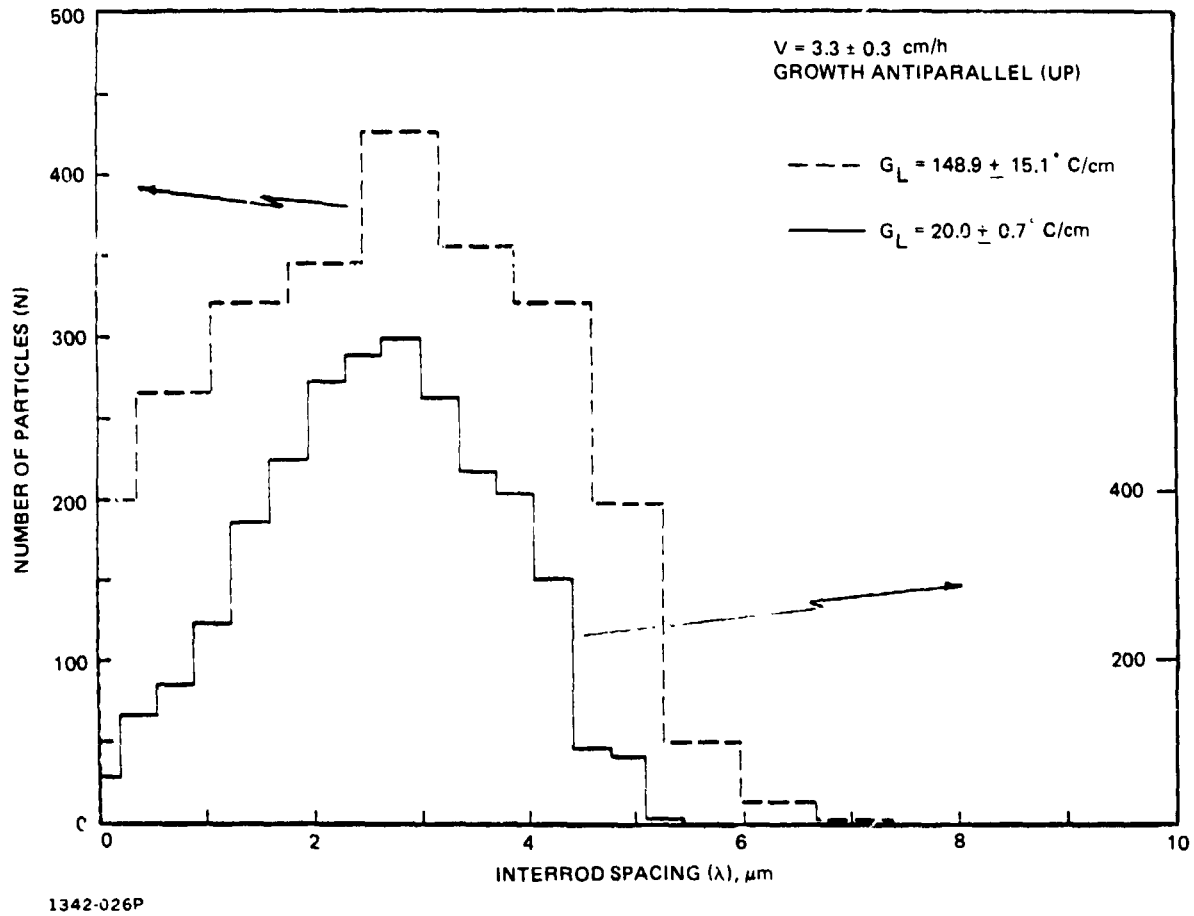

Fig. 26 Interrod Distribution Growth Up in 1-$\bar{g}$ as a Function of Thermal Gradient in Liquid Near Solidification Interface

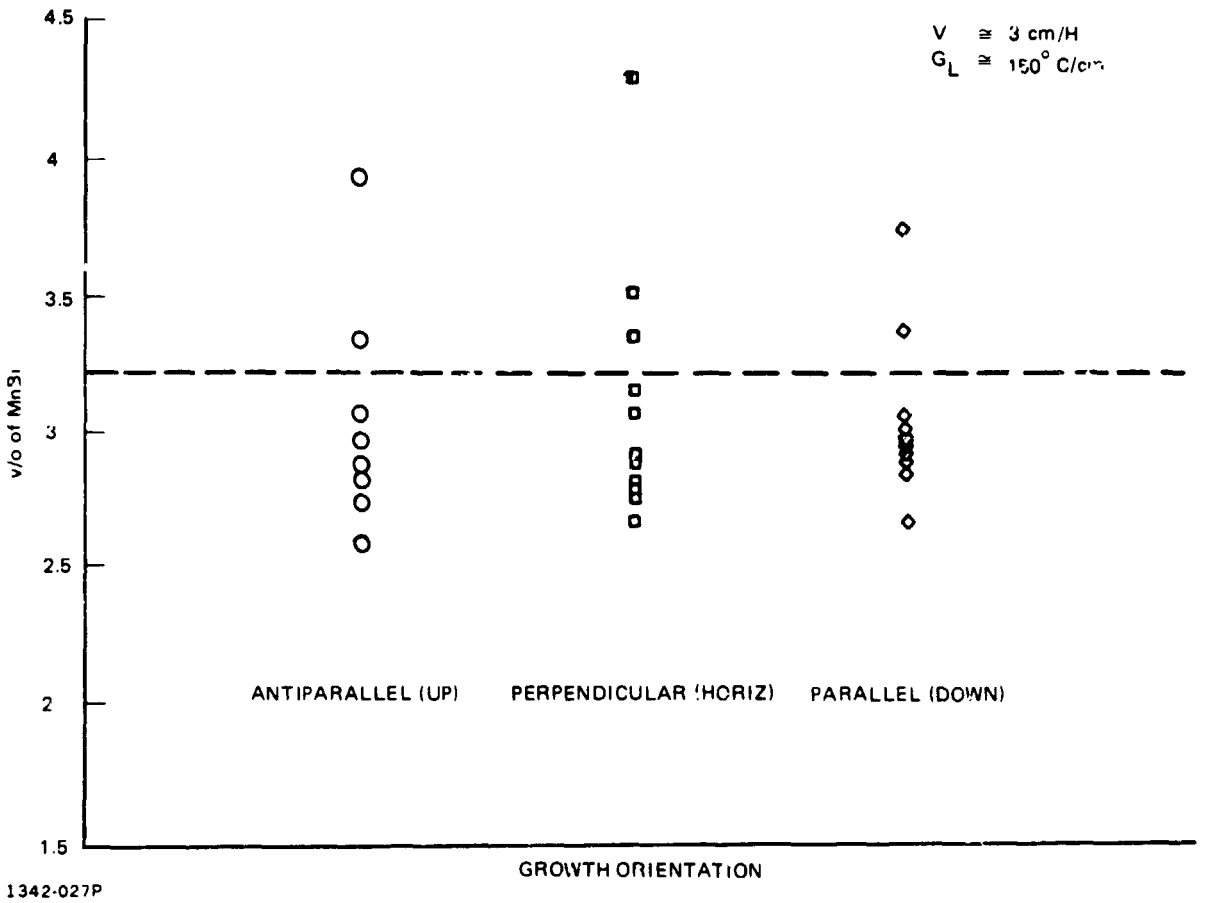

Fig. 27 Measured Local Volume Fraction as a Function of Solidification Orientation in 1-$\bar{g}$ for V=3 cm/h and G_L = 150° C/cm

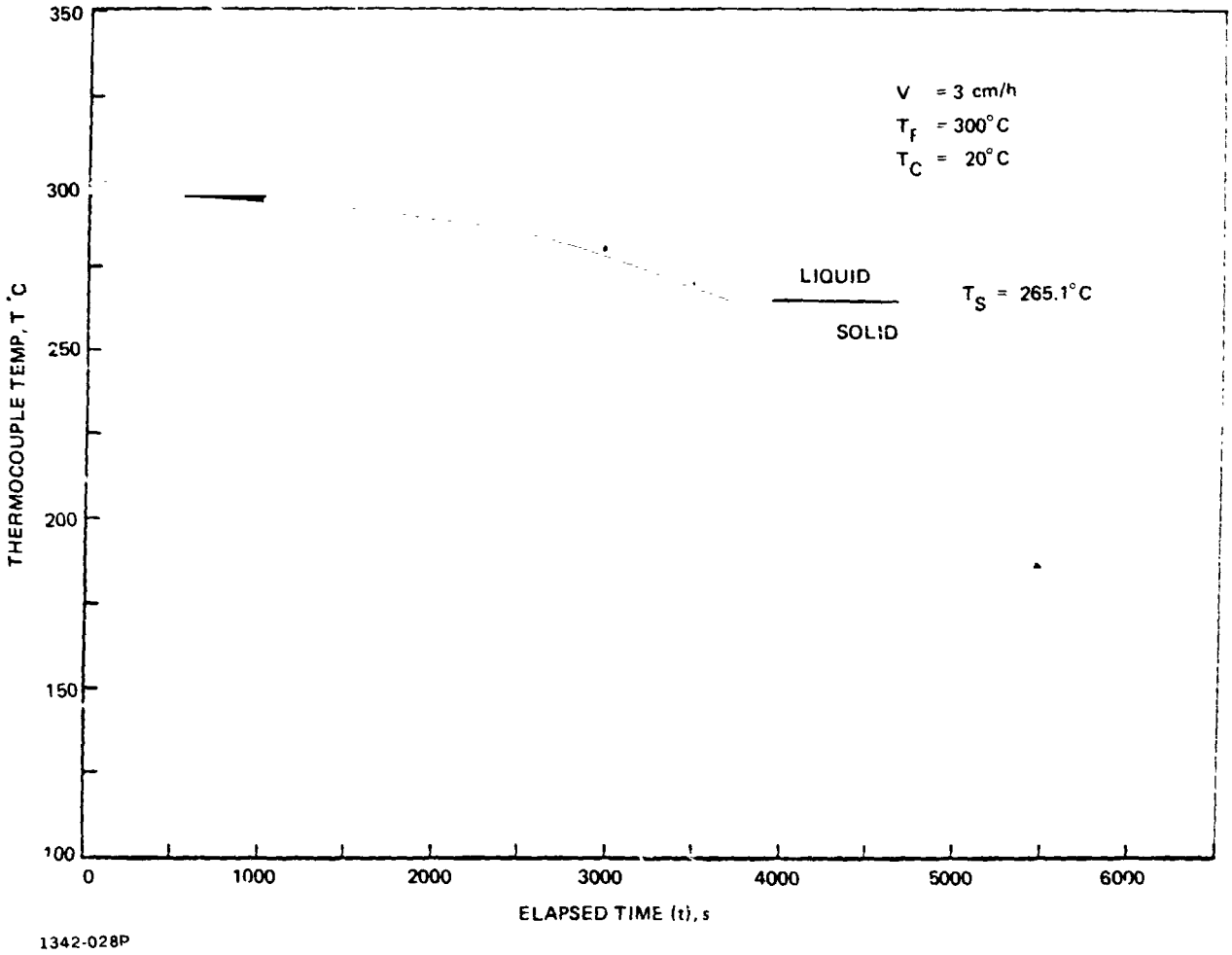

Fig. 28 In Situ Thermocouple Temperature Profile for Plane-Front Solidification of Bi/MnBi Grown Up with Respect to the Gravity Vector

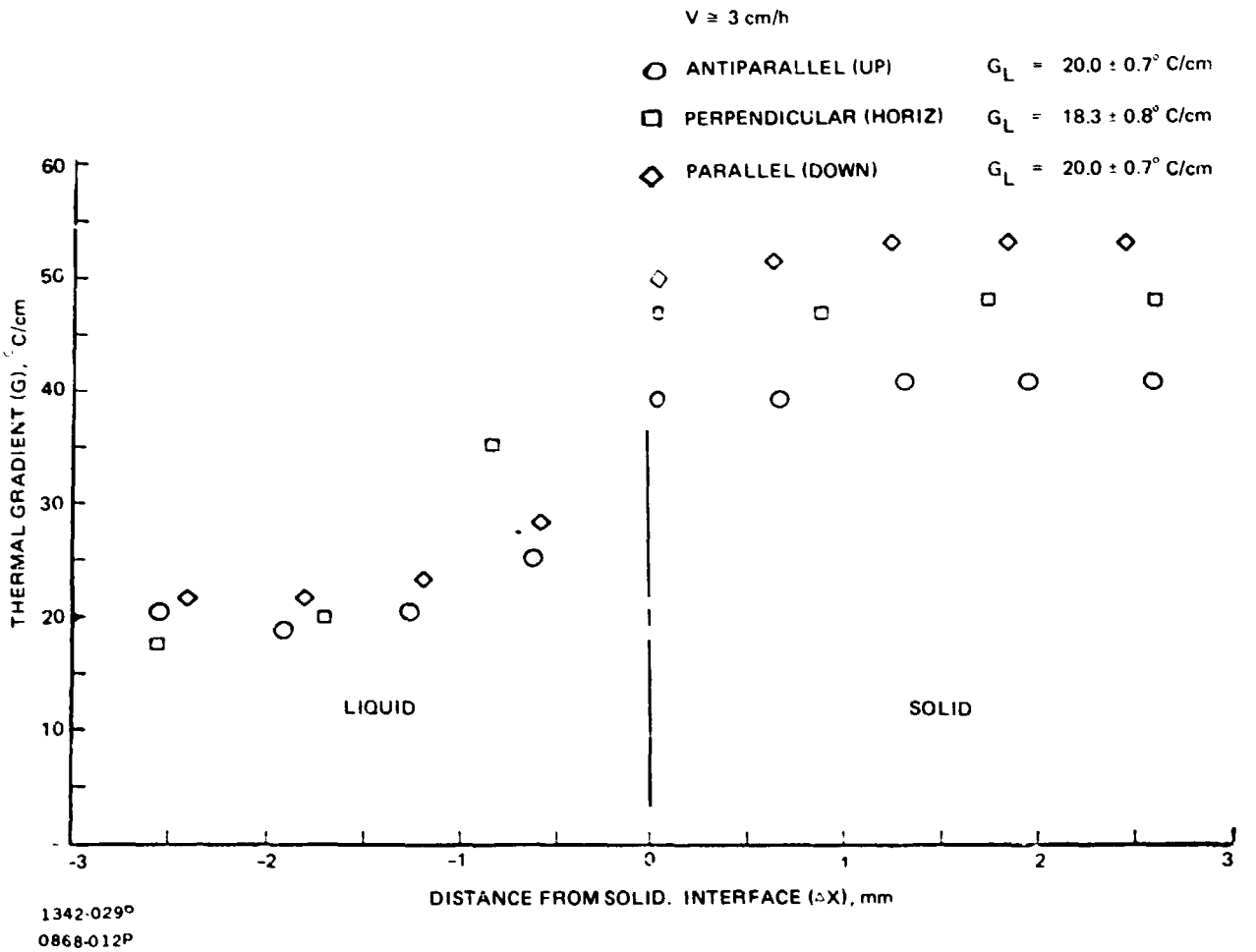

Fig. 29 In Situ Measured Thermal Gradient as a Function of Distance from Solidification Interface

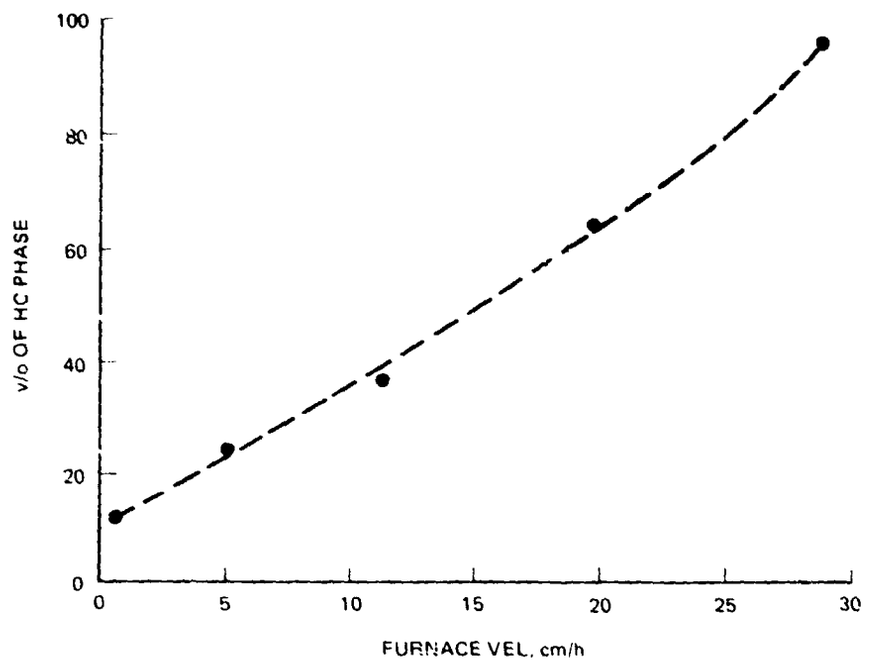

1342-030P

Fig. 30 Volume Percent of HC Phase (Normalized to Dispersed v/o MnBi) as a Function of Furnace Velocity

depends on the thermal gradient in a given growth orientation as well as the growth orientation at a given furnace velocity and thermal gradient as displayed in Fig. 31. By varying the solidification processing conditions, we have been able to isolate the magnetic behavior of the HC phase and, after appropriate heat treatment, the LTP phase in the same plane-front directionally solidified eutectic Bi/MnBi sample as seen in Fig. 32 and 33. In this way, physical observables such as the bulk v/o of dispersed MnBi can be determined from magnetization measurements.

Magnetization as a function of various angles with respect to the solidification direction was also investigated. Samples containing combinations of LTP and HC phases, as well as those containing only the LTP phase, were studied. The expected anisotropy in intrinsic coercivity was observed in all samples suggesting that the c-axis of the hexagonal NiAs structure of LTP MnBi (easy axis of magnetization) lies parallel to the solidification direction regardless of the amount of HC phase present. By monitoring the remanent magnetization as a function of angle with respect to the solidification direction, the degree of alignment of the MnBi rods can be determined since the remanent magnetization is maximum parallel to the solidification direction (long axis of the rods) and zero perpendicular, and should, theoretically, follow a cos θ behavior for an ideal alignment. Figure 34 shows that the All-Systems Test samples were almost perfectly aligned with a variance of $\pm 2°$. In addition, the magnetic properties of the All-Systems Test (1-$\bar{g}$ comparison to SPAR IV flight samples) samples indicated that they contained >95 v/o HC phase regardless of growth orientation at $V \sim 30$ cm/h and $G_L \sim$ 100°C/cm.

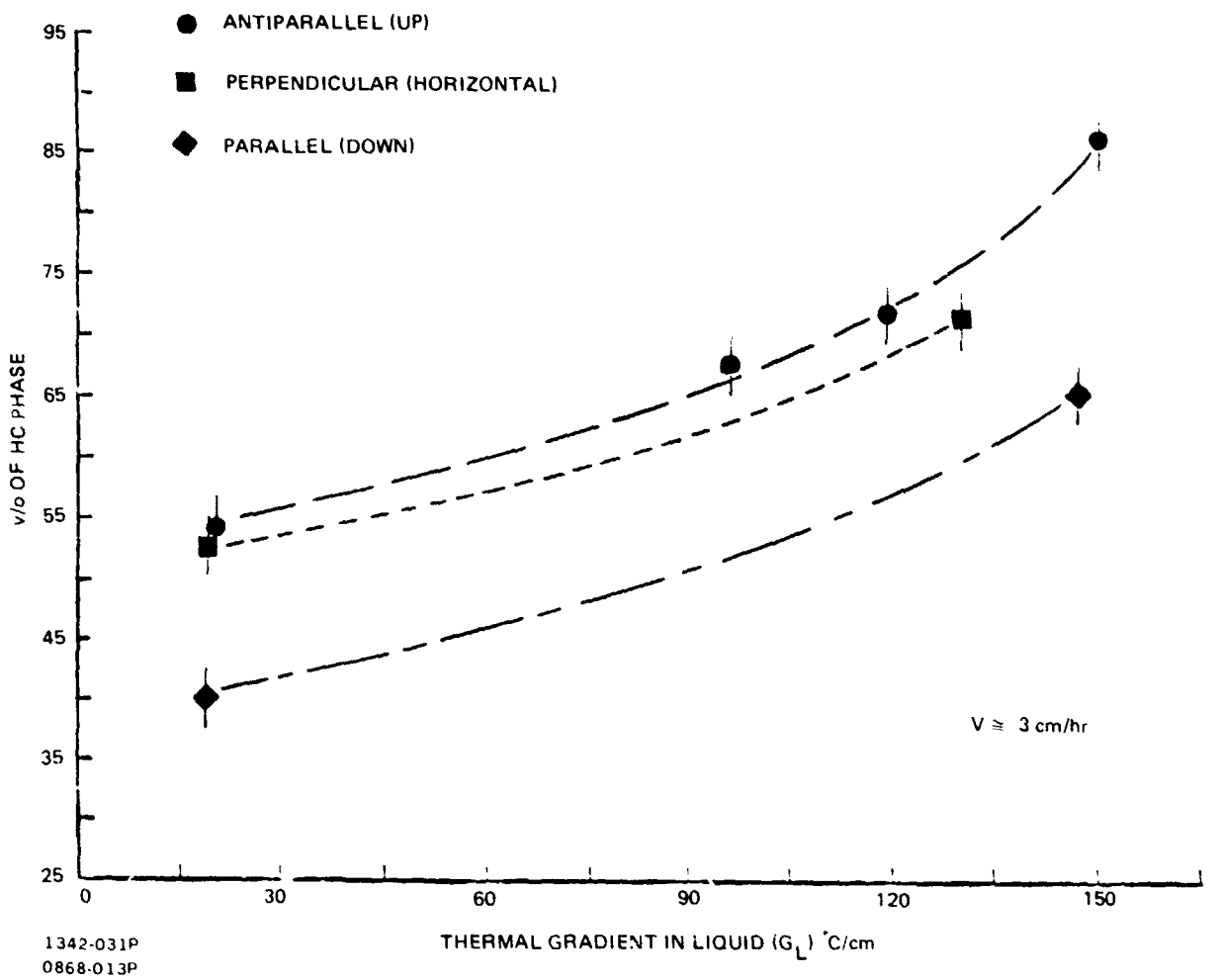

Fig. 31 Effect of Thermal Gradient and Gravity Vector Orientation During Solidification on Formation of HC Phase

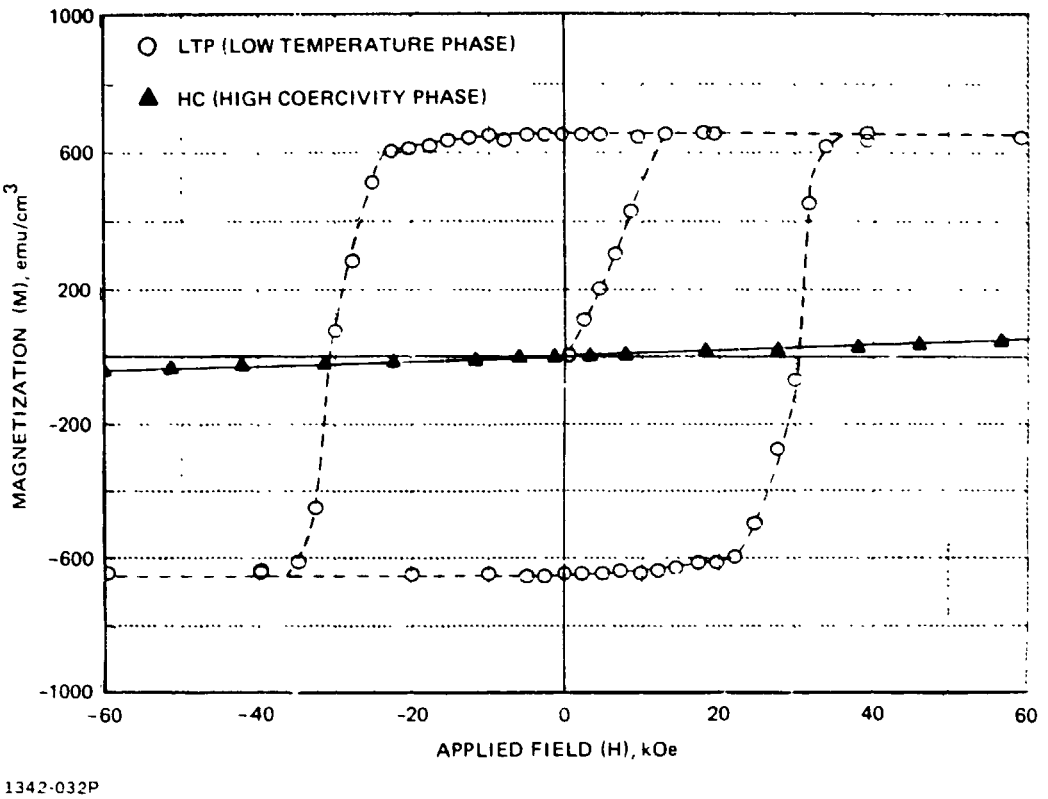

Fig. 32 Magnetization per Unit Volume of Dispersed MnBi at 290 K Parallel to Solidification Direction for a Sample with Average Rod Diameter $< d > = 0.4\ \mu m$ in the As-Grown State (▲) Containing >99 v/o HC Phase and Fully Annealed (o) Containing only LTP Phase

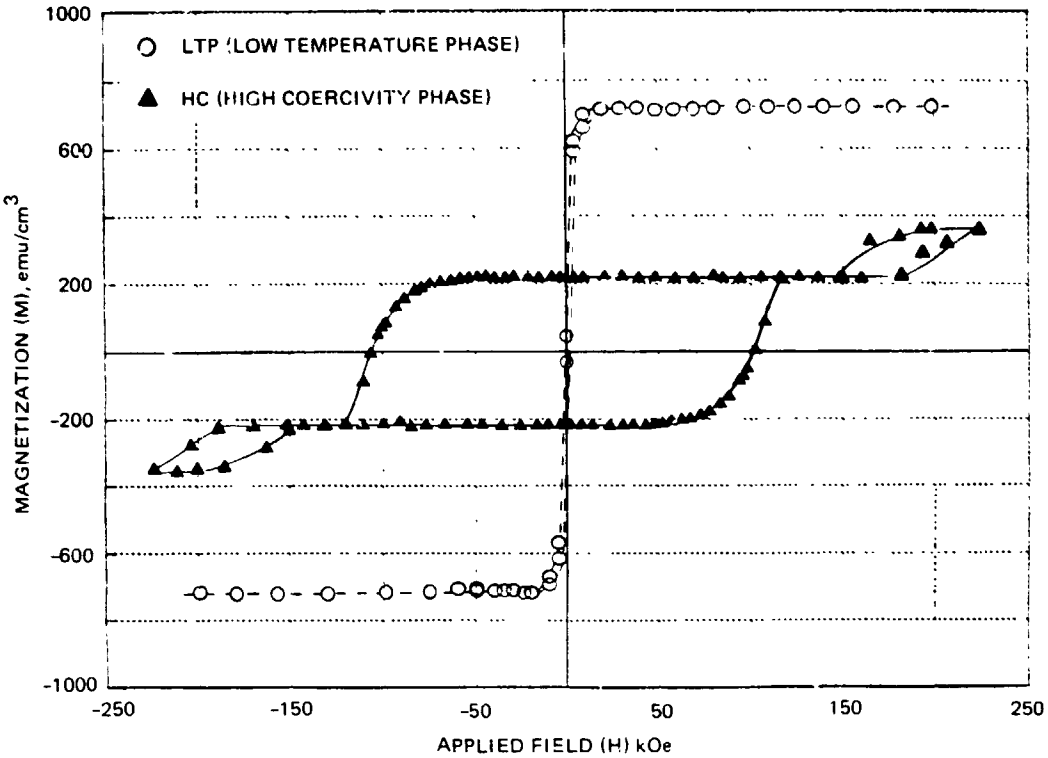

Fig. 33 Hystersis Curve at 77 K Parallel to Solidification Direction for Sample Displayed in Fig. 32

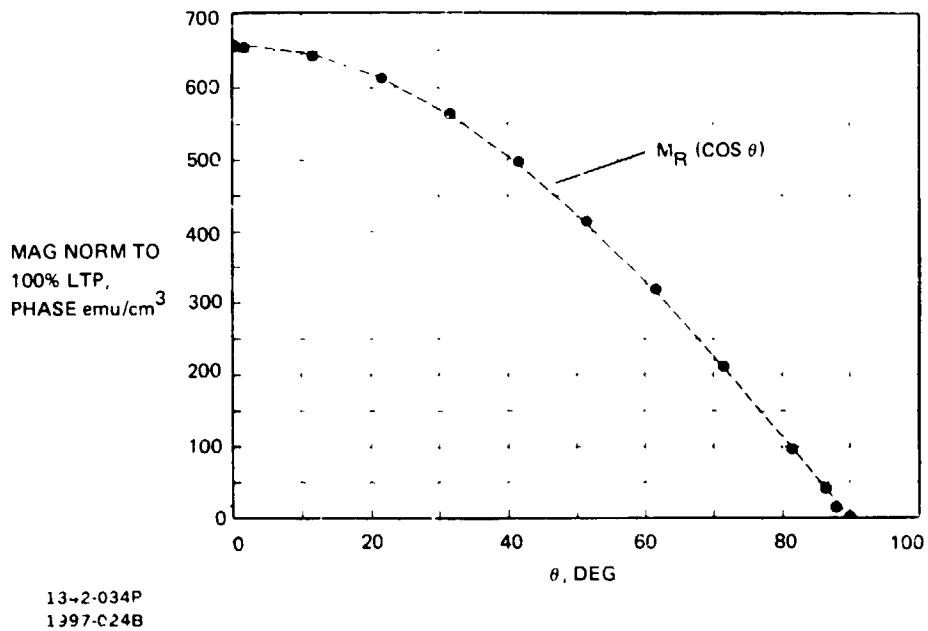

Fig. 34 Remanent Magnetization as a Function of Solidification Direction of LTP MnBi Component for Sample Containing Both LTP and HC Phases

DISCUSSION

CANDIDATE MECHANISM - Low-$\bar{g}$ vs 1-$\bar{g}$ DIFFERENCES

It has been observed that one effect of thermal convection, in plane-front solidification processing, is to introduce temperature fluctuations in the melt when the temperature gradient exceeds a critical value that depends on intrinsic properties of the particular system being solidified (Ref 16-21). Specifically, when the ratio of buoyancy forces to viscous forces in the liquid (Rayleigh number, N_{RA}) exceeds a critical value, regular or oscillatory temperature fluctuations may occur. At very high values of N_{RA}, these fluctuations may become irregular and are thought to represent turbulent flow.

When these temperature fluctuations reach the liquid-solid interface, they may induce nonsteady-state interface motion. For oscillatory fluctuations, the interface would periodically decelerate before moving forward again. Such oscillatory or irregular interface movement would increase as the fluctuations increase (higher thermal gradient). One result of the unsteady interface motion for growth of a rod eutectic might be to decrease the mean interface or growth velocity assuming that insufficient time was available for the rod spacing to adjust to an increasing growth velocity during the period of oscillation by, for example, a branching-type mechanism. As the gravitational force is decreased and the buoyancy forces are reduced (smaller Grashof number, N_{GR}), the amplitude of oscillations would decrease until the interface motion achieved steady state (low-$\bar{g}$), resulting in a higher mean growth velocity that should approach the furnace velocity.

As a result of an increase of mean growth velocity moving from 1-$\bar{g}$ to low-$\bar{g}$, one would expect the relation between rod spacing, λ, total interface undercooling, ΔT and growth or interface velocity, V, to reflect this difference. As is shown in Fig. 35, a schematic illustration of the Hunt and Jackson type function (Ref 22), relating interfacial undercooling to mean growth velocity,

$$\Delta T = AV\lambda + B/\lambda \qquad (4)$$

where A and B are constants that depend on the particular alloy system, suggests that an increase in V (V to 2V) could result in a simultaneous decrease in λ and increase in ΔT. One effect of a change in undercooling would be to alter the

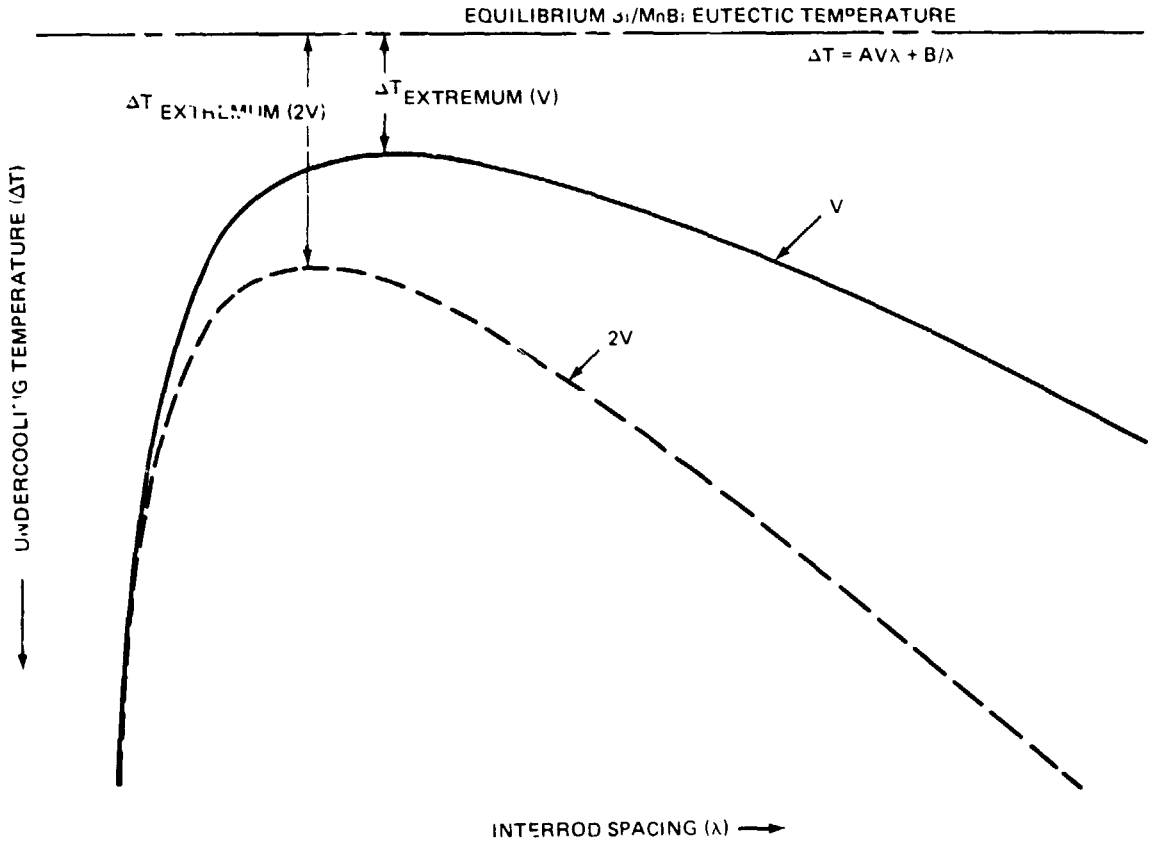

1342-035P

Fig. 35 Hunt-Jackson Relation Among Undercooling of Eutectic Melting Point, Growth Velocity, and Mean Interrod Spacing

phase diagram in the vicinity of the eutectic as shown in Fig. 36. The limit of solid solubility would be increased as would the eutectic composition. However, since Bi/MnBi is a rather low volume fraction eutectic with asymmetrical liquidus slopes near the eutectic composition, a decrease would be anticipated in both weight fraction MnBi (assuming the stoichiometry of MnBi remains at 50 a/o) as well as volume fraction of dispersed MnBi. In fact, such a decrease in MnBi volume fraction was observed in our low-$\bar{g}$ solidified samples.

There are, of course, other explanations that may be responsible for the observed differences between 1-$\bar{g}$ and low-$\bar{g}$. These include the influence of convectively driven fluid flow or the magnitude of the gravitional force on heat and mass transport coefficients and interfacial energies leading to different boundary growth conditions in 1-$\bar{g}$ and low-$\bar{g}$.

1-$\bar{g}$ EFFECTS

The lack of sensitivity of morphology to various levels of convection for samples grown in 1-$\bar{g}$ may indicate that, for boundary layer thicknesses equal to or larger than interrod spacings ($\delta_m \geq \lambda$), the presence of convection has little direct effect on the spacing or rod diameter distributions (Ref 23) of eutectic Bi/MnBi. Even at the lower growth velocities investigated, V = 3.0 cm/h, $\lambda \sim 3$ μm, which is much smaller than the predicted $\delta_m \sim 50$ μm, suggesting that the eutectic is tightly coupled. At this lower growth velocity, however, $p\delta_m \sim 0.2$, which would be expected to lead to, for example, severe convectively-driven macrosegregation for plane-front directionally solidified off-eutectic Bi/MnBi, indicative of a strong convective influence. In fact, such macrosegregation has been observed for Bi-rich off-eutectic Bi/MnBi bulk starting compositions (Ref 24). The variation in observed thermal gradients for eutectic Bi/MnBi grown at V~ 3 cm/h and $G_L \sim 20°C/cm$ ($p\delta_m \sim 0.3$), as a function of growth orientation with respect to $\bar{g}$, also shows a convective effective. Lastly, the amount of metastable magnetic MnBi phase produced in directionally solidified Bi/MnBi varies strongly with growth orientation in 1-$\bar{g}$. The origin of this dependence may be due to the different cooling rates (anneal time at temperature) experienced in different growth orientations or may be indicative of the convective flows or thermal instabilities present at the liquid-solid interface during solidification in 1 $\bar{g}$.

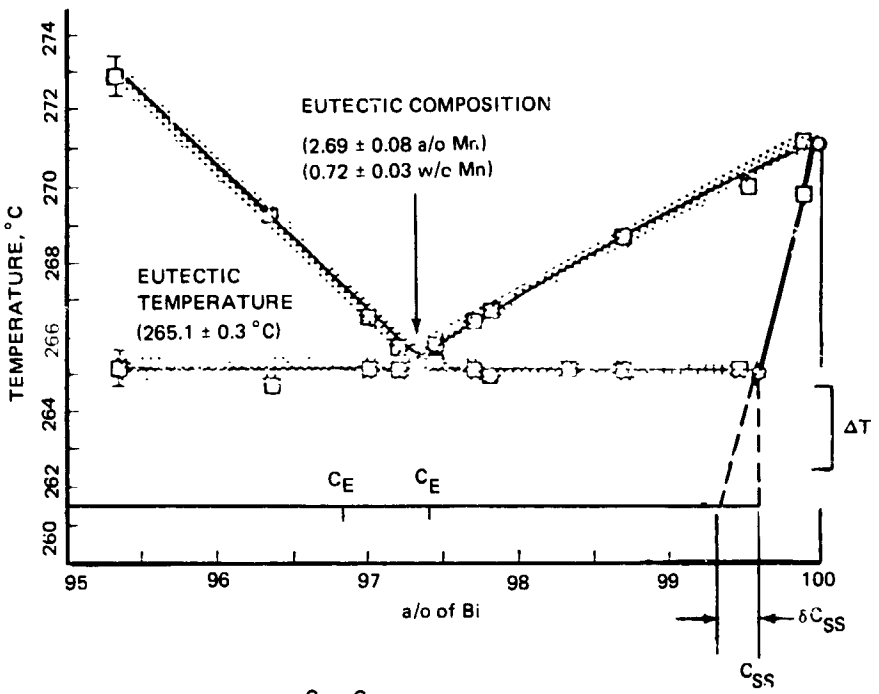

$$\text{WEIGHT FRACTION MnBi} = \frac{C_E - C_{SS}}{C_{MnBi} - C_{SS}} \equiv F$$

$$\frac{\delta F}{F} = \frac{\delta C_{SS}}{C_{E'} - C_{SS}} \cdot \frac{C_{MnBi} - C_{E'}}{C_{MnBi} - C_{SS}}$$

FOR $\Delta T \sim 3°C$, $\delta F/F \sim 7\%$

1342-036P

Fig. 36 Effect of Interfacial Undercooling on Equilibrium Diagram and Weight Fraction MnBi in Vicinity of Eutectic

PRINCIPLE OF PHYSICAL SIMILARITY

It has been recently noted (Ref 25) that additional insight as to the influence of gravity on crystal growth may be obtained by applying the principles of physical similarity to the specific system under investigation on earth and in the microgravity of space. It is necessary to identify a complete set of physical observables that characterize physical phenomena that occur in each system, i.e., 1-$\bar{g}$ of earth and low-$\bar{g}$ of space. It is usually chosen to select dimensionless groups that contain the gravitational force, $\bar{g}$. The corresponding dimensionless groups may be chosen to be $\bar{g}$ divided by some other characteristic acceleration; for example, in the case of thermally driven convection, this characteristic acceleration may be taken to be

$$a_{char} = \gamma^2/(\alpha \Delta T\ L^3) \qquad (5)$$

where γ is the kinematic viscosity, α the percent change in liquid density with temperature, ΔT the temperature difference in the system, and L the charcteristic length. The resulting dimensionless group is then the Grashof number, N_{Gr}

$$N_{Gr} = \bar{g}\ (\alpha \Delta T\ L^3/\gamma^2) \qquad (6)$$

If temperature fluctuations are responsible for a decrease in mean interface velocity, then these fluctuations should be proportional to the Grashof number through the buoyancy forces (gravitational force) and temperature difference of the system. By reducing the gravitational force, we can vary the effective interface velocity with a higher mean velocity and lower MnBi interrod and rod diameter length in low $\bar{g}$.

We have also observed, however, that the microstructure achieved in low $\bar{g}$ ($V \sim 30$ cm/h, $G_L \sim 100°C/cm$) can be duplicated in 1-$\bar{g}$ by growing at a sufficiently higher furnace velocity ($V \sim 50$ cm/h, $G_L \sim$ 0°C/cm) since $\langle d \rangle$, $\langle \lambda \rangle \sim V^{-1/2}$. This behavior for interparticle spacing distributions is shown in Fig. 37. For the growth conditions used in 1-$\bar{g}$, however, the limit of the ADSS apparatus to remove heat in a unidirectional manner is near its limit. Experiments conducted $V \sim 60$ cm/h and $G_L \sim 100°C/cm$ have indicated the onset of severe interface curvature and noncooperative growth, presumably because the temperature at which solidification occurs is no longer within the adiabatic region of the

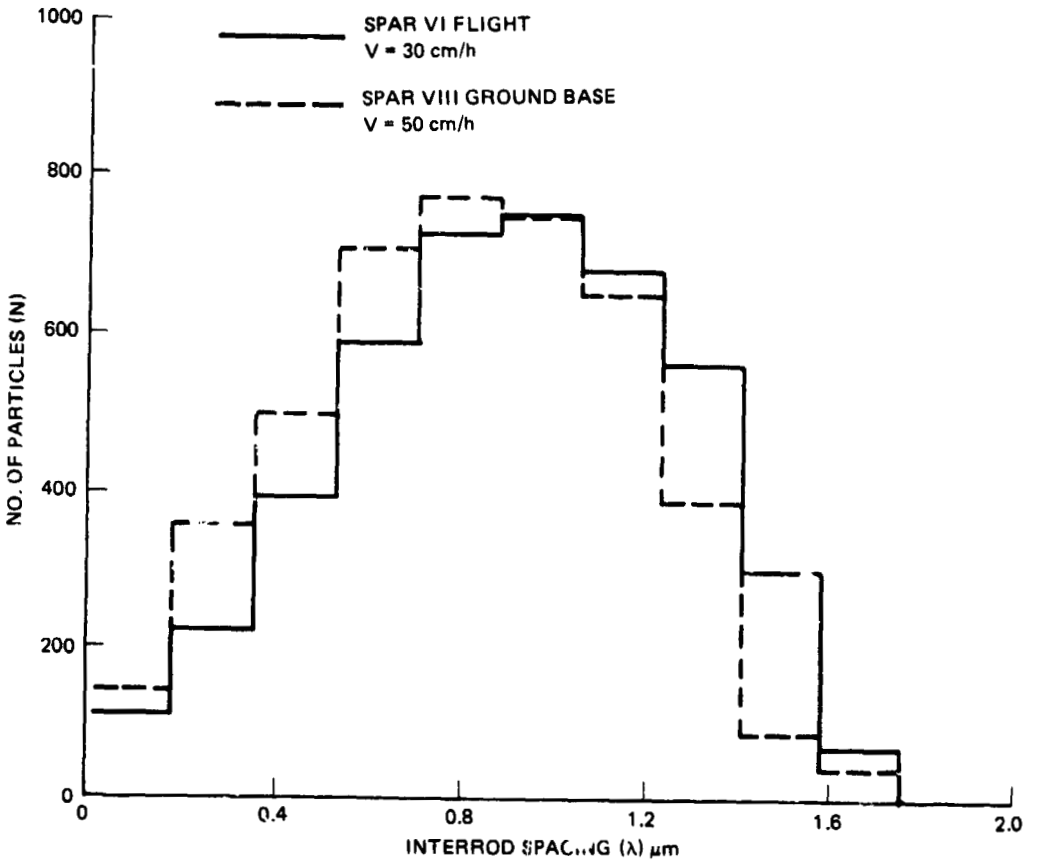

1342-037P

Fig. 37 Comparison of Measured Interrod Spacing Distributions for SPAR VI Flight Sample No. 1 (V = 30 cm/h, G_L = 100° C/cm) and Higher Growth Velocity Ground Base (1-$\bar{g}$) Sample Grown Antiparallel with Respect to Gravity Vector (V = 50 cm/h, G_L = 100° C/cm)

ADSS furnace assembly at these growth conditions. Heat transfer is thus no longer one dimensional. It may, therefore, be possible to achieve microstructures and corresponding magnetic properties for eutectic Bi/MnBi, comparable to a higher furnace velocity, in low-$\bar{g}$ that are impossible to achieve in 1-$\bar{g}$ using the same furnace assembly.

SUMMARY & FUTURE WORK

An experimental investigation of a reduced gravity environment during the SPAR VI flight and the effect of gravity vector orientation in 1-$\bar{g}$ on the plane front directional solidification of eutectic Bi/MnBi has shown:

- Statistically significant reductions in mean rod diameter, interrod spacing, and bulk volume fraction for samples solidified in low-$\bar{g}$ with respect to 1-$\bar{g}$ at V = 30 cm/h and G_L = 100°C/cm.
- No statistically significant dependence of MnBi rod diameter and interrod spacing distributions on gravity vector orientation and imposed thermal gradients during solidification over a range of V = 3 to 30 cm/h and G_L = 20 to 150°C/cm.
- That the thermal gradient in the solid depends on gravity vector orientation for V = 3 cm/h and G_L = 20°C/cm; a larger gradient was observed for the growth down direction (thermally unstable) as compared with growth up (thermally stable).
- The presence of a nonequilibrium metastable magnetic phase that coexists with the equilibirum MnBi phase and transforms during isothermal heat treatment.
- That the admixture of magnetic phases depends on growth velocity, thermal gradient, and gravity vector orientation during solidification.

A candidate mechanism involving convectively induced thermal fluctuations in 1-$\bar{g}$ is proposed to explain the differences between 1-$\bar{g}$ and SPAR VI flight results.

In view of the results obtained and candidate mechanism proposed, future experiments in both low-$\bar{g}$ and 1-$\bar{g}$ are suggested to quantify and understand the phenomena observed. Another low-$\bar{g}$ experiment should be performed at a higher growth velocity. This low-$\bar{g}$ experiment would help corroborate the present low-$\bar{g}$ results as well as provide smaller MnBi particles than we can grow in 1-$\bar{g}$. Another experiment involves utilizing applied magnetic fields and lower thermal gradients in 1-$\bar{g}$ to attempt to damp out and, therefore, minimize thermal fluctuations.

C-4

ACKNOWLEDGMENTS

The authors express their deep appreciation to G. Busch, J. Drauch, R. Lange, E. Marten, and W. Poit of Grumman for their experimental assistance and suggestions, and to P. N. Adler, W. Aubin, and J. Papazian of Grumman for technical guidance and encouragement. We would also like to thank W. Wilcox and P. S. Ravishankar of Clarkson College for their insight, experimental assistance, and guidance. We are indebted to B. Brandt, S. Foner, E. McNiff, and L. Rubin of the Francis Bitter National Magnet Laboratory for their technical assistance and rewarding discussions, as well as to M. Glicksman of Rensselaer Polytechnic Institute and C. Graham of the University of Pennsylvania for many helpful suggestions. Finally, we wish to thank R. Locker of General Electric and J. Noel and F. Reeves of the Marshall Space Flight Center for their untiring efforts in making the SPAR VI flight experiment successful.

REFERENCES

1. W. A. Tiller, "Liquid Metals and Solidification," American Society for Metals, Cleveland, Ohio, p 276, 1958.

2. J. S. Turner, Buoyancy Effects in Fluids, Cambridge, London, 1973.

3. S. R. Coriell, M. R. Cordes, W. J. Boettinger, and R. F. Sekerka, "Convective and Interfacial Instabilities During Unidirectional Solidification of a Binary Alloy, National Bureau of Standards Internal Report 78-1483, 1978.

4. W. R. Wilcox, "Effect of Freezing Rate Changes on the Mean Composition of Binary Composities," Aerospace Report No. TR-1001(2250-10)-11, El Segundo, Calif, 1967.

5. W. R. Wilcox, private communication.

6. T. Chen, "Contribution to the Equilibrium Phase Diagram of the Mn-Bi System Near MnBi," Journal of Applied Physics, Vol 45, p 2358, 1974.

7. R. G. Pirich, G. Busch, W. Poit, and D. J. Larson, Jr., "The Bi-MnBi Eutectic Region of the Bi-Mn Phase Diagram," Metallurgical Transactions A, Vol 11A, p 193, 1980.

8. General Electric Company, Space Sciences Laboratory, "Operating Manual for Automated Direction Solidification System," prepared for NASA under contract NAS8-31536, June 1978.

9. M. R. Notis, D. Shah, C. D. Graham, Jr., and S. R. Trout, "Magnetic Anisotropy in MnBi Particles Grown by Directional Solidification of the Mn-Bi Eutectic," Journal of Applied Physics, Vol 49 p 2043, 1978.

10. M. R. Notis, D. Shah, J. Young, and C. D. Graham, Jr., "Structure and Magnetic Properties of Directionally Solidified Bi-MnBi Eutectic Alloys," IEEE Transactions, Vol MAG-15, p 957, 1979.

11. R. G. Pirich and D. J. Larson, Jr., "Magnetic and Metallurgical Properties of Directionally Solidified Bi/MnBi Composites: The Effects of Annealing," Journal of Applied Physics, Vol 50, p 2425, 1979.

12. R. G. Pirich, D. J. Larson, Jr., and G. Busch, "The Role of Processing Parameters on the Magnetic Properties of Directionally Solidified Bi/MnBi Composites," IEEE Transactions, Vol MAG-15, p 1754, 1979.

13. R. G. Pirich, "Characterization of Effects of Plane-Front Solidification and Heat Treatment On Magnetic Properties of Bi/MnBi Composites," IEEE Transactions Mag, to be published, Sept 1980.

14. W. J. Boettinger, S. R. Coriell, F. S. Biancaniello, and M. R. Cordes, "Solutal Convection During Directional Solidification," National Bureau of Standards Internal Report NBSIR 79-1767, 1979.

15. P. S. Ravishankar, Ph. D. dissertation, Clarkson College of Technology, 1979.

16. A. Muller and M. Wilhelm, "On Periodic Changes of Temperature in Liquid Crystallizing InSb," Z. Naturforsch, Vol 19a, p 254, 1964.

17. W. R. Wilcox and L. D. Fullmer, "Turbulent Free Convection in Czochralski Crystal Growth," Journal of Applied Physics, Vol 36, p 2201, 1965.

18. H. P. Utech and M. C. Flemings, "Elimination of Solute Banding in Indium Antimonide Crystals by Growth in a Magnetic Field," Journal of Applied Physics, Vol 37, p 2021, 1966.

19. H. D. Utech and M. C. Flemings, Journal of Crystal Growth, Pergamon Press, New York, p 651, 1967.

20. D. Hurle, T. J. Jakeman, and E. R. Pike, "Striated Solute Distributions Produced by Temperature Oscillations During Crystal Growth from the Melt," Journal of Crystal Growth, Vol 3/4, p 633, 1968.

21. D. Hurle, Journal of Crystal Growth, Pergamon Press, New York, p 659, 1967.

22. K. A. Jackson and J. D. Hunt, "Lamellar and Rod Eutectic Growth," Transactions of the AIME, Vol 236, p 1129, 1966.

23. J. D. Verhoeven and R. H. Homer, "The Growth of Off-Eutectic Composites from Stirred Melts," Metallurgical Transactions, Vol 1, p 3437, 1970.

24. R.G. Pirich and D. J. Larson, Jr., "The Effect of Gravity Vector Orientation during Directional Solidification on the Magnetic and Microstructural Properties of Bi/MnBi." presented at 157th Electrochemical Soc. Mtg., St. Louis, Missouri, 1980.

25. R. F. Sekerka and S. R. Coriell, "Influence of the Space Environment on Some Materials Processing Phenomena," to be published.